Investigations on ZnO-Graphene Oxide Nanomaterials and Nanocomposites: Synthesis, Functional Properties and Applications

Thesis submitted to

Cochin University of Science and Technology (CUSAT)

in partial fulfilment of the requirements for the Degree of

Doctor of Philosophy in Chemistry

Under the Faculty of Science

By

BABITHA K. B.

(Reg. No. 4175)

Under the Supervision of

Dr. S. Ananthakumar

Materials Science and Technology Division
CSIR-National Institute for Interdisciplinary Science and Technology (NIIST)
Council of Scientific & Industrial Research (CSIR), Govt. of India
Thiruvananthapuram – 695019
INDIA

February 2018

Dedicated to My Husband and

Our beloved Family.....

DECLARATION

I, Babitha K. B., hereby declare that the work presented in the Ph. D. thesis entitled "**Investigations on ZnO-Graphene Oxide Nanomaterials and Nanocomposites: Synthesis, Functional Properties and Applications"** is an independent research work carried out by me for the award of degree of Doctor of Philosophy in Chemistry under the Faculty of Science of the Cochin University of Science and Technology (CUSAT), under the guidance of Dr. S. Ananthakumar, Senior Principal Scientist, Functional Materials Section, Material Science and Technology Division, CSIR-National Institute for Interdisciplinary Science and Technology (CSIR-NIIST), Thiruvananthapuram. I further declare that this thesis or any part of it has not been submitted anywhere else for any other degree, diploma, or other similar title.

BABITHA K. B.

Place: Thiruvananthapuram
Date: 21-2-2018

COUNCIL OF SCIENTIFIC AND INDUSTRIAL RESEARCH
NATIONAL INSTITUTE FOR INTERDISCIPLINARY SCIENCE AND TECHNOLOGY (CSIR-NIIST)
Industrial Estate P. O., Pappanamcode
Thiruvananthapuram-695019, Kerala, INDIA
www.niist.res.in

Dr. S. Ananthakumar
Senior Principal Scientist
Functional Materials Section
Materials Science and Technology Division

Ph: 0471-2515289 (Off)
09497271547 (Mob)
Email: ananthakumar70@gmail.com

CERTIFICATE

Certified that the work embodied in the thesis entitled, "**Investigations on ZnO-Graphene Oxide Nanomaterials and Nanocomposites: Synthesis, Functional Properties and Applications"** is an authentic record of the research work carried out by Mrs. Babitha K. B., Functional Materials Section, Materials Science and Technology Division, CSIR-National Institute for Interdisciplinary Science and Technology (CSIR-NIIST), Thiruvananthapuram under my supervision in partial fulfilment of the requirement for the degree of Doctor of Philosophy in Faculty of Science of the Cochin University of Science and Technology (CUSAT). It is further certified that no part of this thesis has been presented previously anywhere else for the award of any other degree. All the relevant corrections and modifications suggested by the audience during the pre-synopsis seminar and recommended by the Doctoral committee have been incorporated in this thesis.

Dr. S. Ananthakumar
(Research Guide)

Place: Thiruvananthapuram
Date: 21-2-2018

Acknowledgements

I would like to express my sincere gratitude to all the people who have helped me in this journey of completing the thesis work. Truly, words are not enough to express my gratitude to all of them. First of all, I would like to appreciate my thesis supervisor Dr. S. Ananthakumar (Senior Principal Scientist), who has supported me with extremely worthy instructions, encouragement, advice, attention, and valuable criticisms to complete this thesis work. This thesis would not have been possible without his help, support, and patience. I take this opportunity to salute him for his supporting attitude, which helped me to think and work in the right direction.

I extend my deepest gratitude to our Director Dr. A. Ajayghosh, Dr. Suresh Das, and Dr. Gangan Prathap, present and former Directors of CSIR-NIIST for providing me the opportunity as well as necessary facilities to accomplish my research work at CSIR-NIIST.

I also acknowledge Dr. P. Prabhakar Rao, Dr. M. L. P Reddy, and Dr. M. T. Sebastian, present and former Heads of Materials Science and Technology Division (MSTD) for their constant support.

I am very much happy in expressing my deep sense of gratitude to Dr. K. G. K. Warrier, former HOD and Emeritus Scientist (Rtd.) for his constant inspiration and support throughout my research period. I extend my sincere gratitude to Dr. Satyajit Shukla, for helping me to do one year M. Tech project work before this thesis, which really became an inspiration for doing Ph. D.

I extend my sincere thanks to Dr. U. S. Hareesh, Dr. Balagopal, Dr. S. K. Ghosh, Dr. K. G. Nishanth, from Functional Materials Section, for their support, suggestions and advices during the course of my work. I would also like to thank all the other scientists from MSTD for their help and support.

I express my sincere gratitude to my external expert from CUSAT Dr. S. Sugunan, Professor (Rtd.), Department of Applied Chemistry, CUSAT for his help to conduct my presynopsis presentation and all formalities in CUSAT. I would like to extend my sincere gratitude to Dr. T. P. D Rajan (Principal Scientist and DC member), for all the help and support.

I am very much thankful to Mr. A. Peer Mohamed, Technical officer for his technical support to carry out the characterization studies during the research period. I am also thankful to Mr. P. Perumal for his support.

I am very grateful to Dr. R. B. Rakhi, CSTD for the sensor studies reported in this thesis. I am also immensely thankful to Dr. S. Nishanth Kumar, APNP Division for his support with the antibacterial studies. I thank Mr. Kiran Mohan and Mr. Robert Philip for the TEM analysis, Mr. M. R. Chandran, Mrs. Lucy Paul, Mrs. Soumya, and Mr. V. Harish Raj for SEM analysis, Mr. P. Guruswamy and Mr. Prithviraj for XRD.

I always cherish the support and warm friendship of former colleagues Dr. Linsha Vazhayal, Dr. K. V. Mahesh, Dr. Soumya, Dr. S. Anas, Dr. P. S. Suchithra, Dr. K. B. Jaimy, Dr. V. S. Smitha, Dr. K. A. Manjumol, Dr. T. S. Sree Remya, Dr. Asha Krishnan, Dr. Harsha Narayani, Dr. Suyana, Dr. Rahul, Dr. P. V. Shubha, Dr. Sankar Sasidharan, Dr. Manu Jose, and Mr. Hareesh.

I wish to thank all my current and former colleagues Mrs. Jeen Maria Mathews, Ms. Shuhailath, Ms. Minju, Mrs. Sheemol, Mr. Balanand, Mr. S. Vaisakh, Mr. S. S. Sujith, Mr. Y. Dhaneesh, Mr. Akhil Das, Ms. B. Susheela, Mr. Vishnu, Mr. Goutham, Mr. Raimond, Mr. Shibin, Mr. Shinto Alex, Mr. Vishnu Prasad, Ms. Minju Thomas, Mrs. Megha Joy, Ms. Swetha, Ms. K. Shijina, Ms. Nimisha, Mr. M. Firoz, Mr. Gokul, Mr. S. Prashanth, and Mrs. Ambili for their support during my Ph. D. period.

I am thankful to Council of Scientific and Industrial Research (CSIR) for the research fellowship and CSIR-National Institute of Interdisciplinary Science and Technology (CSIR-NIIST) for providing me the platform to work on.

I am thankful to the help and support provided by the Masters Project students Ms. Jani Matilda, Mrs. Pooja Vijayan, Mrs. P. Chithra, Mrs. Asha, and Mrs. Sucheena.

I would like to thank my parents P. C. Babu and Mahila Babu, and my dear sister Sabitha Satheesh for all their love, support, and care. I have no words to express my heartfelt gratitude to my dearest husband, Mr. P. Pratheesh for all his support and care throughout this time period. My in laws Thankappan (Late) and Vijayamma, sister in laws (Preethi and Keerthana), Brother in laws (Praveen, Satheesh, and Manesh), Aadhi, Ammu, Adwaith, and Paru are acknowledged for all the untiring support and prayers during the research period.

I extend my sincere thanks to all my teachers for all the encouragement and blessings. All my friends, classmates, and relatives are acknowledged for their support and inspiration.

Last but not the least I humbly bow before 'The Almighty God' for all the blessings that showered upon me.

Babitha K. B.

CONTENTS

LIST OF FIGURES

LIST OF TABLES

LIST OF ABBREVIATIONS

0D	Zero dimensional
1D	One dimensional
2D	Two dimensional
3D	Three dimensional
APTMS	3-aminopropyltrimethoxy silane
BET	Brunauer-Emmet-Teller
CB	Conduction band
CV	Crystal violet
DMF	N, N, Dimethyl formamide
e^-	electron
EDX	Energy dispersive X-ray spectroscopy
e.g.	Exempli gratia (for example)
et al.	Et alaia (and others)
etc.	Et cetera(and so on)
FTIR	Fourier transform infrared spectroscopy
GO	Graphene oxide
HRTEM	High resolution transmission electron microscopy
i.e.	In est (in other words)
JCPDS	Joint committee of powder diffraction standards
MB	Methylene blue
MG	Malachite green
MW	Microwave
PEG	Poly Ethylene Glycol
rGO	Reduced graphene oxide
Rh6G	Rhodamine 6G
ROS	Reactive oxygen species
rpm	Rotations per minutes
SAED	Selected area electron spectroscopy
S_{BET}	Surface area determined according to the BET theory
SEM	Scanning electron microscopy

TEM	Transmission electron microscopy
TGA	Thermogravimetric analysis
UV-Vis	Ultra-violet visible
VB	Valance band
via	Through or By way of
XRD	X-ray diffraction
ZnO	Zinc oxide

LIST OF SYMBOLS

Å	Angstrom
%	Percentage
^{o}C	Degree celsius
2θ	Diffraction angle in degrees
g	Gram
min	Minute
mL	Milliliter
M	Molar
λ	Wavelength
wt %	Weight percentage
h	Hour
μm	Micrometer
nm	Nanometer
mg	Milligram
P/P_0	Relative pressure
s	Seconds
vs.	Versus
θ	Contact angle/Bragg angle

Preface

Materials processed *via* nanocomposite strategy offer thermo-mechanical and electro-chemical properties compared to their individual nanomaterials. Semiconducting metal oxide nanocomposites prepared with two or more nano scale active reinforcements show synergic effect and such nanocomposites work well as chemical sensors, catalysts, and membranes. Carbon based nanomaterials like carbon nanotubes (CNTs), graphene, graphene oxide (GO), and reduced graphene oxide (rGO) are some of the well-recognized multifunctional nanomaterials largely studied for energy related applications. Incorporation of such carbon based nanostructures can possibly overcome the inherent difficulties of semiconducting nano ZnO. In-situ growth of ZnO nanostructures on such multifunctional graphene based supports is one effective way to obtaining readily dispersed, high surface area, meso/nano porous ZnO.

The present thesis focuses on the synthesis and characterization of nano scale ZnO with and without carbonaceous nano materials and explored the functional properties such as catalytic degradation of some selective pollutants, sensing molecules, and water disinfection.

The entire thesis is framed into seven chapters. **Chapter 1** is the introductory chapter giving the background of the ZnO nanostructures, nanocomposites, and its associated nano morphologies for functional applications. An overview of the crystal structure, synthetic strategies reported so far is briefly mentioned. General physical/chemical properties of nano ZnO reported in the literature are presented. Brief account on the multifunctional applications is also compiled. An overview of synthetic strategies and properties of GO, rGO, and ZnO-GO/rGO nanocomposites are also

presented. The aim and objectives of the work are precisely defined at the end of this chapter.

Since many analytical techniques are involved in the present study to analyze the phase purity, crystallinity, particle dimension, particle morphology, band gap energy, surface area, chemical nature *etc.* using XRD, SEM/TEM, UV-vis spectroscopy, BET surface area, and FTIR, a chapter is dedicated to briefly explain all these advanced techniques. C**hapter 2** is an outline of the instrumentation techniques employed to characterize the nano ZnO, GO, and rGO and its functional properties.

Chapter 3 deals with the microwave assisted in-situ processing of ZnO-rGO nanoarchitectures, a catalytic sorbent for the effective removal of cationic dyes. GO is catalytically activated *via* in-situ growth of nanocrystalline ZnO to result in ZnO@rGO nanocomposite architectures. In the similar way, ZnO/Si@rGO nanocomposites in the presence of APTMS crosslinking agent were also prepared. The combined adsorption and photocatalytic degradation property of both ZnO@rGO and ZnO/Si@rGO against the adsorption and photodegradation of a series of cationic organic dyes were compared. These results were compared with pure ZnO.

Chapter 4 describes design and synthesis of ZPMx/Si@GO nanocomposites with various aspect ratios of ZnO for water disinfection. This study investigated the role of poly ethylene glycol (PEG) in the microwave synthesis of ZnO (ZPMx) nanorods. The molecular weight of PEG was found to strongly influence the aspect ratio of the ZnO nanorods. The as-prepared ZPMx nanorods were post-grafted onto the surface of GO sheets using APTMS as a cross-linking agent to obtain ZPMx/Si@GO nanocomposites. The dependence of the antibacterial behaviour on the aspect ratio of the ZPMx nanorods and GO was also investigated. An antibacterial assay was carried out using both the Gram-positive bacteria and Gram-negative bacteria.

Chapter 5 illustrates enzyme free electrochemical detection of urea and glucose using ZnO@rGO nanocomposites. The electrochemical performance of the nanocomposite was investigated by cyclic voltammetry. A green synthetic strategy was adopted for the preparation of ZnO@rGO nanocomposites. A bio-inspired synthesis of ZnO nano-architectures has been done using monosaccharide, disaccharide, and polysaccharide as bio-templates.The as-prepared morphologically tuned ZnO nanoarchitectures thus obtained were uniformly distributed on the surface of rGO sheets, which results in the ZnO@rGO nanocomposites. Zinc (Zn) dust, a waste by-product from an industry (Binani Zinc Limited, Kerala, India) was employed for the chemical reduction of GO. Finally, the as-prepared ZnO@rGO nanocomposites were employed for the electrochemical detection of urea and glucose.

Chapter 6 comprises of two sections. The first section of this chapter deals with the synthesis and characterisation of 3-aminopropyl trimethoxy silane (APTMS) treated nano ZnO. Ultra fast microwave assisted method is explored for the bulk preparation of nano ZnO with and without APTMS. Aqueous synthesis of size controlled, surface engineered, ZnO nanoarchitectures reported in this work, is found to be potentially useful as nanofiller for the preparation of stable bionanocomposite films. Hence the processing of ZnO/Si@gelatin and ZnO/Si/GO@gelatin bionanocomposites is described in the 2nd section of chapter 6. The bionanocomposite flexible films were fabricated *via* solution casting technique. The experimental results suggest that ZnO/Si/GO has the novel nanofiller for gelatin films that can be used for bio-friendly coatings on food-packs, wound dressing, and adsorbent pads for surgical uses *etc*.

The final chapter of the thesis (**Chapter 7**) briefly summarize the essential outcome of the thesis. Future perspectives are also lightly provided in the same chapter.

CHAPTER 1

ZnO Nanostructures and Nanocomposites containing Graphene based Reinforcements

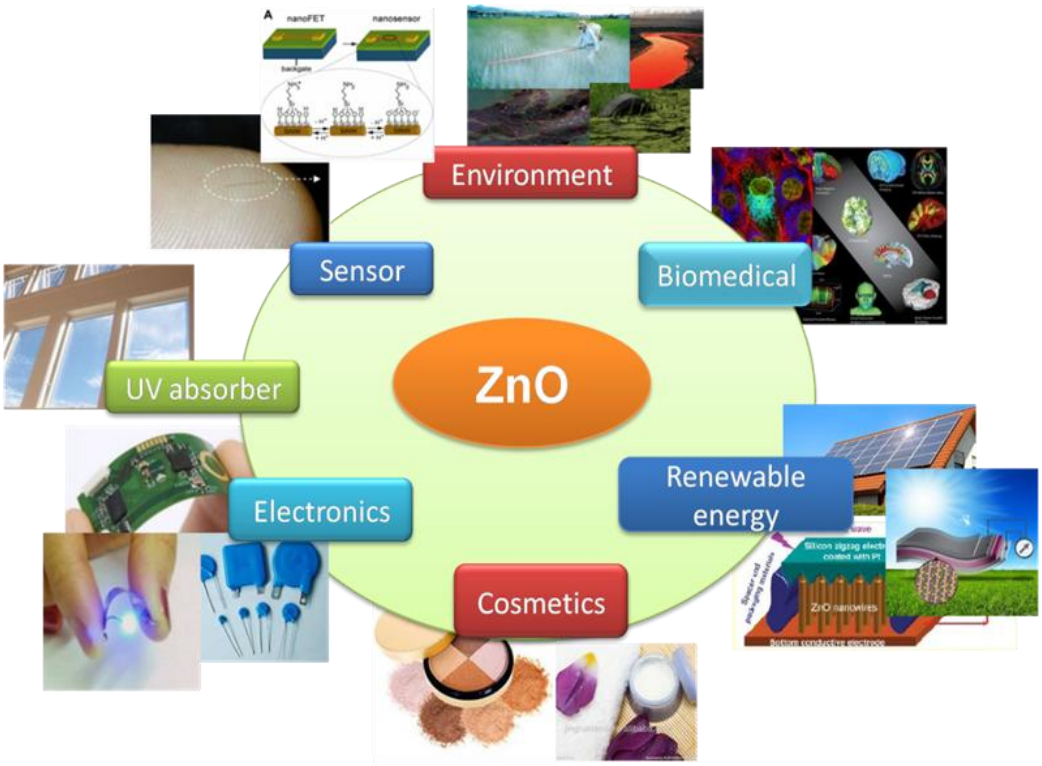

Zinc Oxide: A Versatile Functional Material for Diversified Application Fields

1.1 Zinc Oxide Nanomaterials: Structural Features and Synthetic Strategies

Zinc oxide (ZnO) is a non-toxic technologically important, inorganic material attracted much attention for the design and development of functional coatings, catalytic membranes, hybrid nanostructures, and miniature solid-state components (Costenaro *et al*., 2011; Pueyo *et al*., 2011; Liu *et al*., 2012). It is classified as II-IV semiconducting metal oxide. Typically it has wurtzite crystal structure in which each anion is surrounded by four cations in the corners of a tetrahedron and vice versa. The tetrahedral coordination gives rise to polar symmetry along the hexagonal axis and also results in non-central symmetric structure (Shi *et al*., 2012). It indicates sp^3 covalent bonding (Kenmoe *et al*., 2017). The

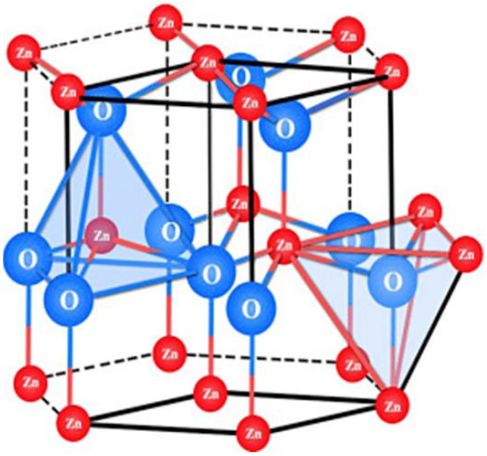

Figure 1.1 Wurtzite ZnO; Zinc atoms are shown in red and oxygen atoms are shown in blue, respectively (http://clipground.com/image-post/53527-rhomboedrische-crystal-structure-clipart-9.jpg.html).

wurtzite ZnO crystal has a hexagonal unit cell (Figure 1.1) with two lattice parameters, a and c. The lattice parameters have values a=3.2495Å and c=5.2069 Å. It belongs to the space group of C^4_{6V} or $P6_3mc$ (Kumar *et al*., 2015). Literature indicates two more crystal structures for ZnO; namely zinc blend and rock salt (Kulkarni *et al*. 2011). In ZnO, the Zn-O bond is strongly ionic in nature and thus ZnO is a compound whose ionicity resides at

the borderline between pure covalent and ionic. The physical properties of well crystalline wurtize ZnO is summarized in Table 1.1.

Table 1.1 Physical properties of Wurtzite ZnO

Parameters	Values
Molecular mass	81.37 g mol^{-1}
Energy band gap	3.37 eV, (Direct)
Density	5.606 g cm^{-3}
Exciton binding energy	60 meV
Melting point	1975 ^{o}C
Refractive index	2.008 to 2.029
Bond length	1.977 μm
Ionic radius	Zn-0.060 nm, O-0.138 nm
Thermal conductivity	0.6-1.16 W K^{-1} m^{-1}
Specific heat	0.125 cal g^{-1} $^{o}C^{-1}$
Electron mobility	210 cm^2 V^{-1} s^{-1}
Thermal constant at 573 K	1200 mV K^{-1}
Electron effective mass	0.28 m_0
Hole effective mass	0.59 m_0

It is evident from the literature that some of these physical properties slightly change when the dimensional features of ZnO are systematically controlled from the micrometre to sub-nanometre scale by adopting appropriate synthesis strategies. It paves the way to tailor the ZnO nanomaterials for various innovative applications. The extensive applications of ZnO and ZnO nanomaterials are; cosmetics, sunscreens, paints, pharmaceuticals, catalysis (Curridal *et al*., 2003; Kamat *et al*., 2002), sensors, varistors (Kim *et al*., 2011; Li *et al*., 2010), electrical and optical devices (Feldmann *et al*., 2003; Zheng *et al*., 2002; Wu *et al*., 2004), solar cells (Gao *et al*., 2006), batteries, electronic devices *etc*. The direct and wide band gap energy (E_g = 3.37 eV) of ZnO in the UV

spectral region enables its application in light emitting diodes, laser diodes, photodetectors, solar cells, nanogenerators, transistors, sensors, and catalysts. Exceptionally large exciton binding energy or Rydberg energy (60 meV) at room temperature makes ZnO a promising material for optical devices (Qi *et al*., 2016). ZnO possess an emission spectrum in the region of near-UV, which make it useful in solar cell applications, photocatalysis, and electronic sensor (Ozgur *et al*., 2005; Jeong *et al*., 2006; Look *et al*., 2001; Moritz *et al*., 2013; Nair *et al*., 2011; Sun *et al*., 2007; Wan *et al*., 2004). Furthermore, ZnO nanoparticles have shown antibacterial activity and regarded as safe to human beings (Chu *et al*., 2010). The excellent antibacterial and UV attenuation properties (Junior *et al*., 2017) makes the material suitable for cosmetics, paints, and plastics (Sawai *et al*., 2003; Ghule *et al*., 2006). Moreover, non-toxicity, environmental friendliness, low cost, abundant natural recourses, and excellent thermal stability (melting point ~2248 K) make this material more attractive for industrial uses (Qi *et al*., 2016). Due to such market potential, materials scientists and engineers are thriving hard to develop high value ZnO based nanomaterials and nanocomposites for its complete commercial exploitation.

ZnO nanostructures are usually synthesized by vapour phase as well as solution phase techniques. Vapour phase methods include physical vapour deposition (PVD) (Zhou *et al*., 2009), chemical vapour deposition (CVD) (Haga *et al*., 2000), molecular beam epitaxy (MBE) (Dhar *et al*., 2005), metal-organic chemical vapor deposition (MOCVD) (Kim *et al*., 2001), thermal evaporation (Yan *et al*., 2003; Pan *et al*., 2001; Yan *et al*., 2003; Li *et al*., 2002), combustion method, aqueous chemical growth (ACG), microwave decomposition *etc*. Similarly, solution phase synthesis methods can be listed as controlled precipitation (Kim *et al*., 2005), sol-gel method (Bao *et al*., 1998), hydrothermal synthesis (Le *et al*., 2006; Liu *et al*., 2006), reflux, solvothermal method (Liu *et al*., 2003; Yang *et al*., 2005; Xu *et al*., 2009), mechano-chemical method (Ao *et al*., 2006), thermal

decomposition, spray pyrolysis and drying (Liu *et al*., 1986), microemulsion synthesis, sonochemical synthesis, and microwave synthesis (Komarneni *et al*., 2000). Most of these synthetic methods produced diversified ZnO nanostructures. It is evident from the literature that numerous authors have shown nano ZnO in the forms of zero-dimensional (0D) spherical particles, quantum dots to one-dimensional (1D) nanowires, nanorods, nanotubes, and nanoneedles; two dimensional (2D) nanosheets, nanoplates, nanocups, and nanobelts; and even three-dimensional (3D) nanotrees, nanocones, nanoflowers, nanorings, nanopyramids, nanobrushes, dandelions, hollow spheres *etc*. (Wang *et al*., 2003; Park *et al*., 2004; Yan *et al*., 2006; Wang *et al*., 2008; Dia *et al*., 2008; Zhang *et al*., 2009; Liu *et al*., 2009; Wang *et al*., 2010; Sinha *et al*., 2010; Jung *et al*., 2011; Li *et al*., 2013). It is clearly documented that in any ZnO nano materials the processing factors such as chemistry of the starting precursors, concentration, capping agents, solvents, reaction time, temperature *etc*., play important role in crystal growth, morphology, and dimensions (Jun *et al*., 2006). In general the growth mechanism is stated as; a polar ZnO crystal is composed of alternating planes of tetrahedrally coordinated Zn^{2+} and O^{2-} ions stacked along the c-axis. These oppositely charged ions produce positively charged (0001) planes rich in Zn^{2+} ions and negatively charged $(000\bar{1})$ planes rich in O^{2-} ions (Karunakaran *et al*., 2013). Normally, ZnO nuclei tend to aggregate along the c-axis, resulting in rod/needle/wire like nanostructures due to the electrostatic interaction. Even though the direct decomposition of high purity metallic zinc *via* vapour phase method is followed in industry scale mass production of ZnO, solution phase technique is preferred for size and shape controlled ZnO nanomaterials (Kim *et al*., 2012; Chun *et al*., 2009).

1.2 Microwave Synthesis of ZnO Nanoparticles

In this research study use of microwave energy is considered for obtaining ZnO nanomaterials. Synthesis of inorganic nanomaterials using microwave energy is a well-

researched area. The main advantage realized with microwave energy is its quick interaction with the matter depending upon the dielectric nature of the reactants. In conventional heating, the heat energy is usually received from the external heating sources (Kajbafvala *et al*., 2009). In microwave heating, the heat is internally generated within the material depending upon the net polarization effect of the molecules and transferred from the bulk to surface. For heating and drying applications the electromagnetic radiation in the frequency range 0.3 to 300 GHz is used. Other notable advantages of microwave heating over conventional heating are (i) high heating rates leads to the rapid particle nucleation and growth (ii) require low reaction time (iii) wide range of reaction conditions can be used (iv) better yield with less by products (v) different microwave absorbing properties leads to better reaction selectivity (vi) easy to handle (vii) does not produce pollution (viii) results in high quality nanomaterials with minimum contamination, and (ix) better reproducibility (Omar *et al*., 2014; Lv *et al*., 2012).

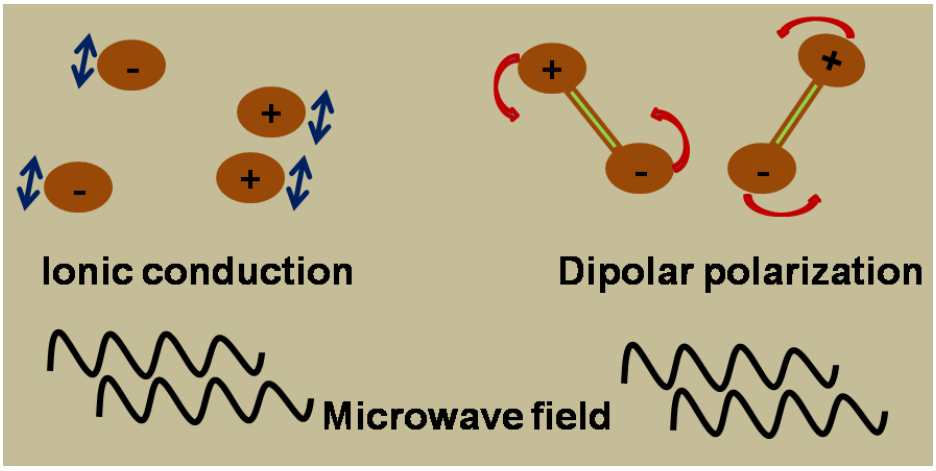

Figure 1.2 Schematic diagram showing microwave mediated heating mechanisms: ionic conduction and dipolar polarization.

Typically, the mechanisms in microwave heating are said to be dipolar rotation and ionic conduction (Figure 1.2). The dipolar rotation occurs when polar molecules having an electrical dipole moment align itself with the applied electromagnetic field. In this process,

energy is lost as heat due to the molecular friction and dielectric loss. The heating mechanism in ionic conduction results from the dissolved or dissociated charged particles or ions. The ions oscillate back and forth under the influence of the microwave radiation and produce heat (Ambrozic *et al*., 2011).

The above said mechanisms are highly effective for the microwave assisted synthesis of colloidal nanoparticles using aqueous methods. Here the required concentration can be easily adjusted and in aqueous synthesis desired impurity phases, low level dopants, capping agents, stabilizers *etc*. can be accurately controlled for obtain the required colloidal nanoparticles. In solution phase synthesis of nano ZnO, the chemical precursors/reactants normally used are; zinc nitrate, zinc acetate, and zinc chloride. In highly polar aqueous medium, the microwave energy readily interacts with these reactants and produced well crystalline nano structures at temperatures as low as 80 ^{o}C. Earlier studies clearly show ZnO nanostructures with morphological features such as nanowires, nanorods, nanoneedles, nanotubes, nanobelts *etc*., were possible in microwave assisted synthesis. In this thesis, microwave assisted reflux technique is explored for obtaining ZnO nanomaterials and graphene based nano reinforced ZnO nanocomposites. The reason for selecting the graphene based nanostructures is described later.

1.3 Limitations of ZnO

Even though ZnO possess many advantages, the scientific issues often seen with ZnO nanostructures are; low tolerance towards highly acid and alkaline conditions (Adams *et al*., 2006), low surface area, uncontrolled crystal growth, and tendency to undergo aggregation (Daniel *et al*., 2004; Wolf *et al*., 2002). In most of the reported works, the problems related to ZnO are tackled by the techniques such as surface modification/composite approach/deposition of nanoparticles on suitable substrates *etc*. In this thesis work a focus is paid on ‘composite approach’.

1.4 Composite Approach

In recent years, nanocomposite architectures have attracted great interest because they offer enhanced thermo-mechanical and electrochemical properties. The term *nanocomposite* refers multiphase solid state matrix materials containing homogenous dispersion of one, two or three dimensional particles (*e.g*. spherical particles/platelets/fibres/sheets *etc*.) as reinforcements. Physicists defined the dispersed phase is strictly fall within the range of <100 nm. However colloidally stable dispersed phase even if it has dimensional length in several micrometres but thickness/width/diameter *etc*., in nano range is acceptable and accounted as nano-reinforcements. Interestingly, the anisotropic nature of dimensionally varied nano size second phases found to exhibit useful optical, electrical, thermal, mechanical, electrochemical, and catalytic properties that triggered and motivated curiosity in 'nanocomposite' functional materials (Ren *et al*., 2016). Functional Nanocomposites are developed either 'in-situ growth' technique or by simply blending nano scale particles with its bulk counterparts. Such nanocomposite systems result in synergic effect to ultimately improve the catalytic/sensing/optical properties of the entire materials.

There are many published reports available on ZnO based nanocomposites. Nano dimensional Al_2O_3, CuO, MgO, MnO_2, TiO_2, SnO_2, ZrO_2, CeO_2, Fe_2O_3 were used as reinforcement to maximize the beneficial properties of nano ZnO. Table 1.2 presents some of the nanocomposite systems reported earlier;

Table 1.2 ZnO based nanocomposites reported for functional applications

Nanocomposites	Synthesis technique	Properties/applications	References
ZnO-Al_2O_3	Heterogeneous precipitation	Adsorption of dye	Tajizadegan *et al*., 2013
ZnO-CuO	Electrochemical route	Photocatalysis	Das *et al*., 2017
ZnO-MgO	High pressure synthesis	Luminescent properties	Baranov *et al*., 2010
ZnO-MnO_2	Hydrothermal	Energy storage	Rafiq *et al*., 2017
ZnO-CeO_2		Photocatalysis	Kaur *et al*., 2016
ZnO-TiO_2	Precipitation	Humidity sensor	Yadav *et al*., 2008
ZnO-SnO_2	Sol-gel method	Photocatalysis	Davis *et al*., 2012
ZnO-ZrO_2	Sol-gel sonochemical	Photocatalysis	Aghabeygi *et al*., 2017
ZnO-CeO_2	Flame spray pyrolysis	CO_2 photoreduction	Xiong *et al*., 2017
ZnO-Fe_2O_3	High energy ball milling technique	Magneto optical properties	Chaudhury *et al*., 2016

In line with the above nanocomposite systems, in the past five years a major drift is seen in the literature for exploring carbon based nano reinforcements to obtain ZnO/TiO_2/SnO_2/CeO_2 based semiconducting metal oxide nanocomposites mainly for energy storage applications. In this thesis graphene based nano reinforcements are made into ZnO. Scientifically it is a challenge to process high surface area ZnO even though it is in nano range. Commercially available nano ZnO has BET bulk surface area only < 20 m^2 g^{-1}. It is a great limitation seen with nano ZnO. However many carbon based nanostructures have surface area as high as 500 m^2 g^{-1}. In fact graphene based carbon nanostructure has high electrical conductivity and surface area as high 1200 m^2 g^{-1}. The carbon based nanostructures also have exceptionally high adsorption to range of pollutants. Hence it is important to develop nanocomposites containing semiconducting metal oxide and carbon nanostructures. The following section gives brief account of graphene based nanomaterials and nanocomposites which is relevant to the present investigation.

1.5 Graphene Based Nanomaterials: Graphene Oxide (GO) and Reduced Graphene Oxide (rGO)

1.5.1 Graphene Oxide (GO)

Graphene oxide (GO) is the first commercial product from the graphene family (Zhu *et al*., 2010). GO is a single-atomic layered material. GO is synthesized by the exfoliation of graphite oxide, which is obtained by the powerful oxidation of natural flaky graphite, which is cheap and abundant (Khan *et al*., 2015). The localized defects in the π-structure may serve as a seed point for the oxidation of graphite (Dreyer *et al*., 2010). GO contains range of reactive oxygen functional groups on the basal planes and edges (hydroxyl, carboxyl, carbonyl, and epoxy). This structural feature is well exploited for chemical functionalization for any specific applications. Since these groups have high affinity to water molecules, it is hydrophilic and can be easily dispersed in water as well as in organic solvents. The surface charge measurements (Zeta potential analysis) confirmed that

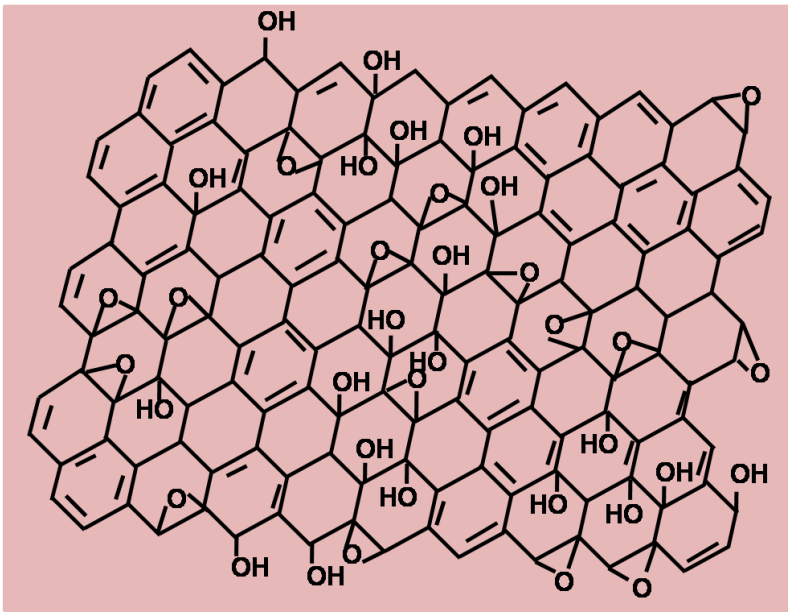

Figure 1.3 Lerf-Klinowski model of GO with the omission of minor groups (carboxyl, carbonyl, ester *etc*.) on the periphery of the carbon plane of the graphitic platelets of GO.

GO sheets acquire negative charge when dispersed in water, due to the dissociation of carboxylic acid, and phenolic hydroxyl groups. Hence GO readily forms a stable colloid in aqueous medium apparently because of the electrostatic repulsion as well as hydrophilicity of GO sheets. Hence complete exfoliation of GO can be achieved by simple sonication technique (Khan *et al*., 2015). The structure and properties of GO mainly depend on the following parameters: synthesis methods, the degree of oxidation, and the source of graphite used (Khan *et al*., 2015). As sp^2 hybridized carbon atoms in graphite are partially degraded in to sp^2-sp^3 hybridised atoms, GO possesses less π-π stacking stability and poor conductivity (Xu *et al*., 2011). However, a suitable treatment with heat, light or chemical reduction the graphene properties are mostly recovered. The well-known model illustrating the structure of GO is proposed by Anton Lerf and Jacek Klinowski. Figure 1.3 represents the Lerf-Klinowski model of GO (Zhu *et al*., 2010), where in the carbon plane is decorated with hydroxyl and epoxy functional groups. Carbonyl groups exist mostly as carboxyl groups and are presented along the sheets edge.

1.5.1.1 Preparation of GO

In 1859, B. C. Brodie performed a reaction to understand the chemical structure of graphite. The reaction was carried out by oxidizing graphite with potassium chlorate ($KClO_3$) and nitric acid (HNO_3). The overall mass of the resulting material was found to be increased compared to the starting graphite. Brodie determined that the resulting material is composed of carbon, hydrogen, and oxygen. Multiple oxidation was further found to increase the molecular mass and the composition of C:H:O. The chemical analysis showed the C:H:O ratio as 61.04:1.85:37.11 with a molecular formula of $C_{2.19}H_{0.80}O_{1.00}$. Later, in 1899, L. Staudenmaier adopted a modified preparation by adding chlorate in multiple aliquots rather than single addition as done by Brodie. This resulted in

overall extent of oxidation similar to Brodie's multiple oxidation approach. In 1959, Hummers and Offeman demonstrated oxidation of graphite by treating with a mixture of potassium permanganate and conc. H_2SO_4 and again found similar level of oxidation. The active species in this oxidation reaction is dimanganese heptoxide (Mn_2O_7). Mn_2O_7 was formed due to the reaction of potassium permanganate with conc. H_2SO_4. The chemical equation for this reduction reaction is given below (Dreyer *et al*., 2010).

$$KMnO_4+3H_2SO_4 \longrightarrow K^++MnO_3^++H_3O^++3HSO_4^- \quad 1.1$$

$$MnO_3^++MnO_4^- \longrightarrow Mn_2O_7 \quad 1.2$$

1.5.2 Reduced Graphene Oxide (rGO)

rGO is a derivative developed from GO. The molecular structure of rGO is much closer to pristine graphene compared to GO. During reduction, oxygen containing functional groups are removed resulting in decreased dispersibility of GO in different solvents. The reduction process found to decrease the hydrophilic character of GO and restoration of π electronic conjugation. In rGO the colour changed from brown to black. The schematic diagram showing the conversion of graphite to rGO is shown in the Figure 1.4.

Reduction of GO is performed with many reducing agents; hydrazine (NH_2-NH_2) and its derivatives, hydroquinone, $NaBH_4$, hydriodic acid (HI), sulphur containing compounds, complex hydrides, vitamin C, hydroxyl amine, nascent hydrogen *etc*., or *via* microwave, hydrothermal, and solvothermal synthetic protocols (Dey *et al*., 2012; Pham *et al*., 2012). The concentration of the remaining oxygen functionalities in rGO has a strong impact on many properties like conductivity and electrochemical activity. During the chemical reduction researchers usually introduced appropriate impurities to obtain desirable properties (Jankovsky *et al*., 2016). Unfortunately, most of the reducing agents are toxic in nature (Dey *et al*., 2012). Hence thermal reduction was preferred over chemical reduction. The mechanism of the thermal reduction is in general described as a process of

decomposition of oxygen containing functional groups yielding carbon dioxide, carbon monoxide, and water released from the structure during the heating process. The evolved gaseous products increase the interlayer pressure finally inducing exfoliation. At high temperatures formation of various hydrocarbons was observed. Hydrocarbons such as benzene, toluene, and naphthalene are possibly released during thermal reduction posing significant issues for this technique (Jankovsky *et al*., 2016). Electrochemical reduction is evolved later and is considered as an effective way for the removal of oxygen containing functional groups from the surface of GO (Zhu *et al*., 2010).

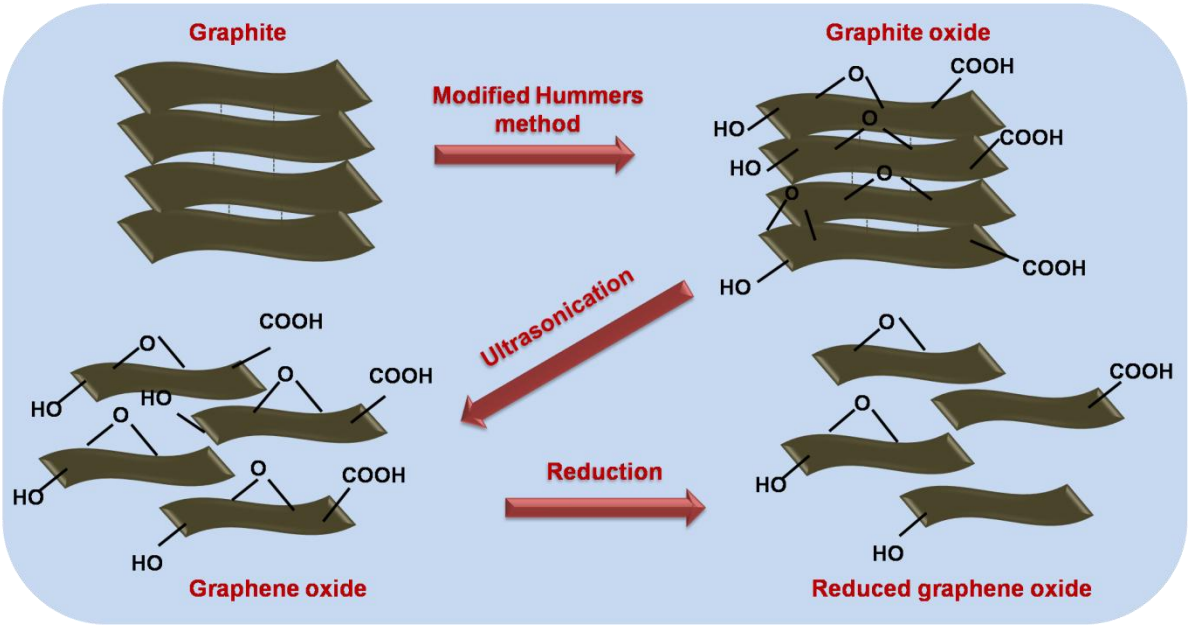

Figure 1.4 Schematic diagram showing the conversion of graphite to graphite oxide, GO, and rGO.

1.5.3 Metal Oxide-GO/rGO Nanocomposites

Design and development of metal oxide-GO/rGO nanocomposites is recommended for improving the beneficial properties of metal oxide nanoparticles so that they can be applied in the niche areas of energy harvesting, energy conversion, and energy storage sectors (Guo *et*

al., 2011). Nano size metal oxides can be grown over rGO sheets for making graphene based nanocomposites. Ex-situ synthesis involves mixing of independently prepared reactant solutions of GO/rGO nanosheets with pre-synthesized metal oxide nanoparticles. In-situ synthesis involves reduction of GO simultaneously with the nucleation and growth of metal oxide nanoparticles from the respective metal salt precursors (Khan *et al*., 2015). The pictorial representation of in-situ and ex-situ methods is given in the Figure 1.5.

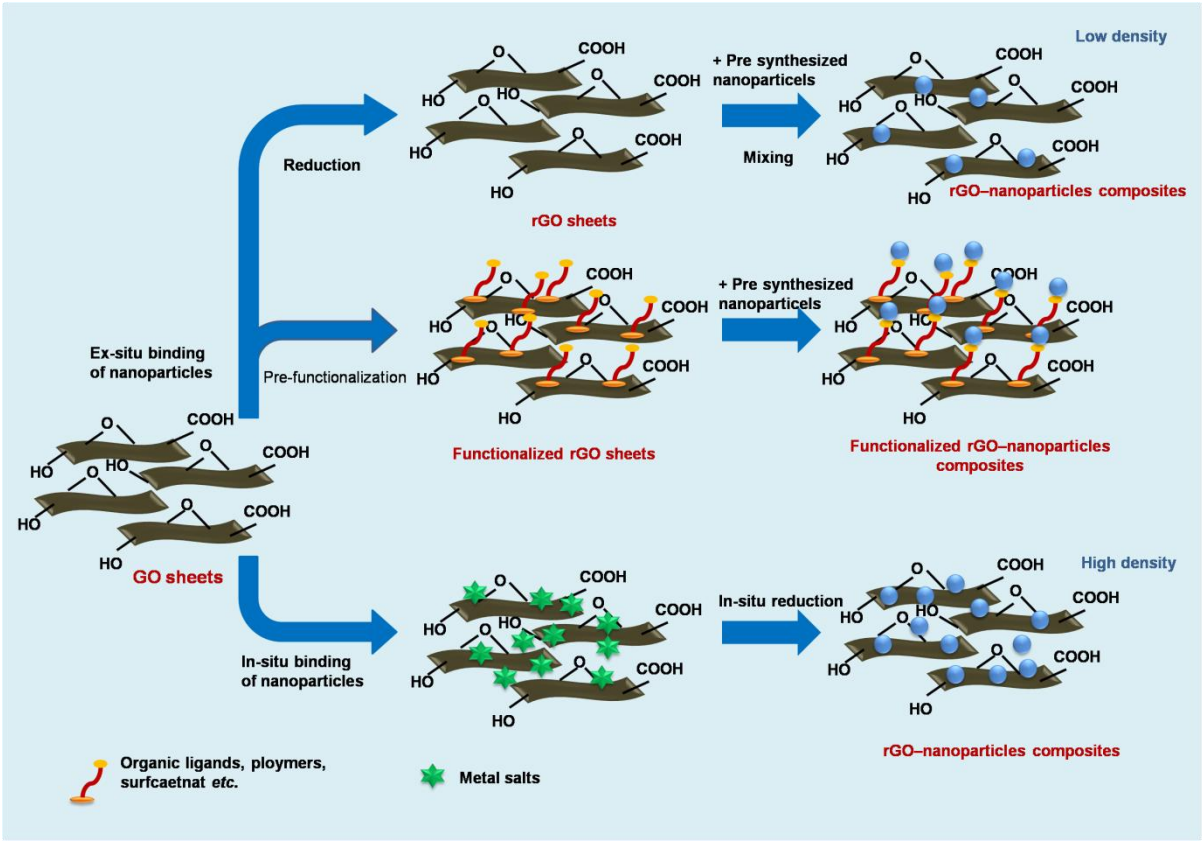

Figure 1.5 Schematic illustration of the binding mechanisms of nanoparticles on to rGO sheets.

Graphene based nanocomposites mostly contains two components. In some cases nanocomposites with multicomponents also attempted based on the end use. In the category of graphene based nanocomposites, the composite architectures are designed as; (i) composites in which GO/rGO act as a continuous phase *i.e*. these nanosheets act as a support

for the attachment of metal/metal oxide nanoparticles (ii) GO/rGO as a nanofillers incorporated in to the continuous matrix of metal/metal oxide and (iii) both GO/rGO and metal/metal oxide nanoparticles act as continuous phase. Within these composite designs, products are mostly seen as films, coatings, and powders. Literature report shows self assembly of GO/rGO with metal/metal oxide components (Khan *et al*., 2015) are highly considered for making functional electronics.

For the successful preparation of high quality graphene based nanocomposites; (i) the GO/rGO should have high solubility in the solution, which is truly critical to retain the GO/rGO as individual sheets to maximise the performance, (ii) the surface of the GO/rGO should contain adequate functional groups to promote the chemical crosslinking of GO/rGO nanosheets with metal oxide nanoparticles, (iii) the morphology of the metal oxide nanoparticles should be well tailored to result in optimum properties (Guo *et al*., 2011). Considering all these factors researchers have prepared GO/rGO based nanocomposites with metal oxide such as SiO_2, Fe_2O_3, TiO_2, SnO_2, ZnO, Al_2O_3, Co_3O_4, MnO_2, Fe_3O_4, clay *etc*. (Guo *et al*., 2011).

1.5.4 Applications of GO/rGO –Metal Oxide Nanocomposites

Literature survey shows graphene based metal oxide nanocomposites can be used mostly for interesting functional applications. Figure 1.6 summarizes the various application studies conducted with graphene based metal oxide nanocomposites. In this present thesis work nanocomposites containing ZnO with GO/rGO are explored for applications like dye adsorption and degradation, water disinfection, sensor, and eco-friendly bionanocomposite films. In the following sections an account of the earlier works conducted on these applications are presented.

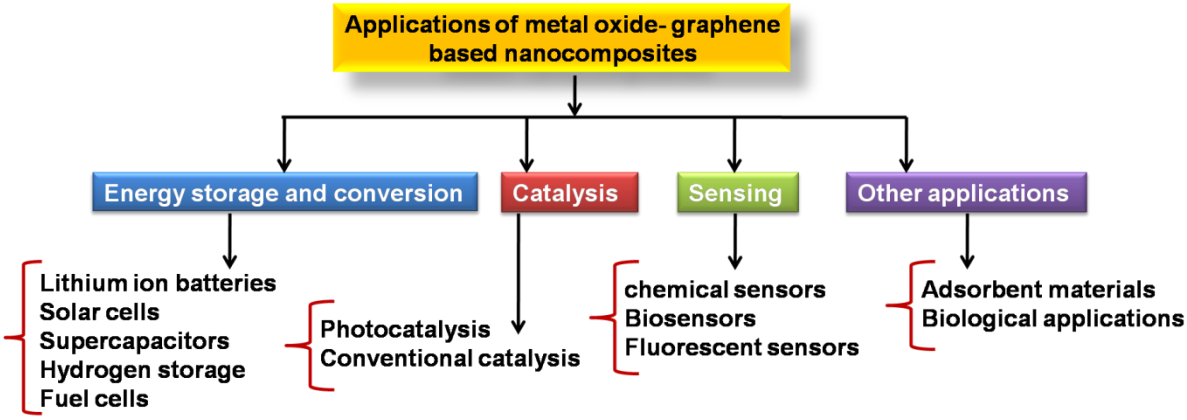

Figure 1.6 Applications aimed in metal oxide-graphene based nanocomposites.

1.5.4.1 Dye Removal

Contamination of water bodies with organic dyes/colorants and also inorganic toxic elements like arsenic, lead, cadmium, and chromium are considered to be the most severe environmental problems faced by the mankind (Rodriguez *et al*., 2010). Dyes are natural or synthetic substances, whether soluble or insoluble, used to add a colour or change the colour. Dyes are classified according to the chemical constituents and application class/end use. Based on the chemical constituents dyes can be classified as azo, monoazo, diazo, nitro, azine, thioazine, anthroquinone, quinoline, sulphur, xanthene, phthalocyanine, and nitoros. Similarly, as per the applications, they are classified as acid dyes, basic dyes, direct dyes, mordant dyes, vat dyes, reactive dyes, disperse dyes, and sulfur dyes. Organic dyes also fall into cationic, non-ionic or anionic types (Geethakarthi *et al*., 2011). The commercially used organic dyes are resistant to biodegradation; and its presence reduce aquatic diversity by blocking the passage of light through water. Thus the removal of dyes from effluents before they are mixed up with natural water bodies is truly crucial (Bhatnagar *et al*., 2005). Conventionally, removal of dyes in waste effluent is achieved *via* physical, chemical, and biological methods (Rodriguez *et al*., 2010); Since these methods can not completely

remove the dye wastes from the water bodies semiconducting metal oxide mediated photocatalytic degradation is strongly considered (Liu *et al*., 2013; Zhu *et al*., 2014).

1.5.4.1.1 ZnO Photocatalysts

Photocatalysis is an advance oxidation process (AOPs) results in complete non-selective destruction of organic contaminants (Rashid *et al*., 2014). Among many photocatalytic materials ZnO is actively considered and widely investigated for pollutant treatment under light illumination because it can absorb a large fraction of UV spectrum and more light quanta. The photocatalytic activity of semiconducting metal oxides including ZnO, TiO_2, CeO_2, SnO_2, MoO_3 *etc*., are well-studied and the photoactivity mechanism is highly understood.

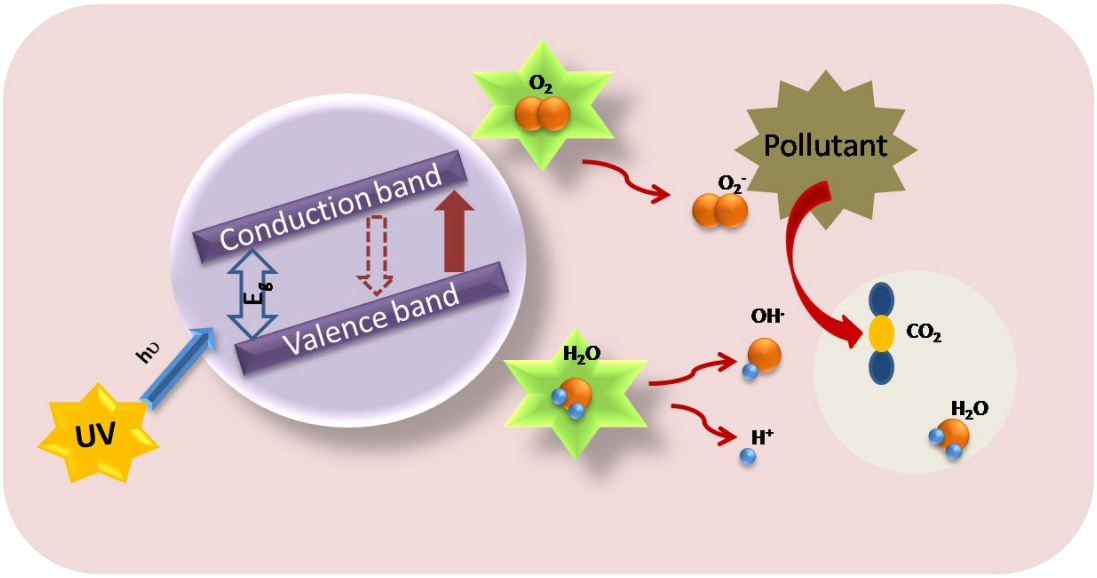

Figure 1.7 Schematic diagram showing radical generation and organic dye degradation upon photo irradiation of a metal oxide semiconductor.

In ZnO, the photoactivity is governed by the defects like oxygen vacancies, zinc interstitials, oxygen interstitials, and the generation of hydrogen peroxide, superoxide, and hydroxyl radicals on the ZnO surface. When ZnO is excited by UV light with energy higher than the band gap energy of the material, excitons are created *i.e.* electrons at the conduction band (CB) and holes at the valance band (VB), respectively (Kochuveedu *et al*., 2013;

Ahmed *et al*., 2014). The electron-hole pairs thus formed are responsible for the degradation of the adsorbed contaminants by initiating a series of chemical reactions as mentioned in the equations 1.3-1.11 at the surface of the ZnO semiconductor (Liu *et al*., 2013). The generated holes may react with the surface-adsorbed OH^- ions forming the $OH^{\cdot}$ free radicals. The $OH^{\cdot}$ free radicals may also be formed by the reaction of dissolved oxygen (O_2) with the generated electrons and the protons forming the hydrogen peroxide (H_2O_2) as an intermediate product, which subsequently gets decomposed to the $OH^{\cdot}$ free radical by releasing the OH^- ion into the aqueous solution. The formation of these active species helps to reduce the electron-hole recombination rate and provides additional time for dealing with the organic pollutants. The photocatalytic mechanism is pictorially represented in the Figure 1.7.

$ZnO + h\upsilon \longrightarrow ZnO + e_{CB}^- + h_{VB}^+$ 1.3

$h^+ + H_2O \longrightarrow H^+ + {\cdot}OH$ 1.4

$h^+ + OH^- \longrightarrow {\cdot}OH$ 1.5

$O_2 + e^- \longrightarrow O_2^-$ 1.6

$2e^- + O_2 + 2H^+ \longrightarrow H_2O_2$ 1.7

$H_2O_2 + e^- \longrightarrow {\cdot}OH + OH^-$ 1.8

Organic pollutant + ${\cdot}OH \longrightarrow$ degradation products 1.9

Organic pollutant + $h_{VB}^+ \longrightarrow$ oxidation products 1.10

Organic pollutant + $e_{CB}^- \longrightarrow$ reduction products 1.11

The important demerits of ZnO based photocatalysts are

- ZnO do not absorb visible portion of the solar spectrum and it can only be activated in the presence of UV light.

- Faster recombination of photoinduced charge carriers (electron-hole pairs) than surface redox reactions
- Tendency for aggregation during catalytic reaction and susceptible to corrosion under UV light (photocorrosion)

The photocorrosion reaction can be represented as

$$ZnO+2h^{+}+nH_2O \longrightarrow Zn(OH)_n^{(2-n)+}+\tfrac{1}{2}O_2+nH^{+} \qquad 1.12$$

The photodissolution of ZnO initially involves the hole trapping on the surface, followed by a rapid formation of oxygen molecule and fast expulsion of Zn^{2+} from the surface (Kumar *et al*., 2015).

$$ZnO+2h^{+} \longrightarrow Zn^{2+}+\tfrac{1}{2}O_2 \qquad 1.13$$

Some of these limitations need to be solved in order to obtain efficient ZnO photocatalysts for any practical applications.

Moreover, if the catalysts also offer good adsorption of pollutants, mainly organic dye molecules, then a single adsorptive-catalytic material itself is sufficient for the effective treatment of contaminated water. Earlier research studies devoted mainly to enhance the catalytic degradation efficiency of ZnO *via* doping strategy. Doping is employed for the band gap engineering but not for making 'sorption-catalysts'. Combining ZnO with carbon materials (carbon–semiconductor composite) (Liu *et al*., 2017; Liang *et al*., 2016; Han *et al*., 2014) form a new class of sorptive-photocatalysts because porous carbon nanostructures readily adsorb organic dyes. In this thesis development of mesoporous ZnO-graphene based composite system with reasonable surface area is aimed because such duel functional material could potentially offer desirable dye adsorption as well as simultaneous dye degradation. Literature survey confirms graphene based metal oxide nanocomposites can be applied in

three different fields: (i) degradation of organic pollutants in to harmless chemical species (ii) hydrogen evolution from photocatalytic water splitting, where solar energy is converted into H_2 fuel (iii) photocatalytic conversion of CO_2 to hydrocarbon fuel (An *et al*., 2011). The schematic diagram in Figure 1.8 shows the photocatalytic applications of metal oxide-graphene based nanocomposites.

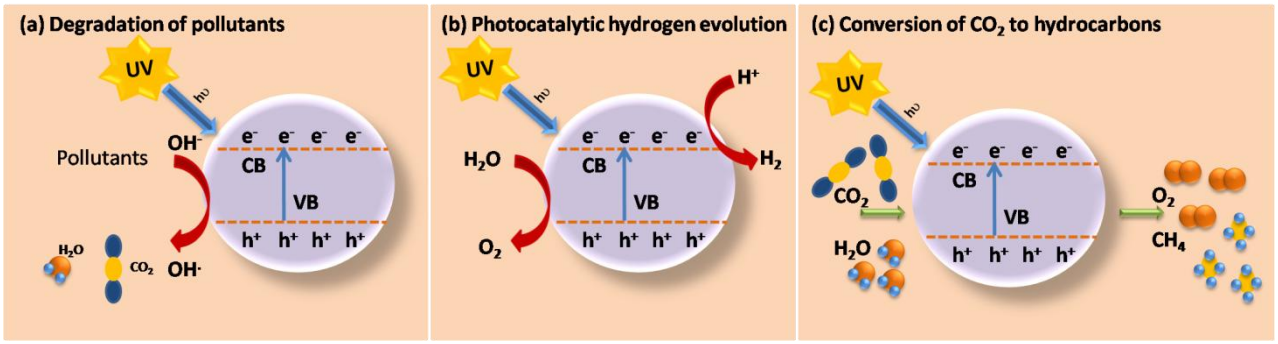

Figure 1.8 The photocatalytic applications of metal oxide-graphene based nanocomposites (a) degradation of organic pollutants (b) photocatalytic hydrogen generation (c) photocatalytic conversion of CO_2 to hydrocarbon fuels.

1.5.4.1.2 Water Disinfection

One of important areas of materials science is water disinfection. The access of safe drinking at affordable cost is becoming difficult in recent days (Zeng *et al*., 2017; Ghosh *et al*., 2012). Millions of people die from diseases caused by waterborne pathogenic microorganisms such as viruses, bacteria, and fungi (Szunerits *et al*., 2016). Therefore efficient methods are designed to control or prevent waterborne pathogens. Strategies like treating water with chemicals such as chlorine, ozone, ultraviolet (UV), heat sterilization (boiling), and filtration are (Zeng *et al*., 2017) traditionally followed. But in such techniques, secondary environmental pollution is realized. Use of antibacterial materials can safely disinfect the water bodies (Gao *et al*., 2013). Antibacterial compounds locally

kill the bacteria or slow down their growth. Organic antibacterial agents are less stable and hence not recommended for water disinfection applications. The advent of nanotechnology produced stable inorganic antibacterial/antimicrobial agents. Earlier studies demonstrated that nanomaterials belong to metal oxides (*e.g.* TiO_2, SiO_2, ZnO, MgO, CaO, CuO, Al_2O_3, Ag_2O, and CeO_2), show good antimicrobial activity (Liu *et al*., 2018; Ghosh *et al*., 2012; Raghupathi *et al*., 2011). In fact ZnO is listed as a safe antibacterial material by United States Food and Drug Administration (21CFR182.8991) (Pang *et al*., 2016). In nano ZnO, factors like photocatalytic bacterial-disruption and reactive oxygen species (ROS) bacterial-attack play critical role in killing the bacteria present in water bodies (Wang *et al*., 2014). The production of reactive oxygen species (ROS) on the surface of ZnO nanoparticles in presence of light causes oxidative stresses in bacterial cells and eventually leads to the death of the cells. The possible antibacterial mechanism offered by semiconducting metal oxide photocatalytic nanoparticles is shown in the Figure 1.9.

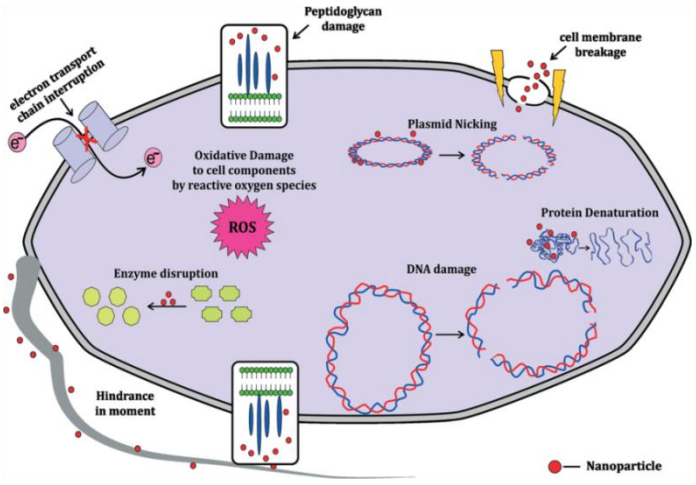

Figure 1.9 Depiction of the general mechanism of action of nanoparticles on a bacterial cell and its components (Qayyum *et al*., 2016).

From the literature it is clear that graphene based GO and rGO nanostructures exhibit strong antibacterial activity. Similar to CNTs, graphene based materials also induce membrane stress on bacterial cells, resulting in the irreversible damages on cell structures.

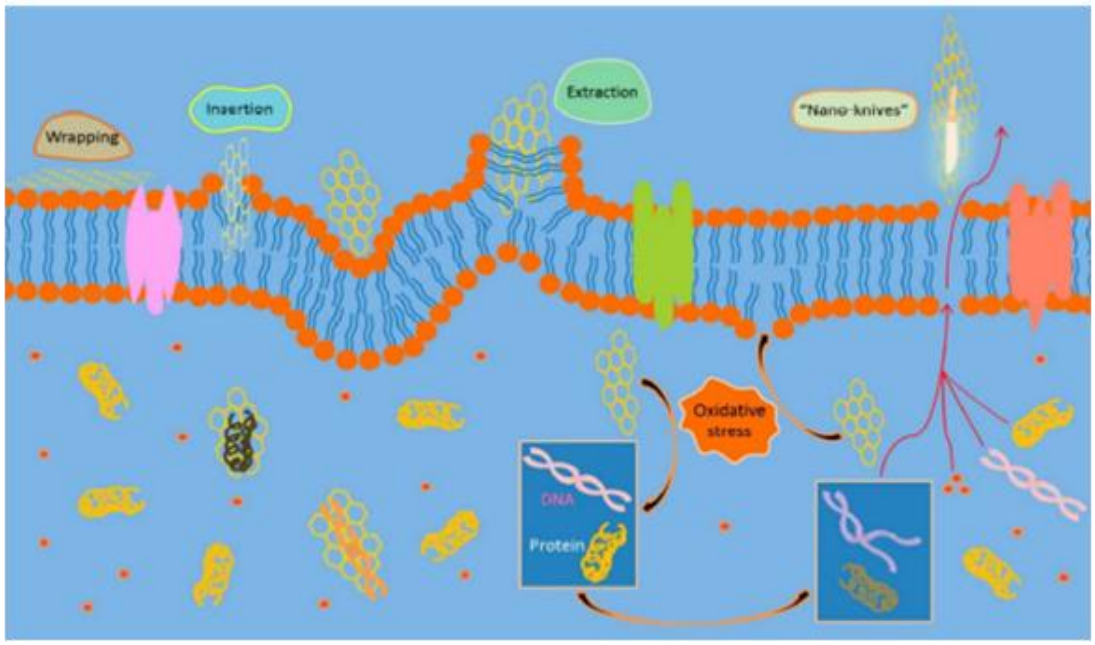

Figure 1.10 Mechanisms of the antimicrobial activities of single component graphene materials (Zeng *et al*., 2017).

GO and rGO are differ in their interactions with bacterial cell. The bacterial cell gets individually wrapped by GO nanosheets whereas the bacterial cells usually get embedded in the large aggregates of rGO sheets (Liu *et al*., 2011). Zou *et al*. summarized different kinds of interactions which contribute to the antibacterial activity of graphene based nanomaterials which are schematically expressed in Figure 1.10. (i) graphene based nanostructures can wrap bacteria and make the cell deposit on the surface, which in turn isolates the cells from external nutrition (ii) membrane stress induced by the direct insertion with sharp edges of nanosheets (iii) membrane damage due to the extraction of phospholipids by the sharp nanosheets (iii) graphene based nanosheets can act "nano knives" which induce pores on the cell membrane (iv) the oxidation stress induced by the free radical such as superoxide anion can also damage the bacterial cell membrane and its cellular components (Zeng *et al*., 2017; Upadhyay *et al*., 2014; Wang *et al*., 2014). Based on literature survey it is understood that the combination of ZnO with graphene based nanostructures/nanocomposites ideally kill the bacteria by both means *i.e.* photoactive

catalytic activity as well as direct interaction by GO and rGO. Some of the recent literature reported on the antibacterial activity of the ZnO-GO/rGO nanocomposites is listed in the Table 1.3.

Table 1.3 Studies on ZnO-graphene based nanocomposites for bacterial inactivation

Materials	Methods	Properties	References
ZnO nanowires on GO sheets	eletrochemical deposition/eletrophoretic deposition	antibacterial/dark/visible	Nourmohammadi *et al*., 2014
Poly(lactic acid)/GO-ZnO nanocomposite	in-situ precipitation	antibacterial/dark/light	Huang *et al*., 2015
Sulfonated GO-ZnO-Ag	hydrothermal/polyol reduction process	antibacterial/visible light	Gao *et al*., 2013
ZnO/GO composites	in-situ precipitation	antibacterial/dark	Wang *et al*., 2014
Noble metal (Ag, Pd, Au, Pt) on graphene	UV assisted photocatalytic reduction	eletrocatalysis for H_2O_2 reduction	Gu *et al*., 2013
rGO/ZnO	selfassembly and in-situ photocatalytic reduction	photocatalysis/ sunlight/ Rhodamine B degradation	Wang *et al*., 2012
ZnO-graphene	Microwave assisted in-situ precipitation	Photocatalysis/reduction of Cr(VI)	Liu *et al*., 2011

1.5.4.1.3 Semiconducting Metal Oxide Nanoparticles for Chemical Sensors

A chemical sensor is a device that transforms chemical information, ranging from the concentration of a specific sample component to total composition analysis, into an analytically useful signal (Theavenot *et al*., 1999; Li *et al*., 2015). Chemical sensors usually contain two basic components connected in series: a chemical (molecular) recognition system (receptor) and a physico-chemical transducer (Li *et al*., 2015). Electrochemical sensors are very popular in the category of chemical sensing methods. It has fast response, good

sensitivity, and in-situ real-time detection (Cai *et al*., 2014). In electrochemical sensors, voltammetric techniques such as cyclic voltammetry (CV), differential pulse voltammetry (DPV), square wave voltammetry (SWV), stripping voltammetry *etc*., amperometry and potentiometric techniques, electrochemiluminescence (ECL), and electrochemical impedance spectroscopy (EIS) are seen in the literature. CV has received great attention because it can be used for the elucidation of electrode processes and redox mechanisms (Li *et al*., 2015; Chen *et al*., 2013; Govindhan *et al*., 2014). The principal stages in the operation of an electrochemical sensor are provided in the Figure 1.11.

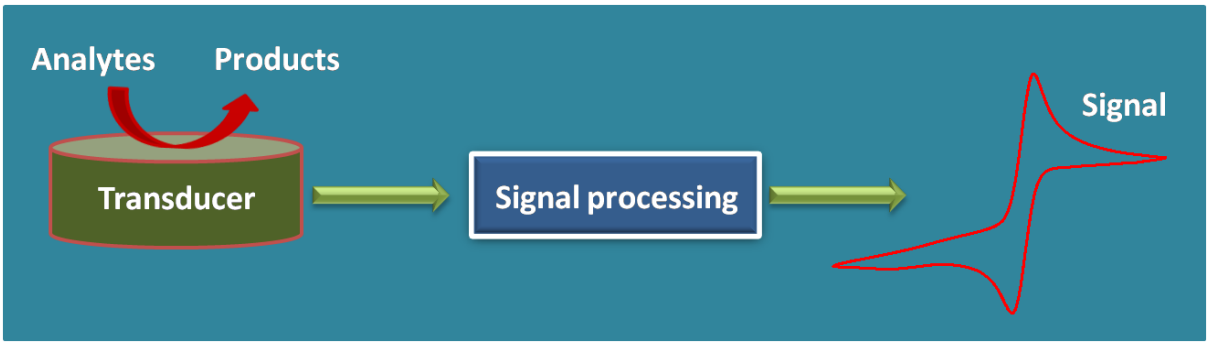

Figure 1.11 Principal stages in the operation of an electrochemical sensor.

Electrochemical sensors are divided into enzyme based and non-enzymatic ones. Enzyme based sensors are popular due to their significant benefits. The main drawbacks of enzymatic sensors are lack of chemical and heat stability (lack of stability due to the intrinsic nature of enzymes), loss of activity (easily denatured during immobilization process) (Bao *et al*., 2008; Tran *et al*., 2011), intolerance to extreme acidic and basic conditions, deactivation by toxic chemicals and humidity, expensive in terms of cost of enzyme, need specific conditions for storage, and time consuming protocols. Furthermore, the thermal, chemical stability, and durability of enzymes during the monitoring process are significantly affected by the pH value, working temperature, oxygen partial pressure, and ambient humidity level that significantly hamper further developments of enzyme-based electrochemical sensors

(Zhu *et al*., 2016). To overcome these restrictions, research on non-enzymatic sensors is becoming more essential (Zhao *et al*, 2016). The advantages of enzyme free sensors are; it needs no specific storage conditions, is capable of performing under ambient conditions, show stability towards temperature, pH, humidity, and toxic chemicals *etc*., simplicity, high sensitivity, unique selectivity, reproducibility, cost effectiveness *etc*. In non-enzymatic sensors, the atoms on the surface of modified electrodes act as the electrocatalysts instead of enzymes (Zhu *et al*., 2016). Research on electrochemical sensors mostly dominates to examine the food adulteration and the main concern is pesticides. Other areas of importance in chemical sensors are determination of glucose. The due importance in designing simple and effective non-enzymatic chemical sensor for glucose determination can be easily understood from the increased numbers of publications in International scientific journals on this subject which is given in Figure 1.12. In the past 15 years, a drastic increase in the number of publications is noticed during the period 2001 to 2015 (Zhu *et al*., 2016).

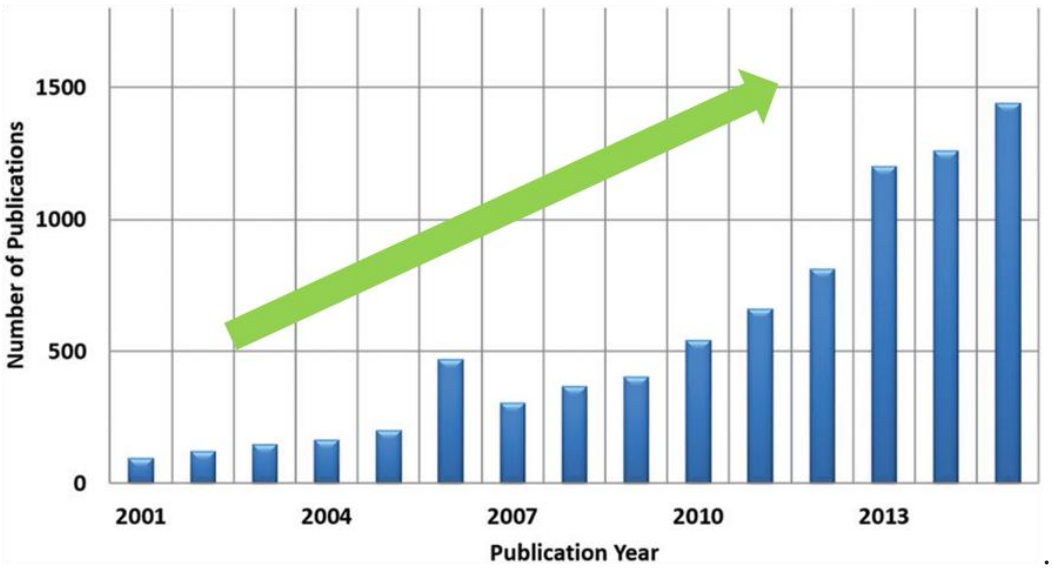

Figure 1.12 Chart of the number of recent publications on enzyme free glucose sensors as a function of the year published (Zhu *et al*., 2016).

The non-enzymatic detection of glucose is based on the direct electrooxidation of glucose on catalytic surface such as metal or metal oxides. Precious metals like Pt, Au, Pd have been employed for the direct electrooxidation of glucose. In Pt and Au based sensors risk of chloride poisoning is noticed. Ni electrodes are unstable at low pH (Zhu *et al*., 2016). These kinds of precious metals based sensors often suffer from slow kinetics, poor operational stability, lack of selectivity, and low antitoxic ability (Dhara *et al*., 2016). Catalytically active semiconducting metal oxides as electrocatalysts have been recently explored. They offer high stability, good sensitivity, and rapid response. Electrochemical sensors based on metal oxide nanoparticles have been studied for species like glucose (Ibupoto *et al*., 2015; Soomro *et al*., 2015), urea (Arain *et al*., 2016), hydrazine (Shukla *et al*., 2014), melamine (Soomro *et al*., 2016) *etc*. Nano scale catalytic particles found to be more active than macroparticles because crystal planes are more exposed which leads to good current responses (Jiang *et al*., 2017).

The advantages in designing non-enzymatic electrochemical sensors with nanoparticles are; (i) tailored optical, electrical, thermal, and catalytic properties (ii) large surface area originating from the quantum size dimensions (iii) high mass transport and enhanced electron transfer kinetics (sometimes sluggish on the unmodified electrodes), and (iv) increased sensitivity therefore short response time, (v) prevention of undesired electrode reactions that enhances the signal to noise ratio (Chen *et al*., 2013; Kannan *et al*., 2015; Chen *et al*., 2016; Jiang *et al*., 2017). For non-enzymatic sensors, metal oxide nanoparticles such as ZnO, Fe_2O_3, CeO_2, SnO_2, Ag_2O, ZrO_2, TiO_2, Co_3O_4, NiO, Cu_2O, MnO_2, MgO, RuO_2, Mn_3O_4 *etc*., have been considered and extensively tried for chemical and biological sensing applications (Hahn *et al*., 2012). Similarly, in carbon based materials CNT, graphene, and rGO are used. They are explored as recognition layer for the modification of electrodes in non-enzymatic electrochemical sensors. In fact some of these

nanostructures are also tried with enzyme based sensors for the fabrication of transducer surface because they exhibit unique features such as ability to promote faster electron transfer between electrode and active site of desired enzymes (Dhara *et al*., 2016).

Nanostructured ZnO offers high catalytic efficiency, strong adsorption ability, high isoelectric point (IEP = 9.5), and high electron communication features. Moreover, high IEP of ZnO is advantageous to immobilize an enzyme having low IEP through electrostatic interactions (Ali *et al*., 2009). ZnO is a candidate nanomaterial for the fabrication of electrochemical biosensors. Diversified nanostructures, high electron mobility, chemical stability, electrochemical activity and high isoelectric point, which are able to promote enzyme adsorption, biocompatibility, and piezoelectric properties, make it more suitable for such sensor applications.

1.5.5 Motivation of the Thesis and the Selection of Research Problem

Literature evidences clearly shows in ZnO nanostructures, their semiconductivity nature, evolution of varied morphologies, associated surface area, and catalytic properties are strongly dependence upon the synthesis techniques and reaction temperatures. By conventional aqueous synthesis under controlled precipitation, it is normally possible to produce aggregated ZnO agglomerates that upon calcination at a moderate temperature of 500 ^{o}C transformed to well crystalline ZnO nanoparticles with large crystallites. It eventually produces low surface area and poor dispersion stability. Hence it is important to develop ZnO nanostructures *via* direct crystallization at significantly low temperatures in the presence of crystal growth inhibiting agents over a suitable nano layered materials. It can possibly produce ZnO nanostructures and nanocomposite architectures with desirable meso/nano porosity and better catalytic property. CNTs and graphene based materials are appropriate supports for obtaining size and shape controlled ZnO particles. Therefore in this

thesis more rapid microwave assisted reflux technique was identified and employed. Reports say the photocatalytic property if nano ZnO can be improved in the presence of rGO. However, in such ZnO-graphene based GO/rGO nanocomposites, their net effect on the simultaneous adsorption and catalytic degradation is seldom reported. Similarly, the influence of graphene based support materials on the well-known antibacterial property of ZnO is also a factor to be investigated. Is it possible to explore such material architectures for water disinfection? How the incorporation of ZnO/GO reinforcements produce stable bio nanocomposites? This question is answered by the study conducted gelatin matrix containing these nanomaterials as reinforcements. In fact gelatin-ZnO-GO composites are not well researched earlier. Finally, ZnO/rGO based non enzymatic sensors are also developed and tested for sensing glucose and urea.

In simple terms, the research statement is defined as, '*design of ZnO nanostructures via microwave assisted reflux technique with and without graphene based GO/rGO support layers and develop multifunctional ZnO nanocomposites containing graphene based GO/rGO nano reinforcements and study the catalytic, antibacterial, and sensing applications*'.

1.5.6 Objectives

The overall objectives of the thesis are:

- Preparation of ZnO/rGO nanocomposites with and without silane and study the adsorption and photo degradation of a few cationic dyes.
- Development of ZnO nanorods with different aspect ratios *via* PEG assisted microwave reflux technique. Study the antibacterial property with respect to the physical dimensions of the nanorods

- Preparation of morphologically tuned ZnO nanoparticles with different biotemplates such as carbohydrates/celluloses. Study the effect of morphologically tuned ZnO and rGO on the non-enzymatic sensing of urea and glucose
- Develop APTMS modified ZnO nanoarchitectures and GO; and explore them as nanofillers to improve the gelatin biopolymer films.

All the above objectives are covered in different working chapters and the salient results are finally summarized in the conclusion chapter.

CHAPTER 2

Characterization Tools and Techniques

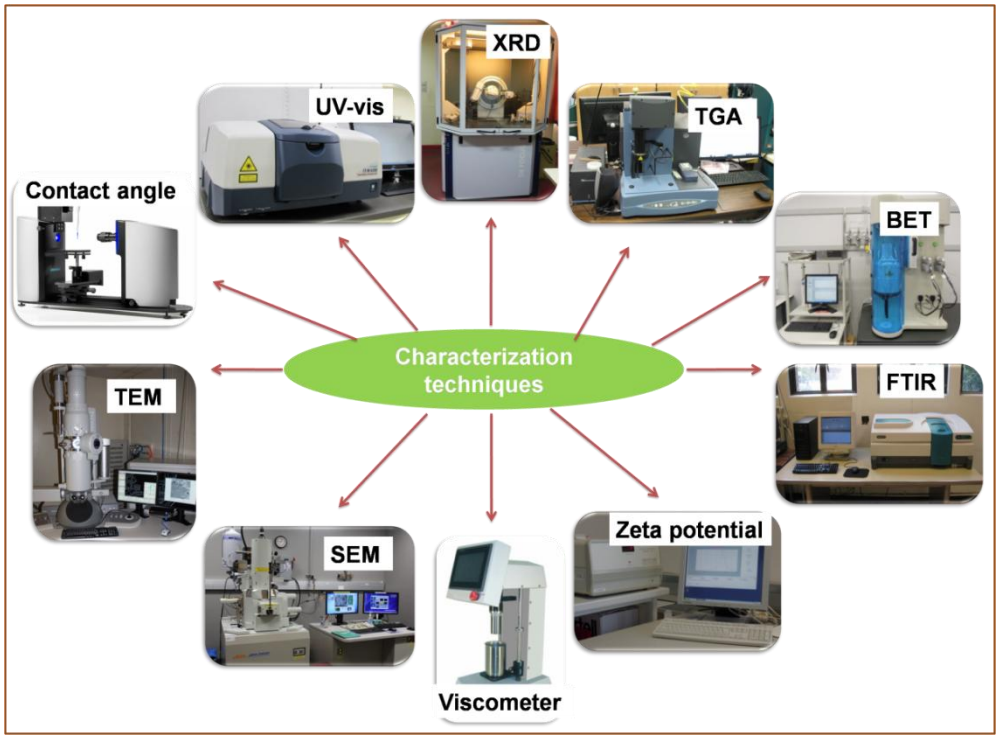

In the current research in materials science and related fields, the term characterization refers to the use of external techniques to probe into the internal structure and properties of a material. These techniques not only help to characterize nanostructure, but also help in the examination of their properties and behaviour. Various analytical tools employed in the present study are X-ray diffraction (XRD), Thermogravimetric analysis (TGA), Fourier transform infra red spectroscopy (FTIR), UV-vis absorption spectroscopy, Scanning electron microscopy (SEM), Transmission electron microscopy (TEM), BET surface area measurement *etc*. The basic principles and instrumental details of various characterization techniques adopted for the characterization of the prepared samples mentioned throughout the thesis will be described briefly in this chapter.

2.1 X-ray Diffraction (XRD)

X-ray diffraction is an important and powerful analytical tool to study crystallinity, crystal structure, phase purity, crystallite size determination, and chemical composition of a material. When the beam of X-rays strikes on the crystal surface, electrons are scattered at different directions (Chua *et al*., 2014) and gets a diffraction pattern. Therefore, X-ray diffraction pattern of a pure substance is like a fingerprint of the substance. Powder X-ray diffraction method is therefore ideally suited for the characterization and identification of the polycrystalline phases.

In 1913, Bragg was first performed crystal structure measurement by using X-rays. The basic concept of XRD involves the interaction of X-rays with the periodic atomic structure of crystals and is presented in the Figure 2.1. The diffraction of X-rays by crystal planes helps to derive the interplanar distance (d spacing) by using the Bragg relation (equation 2.1).

$$n\lambda = 2d \sin \theta \qquad 2.1$$

where λ is the wavelength of X-rays, d is the distance between two lattice planes, θ is the angle between the incoming X-rays and the normal to the reflecting lattice plane and n is the integer called order of the diffraction.

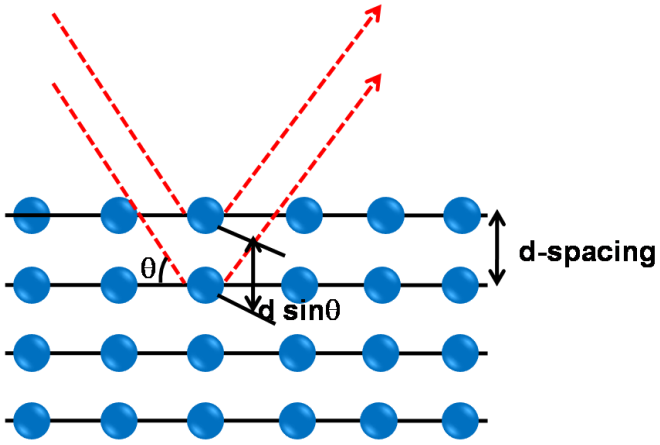

Figure 2.1 Diffraction of X-rays by a crystal.

XRD is a plot of intensity verses scattering angle 2θ. The peak intensity, width, shape, position *etc*. will give information regarding the structure of the crystal. Sharp peak with high scattering intensity shows that sample has a good crystallinity (Wang *et al*., 2012). In the present study the X-ray diffraction patterns were collected using a Philips X'Pert Pro diffractometer within the 2θ range of 10-80 ^{o} with Ni-filtered CuKα$_1$ radiation (λ_{Cu} = 1.542 Å). Debye Scherrer equation relates crystallite size with line width and the nano crystallite size was calculated using the formula 2.2 (Yoshitake *et al*., 2008).

$$D_{XRD} = 0.9\lambda / \beta \, Cos \, \theta \qquad 2.2$$

where D_{XRD} is the average nanocrystallite size in nm, λ is the wavelength of the X-ray radiation (nm), β is the full width at half maximum intensity (radian), and θ is the diffraction angle (degree). The lattice parameter of the samples was calculated from the X-ray diffraction data using the equation 2.3 (Jayanthi *et al*., 2010),

$$1/d^2 = 4/3[1/a^2] + 1/c^2 \qquad 2.3$$

where d is the interplanar distance, a and c are the lattice parameters in nm (being hexagonal $c/a = (8/3)^{-1}$).

The number of unit cells in a crystal was calculated using the formula given as equation 2.4.

$$4/3\pi(D/2)^3 = nV \qquad 2.4$$

where D is the crystallite size (nm), V is the volume of a unit cell; $V = (3(3)^{1/2}a^2c)/2$ and n is the number of unit cells (Thool *et al*., 2014).

2.2 Thermo Gravimetric Analysis (TGA)

TGA measures the amount of weight change of a material as a function of increasing temperature in a controlled atmosphere. TGA measurement used primarily to determine the material composition and to understand their thermal stability at temperatures up to 1000 °C. At elevated temperature, the changes in the weight may occurs due to absorption/desorption, decomposition, dehydration/evaporation, and reduction/oxidation. Thermo gravimetric curves are characteristic for a given compound because of the unique sequence of the physiochemical reaction that occurs over specific temperature ranges and heating rates and are function of the molecular structure. The mass change characteristics of a material are strongly dependent on the experimental conditions employed. Factors such as sample mass, volume and physical form, the nature and pressure of the atmosphere in the sample chamber, and the scanning rate have significant influences on the characteristics of the recorded TG curve. The TGA analyzer consists of a high precision balance with a pan loaded with the sample and a furnace. The furnace can be programmed either for a constant heating rate, or for heating to acquire a constant mass with time. The

sample is placed in a small, electrically heated furnace equipped with a thermocouple to accurately measure the temperature. The maximum temperature is selected so that the specimen weight is stable at the end of the experiment, implying that all chemical reactions are completed (*i.e.*, all of the carbon is burnt off leaving behind metal oxides). If required, the atmosphere in the sample chamber may be purged with an inert gas to prevent oxidation or other undesired reactions. Analysis is carried out by raising the temperature gradually. Results are plotted with temperature on the X-axis and weight loss on the Y-axis. In the present study, the thermal decomposition of the as prepared materials have been carried out using the thermo gravimetric analyzer TG-50 (SHIMADZU, Japan) at temperatures between room temperature to 1000 ^{o}C at a constant heat flow of 10 ^{o}C min^{-1} in O_2 atmosphere.

2.3 UV-vis Spectroscopy

Ultraviolet-visible spectroscopy or UV-visible spectrophotometry refers to absorption spectroscopy in the UV-visible spectral region. UV-vis spectroscopy uses light in UV (200-400 nm) and visible (400-800 nm) part of the electromagnetic spectrum. It involves the excitation of electrons from the atomic or molecular ground state to the higher energy levels. The energy of the ultra-violet radiation that are absorbed is equal to the energy difference between the ground state and higher energy states, ($E = h\upsilon$). Molecules containing π-electrons or non-bonding electrons (n-electrons) can absorb the energy in the form of ultraviolet or visible light to excite these electrons to higher anti-bonding molecular orbitals (π^* or n*). Generally, the most favoured transition is from the highest occupied molecular orbital (HOMO) to lowest unoccupied molecular orbitals (LUMO). The resulting species said to be an excited state. An optical spectrometer records the

wavelength at which absorption occurs, together with the degree of absorption at each wavelength to produce a spectrum.

UV spectroscopy obeys Beer-Lambert law. The absorbance of a sample at a given wavelength is proportional to the concentration of the absorbing sample in solution and it can be used to measure the concentration of a given sample. Beer-Lambert law can be expressed in the form of the following equation

$$A=\varepsilon bc \qquad 2.5$$

where A is the absorbance, ε is the molar absorptivity ($M^{-1}\,cm^{-1}$), b is the path length in cm and c is the sample concentration in moles L^{-1}. From the absorbance information and using a relationship known as Beer-Lambert Law, one is able to determine either the concentration of a sample or the molar absorptivity, if the concentration is known. Molar extinction coefficients are specific to particular compounds; therefore UV-vis spectroscopy can aid one in determining an unknown compound's identity. Furthermore, the energy of a compound can be ascertained from this technology by using the equation

$$E = hc/\lambda \qquad 2.6$$

where E is the energy, h is Planck's constant, c is speed of light, and λ is the wavelength. Since photons travel at the speed of light, and h and c are constants, one can find the energy

The UV-visible spectrophotometer can also be configured to measure reflectance and transmittance. The absorbance, A is based on the transmittance (T):

$$A = -\log (\%T/100\%) \qquad 2.7$$

$$\%T = I/I_0 \qquad 2.8$$

where I is the intensity of light passing through a sample, I_0 is the intensity of light before it passes through the sample. In the case of reflectance (R), % T can be changed into % R.

A spectrophotometer can be either single beam or double beam. In a single beam instrument all of the light passes through the sample cell. I_0 must be measured by removing the sample. In a double-beam instrument, the light is split into two beams before it reaches the sample. One beam is used as the reference; the other beam passes through the sample. The reference beam intensity is taken as 100% Transmission (or 0 Absorbance), and the measurement displayed is the ratio of the two beam intensities. Some double-beam instruments have two detectors (photodiodes), and the sample and reference beam are measured at the same time. In other instruments, the two beams pass through a beam chopper, which blocks one beam at a time. The detector alternates between measuring the sample beam and the reference beam in synchronism with the chopper.

In the present study, the UV-vis absorption spectra of the materials in aqueous solution were recorded using UV-2401 PC spectrophotometer (Shimadzu, Japan) within the wavelength range of 200 to 800 nm. The direct band gap energies of the samples were calculated by the equation (Sun *et al*., 2012),

$$(\alpha h\upsilon)^2 = A(h\upsilon - E_g) \qquad 2.9$$

where α, $h\upsilon$ and E_g are the absorption coefficient, photon energy and optical band gap, respectively and A is a constant. The band gap energy (E_g) was determined by plotting $(\alpha h\upsilon)^2$ versus $(h\upsilon)$ and then extrapolating the tangent of the curve to $(\alpha h\upsilon)^2 = 0$.

2.4 Fourier Transforms Infrared Spectroscopy (FTIR)

FTIR spectroscopy describes the interaction of matter and electromagnetic fields in the IR region and excited to a higher vibrational state. It provides information about the chemical

bonding or molecular structure of materials, whether the material is organic or inorganic. Most important part of the FTIR spectrometer is the interferometer, which is placed around the sample chamber. The interferometer consists of movable mirror, fixed mirror, splitter, laser and detector. The radiation goes from the IR source is directed through the sample cell to the beam splitter and splits the beam into 2 parts. Half of the radiation is reflected from a moving mirror while the other part is reflected from a fixed mirror. When the two beams are combined at the detector, an interference pattern is produced. This interference pattern is called interferogram.

In the present study the bonding characteristics of the samples presented in Chapter 3, 4 and 5 were recorded at room temperature using Nicolet Magna-560-IR Spectrometer, USA. In chapter 6, the chemical bonding characteristics of ZnO and ZnO/Si were done by IR Prestige 21 SHIMADZU, Japan. In these cases the conventional KBr pellet technique was followed for the spectra in the wavenumber region 400 to 4000 cm^{-1}.

2.5 Attenuated Total Reflectance (ATR)

ATR is a characterization technique used in conjunction with infrared (IR) spectroscopy used for the examination of solid samples without any further preparation. ATR operates by measuring the changes in the total internal reflection of the IR beam when the beam comes into contact with a sample.

In the present study the bonding characteristics of the film samples presented in Chapter 6 were recorded at room temperature using Perkin Elmer FTIR C109097 spectrometer, USA. In these cases the spectra was recorded wavenumber region of 500 to 4000 cm^{-1}.

2.6 Optical Microscopy

Optical microscope is also known as light microscope and it uses visible light for the formation of magnified image of a small object. It is the most widely used instrument for material characterization due to its simplicity and cheapness. The instrument consists of two lenses, an objective and an eyepiece, the product of whose magnification gives the magnification of the final image.

The surface morphology of the as-prepared films was also observed with an optical microscope Leica L2, HCM780M.

2.7 Transmission Electron Microscopy (TEM)

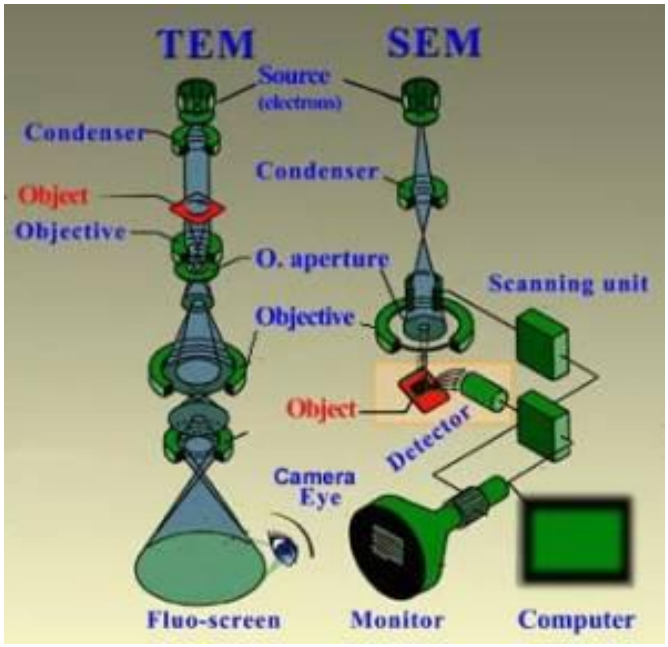

Figure 2.2 Schematic diagrams of TEM and SEM (http://www.vcbio.science.ru.nl/en/fesem/info/principe/).

The first TEM was developed by Max kroll and Ernst ruska in 1931. TEM is an imaging technique developed to obtain higher magnification images of a sample much better than a conventional optical microscope. It is a very useful technique for materials characterization

because it can provide information relating to the morphology, composition and crystal structure. When a beam of electrons accelerated up to higher energy levels and focused on a material, they can scatter or backscatter elastically or in elastically, or may produce many interactions. Some of them are used in TEM. TEM image is formed from the interaction of the electrons transmitted through the sample; the image is magnified and focused on to an imaging device, such as a fluorescent screen, on a layer of photographic film, or to be detected by a sensor such as a CCD camera. The schematic diagram of TEM is given in the Figure 2.2.

In the present study the morphology of the as prepared materials were studied using the TEM instrument Tecnai G^2, FEI, Netherlands. The images were taken at 300 kV.

2.8 Scanning Electron Microscopy (SEM)

SEM is a powerful technique for the high resolution examination of microstructure and morphology of the samples. The important components of a SEM instrument are pictorially represented in the Figure 2.2. When an electron beam interacts with a matter, a large number of signals are generated. These signals include secondary electrons, back scattered electrons, X-rays, cathodoluminescence, auger electrons, and transmitted electrons. The ionization of the specimen atoms occurred due to the interaction of primary electron beam and the sample surface results in the emission of loosely bounded atoms (called secondary electrons) is the most common method of detection. Secondary electrons are principally used for the visualization of surface texture and roughness (*i.e.* topographic contrast). Back scattered electrons come from deep beneath the surface and hence they carry information on the composition of the sample. Auger electrons and X-rays provide chemical information of the sample. All these signals providing detailed information about the surface structure and morphology of the sample. Using the scale bar provided with the SEM images we can calculate the size of the particles in the SEM image.

In the present study the surface morphology of the prepared samples was examined using a scanning electron microscope JEOL JSM 5600LV SEM and ZEISS EVO 18 with an acceleration voltage of 20 KV. The SEM samples were prepared by sonicating a small amount of the corresponding material in acetone and subsequently drop casting the solution on a copper stub. It was then coated by cathode sputtering with a layer of gold at vacuum to minimise the charge effects. For the morphological analyzes of bacterial cell, the prepared samples were directly drop cast on the SEM stub and kept for drying (dried bacterial cells were sputter coated with gold for SEM imaging) before being subjected to SEM analyzes.

2.9 BET Surface Area Analysis

BET theory deals with the physical adsorption of gas molecules on a solid surface and serves as the basis for the measurement of the specific surface area of a material. In 1938, Stephen Brunauer, Paul Hugh Emmett, and Edward Teller published an article about the BET theory, where "BET" stands for the first initials of their family names. The BET model extends the monolayer Langmuir model to multilayer adsorption. In the BET theory, it is assumed that the surface is homogeneous and the molecules present in different layers do not interact with each other. Each adsorbed molecule in the monolayer is assumed to be adsorption site for second layer of molecules, and so on. According to BET theory,

$$P/V[P_0\text{-}P] = 1/V_mC + C\text{-}1/V_mC\ P/P_0 \qquad 2.10$$

where, P is the pressure, P_0 is the saturation pressure, V is the amount of gas adsorbed at the relative pressure P/P_0, V_m is the monolayer capacity, C is the BET constant. A plot of $P/V\ (P_0\text{-}P)$ versus relative pressure (P/P_0) is a straight line with a slope of $(C–1)/(V_mC)$ and intercept of $1/(V_mC)$, respectively. V_m is calculated from slope and intercept. Subsequently the specific surface area of the sample can be determined by the following equation.

Specific surface area = $V_m N_A A_M / W V_0$ 2.11

where, V_m is volume of monolayer, N_A is the Avagadro's constant (6.023 x 10^{23} molecules mol^{-1}), A_M is the cross sectional area of the adsorbate molecules (For N_2, A_M =0.162 nm^2 at 77 K) and V_0 is the molar volume of the gas (22414 mL mol^{-1}).

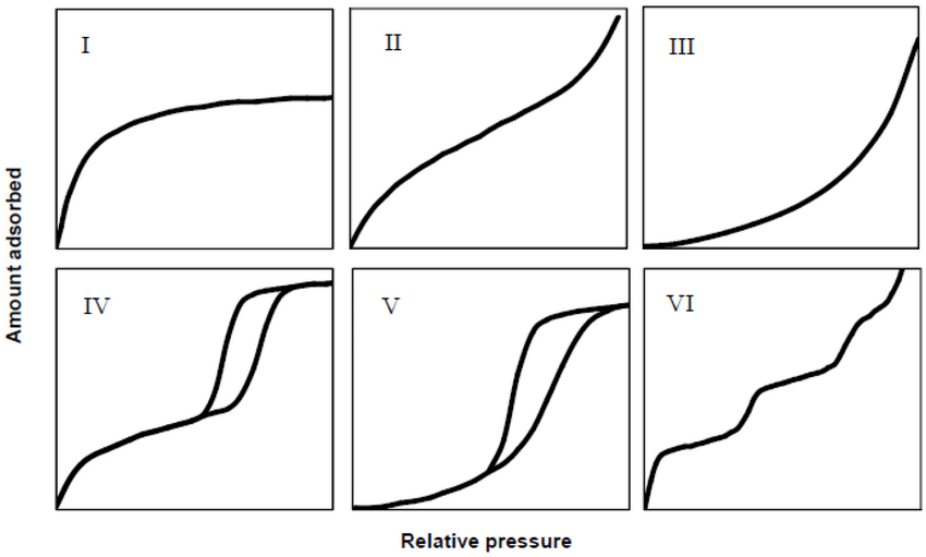

Figure 2.3 IUPAC classification of adsorption isotherm (https://gasadsorptiontech.wordpress.com/tag/adsorption-isotherm-types/).

An adsorption isotherm is obtained by measuring the amount of gas adsorbed across a wide range of relative pressures at a constant temperature. Similarly, desorption isotherms are achieved by measuring gas removed with reducing pressure. The shape of the isotherm gives idea about the porous texture of the material. Mainly, the isotherms can be classified into six types. According to IUPAC classification (Figure 2.3), Type I identifies that pores are typically microporous nature. Type II and III corresponds to mesoporous solids with strong and weak affinities, respectively. Type IV and V characterize adsorption isotherms of mesoporous solids with strong and weak affinities, respectively. Type VI corresponds to the step wise multilayer adsorption at weak adsorbate-solid interactions. In the present study, BET surface area of as prepared samples

was analyzed using N_2 adsorption-desorption measurements [Micromeritics Gemini 2375 Surface Area Analyzer, USA].

2.10 Selected Area Electron Diffraction (SAED)

SAED are crystallographic data that can be obtained within a TEM instrument. SAED is employed to select the interest of the specimen to obtain its diffraction patterns in a screen that is projection of the reciprocal lattice of interest, appearing as sharp diffraction spots. In SAED, the brightest spot (called as transmitted spot) usually appears in the centre of the diffraction pattern; the other spots are diffraction patterns. In general, one projected SAED can provide two-dimensional (2D) crystallographic information, such as two axes of the lattice parameters. To obtain complete crystallographic information, including lattice parameters of interest (a, b, c, and relative angles), defects, and orientational relationships, it is necessary to tilt the sample to obtain a series of SAEDs (Lin *et al*., 2014). In this research work, the SAED patterns are obtained using the TEM instrument Tecnai G^2, FEI, Netherlands to confirm the nanocrystallinity and nature of phases.

2.11 Energy Dispersive X-ray Spectroscopy (EDS)

EDS is an important technique in the material analysis, which allows identifying the presented elements or their relative proportions (*e.g*. Atomic %). EDS is mainly equipped with SEM or TEM instrument. EDS makes use of the X-ray spectrum emitted by a solid sample bombarded with a focused beam of electrons to obtain a localized chemical analysis. In the EDS, y-axis shows the counts (the number of X-rays received and processed by the detector) and the x-axis shows the energy level of those counts. All elements from atomic number 4 (Be) to 92 (U) can be detected in principle, though not all instruments are equipped for 'light' elements ($Z < 10$). In the present study, an EDS analyser equipped with the SEM instrument (ZEISS EVO 18) was used for the elemental analysis of the as prepared samples.

2.12 Zeta Potential

Zeta potential is related surface charge possessed by all materials when dispersed in a fluid. All materials spontaneously acquire a surface charge when come in contact with a polar medium (*e.g.* water) and it occurs due to ionization, ionic adsorption, and ionic dissolution. This surface charge affects the distribution of neighbouring ions of the polar medium. It results in the increased concentration of oppositely charged ions near to the particle surface. Thus an electrical double layer is formed around each particle. The liquid layer surrounding the particle exists as two parts. The inner layer where the ions are strongly bound is called Stern layer. The outer layer where the ions are less firmly attached is called diffuse region. There is a notational boundary exist within the diffuse layer. When a particle moves, ions with in boundary move along the particle motion, but the ions beyond the boundary remains stationary. This boundary is called the surface of hydrodynamic shear or slipping plane. The potential that exists at this boundary is known as the Zeta potential. In the present study, the zeta potential was measured at pH 7 using Zeta sizer (3000H, Malvern instrument).

2.13 Viscosity Measurement

Viscosity is defined as the internal friction of a liquid. This internal friction is generated along the both sides of a hypothetical plane parallel to the movement of the liquid. The internal friction per unit area on the parallel plane is called slip stress or shear stress, and the velocity gradient with respect to the direction rectangular to that of the flow is called slip velocity or shear velocity. A liquid of which the slip velocity is proportional to its slip stress is called a Newtonian liquid. The proportionality constant μ, is a characteristic of a liquid at a certain temperature and is called viscosity. The viscosity is expressed in the unit of Pascal second (Pa. s) (equivalent to N s m^{-2} or kg m^{-1} s^{-1}) and also in milli Pascal second

(mPa. s). A liquid whose slip velocity is not proportional to its slip stress is called a non newtonian liquid. In the present research work, viscosity of the ZnO/Si and ZnO/Si/GO dispersed gelatin bionanocomposite solutions were measured using the Rheometer, Viscotherm VT2, Physica, anton Paar.

2.14 Contact Angle Measurement

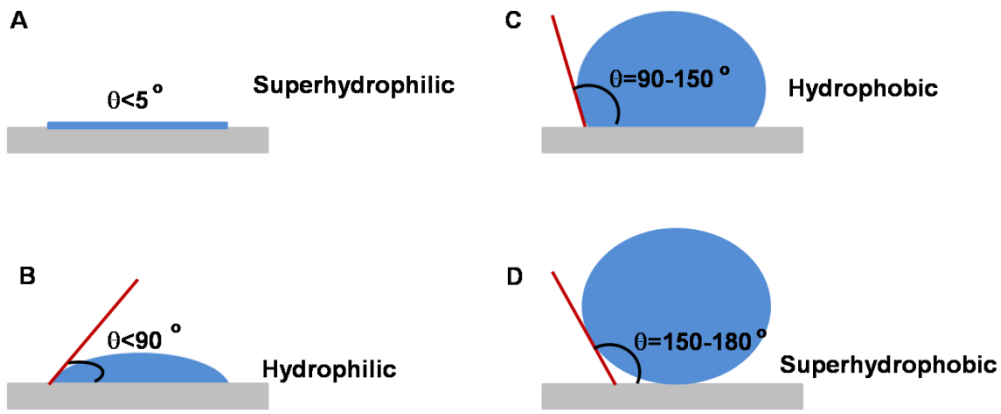

Figure 2.4 Schematic diagrams for the (A) superhydrophilic (B) Hydrophilic (C) Hydrophobic and (D) superhydrophobic surfaces.

When an interface exists between a liquid and a solid, the angle between the surface of the liquid and the outline of the contact surface is named as the contact angle or wetting angle (θ). The contact angle is a measure of the wettability of a solid by a liquid. In the case of complete wetting or spreading, the contact angle is < 5^o. In the case of a wettable surface the contact angle is < 90^o. In the case of surfaces which are not wettable, the contact angle is between 90-150^o. If the contact angle approaches theoretical limit of 180^o, the surface is called superhydrophobic. This phenomenon is called as lotus effect. The schematic diagrams for superhydrophilic, hydrophilic, hydrophobic and super hydrophobic surfaces are shown in Figure 2.4. In the present study, contact angle was measured using sessile drop method using the instrument kruss DSA30, Germany.

2.15 Fluorescence Microscopy

Fluorescence microscope is same as an optical microscope but it uses fluorescence to generate an image. Molecules raise their energy level to an excited state and they emit fluorescent light when they decay from this excited state. A fluorescence microscope uses higher ultra violet for excitation then it will emit a longer wavelength light which produces the magnified image of the sample. In the present study, the fluorescence images of ZnO and ZnO/Si are obtained using epifluorescent microscope (Leica DM-2500).

CHAPTER 3

In-situ Processing of ZnO/rGO Nanoarchitectures and its Photocatalytic Studies on Cationic dyes

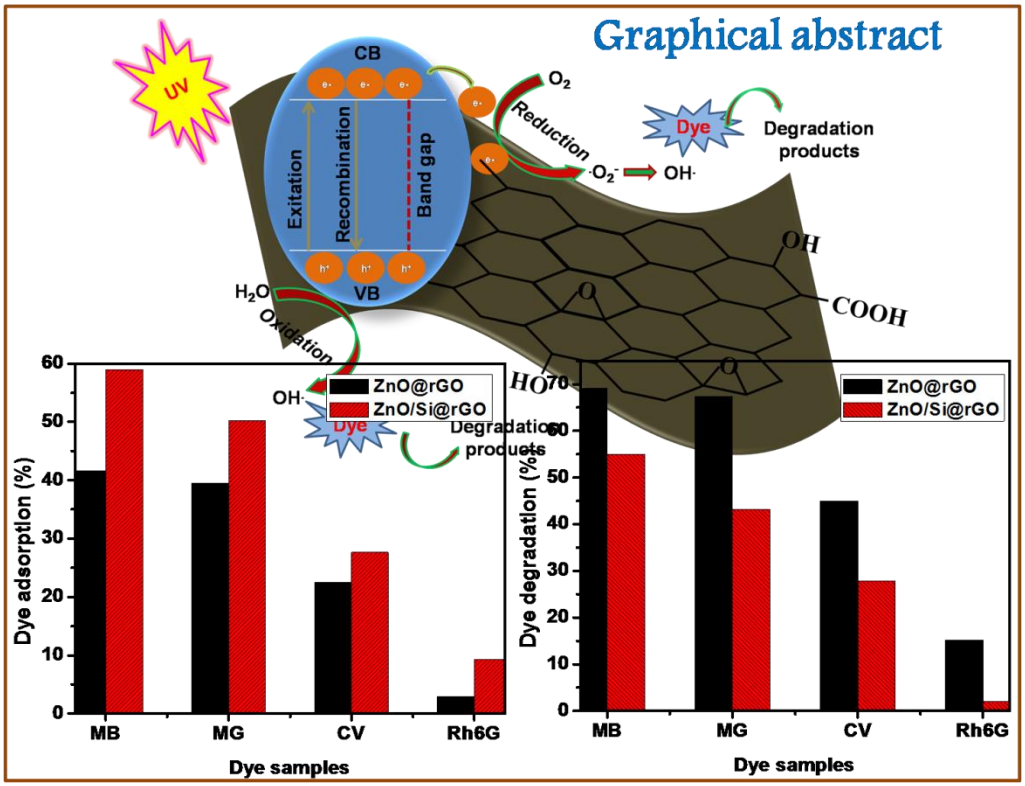

3.1 Abstract

Exfoliated GO is catalytically activated *via* in-situ growth of nanocrystalline ZnO resulting in ZnO@rGO nanocomposite. In-situ crosslinking of nano ZnO with 3-aminopropyltrimethoxy silane (APTMS) leads to ZnO/Si@rGO nanocomposite architectures. Structural and morphological features are systematically ascertained using XRD, SEM, TEM, TGA, UV-vis, FTIR, and BET techniques. The adsorption and photocatalytic degradation property of both ZnO@rGO and ZnO/Si@rGO against the adsorption and photodegradation of a series of cationic organic dyes were studied. In addition to this, ZnO-rGO composite was also prepared by physical blending method and the adsorption and photodegradation was compared with ZnO@rGO and ZnO/Si@rGO nanocomposites. ZnO@rGO nanocomposite shows good photocatalytic activity (69%) compared to ZnO/Si@rGO, ZnO-rGO and pure ZnO. ZnO/Si@rGO nanocomposites exhibit high surface area of about 78 $m^2 g^{-1}$. It is significantly large compared to phase pure nano ZnO where the surface area is only 18 $m^2 g^{-1}$. ZnO/Si@rGO nanocomposite also shows ~55% photocatalytic activity and ~59% adsorption of dye from aqueous system containing 340 μM methylene blue (MB) dye. The adsorption and photodegradation of ZnO@rGO and ZnO/Si@rGO was compared with pure ZnO, which shows only ~0% adsorption and ~31% photocatalytic activity.

3.2 Introduction

Design of functionally activated catalytic materials has received great attention in recent years with special focus on environmental remediation applications (An *et al*., 2011; Tu *et al*., 2013). GO offers many oxygenated surface hydrophilic functionalities preferred much for sorption as well as membrane applications due to its meso/nano porous layered microstructures, readily dispersion in aqueous/organic media, resistance against bacterial

activity and tuneable surface functionality (Wang *et al*., 2014; Dreyer *et al*., 2010). 2D GO nanosheets have been demonstrated for the adsorption of Pb(II), Co(II) and Cd(II) heavy metal ions (Upadhyay *et al*,. 2014). Wang *et al*. (Wang *et al*., 2012) and Zhang *et al*. (Zhang *et al*., 2012) conducted the adsorption of polycyclic aromatic hydrocarbons such as naphthalene, phenanthrene, and pyrene on graphene nanostructures. Yang *et al*. proposed GO-Fe_2O_3 nanocomposites for the adsorption of organic and inorganic pollutants (Yang *et al*., 2012). These reports strongly indicate that nanostructured GO is a potential sorbent for many hazardous chemical pollutants. Researchers made attempts to catalytically modify GO/rGO in order to chemically decompose the hazardous pollutants and subsequently regenerate the material for any continuous use. It is achieved *via* in-situ growth of catalytic grade semiconducting metal oxide nanostructures that successfully introduced dual-functionality; simultaneous adsorption and degradation of organic/inorganic contaminants; and self-regeneration capacity.

In this context, design of GO nanocomposite architectures involving catalytically active nano crystalline TiO_2, CdS, ZnO *etc*., has received prime importance. Gu *et al*., have grown anatase nano TiO_2 on rGO nanosheets and reported that rGO/TiO_2 hybrid had better photoactivity compared to its nano counterpart (Gu *et al*., 2013). Jia *et al*. reported (N-graphene)/CdS nanocomposite as co-catalyst for photocatalytic H_2 production (Jia *et al*. 2011). Zhang *et al*. developed CdS-graphene-TiO_2 hybrids through in-situ strategy on the flatland of GO for the selective photocatalytic oxidation of alcohols to aldehydes (Zhang *et al*., 2012). An enhanced visible light photocatalytic performance of graphene/TiO_2 nanocomposites is also reported in this series (Stengl *et al*., 2011). It is clear from these reports that rGO is extensively studied with photoactive TiO_2 compared to its competitive

ZnO/rGO architectures. ZnO has poor surface area and it is prone to electron-hole recombination which limits its use as efficient photocatalyst. Growth of rGO supported ZnO nanocatalyst can partially resolve these limitations (Liu *et al*., 2011).

In this work, in-situ synthesis of ZnO@rGO and APTMS crosslinked ZnO/Si@rGO nanocomposite is designed *via* microwave reflux technique and the beneficial properties of nano architectures are studied for the adsorption and photodegradation properties. The performance of nanocomposites is compared with the physically blended ZnO-rGO. Comparative studies with respect to the physio-chemical properties, adsorption as well as photocatalytic degradation of catalytically modified ZnO@rGO, ZnO/Si@rGO and ZnO-rGO architectures were systematically attempted and reported for the first time.

3.3 Experimental Section

3.3.1 Materials

Graphite was procured from Sigma Aldrich, Germany (99.9%). Sodium nitrate ($NaNO_3$, 99.5%), Potassium permanganate ($KMnO_4$, 99%) and Hydrogen peroxide (H_2O_2, 99%) were obtained from S. D. Fine Chemicals Limited, India. Zinc nitrate hexahydrate ($Zn(NO_3)_3.6H_2O$, 99%) and Conc. Sulphuric acid (H_2SO_4 , 99%) were supplied by Merck, India. Lithium hydroxide (LiOH, 99%), Methylene blue (MB) ($C_{16}H_{18}ClN_3S$) and Crystal violet (CV) ($C_{25}H_{30}ClN_3$) were purchased from SRL, India. Malachite green (MG) ($C_{23}H_{25}ClN_2$) and Rhodamine 6G (Rh6G) ($C_{28}H_{31}ClN_2O_3$) were obtained from Qualigen Fine Chemicals, India and S. D. Fine Chemicals Limited, India respectively. All the reagents were used as received without any further purification.

3.3.2 Synthesis of GO

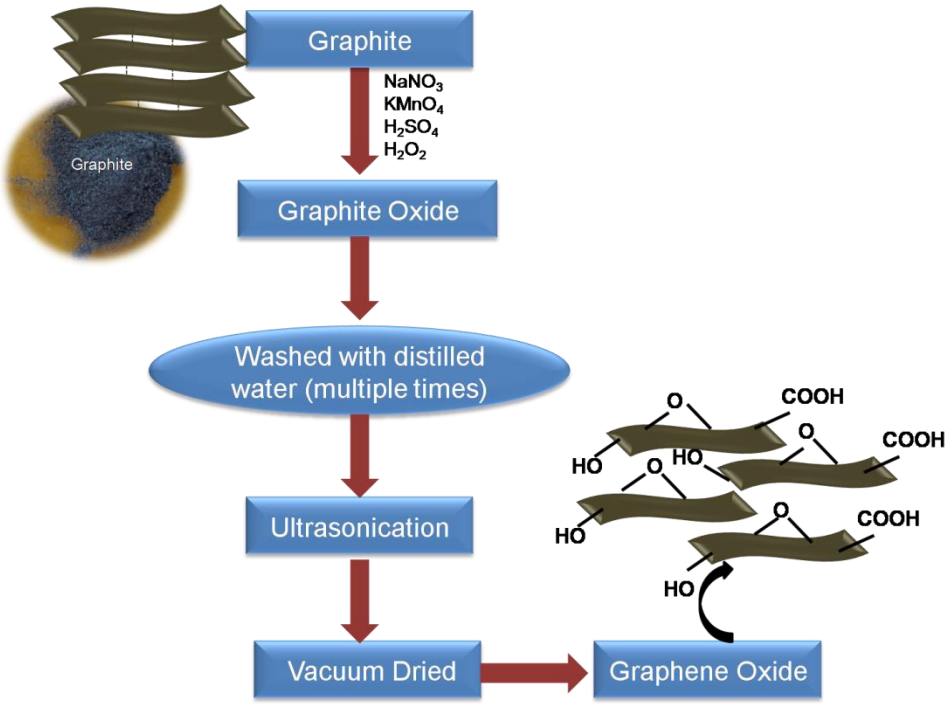

Figure 3.1 Synthetic procedure for the synthesis of GO.

GO was synthesized by the oxidation and exfoliation of powder graphite (GR) *via* a well reported modified Hummer's method (Krishna *et al*., 2012). In a typical experiment, 1 g GR, 1 g $NaNO_3$ and 50 mL conc. H_2SO_4 were successively added to a beaker and stirred magnetically for 30 min in an ice bath. To this 3 g of $KMnO_4$ was added and the resultant mixture was transferred to a water bath maintained at 35 ^oC. The whole reaction mixture was diluted with 150 mL of distilled water. To this diluted mass, 10 mL of 30 % H_2O_2 was gradually introduced. After vigorous stirring for 60 min, the end product was centrifuged and purified by repeated washing with double distilled water until the pH became 7. The resultant mass was ultrasonicated (1h) to exfoliate the GO sheets. Finally, the exfoliated GO was dried by vacuum drying at 65 ^oC. The synthetic procedure is given in Figure 3.1.

3.3.3 Preparation of ZnO/rGO Nanoarchitectures (ZnO@rGO, ZnO/Si@rGO, and ZnO-rGO)

A desired amount of GO was dispersed in aqueous medium and sonicated for 30 min. To this, 0.2 M $Zn(NO_3)_3.6H_2O$ solution was added under ultrasonication by keeping the ZnO:GO weight (wt) ratios 8:1, 4:1, 2:1, and 1:1. The reaction mixture was subsequently treated with 10 wt.% LiOH for the in-situ precipitation of $Zn(OH)_2$ at room temperature (Since LiOH is a weak base, it leads to the slow nucleation of $Zn(OH)_2$ particles). The pH of the reaction was maintained as ~8.5, otherwise the formed $Zn(OH)_2$ particles may get dissolved in the reaction medium at higher or lower pH. A homogeneous dispersion of GO deposited with $Zn(OH)_2$ was obtained which was taken to the microwave synthesis work station (Sineo, MAS II) operating at a frequency of 2.45 GHz and having a microwave power in the range 0-1000 W. A constant temperature of 80 ^oC was kept for the microwave refluxing and the reactant mixture was refluxed for 30 min at microwave power 300 W. Microwave irradiated ZnO modified rGO was finally centrifuged and washed with double distilled water until the pH of the filtrate became neutral. The ZnO@rGO nanocomposite products were then vacuum dried at 65 ^oC.

Similarly, the same procedure was followed for the synthesis of ZnO/Si@rGO nanocomposites by taking 1:1 ZnO/GO (wt. ratio) composition. It was prepared by the in-situ addition of APTMS. Silane/ZnO molar ratio of 0.3 was maintained. For comparison, a ZnO-rGO composite mixture was further prepared by physical blending. Nano ZnO was synthesized *via* microwave assisted precipitation of 0.2 M $Zn(NO_3)_2.6H_2O$ using LiOH. rGO was prepared *via* simple microwave treatment of GO at 80 ^oC. Without any heat treatment the nano ZnO was physically blended with equal amount of rGO to obtain ZnO-rGO with wt.

ratio 1:1. A schematic illustration of as-prepared ZnO@rGO, ZnO/Si@rGO, and ZnO-rGO nanocomposites is shown in the Figure 3.2.

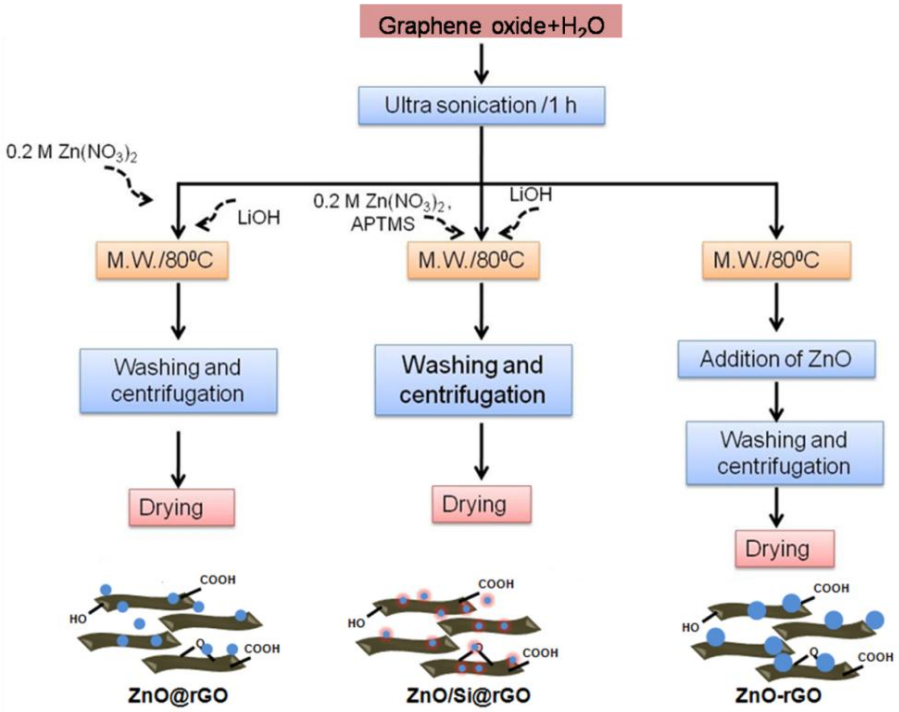

Figure 3.2 Illustration of the processing of different ZnO-rGO nanoarchitectures: ZnO@rGO, ZnO/Si@rGO, and ZnO-rGO.

3.3.4 Dye Adsorption and Photocatalytic Activity Studies

The adsorption and degradation experiments were conducted with UV-vis spectroscopy by measuring the absorbance from 200-800 nm. The concentration of the dye in the solution was determined by Beer-Lambert law expression. Since the concentration of the dye used was high (340 μM), the dye samples were diluted before absorbance measurements. Batch adsorption as well as degradation experiments were conducted. Preliminary experiments indicated that the adsorption as well as degradation of dye reached equilibrium in ~1 h. Thus the contact time of 2 h was given for all the batch experiments. All experiments were conducted in duplicate, and only the mean values were reported. Blank experiments without the addition of catalyst were also conducted to ensure that the decrease in the concentration was actually due to the

adsorption as well as degradation of catalytically activated rGO architectures rather than by the adsorption on glass bottle wall.

The adsorption experiments were performed by adding a specific amount of ZnO/rGO nanoarchitectures (0.4 g L^{-1}) to the beakers containing 75 mL of 340 μM dye solutions each. The aqueous suspension was stirred continuously under dark condition. Small amount of aliquots were collected at different time intervals, centrifuged to separate the dye adsorbed powder. The remaining concentration of the dye was measured from the absorbance peak before and after the adsorption by UV-vis absorption spectroscopy. The characteristic absorption band of MB, MG, CV, and R6G occurred at 656, 620, 590 and 530 nm, respectively. The % of dye adsorption was calculated using the equation,

$$\% \text{ of adsorption} = [(C_0\text{-}C)/C_o]100 \qquad 3.1$$

where Co (mg L^{-1}) and C (mg L^{-1}) are the initial dye concentration and dye concentration after time t, respectively (Hareesh *et al*., 2012).

The photocatalytic activity of the ZnO/rGO nanoarchitectures was evaluated from the photodegradation of 340 μM dye solution under UV radiation. For a typical experiment, 0.4 g L^{-1} catalyst powders was added to 75 mL of 340 μM dye solution and stirred continuously for 30 min under dark condition in order to obtain stabilisation of dye solution over the catalyst powder subsequently exposed to UV radiation. Aliquots were collected at different time intervals, and same procedure was adopted (Baiju *et al*., 2007). The % of dye degradation was calculated using the equation,

$$\text{Dye degradation (\%)} = (C/C_0)100 \qquad 3.2$$

The photocatalytic degradation follows Langmuir-Hinshelwood mechanism, (Jaimy *et al*., 2012) which may be represented as

$dC/dt=k_{app}C$ 3.3

where, dC/dt is the rate of change of MB concentration with respect to UV irradiation time t. k_{app} is the apparent first order reaction rate constant (min^{-1}) and C is the concentration of MB dye at time t. The solution obtained when integrating the above equation is

$ln(C_0/C)=k_{app}t$ 3.4

where C_0 is initial concentration of the MB dye solution. The plot of $ln(C_0/C)$ against UV irradiation time t gives a straight line. k_{app} was obtained from the slope of $ln(C_0/C)$ against t. In the present work, adsorption and photodegradation of MB, MG, CV and R6G dyes were analysed using ZnO/rGO nanoarchitectures.

3.4 Results and Discussion

3.4.1 Conversion of GR to GO

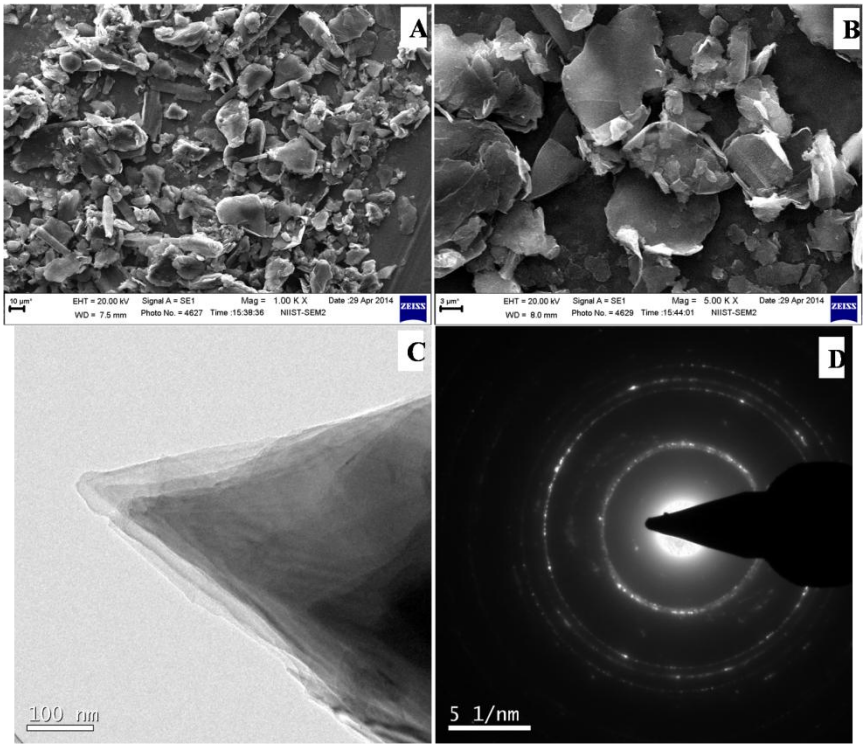

Figure 3.3 Typical (A) low magnification and (B) high magnification SEM images of GR, (C) Typical TEM image and (D) SAED pattern of GR.

Typical low and high magnification SEM images of GR particles are shown in the Figure 3.3A and 3.3B. Huge lumbs of GR particles are seen in the SEM images with a particle size of ~5-10 μm. The multilayered nature of GR is confirmed from the TEM image given in the Figure 3.3C. The TEM image of GR displays that ~10 layers of carbon sheets are there in the graphite particle. The SAED pattern obatined from the TEM instrument shows the high crystalline nature of GR particles (Figure 3.3D).

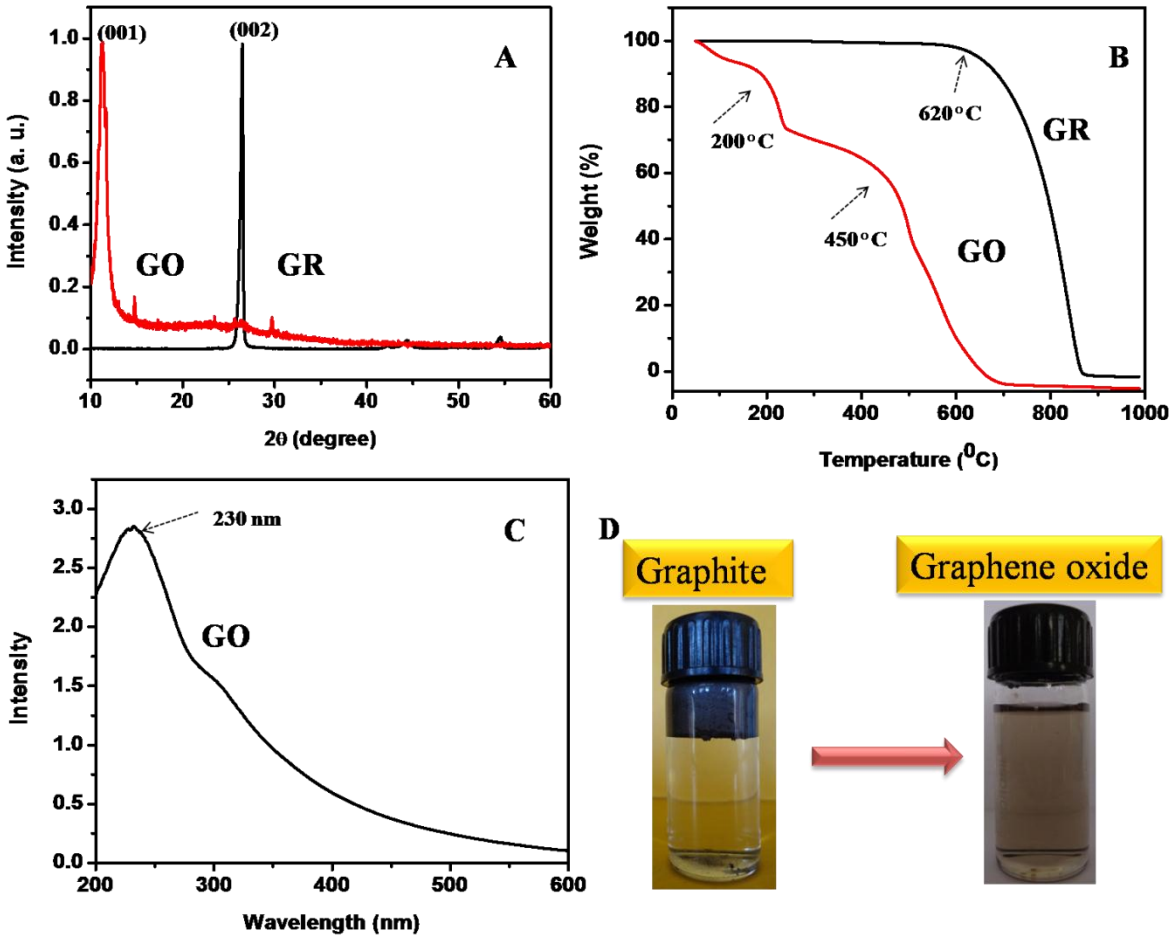

Figure 3.4 (A) X-ray diffraction analysis and (B) TG analysis of GR and GO, respectively (C) UV-vis absorption spectra of GO (D) The photographs of GR and GO in water.

In Hummer's method, $KMnO_4$ and H_2SO_4 are used as oxidizing agents, where dimanganese heptoxide act as the active species in the oxidation process (Dreyer *et al.*, 2010).

Adequate ultrasonication in water leads to the exfoliation of the oxidized layers. These exfoliated sheets usually contain one or few layers of carbon atoms similar to graphene and resulted in GO. The conversion of GR to GO was established by various characterization tools. The powder X-ray diffraction analysis (Figure 3.4A) shows the characteristic diffraction peak of hexagonal GR with a reflection peak centred at 26 ^{o} (002). It also shows the crystalline nature of GO where the diffraction peak at 10.8 ^{o} represents the (001) plane of GO (Zhao *et al.*, 2012; Wang *et al.*, 2012). This indicates that GR is completely oxidized to GO sheets.The thermal stability of as-received GR measured by TG analysis is given in the Figure 3.4B. As

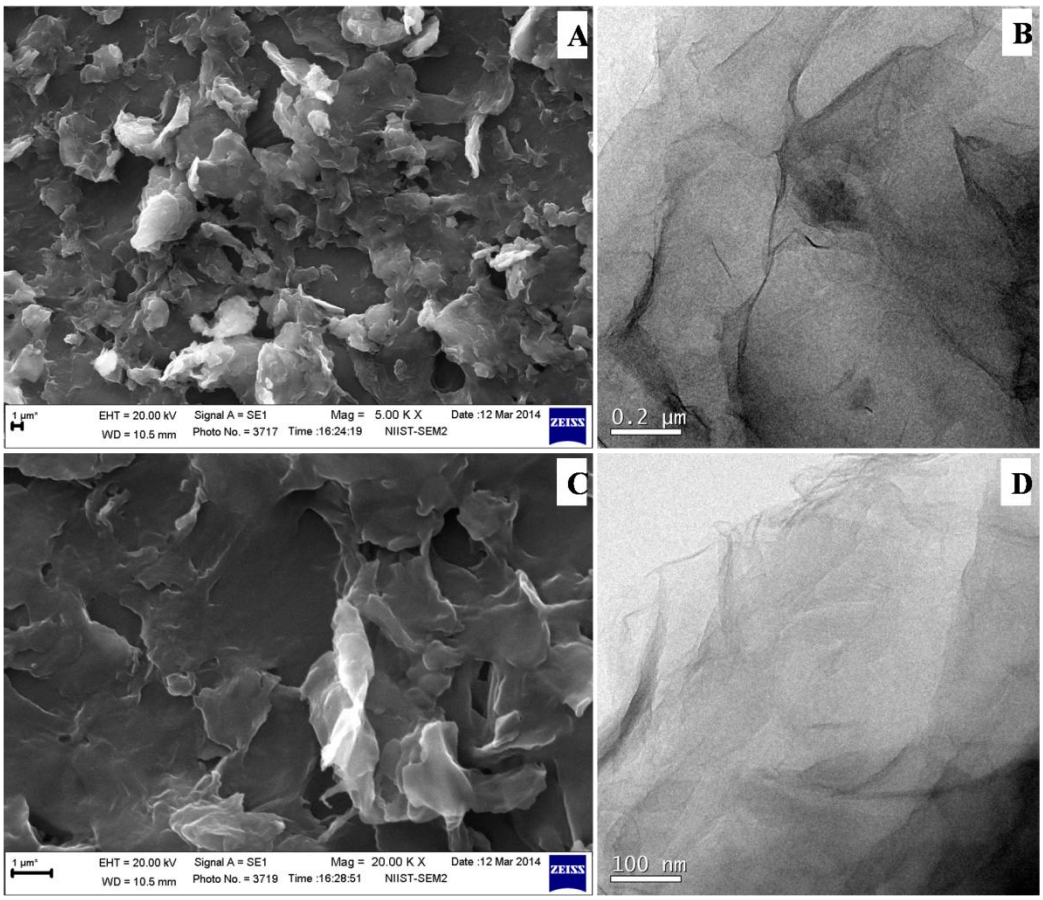

Figure 3.5 (A and C) low and high magnification SEM images of GO, (B and D) low and high magnification TEM images of GO.

seen in the figure, GR is stable up to 620 ^{o}C. A rapid and one step reduction in the weight is observed after 620 ^{o}C due to the decomposition of the graphitic carbon. The TG analysis of GO showed three step decompositions. The weight loss (~5 %) found below ~ 100 ^{o}C is associated with the decomposition of physically adsorbed water molecules on the surface of hydrophilic GO sheets. The second weight loss of ~8 % between 200 to 250 ^{o}C is actually due to the loss of oxygen containing functional groups (eg. –COOH, -O- etc.,) decorating the surface of GO. This was followed by a complete oxidative decomposition of the graphitic substrate in between 450-690 ^{o}C. The UV-vis absorption spectra of GO given in the Figure 3.4C describes the absorption maxima at 230 nm and a shoulder peak at 302 nm corresponding to the π-π^* transition of the aromatic C-C and C=O, respectively. It is consistent with the λ_{max} value of GO reported in previous literatures (Liao *et al*., 2013). Due to the lack of functional groups in GR, it is difficult to disperse GR in water (Figure 3.4D). A homogeneous dispersion of hydrophilic GO is obtained in water and the photograph shows the stable GO dispersion. A high stability confirms the polarity of the GO surface (Dreyer *et al*., 2010).

The low and high magnification SEM images given in the Figures 3.5A and 3.5C, which shows that micrometer sized sheets of GR particles are completely delaminated into sub micron sized thin layers of GO sheets with single or few layers. The low and high magnification TEM images of GO given in the Figure 3.5B and 3.5D, displays exfoliated sheets of GO derived from GR. It appeared curly in nature (Gawande *et al*., 2013).

3.4.2 Characterization of ZnO Particles

The low and high magnification TEM images of as-prepared ZnO particles are provided in the Figures 3.6A and 3.6B. Analyzing the TEM micrographs it was evident that ZnO nanoparticles obtained *via* microwave assisted method are nearly spherical in shape with a particle size of ~50-70 nm. The highly crystalline nature of ZnO nanoparticles are confirmed from the SAED pattern given in the Figure 3.6C.

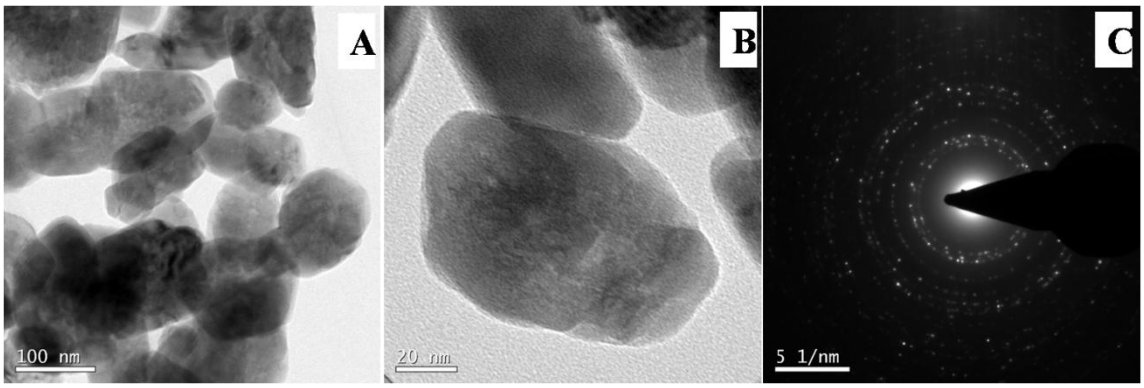

Figure 3.6 Typical (A) TEM (B) HRTEM and (C) SAED pattern of ZnO nanoparticles.

3.4.3 Characterization of ZnO/rGO Nanoarchitectures

The SEM images of ZnO@rGO nanocomposites with various ZnO:GO wt ratios 8:1, 4:1, 2:1, and 1:1 are presented in the Figure 3.7. From the SEM images it is clear that ZnO:GO wt ratio 1:1 provides homogeneous distribution of ZnO on GO nanosheets. But in samples with ZnO:GO wt ratios 8:1, 4:1, and 2:1, intimate contact between ZnO and GO is poor because of the higher amount of ZnO on the low amount of GO sheets. Equal distribution of ZnO on the GO sheets can be achieved in the sample with ZnO:GO ratio 1:1.

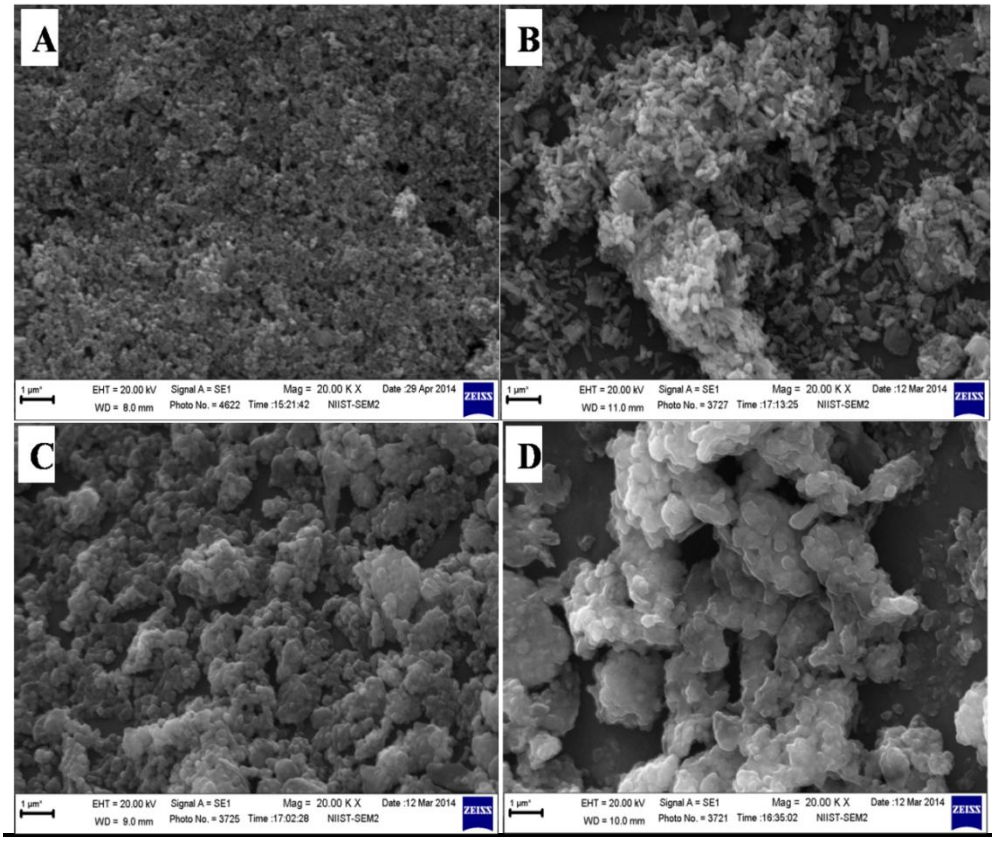

Figure 3.7 SEM images of ZnO@rGO composites in various ZnO:GO wt ratios (A) 8:1 (B) 4:1 (C) 2:1, and (D) 1:1.

Figure 3.8 is the TG analysis of GO and ZnO@rGO nanocomposites in various ZnO:GO wt ratios 1:1, 2:1, 4:1, and 8:1. During microwave treatment GO is completely reduced to rGO which is mainly attributed to the higher thermal stability of ZnO@rGO nanocomposite than GO. From the TG analysis it is clear that the wt. loss significantly decreases as the amount of ZnO increases. ZnO@rGO nanocomposites with 8:1 ZnO:GO wt ratio shows higher thermal stability. Binding of higher amount of ZnO on GO surface is contributing higher thermal stability in 8:1 wt ratio compared to other samples. The BET surface area values of ZnO@rGO nanocomposites were shown in the Figure 3.9. The BET surface area of ZnO is 18 m^2g^{-1}. The incorporation of rGO increased the surface area of ZnO.

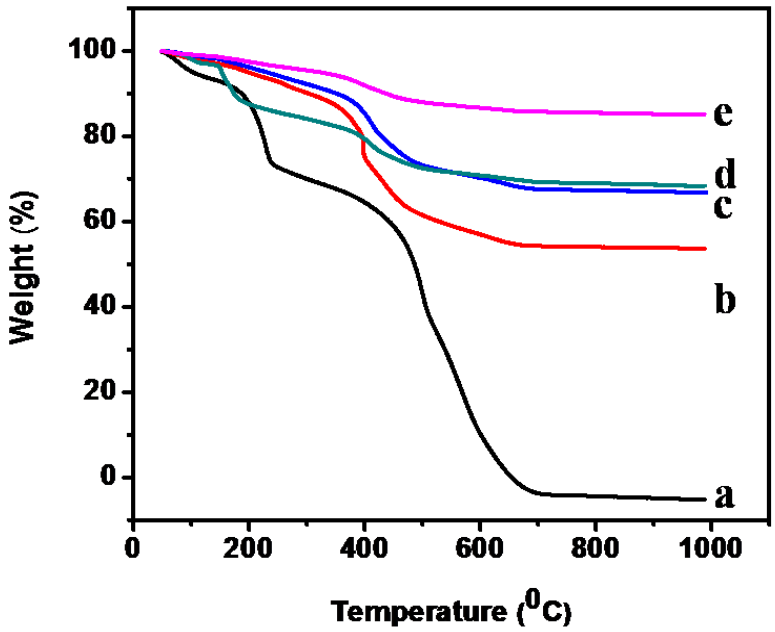

Figure 3.8 TG analysis of GO and ZnO@rGO nanocomposites in various ZnO:GO wt ratios (a) GO (b) 1:1 (c) 2:1 (d) 4:1 and, (e) 8:1.

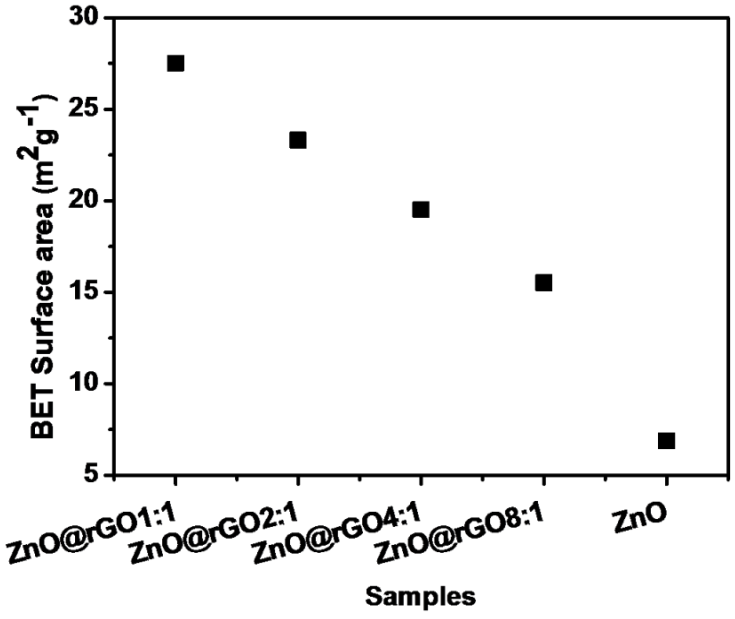

Figure 3.9 BET surface area analysis GO, ZnO, and ZnO@rGO nanocomposites in various ZnO:GO wt ratios 1:1, 2:1, 4:1, and 8:1.

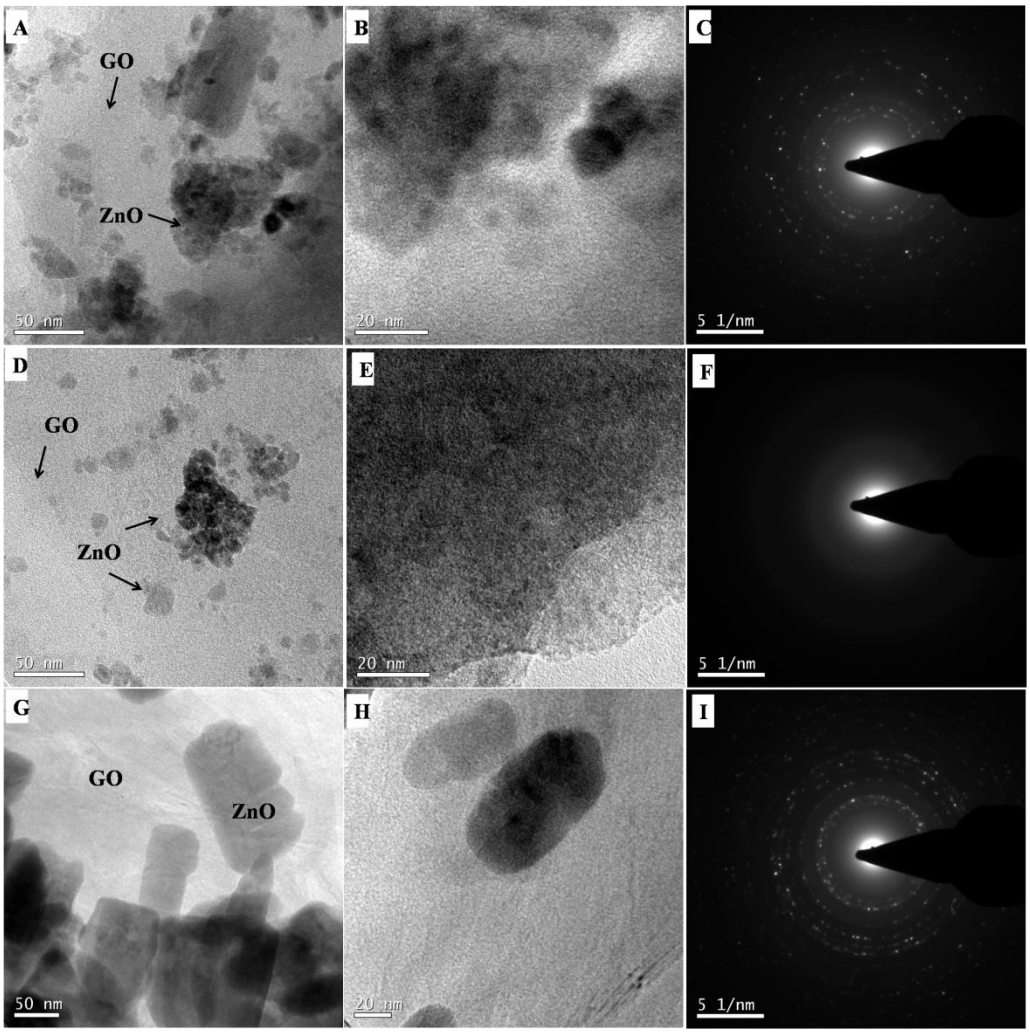

Figure 3.10 (A-C) Representative TEM, HRTEM, and SAED pattern of ZnO@rGO (D-F) TEM, HRTEM, and SAED pattern of ZnO/Si@rGO (G-I) TEM, HRTEM and SAED pattern of ZnO-rGO.

As the amount of ZnO in the nanocomposite increases from 1:1 to 8:1, the surface area got reduced. Due to good homogeneity and reasonable surface area of ZnO@rGO nanocomposite with 1:1 ZnO:GO wt ratio, this particular composition is used for the preparation of ZnO/Si@rGO and ZnO-rGO.

The representative TEM images given in Figure 3.10A, B, D, E, G and H show the growth of well defined nanocrystalline ZnO. The TEM morphologies clearly show the

advantage of rGO supported in-situ growth because nucleation and growth of nanocrystalline ZnO are preferably occurred on the carbon layers of rGO sheets. In fact, rGO supported in-situ growth resulted in size controlled nano ZnO over rGO substrates. For example, in absence of APTMS, the TEM and HRTEM images corresponding to ZnO@rGO (Figure 3.10A and B) shows that the rGO sheets are decorated with ~10-20 nm sized ZnO nanoparticles. On the other hand, in silane cross linked ZnO/Si@rGO nanocomposites, the rGO support contains thin layer of evenly distributed ZnO with particle size below 3 nm (Figure 3.10D and E). It indicates the capping effect of APTMS in controlling the ZnO growth (Shi *et al*., 2011). In case of ZnO-rGO composites prepared *via* physical blending technique, the distribution of physically adhered, large size ZnO with particle size ~100 nm is seen over rGO sheets (Figure 3.10G and H). The characteristic particle size seen in TEM/HRTEM images proves that the rGO substrates are extremely helpful in suppressing the aggregation of ZnO nanocrystals.

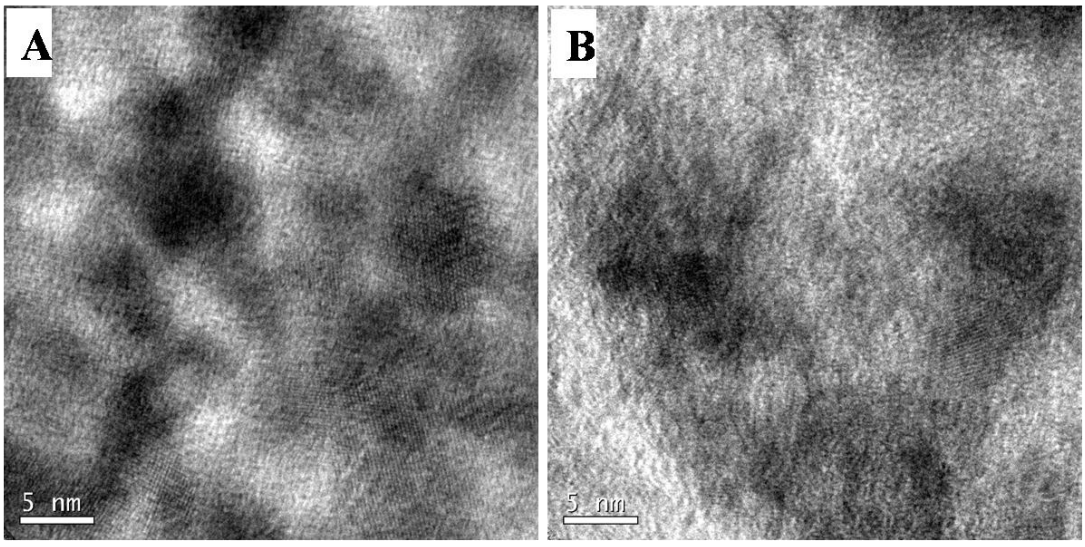

Figure 3.11 Representative HRTEM images of (A) ZnO@rGO and (B) ZnO/Si@rGO.

The SAED pattern shown in the Figure 3.10C and I explains the polycrystalline nature of ZnO modified rGO nanomaterials. In ZnO/Si@rGO nanocomposites, the APTMS is found

to reduce the crystalline nature slightly which is expected (Figure 3.10F). The HRTEM images of ZnO@rGO and ZnO/Si@rGO given in the Figure 3.11A and B shows the presence of nanocrystalline ZnO in the composites. The EDS results of ZnO, ZnO@rGO, and

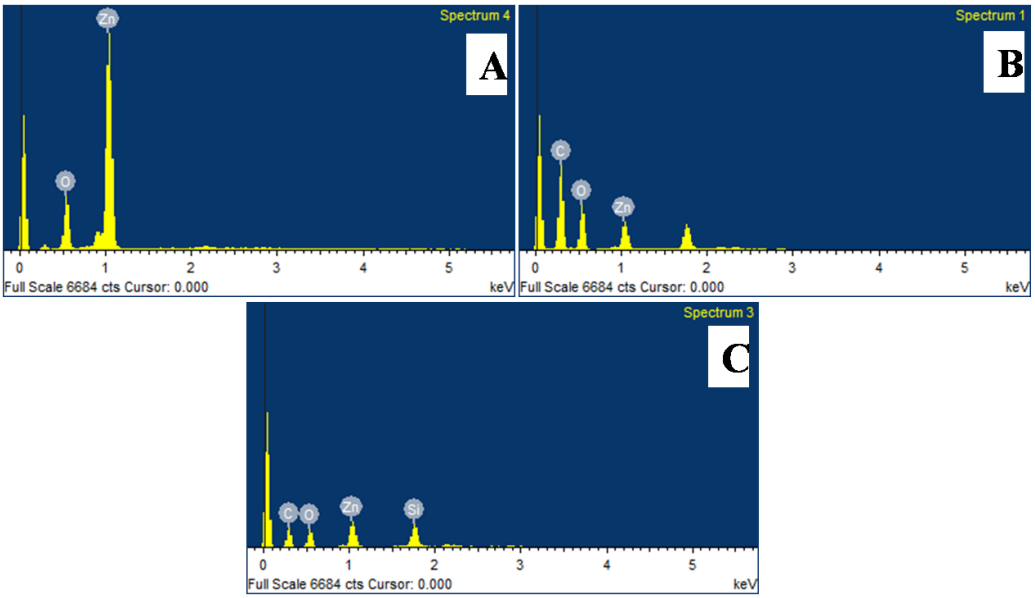

Figure 3.12 EDS analysis of (A) ZnO (B) ZnO@rGO, and (C) ZnO/Si@rGO.

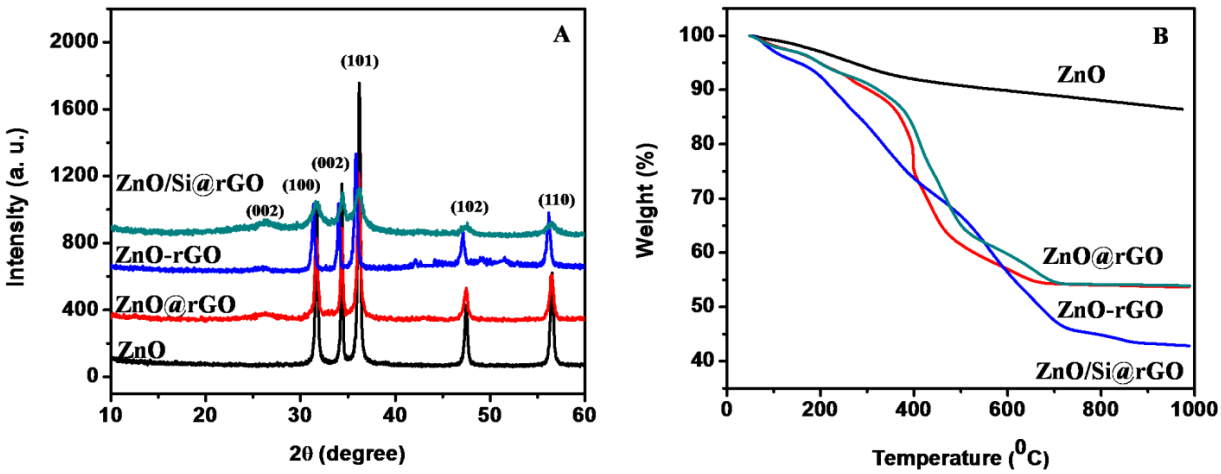

Figure 3.13 (A) XRD patterns of ZnO, ZnO@rGO, ZnO-rGO, and ZnO/Si@rGO. (B) TG analysis of ZnO, ZnO@rGO, ZnO-rGO, and ZnO/Si@rGO.

ZnO/Si@rGO as obtained from the SEM analysis are given in Figure 3.12A, B, and C. In sample ZnO@rGO, the presence of C, O, and Zn is evidenced (Figure 3.12B). In ZnO/Si@rGO nanocomposite (Figure 3.12C) the additional peak of Si is noticed which proves silane linkage between rGO and ZnO.

In the present work, we adopted microwave reflux technique for the synthesis of the ZnO/rGO nanoarchitectures. In presence of a base, microwave heating resulted in the partial reduction of GO (Wu *et al*., 2014). The XRD analysis in Figure 3.13A gives the crystalline nature of ZnO@rGO, ZnO/Si@rGO and ZnO-rGO. The XRD patterns consist all the characteristic peaks of ZnO at 2θ values 32 ^{o}, 34 ^{o} and 36 ^{o} which correspond to the (100), (101) and (002) planes. The diffraction peaks seen in ZnO@rGO, ZnO-rGO and ZnO/Si@rGO matches well with the crystal structure of wurtzite ZnO. In addition to that, all the composites shows additional peak at 26 ^{o}, which clearly shows the conversion of GO to rGO under microwave irradiation. The ZnO crystallite sizes determined from the Debye Scherrer equation are 17, 17, 13 and 6 nm, respectively that can be put in the order of ZnO > ZnO-rGO > ZnO@rGO > ZnO/Si@rGO.

Figure 3.13B shows the weight loss characteristics of ZnO, ZnO-rGO, ZnO@rGO and ZnO/Si@rGO grown in microwave irradiation. Among these, the APTMS capped nanocomposites have comparatively higher weight loss in the entire thermal heating range which is actually contributed by the decomposition of organosilane and surface adsorbed nitrates. In this case, ZnO/Si@rGO, a weight loss of ~45% was observed in the temperature range 200–700 ^{o}C. ZnO-rGO and ZnO@rGO show similar weight loss up to 260 ^{o}C. At higher temperatures ZnO@rGO shows more weight loss than ZnO-rGO because of the presence of nitrates during the in-situ formation of ZnO on rGO.

Results on the optical absorption properties of ZnO, ZnO-rGO, ZnO/Si@rGO, and ZnO@rGO studied using UV-vis spectral analysis are presented in Figure 3.14. Freely grown bulk nano ZnO has on-set absorption band at 368 nm. It is red shifted to 375 nm when ZnO nanocrystals are grown on rGO supports. It is evident that there is a chemical interaction between rGO and catalytic nano ZnO. The narrowing in band gap energy (3.15 eV to 3.00 eV) can demonstrate the significant influence of rGO on the optical characteristics.

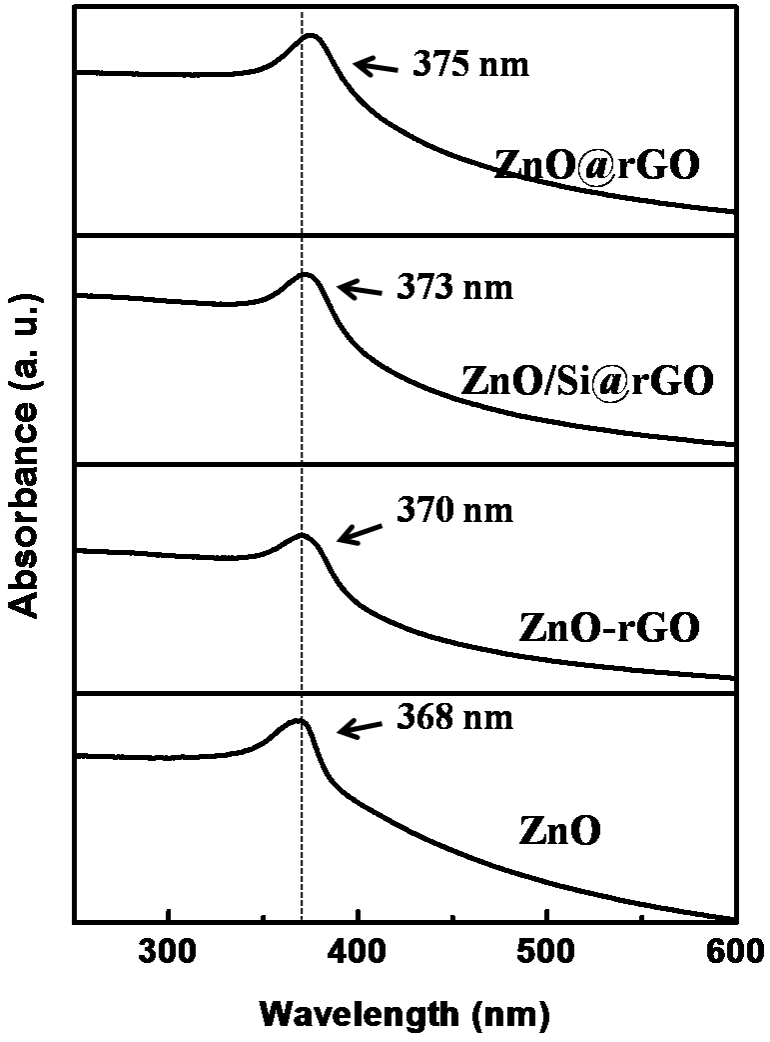

Figure 3.14 UV-vis absorption spectra of ZnO, ZnO-rGO, ZnO/Si@rGO, and ZnO@rGO.

Figure 3.15 shows the FTIR analyses of ZnO, GO, ZnO@rGO, and ZnO/Si@rGO. In the FTIR spectrum of ZnO, absorption band at 527 cm^{-1} is attributed to the vibration of Zn-O bonds. The interaction of rGO shifted this peak to 490 cm^{-1} for ZnO@rGO and ZnO/Si@rGO. The stretching vibration of surface hydroxyl groups (-OH) is confirmed by the broad absorption band observed in between 3000-3400 cm^{-1} (Costenaro *et al*., 2011). The bands corresponding to C=O carbonyl stretching at 1726 cm^{-1}, and C=C stretching at 1617 cm^{-1} indicates the presence of GO in the sample (Long *et al*., 2013). The IR spectrum of the

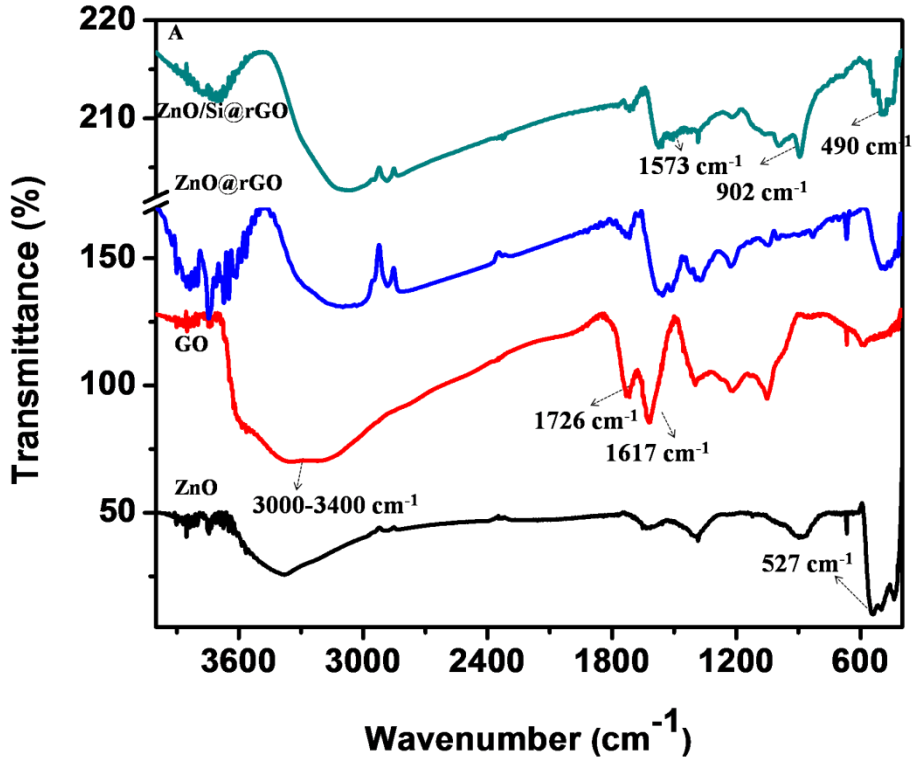

Figure 3.15 FTIR spectra of ZnO, GO, ZnO@rGO, and ZnO/Si@rGO.

ZnO/Si@rGO shows the presence of new bands at 1660 cm^{-1} and 1128 cm^{-1} corresponding to amide C=O stretching and C-N bond stretching (Valentini *et al*., 2012) vibrations. This confirms the presence of the amide functional group formed due to the interaction of rGO and APTMS. For ZnO/Si@rGO, the absorption bands observed at 3310-3350 cm^{-1} is attributed to

the stretching vibration of N-H bonds (Danon *et al*., 2011), which could be overlapped with the strong bands of -OH groups. The absorption band at 2930 cm^{-1}, 2850 cm^{-1} and 1395 cm^{-1} corresponds to the asymmetric stretching, symmetric stretching (Mallakpour *et al*., 2013) and bending vibrations (Bressy *et al*., 2012) of $–CH_2$ groups present in APTMS, respectively. The newly formed peak at 902 cm^{-1} shows the formation Zn-O-Si bond in the nanocomposite (Guo *et al*., 2009; Hong *et al*., 2009).

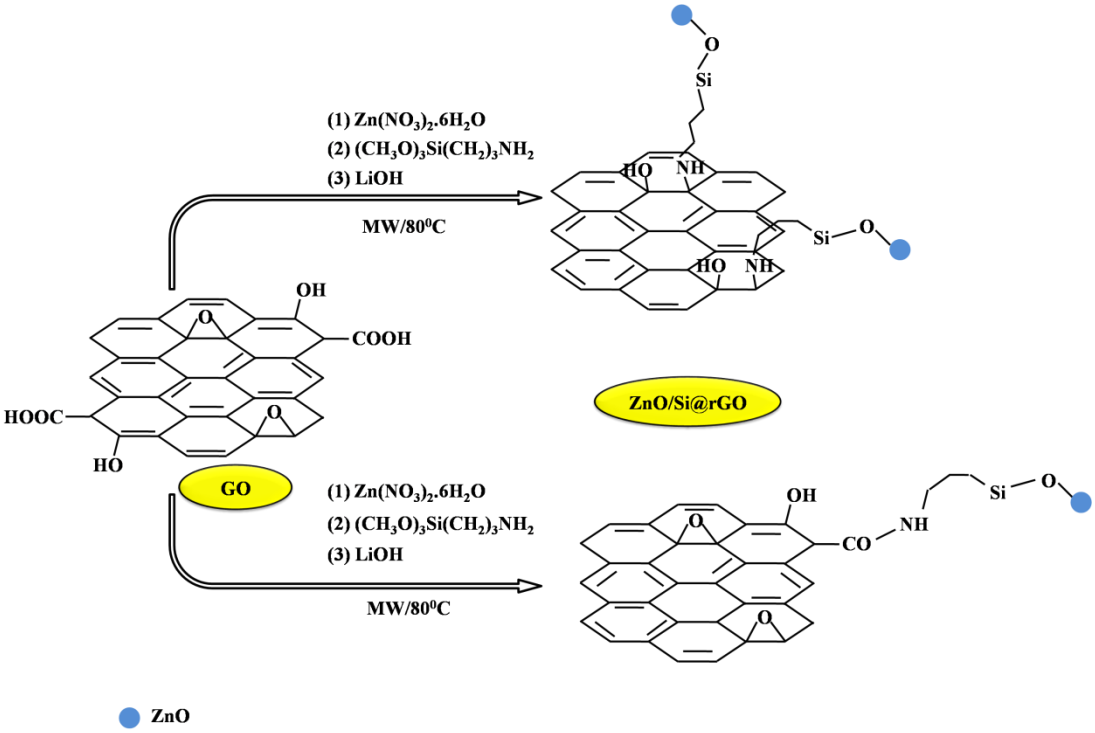

Figure 3.16 Proposed schematic illustration showing the mechanism of ZnO/Si@rGO formation.

Based on the FTIR analysis, the possible mechanisms for the synthesis of ZnO/Si@rGO nanocomposite are proposed and illustrated in the Figure 3.16. APTMS is a known and well reported cross linking agent. In the presence of water, APTMS undergoes hydrolysis and forms hydrolyzed APTMS (silanol). On partial condensation, these silanol

oligomers co-condense with the surface hydroxyl groups of ZnO via Zn-O-Si bonds (Guo *et al*., 2009). Simultaneously, the $–NH_2$ groups present in the APTMS interact with the epoxy group in rGO, hence $NH(CH_2)_3Si(OCH_3)_3$ is attached to rGO (Dreyer *et al*., 2010). The absorption band of ZnO/Si@rGO obtained at 3310-3350 cm^{-1} agrees with this mechanism. Another possibility is the interaction between $–NH_2$ groups of APTMS and the –COOH groups of rGO sheets resulting in the formation of amide linkage. Consequently ZnO continuously grafted on rGO sheets *via* Zn-O-Si bonds.

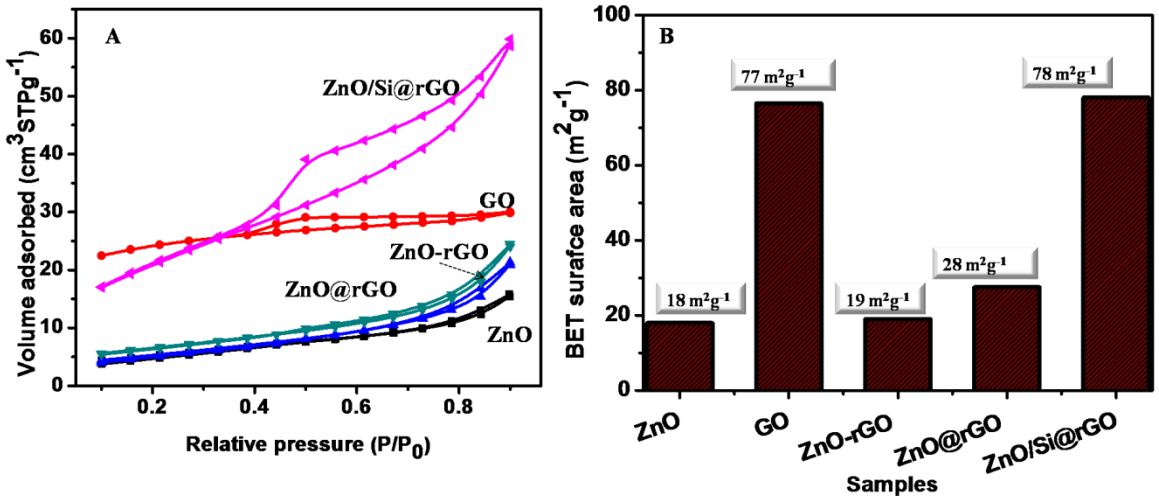

Figure 3.17 (A) N_2 adsorption-desorption isotherms for (a) ZnO, GO, ZnO-rGO, ZnO@rGO and ZnO/Si@rGO (B) BET surface area values of ZnO, GO, ZnO-rGO, ZnO@rGO, ZnO/Si@rGO.

The N_2 adsorption-desorption isotherms and the BET surface area values of the samples prepared in this work are given in the Figure 3.17A and 3.17B. Microwave strategy produced nano ZnO with BET surface area of 18 m^2 g^{-1}. The modified Hummer's route resulted in GO nanostructures having bulk surface area approximately 77 m^2 g^{-1}. In physically blended ZnO-rGO composite mixture, the surface area is decreased because of the preferential blocking of the pores by the large size nanocrystalline ZnO. It can be understood from the

reduction in the mesopore volume of GO wherein the actual pore volume is decreased from 0.0957 $cm^2 g^{-1}$ to 0.000933 $cm^2 g^{-1}$. When the ZnO growth is developed in-situ on the rGO, due to controlled size of ZnO nanocrystals, the ZnO@rGO nanocomposite gives improved surface area. In this case surface area of 28 $m^2 g^{-1}$ is obtained. In ZnO/Si@rGO nanocomposite appreciably high surface area is seen as an effect of APTMS capping. The addition of APTMS resulted in the in-situ anchoring of grown ZnO on the rGO sheets. ZnO/Si@rGO nanocomposites have bulk surface area of 78 $m^2 g^{-1}$. It also has the mesopore volume of about 0.101305 $cm^2 g^{-1}$, which is close to that of GO nanosheets.

3.4.4 Adsorption and Photodegradation Studies of Organic Cationic dyes

Adsorption and photoactivity of catalytically modified rGO is validated through the adsorption/degradation of a most preferred MB dye (Wang *et al*., 2012). The comparative performance of the ZnO and ZnO/rGO nanoarchitectures on MB dye adsorption was studied and is shown in Figure 3.18A. Bare ZnO does not show any adsorption. When rGO is present, the ZnO based ZnO/Si@rGO nanocomposite shows ~59% where as ZnO@rGO nanocomposite shows ~42% of adsorption. The adsorption is mainly due to the high surface area and the mesoporous nature of rGO nanostructures. The adsorption is possibly governed by the π-π conjugation between dye molecules and the aromatic regions of the rGO as well as the ionic interactions of the dye molecules with the oxygen containing surface functional groups of the rGO nanosheets (Sharma *et al*., 2013; Xu *et al*., 2012). A high BET surface area of ZnO/Si@rGO nanocomposite is a reason for better adsorption of MB dye compared to ZnO@rGO and ZnO-rGO.

The strong absorption in the UV region confirms the UV light activity of the samples (Figure 3.14). A comparative photocatalytic degradation of MB over ZnO and ZnO/rGO

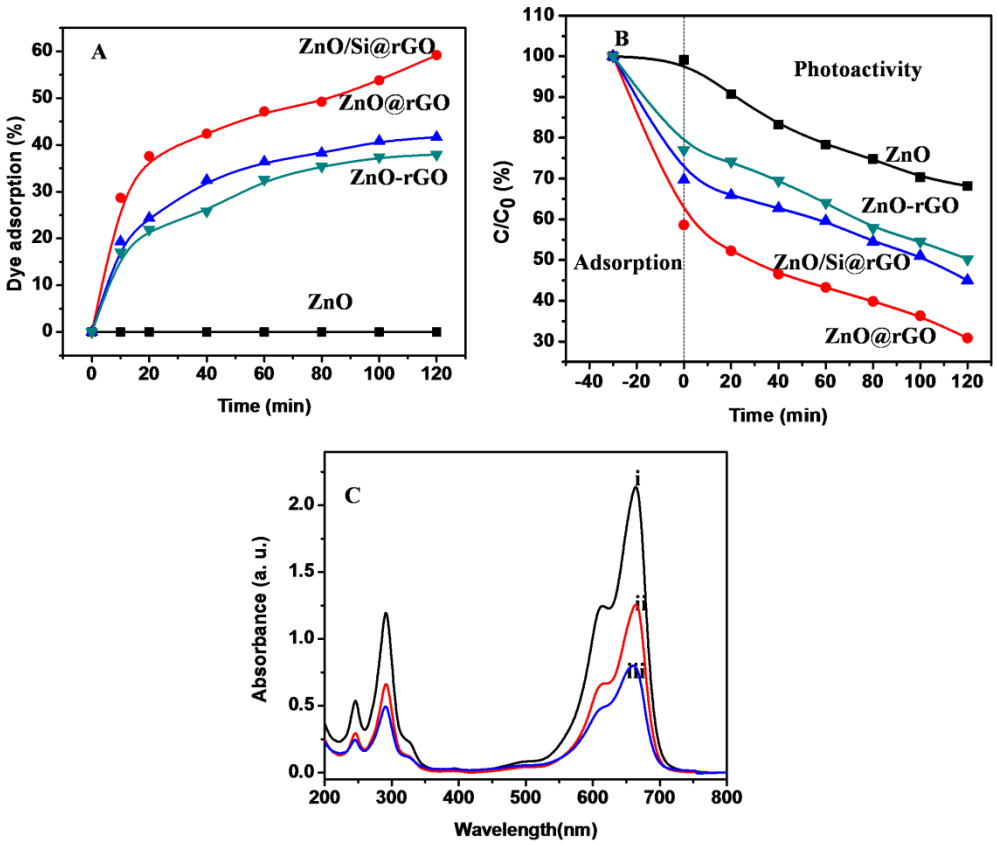

Figure 3.18 (A) Adsorption studies using adsorbents ZnO, ZnO-rGO, ZnO@rGO, and ZnO/Si@rGO (B) photoactivity studies using ZnO, ZnO-rGO, ZnO/Si@rGO and ZnO-rGO (concentration of MB=340 μM and concentration of catalyst=0.4 g L^{-1}). (C) Adsorption and photodegradation study using ZnO@rGO (i) 340 μM MB (ii) after adsorption 120 min (iii) after photocatalytic activity 120 min (adsorbent dosage=0.4 g L^{-1}).

nanoarchitectures under UV light irradiation is presented in the Figure 3.18B. The dye degradation activity in ZnO@rGO photocatalyst is significantly higher compared to that of bare ZnO. About ~69% of MB is degraded by ZnO@rGO within 2 h UV irradiation. This experiment shows the combined effect of ZnO and rGO for the photodegradation of MB than ZnO alone. The mechanism for the enhancement in the photodegradation of ZnO/rGO nanoarchitectures is given in the Figure 3.19 and the main reactions involved in the photodegradation are presented in equations 3.5 to 3.8.

$$ZnO/rGO \xrightarrow{h\nu} ZnO(h^+)/\,rGO(e^-) \quad 3.5$$

$$rGO\ (e^-) + O_2 \rightarrow rGO + O_2^- \quad 3.6$$

$$ZnO\ (h^+) + H_2O/OH^- \rightarrow ZnO + OH^{\cdot} \quad 3.7$$

$$OH^{\cdot}\text{+organic dye} \rightarrow \text{degradation products} \quad 3.8$$

The 2D planar conjugation structure of rGO makes this material a very good acceptor for the photogenerated electron from nano ZnO under UV irradiation. This leads to the rapid transfer of the photogenerated electrons from the conduction band of ZnO to the rGO and helps in the suppression of electron–hole recombination rate. This results in the enhanced photocatalytic activity of the ZnO/rGO nanoarchitectures (Gu. *et al*., 2013). The photogenerated electrons covert dissolved oxygen to reactive oxygen species, which further react with water forms hydroxyl radicals. Then the dye gets degraded by the hydroxyl radicals. On the other hand holes react with water molecules or surface absorbed hydroxyl

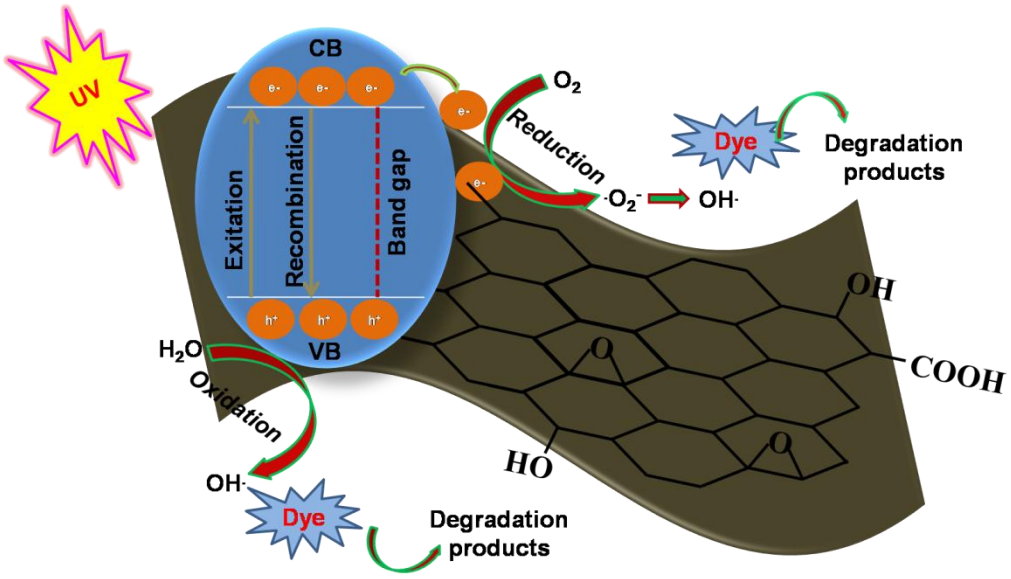

Figure 3.19 Photocatalytic mechanism of MB degradation on the ZnO/rGO nanoarchitectures.

groups to form hydroxyl radicals, which then degrade dye molecules (Shah *et al*., 2012).

The photocatalytic efficiency of ZnO@rGO, ZnO/Si@rGO, ZnO-rGO, and ZnO are ~69%, ~55%, ~49%, and ~31%, respectively. This was explained from the red shift observed in the UV-vis absorption spectra of the ZnO/rGO nanoarchitectures given in the Figure 3.14. The better interfacial interactions of nano ZnO crystallites with rGO possibly increase the photocatalytic activity in ZnO@rGO. The reduced crystallite size of in-situ grown ZnO in ZnO@rGO makes this material more photoactive than ZnO-rGO composite prepared *via* physical blending technique. Even though, ZnO/Si@rGO shows good distribution of nano ZnO over rGO sheets compared to ZnO@rGO, the presence of aminosilane crosslinking agent retards its efficiency. From the experimental data, the k_{app} values were calculated and the k_{app} value of ZnO@rGO is 0.005 min^{-1}, which is higher than that of bare ZnO (0.003 min^{-1}). This high photodegradation rate constant confirms the influence of rGO in the improved photocatalytic activity of ZnO@rGO nanocomposite than bare ZnO.

In order to understand whether photocatalytic degradation is taking place under UV irradiation in presence of ZnO/rGO nanoarchitectures, we conducted adsorption and photocatalytic degradation experiments separately by keeping the catalyst and dye solution for a time of 120 min. As shown in the Figure 3.18C, we could see a significant reduction in the peak intensity after 120 min of adsorption experiment, which corresponds to ~58.12% of dye removal *via* surface adsorption mechanism. In the same time, ~62.8% of dye removal was obtained after 120 min of photocatalytic experiment. It clearly indicates the influence of UV light activity of ZnO@rGO.

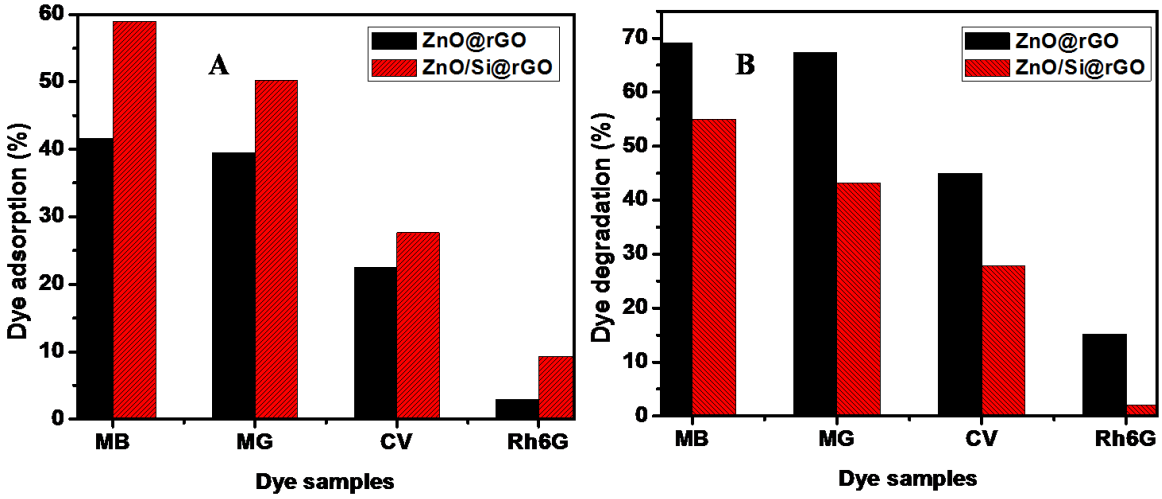

Figure 3.20 (A) % of dye adsorption and (B) % of dye degradation studies of MB, MG, CV, and Rh6G using ZnO@rGO and ZnO/Si@rGO.

Figure 3.20A and 3.20B gives the adsorption and degradation performance of ZnO/Si@rGO and ZnO@rGO on a series of cationic organic dyes (MB, MG, CV, and Rh6G). ZnO/Si@rGO nanocomposites show comparatively high adsorption (~59% of MB, ~50% of MG, ~28% of CV, and ~9% of Rh6G). Unfortunately, they are poor in photoactivity because the APTMS inhibits the UV interaction. In case of ZnO@rGO, the photocatalytic activity is better (~69% of MB, ~67% of MG, ~46% of CV, and ~16% of Rh6G). In both ZnO@rGO and ZnO/Si@rGO, the adsorption and degradation are showing dependence with the molecular weight of the selected cationic dyes. From the Figure 3.20A and 3.20B, we can understand that as the dye molecular weight increases, the adsorption and photodegradation decreases. We can see a drastic reduction in the adsorption of the dye with high molecular weight (Rh6G), which subsequently reduces the photodegradation behavior as well.

The as-prepared materials can be used for the adsorption and photocatalytic degradation of real effluent samples. Since real effluent may contain various dye samples with

different molecular weights, chemicals, water soluble contaminants, the adsorption and photodegradation efficiency is expected to be slightly low compared to the pure dye solutions.

3.5 Conclusions

A catalytic-adsorbent material architecture is designed with ZnO@rGO and ZnO/Si@rGO nanocomposite *via* a facile, one-pot microwave technique. Beneficial properties of ZnO nanocrystals as well as rGO nanosheets for the combined adsorption and photodegradation were studied using different organic cationic dyes. It was found that rGO acts as dual-functional material. It acts as a good support, which helps in the distribution of ZnO nanoparticles. Most of the ZnO particles get exposed to the UV radiation in the nanocomposites and which further interacts with the organic dye. Moreover, the rGO favors in promoting adsorption of cationic dyes in nano ZnO which otherwise fails miserably. Compared to phase pure nano ZnO, the ZnO@rGO nanocomposite shows better photocatalytic activity (69%) and 42% of adsorption. ZnO/Si@rGO nanocomposite exhibits a surface area of 78 $m^2 g^{-1}$ and was found to retain ~59% adsorption and ~55% photoactivity from aqueous system containing 340 μM methylene blue (MB) dye. The combined adsorption and photocatalytic degradation property of both ZnO@rGO and ZnO/Si@rGO against the adsorption and photodegradation of a series of cationic organic dyes were compared.

CHAPTER 4

Processing of 2D Graphene Oxide Layers Catalyzed with ZnO Nanostructures for Water Disinfection

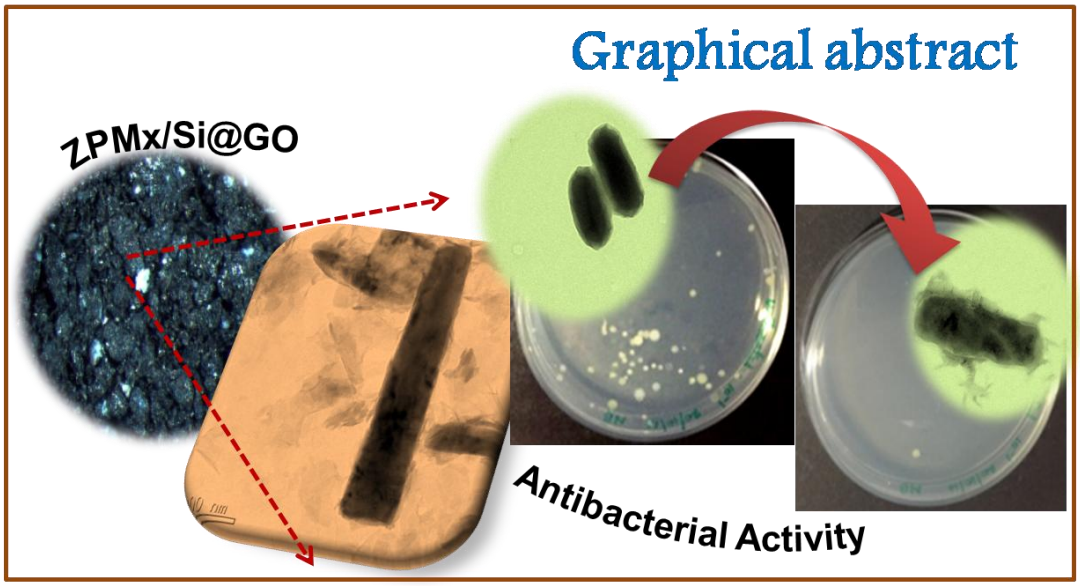

4.1 Abstract

This study investigated the role of poly ethylene glycol (PEG) in the microwave synthesis of ZnO (ZPMx) nanorods. The molecular weight of PEG was found to strongly influence the aspect ratio of the synthesized material. The as-prepared ZPMx nanorods were post-grafted onto the surface of GO sheets using 3-amino propyl trimethoxy silane (APTMS) as a cross-linking agent to obtain ZPMx/Si@GO nanocomposites. Microscopic observations showed that ZPMx nanorods with different aspect ratios were evenly distributed on the surface of the GO sheets. It also showed enhanced thermal and chemical properties. The dependence of the antibacterial behavior on the aspect ratio of the ZPMx nanorods and GO was also investigated. An antibacterial assay was carried out using both the Gram-positive bacteria *Staphylococcus aureus (S. aureus*) and Gram-negative bacteria *Escherichia coli (E. coli),* and *Klebsiella pneumonia (K. pneumonia*). The results showed that the ZPMx/Si@GO nanocomposite had an excellent antibacterial property toward the test bacteria compared to pure ZPMx and GO. The synergistic effect of ZPMx and GO resulted in a superior antibacterial activity in ZPMx/Si@GO. Interestingly, the nanocomposite with a higher ZPMx aspect ratio (ZPM6000/Si@GO) showed excellent inhibition zones with diameters of ~3.7, 3.1, and 2.4 cm corresponding to *S. aureus*, *E. coli*, and *K. pneumonia*, respectively. An optical density measurement, as well as the morphological changes in the bacteria, again confirmed the excellent bacterial growth inhibition of ZPM6000/Si@GO. The studies indicated that the ZPMx/Si@GO nanocomposite is a promising candidate for use in real waste-water disinfection.

4.2 Introduction

The presence of microbial pathogens in water adversely affects the quality of water, which can cause long-term health problems in humans. To solve this problem, a large number of inorganic materials such as silver nanoparticles, CuO, TiO_2, ZnO (Chowdhuri *et al*., 2015),

GO, and CNTs (Bykkam *et al*., 2015) have already been investigated with respect to their potential antimicrobial activity and the details are presented in the Chapter 1. Many reports discuss the superior antibacterial property of ZnO and its nanocomposites. The literature shows that a ZnO/TiO_2 composite has excellent antimicrobial activity against Gram-negative and Gram-positive bacteria compared to pure ZnO nanoparticles (Hwang *et al*., 2011). Agnihotri *et al.* found that silver-decorated ZnO nanorods had a superior antibacterial activity compared to pure ZnO nanorods, as well as colloidal Ag nanoparticles (Agnihotri *et al*., 2015). All these reports clearly demonstrated the enhanced antibacterial activity of ZnO-based composites.

The enhanced photocatalytic performance of graphene-metal oxide nanocomposites has also been thoroughly reported (Zhang *et al*., 2012; Zhang *et al*., 2015). Moreover, graphene-based materials with tailored morphologies such as 0D graphene quantum dots, 1D graphene nanoribbons, and 3D graphene frame-works have been developed to enhance the photocatalytic efficiency (Han *et al*., 2016). Graphene has also been found to be an ideal candidate for preparing nanocomposites for energy storage and its conversion *via* a photocatalysis process (Han *et al*., 2014). 1D metal oxide-graphene composites have been widely studied and reported in the literature. Chen *et al.* demonstrated the solvothermal synthesis of ZnO nanorods, but the process required more than five days (@60 ^{o}C) (Chen *et al*., 2013). It was then mixed with GO, and the mixture was hydrothermally reduced to obtain ZnO-rGO composites. Moreover, Liu *et al.* prepared CdS nanowire-rGO composites *via* electrostatic self-assembly, followed by a hydrothermal reduction process (Liu *et al*., 2013). These reports only exemplify the synthesis of 1D metal oxide-rGO composites. The synthesis of 1D metal oxide-GO composites has not been extensively studied and reported.

The antibacterial property of graphene-based materials has also been well established and the literature review is presented in Chapter 1. Liu *et al.* reported a higher antibacterial activity in GO compared with GR and rGO (Liu *et al*., 2011). Wang *et al*. reported that along with other factors, the synergistic effects of GO and ZnO contribute a superior antibacterial activity to ZnO-GO composites (Wang *et al*., 2014). In another report, Chowdhuri *et al.* developed ZnO nanoparticles on the surface of chitosan-modified GO, and these showed more antibacterial potency toward both Gram-positive and Gram-negative bacteria (Chowdhuri *et al*., 2015). More literatures related antibacterial activity of ZnO incorporated graphene based nanostructures is presented in Chapter 1.

In the present work, ZPMx nanorods with various aspect ratios were prepared using a surfactant PEG with different molecular weights. Because a microwave-assisted method is a very simple and an easy route for this synthesis, it was followed here for the preparation of ZnO nanorods. The as-prepared ZPMx nanorods with different aspect ratios were used for the preparation of nanocomposites, and a post-grafting technique was adopted for the synthesis. APTMS with two different functional groups at the ends was used as a cross-linking agent for the homogeneous attachment of ZPMx nanorods on the surface of the GO. Structural and morphological studies of the as-prepared materials were carried out using a series of characterization techniques. The roles of both the ZPMx nanorod aspect ratio and GO on the disinfection of water were further investigated. We used one Gram-positive bacteria (*S. aureus*) and two Gram-negative bacteria (*E. coli* and *K. pheumonia*) for the entire study. Based on the experimental results, it was clear that, ZPMx nanorods with a higher aspect ratio showed an enhanced antibacterial activity compared to samples with lower aspect ratios. The synergistic effect of the ZPMx and GO in the ZPMx/Si@GO led to a remarkable enhancement in the antibacterial property compared to pure ZPMx and GO.

4.3 Experimental Section

4.3.1 Materials

Graphite and 3-Amino propyl trimethoxy silane (APTMS) were procured from Sigma Aldrich, Germany (99.9%). Sodium nitrate ($NaNO_3$, 99.5%), Potassium permanganate ($KMnO_4$, 99%), and Hydrogen peroxide (H_2O_2, 99%) were obtained from S. D. Fine Chemicals Limited, India. Zinc nitrate hexahydrate ($Zn(NO_3)_2.6H_2O$, 99%) and conc. Sulphuric acid (H_2SO_4 , 99%) were supplied by Merck, India. Lithium hydroxide (LiOH, 99%) was purchased from SRL, India. Poly ethylene glycol with different molecular weights (PEG 200 and PEG 6000) obtained from Merck, India. All the reagents were used as received without any further purification.

4.3.2 Synthesis of GO

GO nanosheets were synthesized *via* the modified Hummer's method (Krishna *et al.*, 2012) using the detailed procedure provided in the Chapter 3. The obtained GO was then freeze dried to get fluffy mass of nanosheets. The steps involved in the preparation of GO is given in the Figure 4.1.

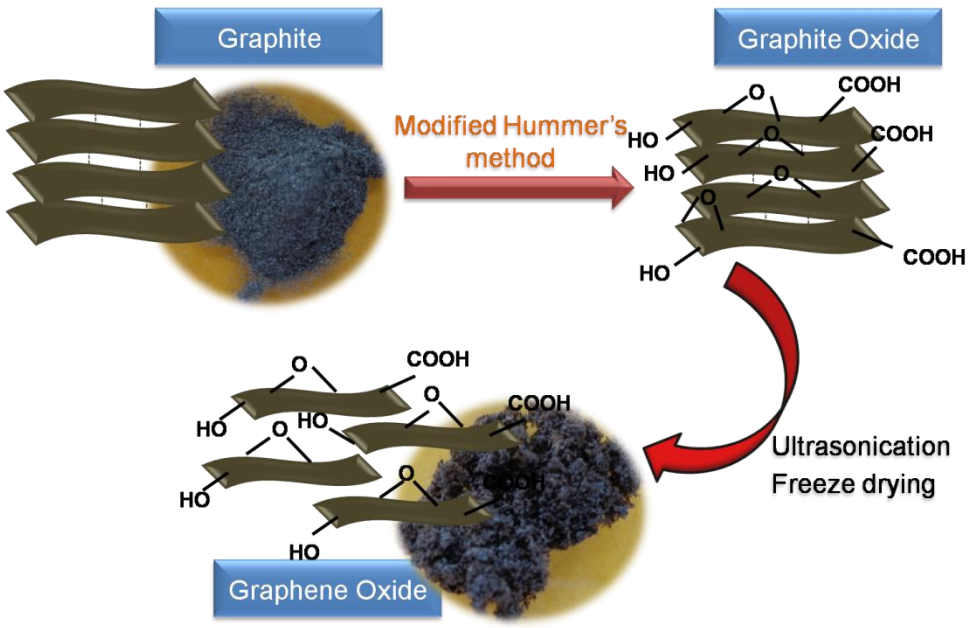

Figure 4.1 Schematic illustration for the synthesis of GO.

4.3.3 PEG Mediated Synthesis of ZPMx (ZPM200, ZPM6000)

ZPMx nanoparticles were prepared *via* microwave-assisted technique. In a typical procedure, 0.3 M $Zn(NO_3)_2.9H_2O$ was dissolved in 500 mL of double distilled water and an appropriate amount of PEG 200/PEG 6000 was eventually dispersed by maintaining a $Zn(NO_3)_2.9H_2O$ and PEG wt ratio of 2 : 1. The pH of the solution was adjusted using a 10 wt% LiOH solution. Then, the prepared solution was kept in a microwave synthesis work station (Sineo MAS II) at 80 ^oC for 30 min (P= 300 W). The powder thus obtained was washed with double distilled water to remove the impurities. The final product was dried in the oven at 50 ^oC. The obtained samples were denoted as ZPM200 and ZPM6000. Bare ZPMx without adding PEG was also prepared for comparison (denoted as ZPM0).

4.3.4 Synthesis of APTMS Modified ZPMx (ZPMx/Si)

The post-grafting of APTMS on ZPMx nanorods was conducted using the following procedure. The as-prepared ZPMx was dispersed in ethanol : water mixture (3 : 1) and APTMS was added drop wise while stirring (APTMS/ZPMx was ~0.15). It was stirred for 4 h, and the temperature was maintained at 60 ^oC. The APTMS-modified ZPMx (ZPMx/Si) was then washed with double distilled water and finally dried in the oven.

4.3.5 Synthesis of ZPMx/Si@GO Nanocomposite

The APTMS modified ZPMx was dispersed in GO solution by maintaining the ZPMx : GO wt ratio at 1 : 1. The obtained ZPMx/Si@GO nanocomposite was then freeze dried. The schematic illustration for the preparation of ZnO and ZPMx/Si@GO is presented in the Figure 4.2.

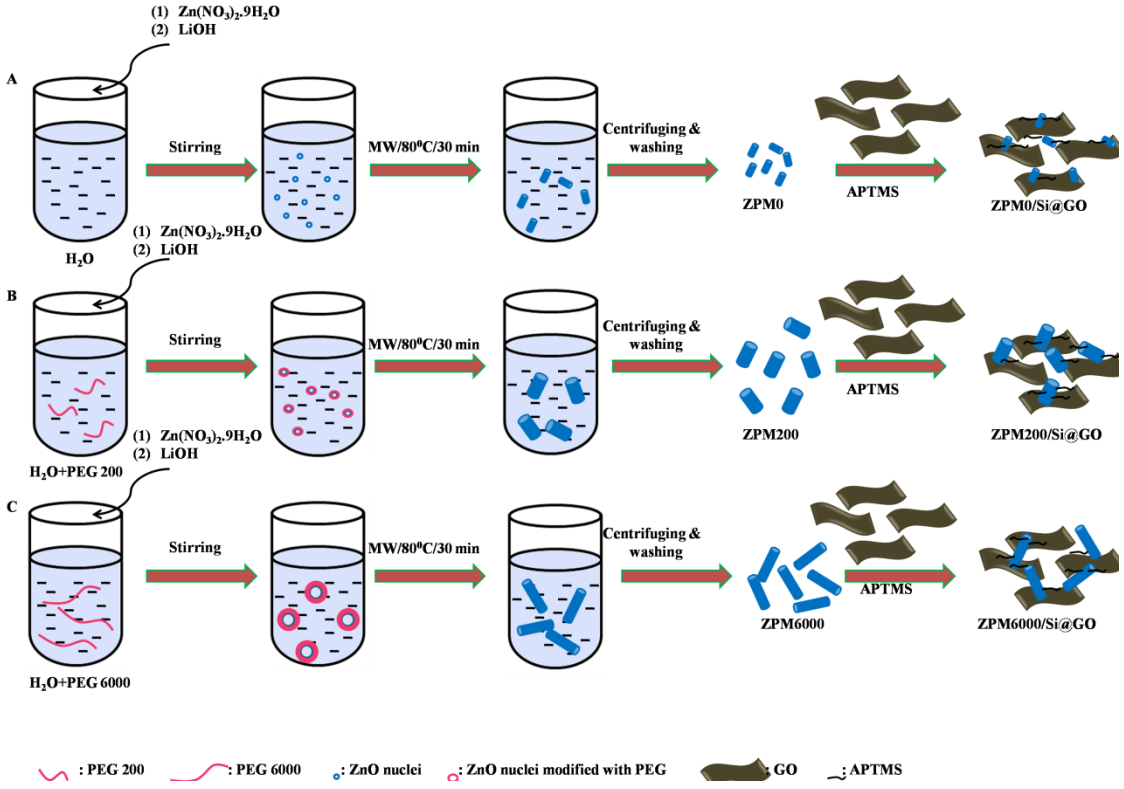

Figure 4.2 Schematic diagram for the formation of ZnO with different aspect ratio and corresponding ZPMx/Si@GO nanocomposite.

4.3.6 Antibacterial Studies

The antibacterial properties of the ZPMx, GO, and ZPMx/Si@GO nanocomposite were investigated using both Gram-negative and Gram-positive bacteria. In our investigation, we selected Gram-positive *S. aureus* and Gram-negative *E. coli* and *K. pneumonia* as model bacteria to evaluate the antibacterial activities of the materials ZPMx, GO, and ZPMx/Si@GO. The antibacterial activities of the samples were evaluated using a modified disk diffusion method, and the procedure is given here. Agar disc diffusion method for antibacterial tests was carried out using Muller Hinton Agar (MHA). The inoculum was prepared using 24 h plate cultures of the test bacteria (*S. aureus, E. coli* and *K. pneumonia*). The colonies were suspended in 0.85% saline, and the turbidity was compared with the 0.5 McFarland standards, to produce a suspension of 1×10^6 CFU mL^{-1}. The suspension was loaded on a sterile cotton swab that was rotated several times and

pressed firmly against the inside wall of the tube to remove excess inoculum from the swab. The dried surface of a MHA plate was inoculated by streaking the swab over the entire sterile agar surface. Discs containing 5×10^{-3} mg μL^{-1} of GO, ZPMx, and ZPMx/Si@GO were placed on top of the inoculated plates and incubated at 30 ^{o}C for 24 h. The bacterial activity was evaluated by measuring the zone of growth inhibition surrounding the discs. The zone of inhibition is the region where no bacterial growth was found around the disc, which was induced by the interaction of the material present in the disc and the bacteria (Suyana *et al*., 2014). A larger diameter for the zone of inhibition indicated a greater antimicrobial activity.

4.3.6.1 Morphological Analysis of Bacteria Before and After Treatment with ZPMx/Si@GO

Both SEM and TEM analyzes were conducted to visualize the morphological changes in the bacteria (*S. aureus*, *E. coli*, and *K. pneumonia*) during the treatment of ZPMx/Si@GO. For this experiment, the test bacteria were cultured in a Luria-Bertani (LB) medium containing 10 $\mu g\ mL^{-1}$ of ZPMx/Si@GO for 12 h. This was followed by centrifugation for 10 min (5000 rpm). The settled bacteria were collected after the decantation of the top solution. Subsequently, they were washed with 100 μL of a phosphate buffered saline (PBS) solution. After centrifugation, the supernatant solution was decanted, and the bacteria were fixed in a 0.25% glutaraldehyde solution (100 μL) at 4 ^{o}C for 12 h. Then, they were centrifuged, and resuspended in 100 μL of PBS solution; and finally kept in the refrigerator.

4.3.6.2 Bacterial Growth Kinetics

To examine the effect of as-prepared materials on the bacterial regrowth, the test bacteria were treated with 10 μg mL^{-1} of GO, ZPMx and ZPMx/Si@GO separately. The entire solution was subjected to continuous shaking at 150 rpm, and the temperature was maintained at 37 ^{o}C for 48 h in a nutrient broth. 100 μL samples were withdrawn at specific time intervals (0, 1, 2, 4, 8, 12, 24, and 48 h) and stored at 4 ^{o}C. All these experiments were performed in triplicate and the average values are reported. The control assay was performed without adding any materials.

4.3.6.3 Application Study of ZPMx/Si@GO for Real Pond Water Treatment

Real pond water was taken for a bacterial growth inhibition study using ZPMx/Si@GO. Initially, 0.1 g of ZPM6000/Si@GO was dispersed in 80 mL of pond water under continuous magnetic stirring at ambient conditions. Samples were collected in vials after 2, 8, 12, 24, and 48 h. Each sample was further centrifuged to separate the dispersed catalytic material, and the supernatant solution was collected. The sample solutions were further incubated in an orbital shaker at 160 rpm and 35 ± 2 ^{o}C. The shaking incubation minimized the clumping and bottom settlement of the material during the incubation of the bacteria. The inhibition of bacterial growth was determined by measuring the absorbance at 600 nm using a spectrophotometer. The experiment was repeated in triplicate, and the average value was noted. The initial concentration of bacteria in the pond water was 2×10^5 CFU mL^{-1}. The percentage of bacterial inhibition was calculated using the following formula, % of bacterial inhibition = (C-T)/C × 100, where C is the OD value of the control and T is the OD value of the treated pond water.

4.3.6.3.1. Enumeration of Microorganisms in Treated and Untreated Water Samples

Initially, the treated and untreated water samples were serially diluted in autoclaved distilled water according to a conventional serial dilution technique. Later, 100 µL of each dilution (10^{-1} to 10^{-5}) was surface plated onto two different media: nutrient broth (NB) agar and LB agar. These two media were selected because they are the common culture media used for the isolation of microorganisms from different sources like soil, water, and air. Inoculated Petri plates were incubated at 30 ^{o}C, for 24 h to determine the microbial growth in the treated and untreated samples.

4.4 Results and Discussion

4.4.1 Characterization of GO Prepared *via* Modified Hummers Method

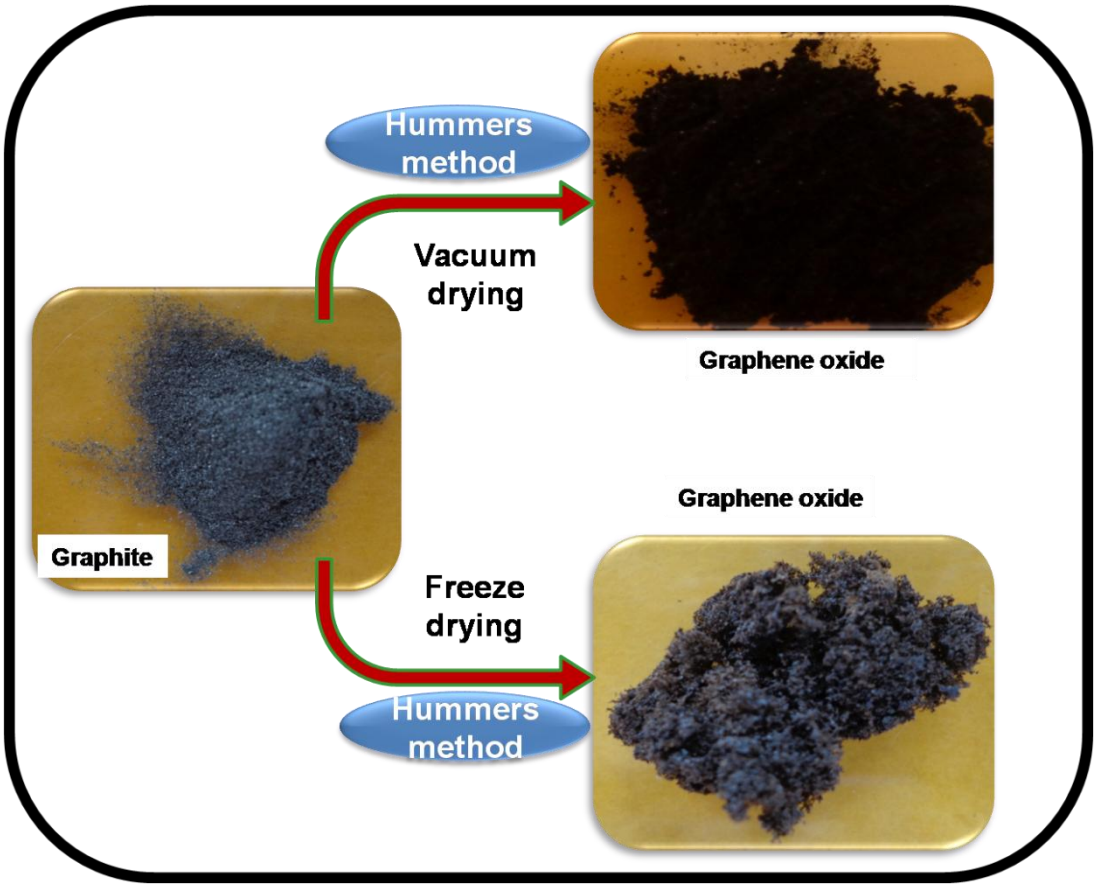

Figure 4.3 Photographs of GR powder and the GO prepared *via* vacuum drying and freeze drying techniques.

The photographic images of vacuum dried and freeze dried GO are shown in the Figure 4.3. Freeze drying is also known as lyophilisation or cryodesiccation. Freeze drying technique helps in the complete removal of water without making any damage to the structure of graphene oxide. Fluffy nature of the GO sheets is maintained after freeze drying. This is due to the reason that during freeze drying initially the material get frozen and subsequently the reduction of the surrounding pressure allows the frozen water in the material to sublimate directly from the solid phase to the gas phase. But the vacuum drying results in the aggregation of GO sheets. The effect of vacuum drying and freeze drying on the formation of GO is presented in the Figure 4.4.

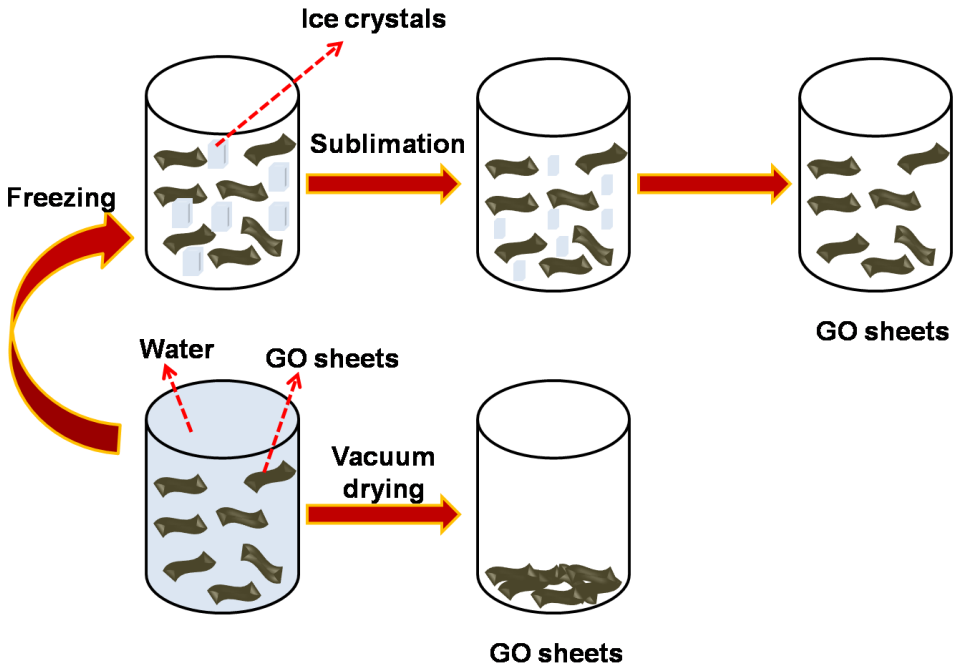

Figure 4.4 Effect of vacuum drying and freeze drying on the formation of GO sheets.

From the BET surface area analysis, it could be seen that the mode of drying technique has a major role in the preparation of GO. The N_2 adsorption-desorption isotherms for vacuum dried and freeze dried GO are shown in the Figure 4.5. As shown in the figure, vacuum dried GO has a BET surface area of 77 $m^2 g^{-1}$; it got enhanced to 162 $m^2 g^{-1}$ for freeze dried sample. More than two times enhancement in the surface area was

observed for freeze dried sample. This is because of the fact that the pore features of the prepared GO are retained during freeze drying, but they got collapsed upon vacuum drying. Hence, in the present investigation, we followed freeze drying technique to dry all the samples.

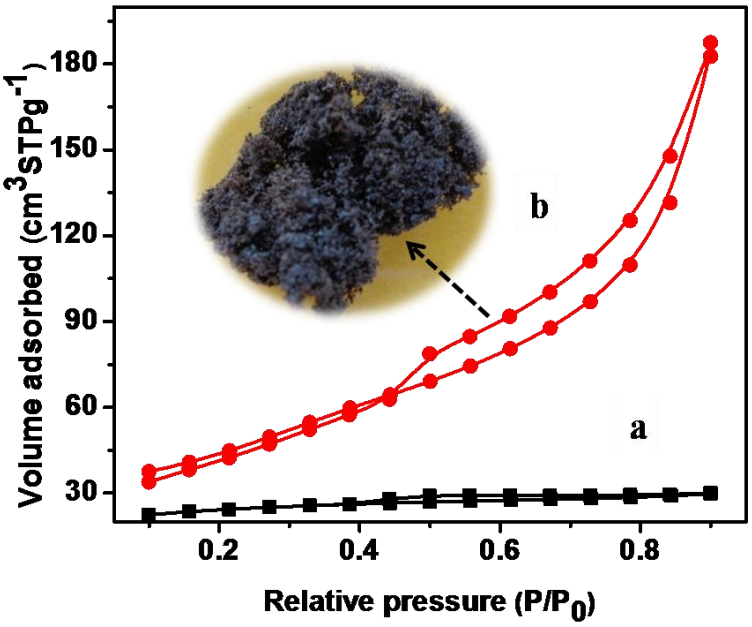

Figure 4.5 N_2 adsorption-desorption isotherms of GO prepared *via* (a) vacuum drying and (b) freeze drying techniques. The photographic image of freeze dried GO is shown in the inset.

The morphology and the microstructures of the as prepared GO examined with optical and SEM analyzes and was presented in the Figure 4.6. The fluffy nature of the obtained GO is confirmed from the low and high magnification optical images (Figure 4.6A and 4.6B). The exfoliated graphitic layers were evident from the micro-structural analysis, and the curled layers of GO are also distinctly seen in the images (Figure 4.6C and D). The same observation was reported by Liu *et al.* in the literature (Liu *et al*., 2015). As shown in the low and high magnification SEM images and as reported in the literature, GO is curled layers of graphitic sheets. Thin layered graphitic sheets of GO were again confirmed from the TEM images (Figure 4.7).

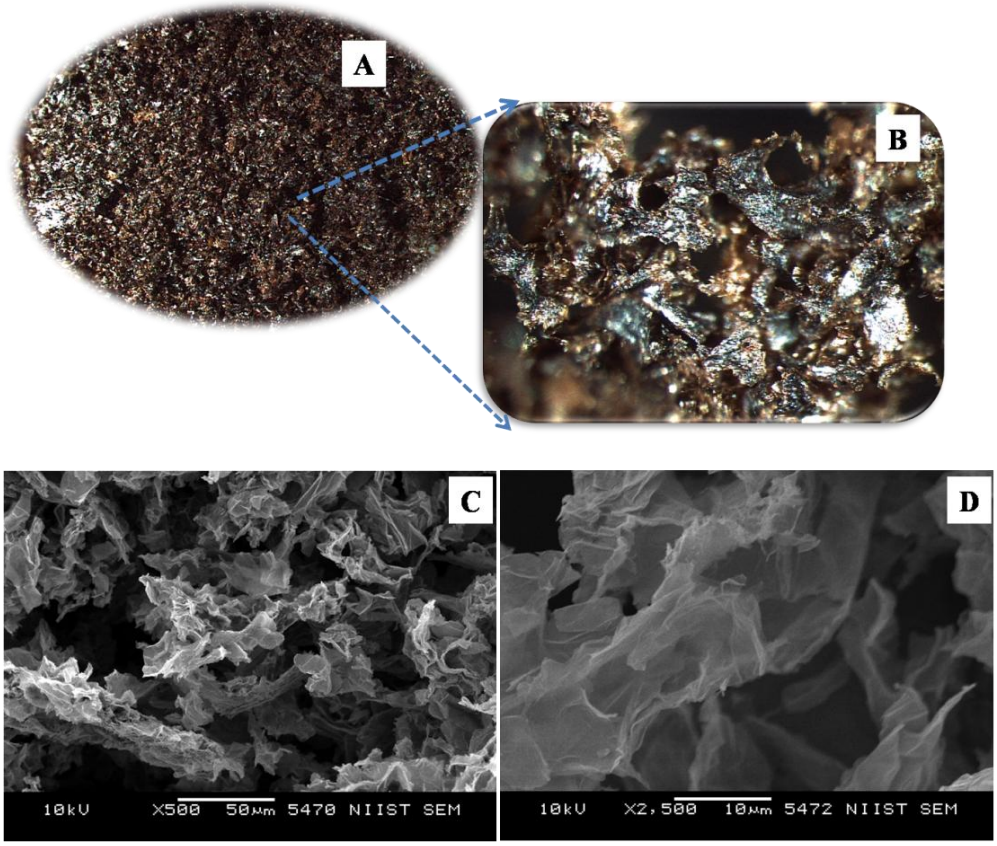

Figure 4.6 (A and B) Low and high magnification optical images and (C and D) low and high SEM images of freeze dried GO sheets.

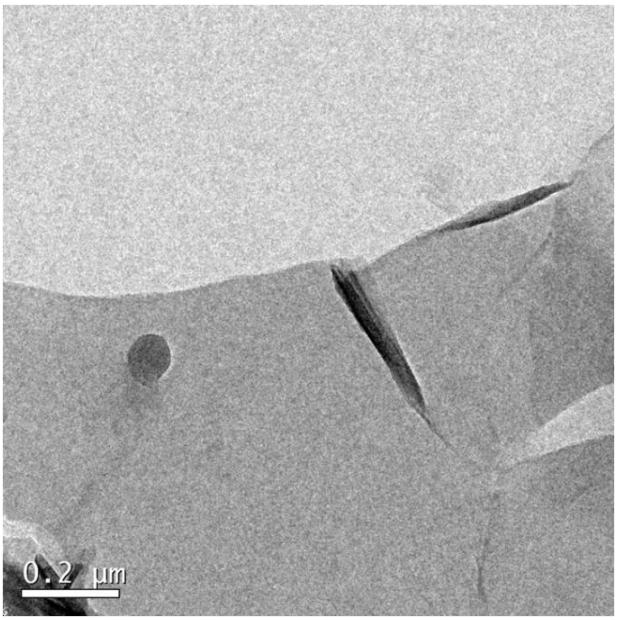

Figure 4.7 TEM image of freeze dried GO sheets.

4.4.2 Characterization of ZPMx prepared *via* microwave-assisted method

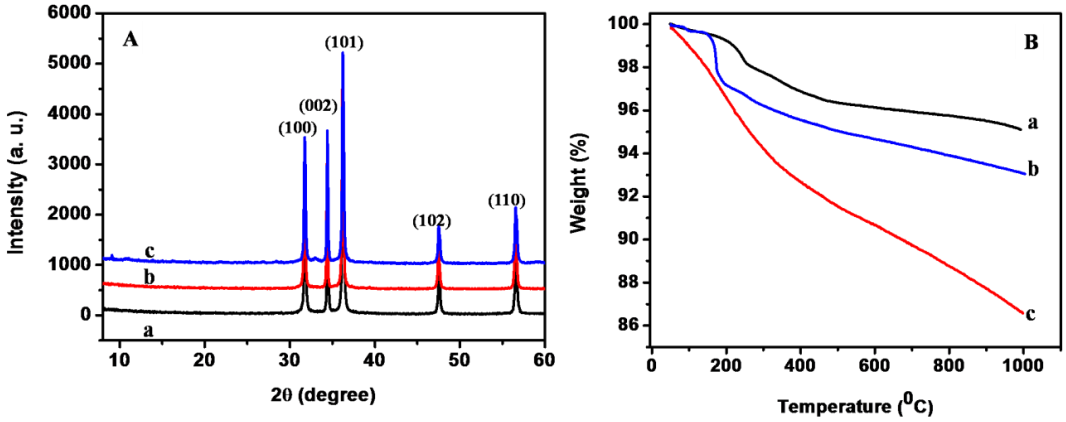

Figure 4.8 (A) XRD pattern and (B) TGA of (a) ZPM0 (b) ZPM 200 (c) ZPM 6000.

The as-prepared ZPMx was analyzed using different characterization tools. The XRD results for the ZPMx prepared with (PEG with different molecular weights) and without PEG are presented in Figure 4.8A. XRD was recorded to confirm the formation of ZPMx and also used to determine the crystallographic phases, mainly in terms of crystal size and lattice parameter. The XRD results for ZPMx (prepared without PEG, with PEG 200 and with PEG 6000) shown in a, b and c give all the characteristic peaks of ZnO at 32^{o}, 34^{o}, 36^{o}, 47^{o}, and 56^{o} corresponding to the (100), (002), (101), (102), and (110) planes, which agree with the XRD peaks for ZnO in JCPDS file no.79-0205 and reveal the hexagonal wurtzite structure. The absence of other peaks for impurities like $Zn(OH)_2$, indicates the formation of a pure ZnO phase in all of the prepared samples. The high crystallinity of the as-prepared samples was also confirmed from the intense diffraction peaks.

The TGA results for the ZPMx prepared with and without PEG with different molecular weights are shown in Figure 4.8B. In all of the samples, the weight loss at 100-150^{o}C is mainly due to the elimination of surface-adsorbed water molecules. The weight loss at 200-480 ^{o}C is associated with the elimination of nitrates from the system. Based on the TGA results for ZPM200, the weight loss at 150-200 ^{o}C is associated with the removal

of PEG molecules. In Figure 4.8B, a drastic increase in the weight loss is observed when the molecular weight of PEG increases from 200 to 6000 g mol^{-1}. For the ZPMx prepared with and without PEG, ZPM6000 shows the maximum weight loss, and the weight loss at 120-320 ^{o}C is mainly due to the removal of the high molecular weight carbon chain from the PEG6000 matrix.

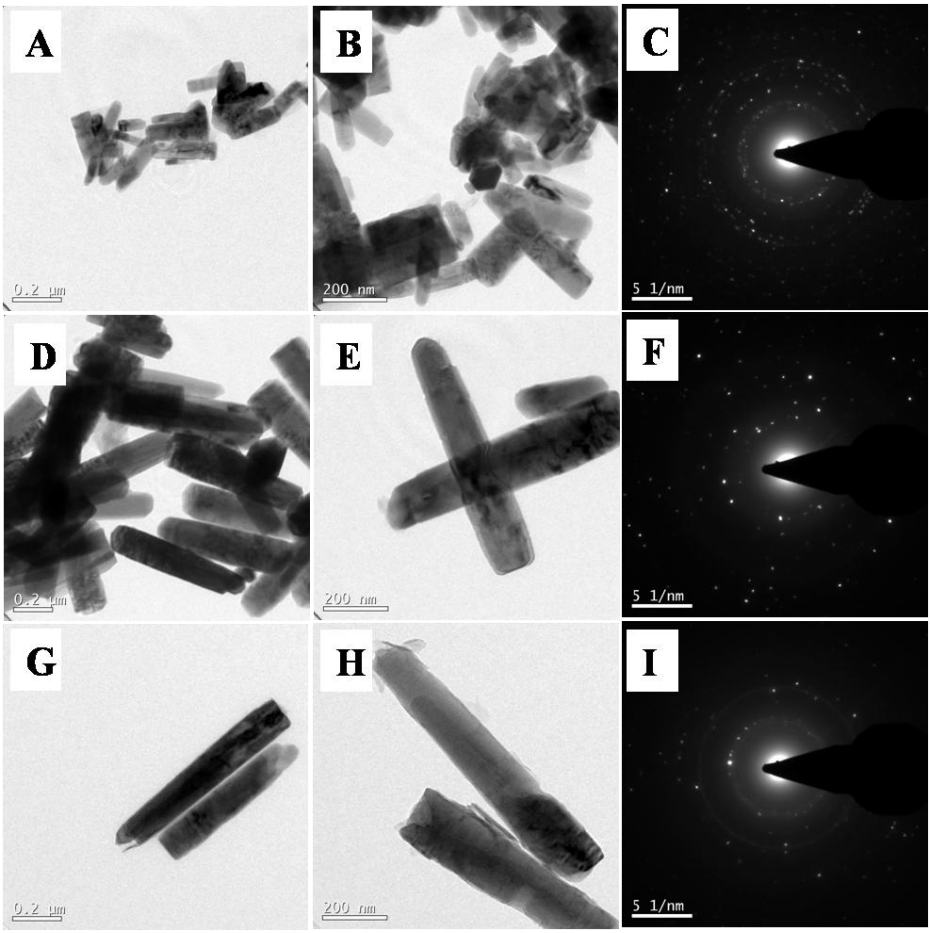

Figure 4.9 Low and high magnification TEM images of (A and B) ZPM0, (D and E) ZPM200 and (G and H) ZPM 6000. (C, F, and I) SAED patterns of ZPM0, ZPM200, and ZPM 6000.

TEM images and SAED patterns of ZPMx prepared using PEG with different molecular weights are shown in Figure 4.9. Direct evidence of the formation of ZPMx nanorods was obtained from the TEM analysis. It was observed that small ZPMx nanorods with a length of 197.808 nm and a width of 79.95 nm were formed in the absence of PEG.

However, the presence of PEG in the reaction mixture resulted in ZPMx nanorods with a length of 800 nm and a width of 150-200 nm. The TEM images reveal that the length of the ZPMx nanorods increases with an increase in the molecular weight of the PEG in the reaction mixture. This means that the molecular weight of PEG or the length of the polymer chain acts as a template for the formation of ZPMx nanorods with different aspect ratios (length-to-width ratios).

4.4.3 Characterization of ZPMx/Si@GO Nanocomposite

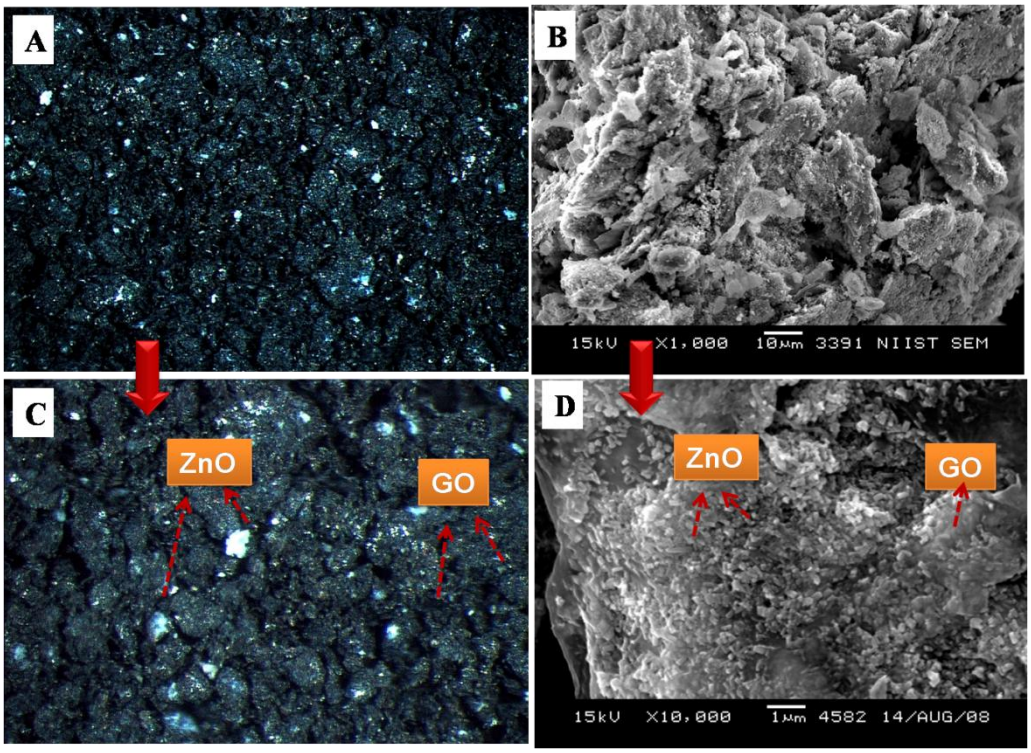

Figure 4.10 Low and high magnification (A and C) optical and (B and D) SEM images of ZPMx/Si@GO.

The optical images ZPMx/Si@GO were presented in the Figure 4.10A and 4.10C. From the figure, it is clearly seen that the nanocomposite shows the presence of both two dimensional GO and ZnO. From the figure we can also say that ZnO particles are evenly

distributed on the surface of GO sheets in the ZPMx/Si@GO nanocomposite. Typical SEM images of the ZPMx/Si@GO are shown in Figure 4.10B and 4.10D. As seen in the SEM images, the as-prepared composite material is composed of a large quantity of uniform nanorods of ZPMx.

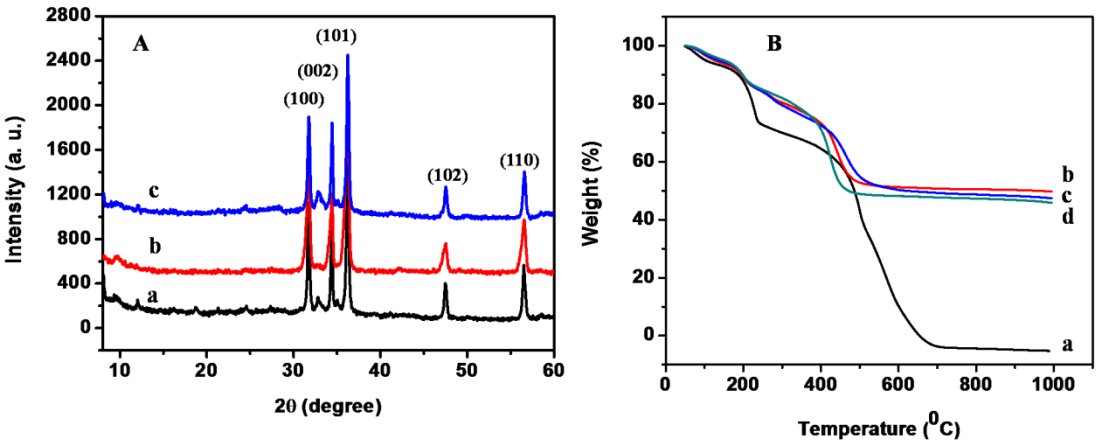

Figure 4.11 (A) XRD patterns of (a) ZPM0/Si@GO, (b) ZPM200/Si@GO, and (c) ZPM 6000/Si@GO, and (B) TGA of (a) GO (b) ZPM0/Si@GO (c) ZPM200/Si@GO, and (d) ZPM6000/Si@GO.

In most of the literature, it is reported that ZnO was being prepared *via* one of the following techniques such as precipitation, hydrothermal or electrochemical deposition and later it is mixed with GO followed by reduction to obtain ZnO-graphene composites (Wang *et al*., 2012). However, the main focus of the present study was the preparation of a ZnO-GO composite rather than ZnO-graphene/ZnO-rGO composites. Thus, the direct mixing of the ZPMx/Si and GO sheets was adopted for the preparation of ZPMx/Si@GO nanocomposites. A hydrothermal/UV-assisted photoreaction was avoided, which would have reduced the GO to graphene/rGO.

The XRD patterns of the ZPMx/Si@GO demonstrated in Figure 4.11A show an additional peak for GO at 9.8^{o} corresponding to the (002) plane of GO, without affecting

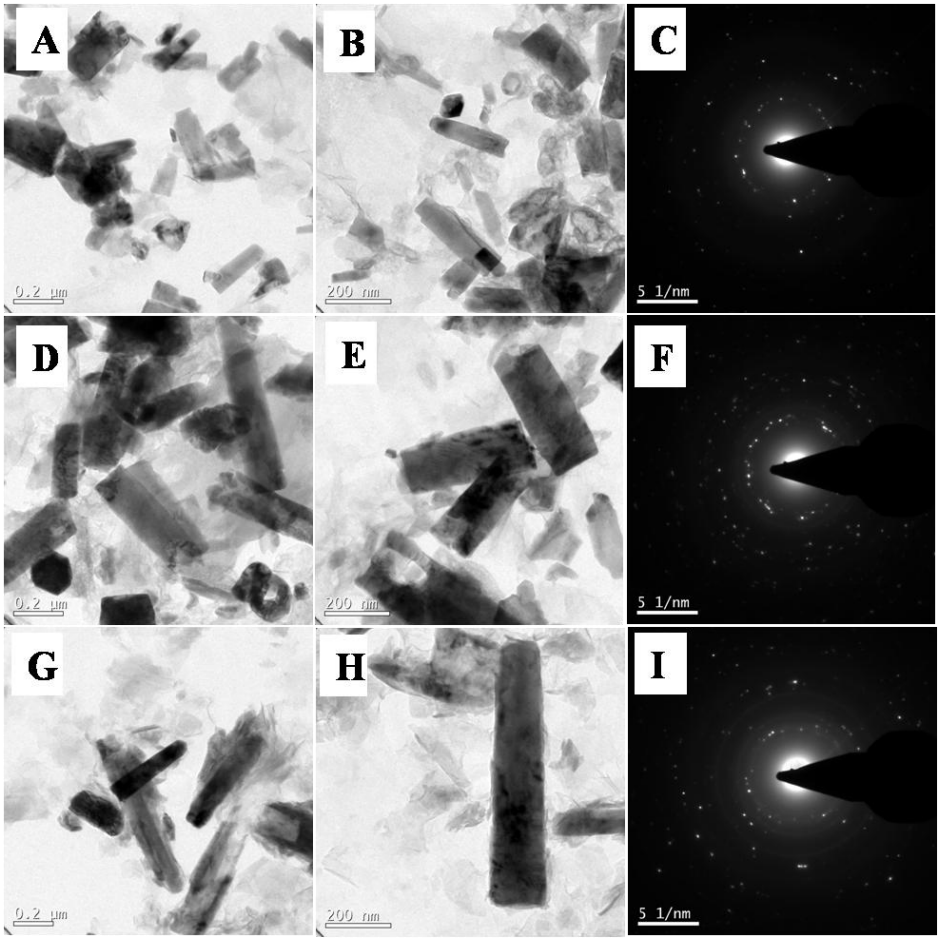

Figure 4.12 Low and high magnification TEM images of (A and B) ZPM0/Si@GO (D and E) ZPM200/Si@GO (G and H) ZPM6000/Si@GO.

the ZnO peaks. These XRD results confirm the presence of pure GO in the nanocomposite rather than graphene/rGO. Figure 4.11B displays the TGA results for GO and ZPMx/Si@GO nanocomposites. As shown in Figure 4.11B (a), the GO underwent a three-step decomposition and the details are explained in the Chapter III (Song *et al*., 2014). The significant weight loss observed for ZPMx/Si@GO indicated the presence of GO in this material. The weight loss at 100 ^{o}C was due to the removal of water molecules. A 22.9 % weight loss was observed at 100-400 ^{o}C due to the loss of nitrates and surface functional groups of the GO. The weight loss of 21.76 % in the temperature range of 400-500 ^{o}C is due to the removal of graphitic carbon in GO. Based on the results of the TG analysis, we

could see that the percentage of weight loss was decreased by the presence of GO in the nanocomposite.

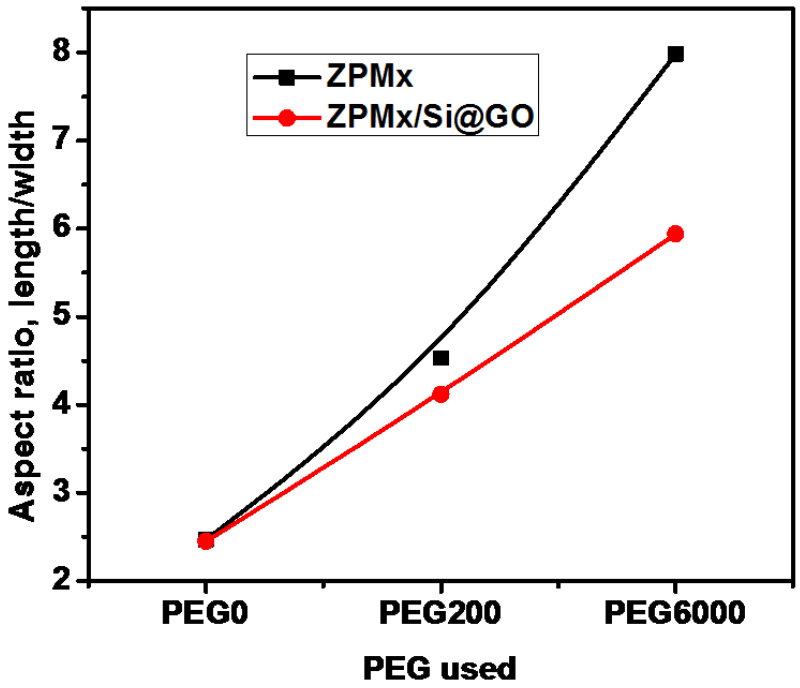

Figure 4.13 Aspect ratio of ZnO rods in bare ZnO and ZPMx/Si@GO nanocomposites prepared using PEG with different molecular weight.

In a similar way, the presence of ZPMx nanorods on the GO was also confirmed by the TEM analysis of ZPMx/Si@GO (Figure 4.12). The grafting of APTMS onto the ZPMx nanorods and the subsequent attachment of GO reduced the length of the nanorods. This was very evident from the microscopic analysis. A subsequent increase in the length of the nanorods was observed with an increase in the molecular weight of PEG in the ZPMx/Si@GO. The length and width of the ZPMx and ZPMx/Si@GO prepared with different molecular weights are tabulated in Table 4.1. All of these results support the data obtained from the XRD analysis. The SAED patterns of the ZPMx and ZPMx/Si@GO are shown in the insets of the corresponding TEM images. The poly-crystalline nature of the ZPMx and ZPMx/Si@GO were confirmed from the SAED patterns. The aspect ratios of

the ZPMx nanorods in the bare ZPMx and ZPMx/Si@GO nanocomposites prepared using PEG with different molecular weights were calculated based on the TEM analysis and are shown in Figure 4.13. This enhancement in the aspect ratio of the ZPMx nanorods with an increase in the molecular weight of PEG supports the XRD results.

Table 4.1 D_{XRD}, d-spacing, lattice parameters (a and c) and number of unit cells obtained from XRD analysis; length of nanorods, width and the corresponding aspect ratios of ZPMx nanorods measured from TEM analysis

Samples	XRD						TEM		
	D_{XRD} (nm)	d (nm)	a (nm)	c (nm)	c/a	No. of unit cells	l (nm)	w (nm)	l/w
ZPM0	38	0.24765	0.32365	0.52842	1.6327	2,04,593	197.81	79.95	2.47
ZPM200	42	0.247749	0.32378	0.52863	1.6327	2,70,217	787.55	173.7	4.53
ZPM6000	43	0.28002	0.32411	0.52917	1.6327	2,87,161	812.96	101.7	7.98
ZPM0/Si@GO	21	0.247863	0.32338	0.52798	1.6327	33,433	172.8	70.53	2.45
ZPM200/Si@GO	28	0.247456	0.32374	0.52857	1.6327	81,220	602	146	4.12
ZPM6000/Si@GO	30	0.247456	0.323883	0.52879	1.6327	96,783	641.09	107.8	5.94

The mechanism for the formation of ZnO nanorods using surfactant PEG is shown in Figure 4.14. In the initial stage of the synthesis itself, PEG is added to the ZnO precursor to enable effective capping on $Zn(OH)_2$ when it is formed after the addition of LiOH. It has been found that PEG has a high affinity to forming a complex with Zn^{2+}, which results in the formation of a Zn^{2+}-PEG complex. It has been further treated with LiOH to obtain a PEG-$Zn(OH)_2$ complex. Microwave heating leads to dehydration and the subsequent formation of ZnO nuclei, which causes further aggregation and the formation of ZnO nanorods (denoted as ZPMx). This is because the surfactant PEG will adsorb on the surface of the ZnO nuclei, which leads to the formation of a 1D architecture in the

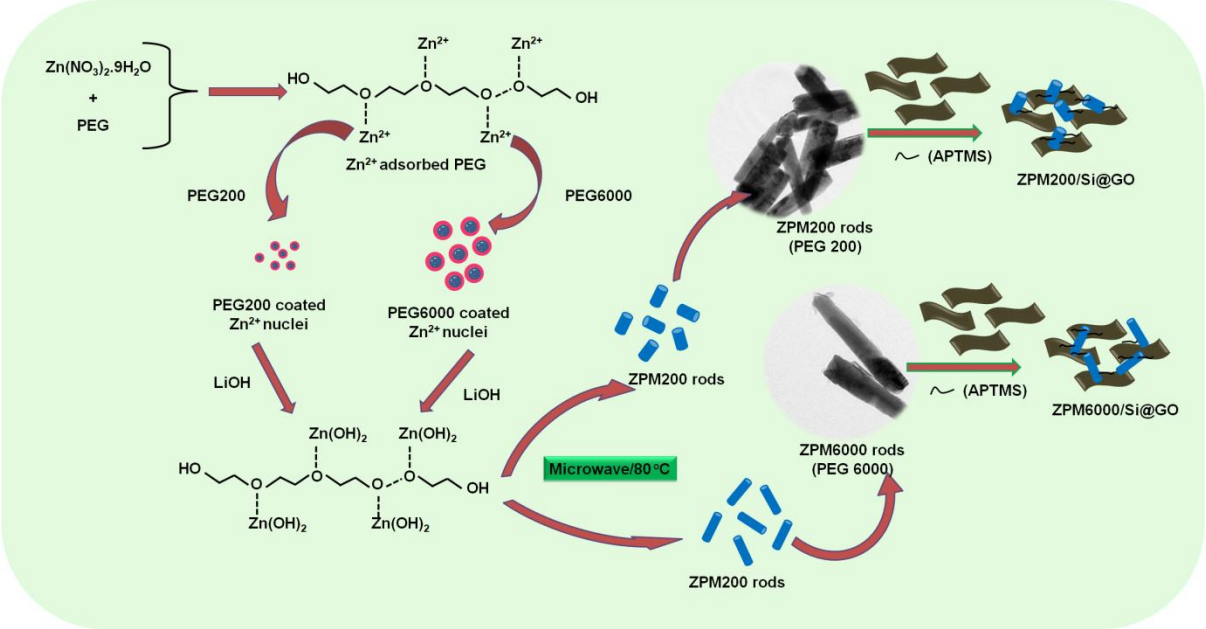

Figure 4.14 Schematic diagram for the formation of ZPMx nanorods with different aspect ratios and ZPMx/Si@GO nanocomposites.

(0001) direction (Panigrahy *et al*., 2009). Because the length of the PEG chain or the molecular weight of PEG increases, the length of the ZPMx nanorods also increases. This may be due to the fact that a greater number of ZnO crystals get capped, which subsequently leads to ZPMx nanorods with a higher aspect ratio. Here, the aspect ratio of the ZPMx nanorods was controlled using PEG with different molecular weights. A schematic illustration for the attachment of ZPMx on GO using APTMS is also shown in Figure 4.14. Both the surface hydroxyl groups on ZPMx and surface functional groups of GO help in the cross-linking reaction of APTMS with ZPMx and GO.

The structural characteristics of the as-prepared ZPMx and ZPMx/Si@GO were studied using FTIR analysis, and the spectra are displayed in Figure 4.15. The FTIR spectra of ZPMx show a broad absorption band at 556 cm^{-1}, which is attributed to the stretching vibration of the Zn-O bonds. The presence of a broad band at 3000-3400 cm^{-1} is mainly due to the presence of the surface adsorbed hydroxyl groups of ZnO in ZPMx.

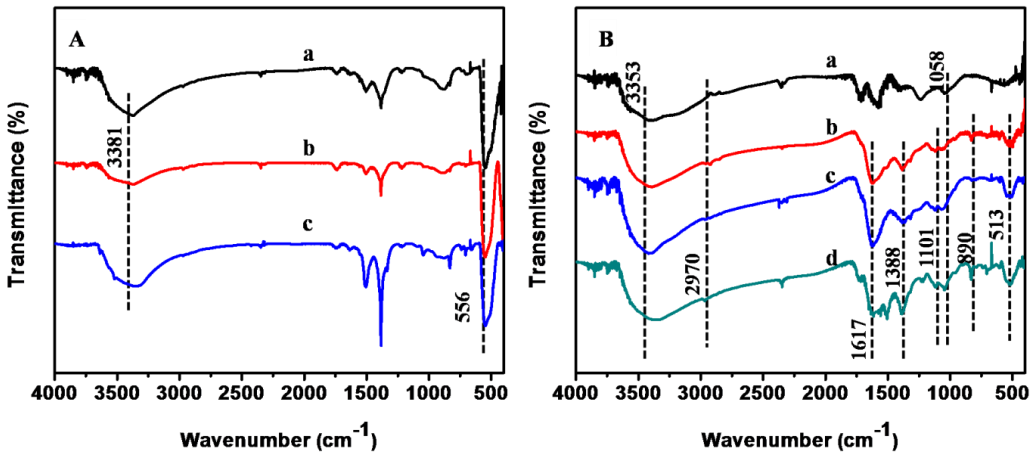

Figure 4.15 FTIR spectra of (A) ZnO (a) ZPM0 (b) ZPM200 (c) ZPM6000 and (B) ZnO/Si@GO nanocomposites (a) ZPM0/Si@GO (b) ZPM200/Si@GO (c) ZPM6000/Si@GO.

From the FTIR spectra of GO, it can be clearly seen that the stretching vibration of the C=O group is at 1719 cm^{-1}. The broad band observed at 3000-3600 cm^{-1} is assigned to the appearance of the hydroxyl groups of water molecules adsorbed on its surface. The peak at 1589 cm^{-1} originates from the stretching vibrations of GO. The peak at 1388 cm^{-1} is attributed to the deformation bands of the hydroxyl groups. The band at 1230 cm^{-1} is associated with the stretching vibration of the C-O-C bond of the epoxy group. In the FTIR spectra of ZPMx/Si@GO, the presence of a distinct band at 513 cm^{-1} is mainly attributed to the Zn-O bond, which indicates the existence of ZnO in the nanocomposite. Again, the band at 3353 cm^{-1} is due to the surface hydroxyl groups. The presence of a series of absorption bands at 1617, 1373, and 1058 cm^{-1} corresponding to the functional groups of GO indicates the existence of GO in the nanocomposite. A new absorption band at 1101 cm^{-1} was observed in the nanocomposite which may originate from the formation of a Zn-O-Si bond due to the APTMS enabled cross-linking of ZnO with GO (Hong *et al.*, 2009). Hence, the covalent interaction of ZPMx nanorods and GO sheets was confirmed from the FTIR analysis.

Table 4.2 BET surface area, total pore volume, and pore diameter of the as prepared samples

Samples	BET S.A (m^2g^{-1})	Total pore volume (cm^3g^{-1})	Pore diameter (nm)
GO	162	0.2895	6.3
ZPM0	11	0.0779	19.3
ZPM200	8	0.0386	11.3
ZPM6000	7	0.0335	12.5
ZPM0/Si@GO	12	0.0927	17.6
ZPM200/Si@GO	9	0.0806	13.0
ZPM6000/Si@GO	6	0.0423	15.6

To better understand the porous nature and surface area of the as-prepared ZPMx and ZPMx/Si@GO nanocomposite, N_2 adsorption-desorption experiments were conducted, and the results are shown in Figure 4.16. All the samples showed the type IV isotherm, which predominantly indicated the presence of a mesoporous behavior for the samples (Singh *et al*., 2013). BET surface area analyzes of the ZPMx and ZPMx/Si@GO prepared with and without PEG with different molecular weights was conducted, and the isotherms are presented in Figure 4.16A and 4.16B, respectively. Based on the results, it was inferred that the surface area decreased as the aspect ratio of the ZPMx nanorods increased. This was also in agreement with the XRD results, in which the surface area decreased with an increase in the crystallite size. The pore volume and pore diameter also decreased. The presence of ZPMx nanorods on the surface of GO effectively reduced the surface area of the GO in the ZPMx/Si@GO. As shown in Figure 4.5, the GO has a surface area of ~162 $m^2 g^{-1}$. However this decreased to 6-12 $m^2 g^{-1}$ in the ZPMx/Si@GO.

This was due to the blocking of the GO pores with ZnO. The BET surface area values for the ZPMx and ZPMx/Si@GO prepared using PEG with different molecular weights, pore volumes, and pore diameters are listed in Table 4.2.

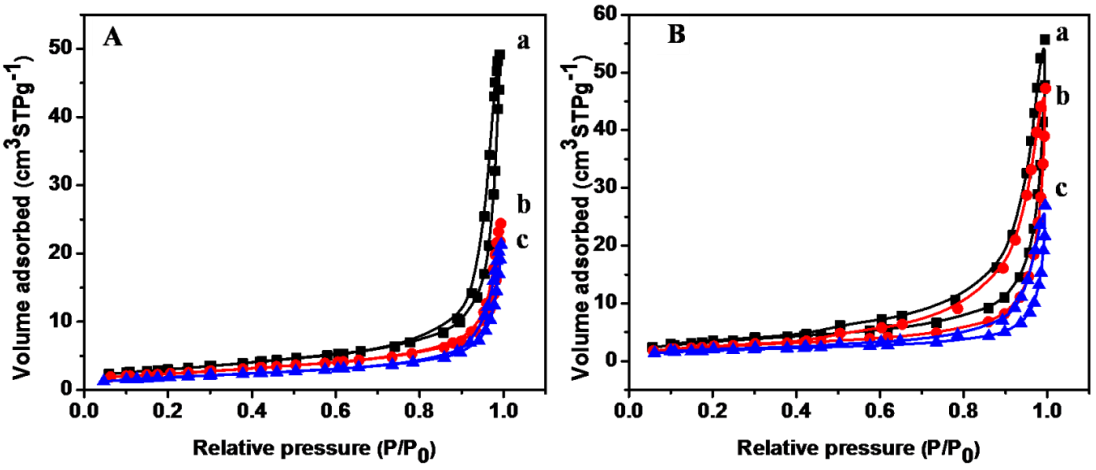

Figure 4.16 N_2 adsorption-desorption isotherms of (A) ZnO prepared with and without PEG (a) ZPM0 (b) ZPM200, and (c) ZPM6000 and (B) ZPMx/Si@GO nanocomposites prepared with and without PEG (a) ZPM0/Si@GO (b) ZPM200/Si@GO, and (c) ZPM6000/Si@GO.

4.4.4 Antibacterial Studies

To elucidate the health and environmental impacts of the materials, we conducted antibacterial activity studies of the as-prepared materials toward both Gram-positive and Gram-negative bacteria, and the results were discussed. Initially, the antibacterial activities of the GO, ZPMx, and ZPMx/Si@GO were qualitatively investigated using a disc diffusion assay, and the results are presented in Figure 4.17. Very small or negligible inhibition zones were observed around the discs containing GO, ZPM0, and ZPM200. This might have been due to the fact that the GO sheets or ZPMx nanorods (ZPM0 and ZPM200) had low concentrations and are not very toxic at low levels. Moreover, the bacterial proliferation was not inhibited very effectively by the pure GO or ZPMx particles at this low concentration. From Figure 4.17, it is clear that the ZPM6000 presents good inhibition rings with diameters of ~1.7, 0.9, and 1.6 cm for *S. aureus*, *E. coli*, and *K.*

pneumonia, respectively, which are larger than those of GO, ZPM0, and ZPM200. This proves that ZPMx nanorods with a higher aspect ratio (ZPM6000) have a significant antibacterial property against both Gram-positive and Gram-negative bacteria. However, in

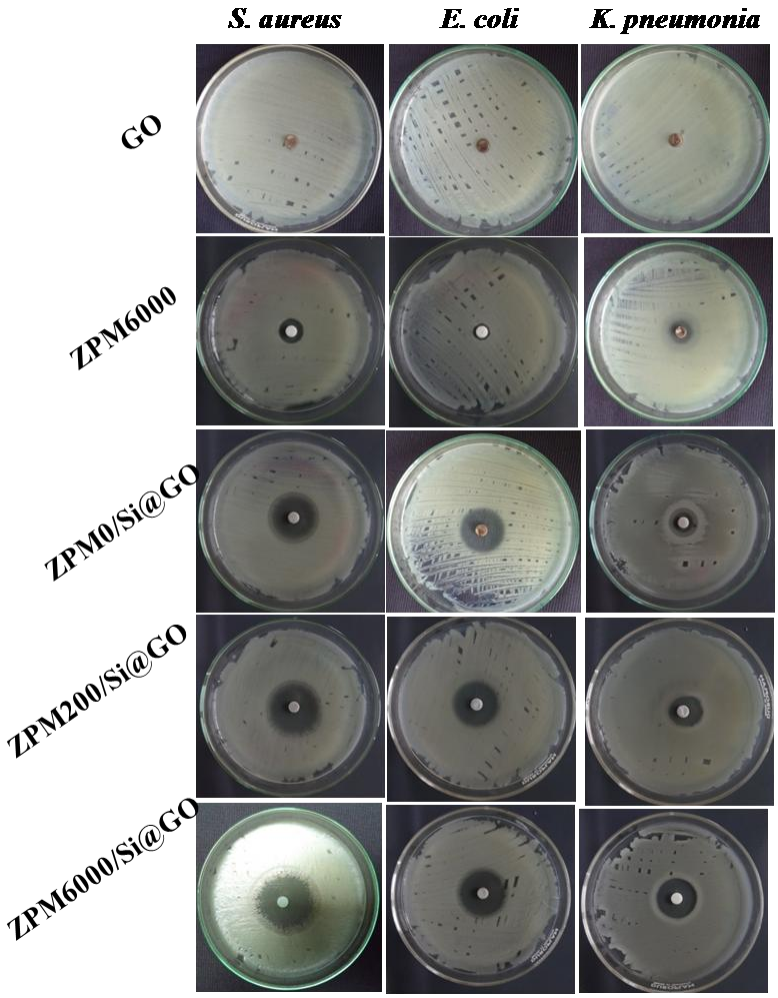

Figure 4.17 Photographs of the antibacterial activity of GO, ZPM0, ZPM200, ZPM6000, ZPM0/Si@GO, ZPM200/Si@GO, and ZPM6000/Si@GO.

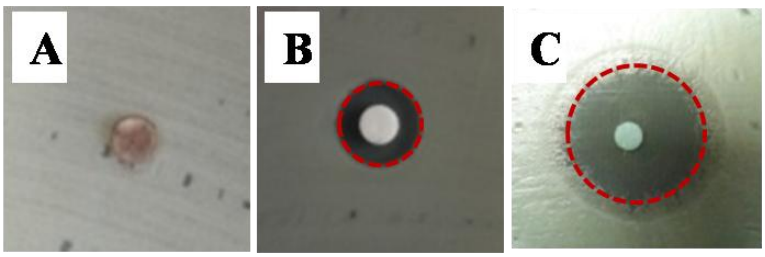

Figure 4.18 Photographs of the antibacterial activity of (A) GO (B) ZPM6000, and ZPM6000/Si@GO towards *S. aurues*.

the treatments with the ZPMx/Si@GO nanocomposites, the inhibition zones were much more visible than those of GO and ZPMx. This indicated that the effective inhibition of bacterial proliferation was a result of the interaction of the ZPMx/Si@GO nanocomposites with the bacteria. The photographs of antibacterial activity of GO, ZPM6000, and ZPM6000/Si@GO towards *S. aurues* are presented in the Figure 4.18.

The diameters of the inhibition rings of the ZPMx and ZPMx/Si@GO nanocomposites were measured and are presented in Figure 4.19. ZPMx/Si@GO shows inhibition zones with diameters of 3.1-3.7, 2.4-3.1 and 1.7-2.4 cm for *S. aureus, E. coli,* and *K. pneumonia*, respectively, demonstrating the excellent antibacterial property of the nanocomposites. From our experimental results, we could also see that the ZPM6000/Si@GO nanocomposite containing ZPM6000 nanorods with a higher aspect ratio showed higher antibacterial activities with zones of inhibition of ~3.7, 3.1, and 2.4 cm for *S. aureus*, *E. coli* and *K. pneumonia*, respectively. Based on the results, it can be concluded that the enhanced antibacterial activity of ZPMx/Si@GO was mainly due to the synergistic effect of the GO and ZPMx (Wang *et al*., 2014). As reported in the literature, the antibacterial properties of GO and ZPMx arise from the following actions. Mainly, the interaction of GO with bacterial cells leads to membrane stress, which subsequently damages the bacterial cell wall. In addition, GO layers wrap the bacterial cells, which leads to the complete destruction of the bacteria (Upadhyay *et al*., 2014).

The antibacterial activity of ZnO depends mainly on various parameters such as the crystal size, surface area, morphology, and polar surfaces (Sirelkhatim *et al*. 2015). The formation of reactive oxygen species and the dissolution of Zn^{2+} ions (Vijayalakshmi *et al*., 2015) also play significant roles in the antibacterial activity of ZnO. The generation of reactive oxygen species is mainly induced by UV/sunlight irradiation. However, under a dark condition, the possible mechanisms for the antibacterial activity include the

following: (i) the surface abrasiveness of ZnO (Raqo *et al*., 2014). (*i.e.*, the sharp edges of the ZnO nanorods rupture the cell) and, (ii) release of Zn^{2+} ions to the bacterial medium (Zhong *et al*., 2015). Previous reports have demonstrated that particles with a low crystallite size and high surface area have enhanced antibacterial activity. However, in this study, an excellent antibacterial activity was observed for ZPMx nanorods with a high aspect ratio (~7.9). This may have been due to the diffusion of Zn^{2+} ions from the polar faces to the bacterial cells one after the other. This slow and steady release of Zn^{2+} ions from the polar faces is considered to be the most important mechanism for the superior

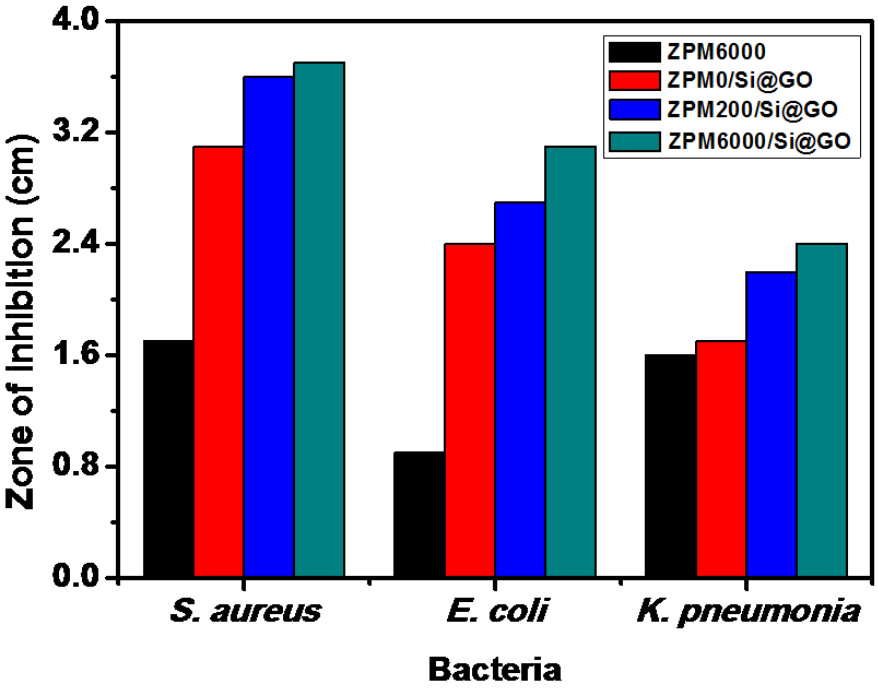

Figure 4.19 Zone of inhibition of ZPMx and ZPMx/Si@GO samples.

antibacterial activity of ZPM6000 compared to the other ZPMx nanorods with lower aspect ratios. In the case of ZnO nanorods, this partial dissolution of Zn^{2+} ions occurs mainly in an aqueous environment (Zhong *et al*., 2015). The released Zn^{2+} ions have nanotoxicity toward bacteria, and can penetrate bacterial cell, which results in the cellular inhibition. In addition, equal amounts of ZPM6000 and GO, *i.e*., in a 1 : 1 wt ratio

(ZPM6000/Si@GO), helps with the effective distribution of ZPM6000 nanorods on GO sheets, which is again responsible for its good antibacterial activity. Moreover, the post-grafting of APTMS onto ZPMx particles also plays a key role in the effective distribution of these ZPMx nanorods on the thin layers of GO, which enhances the antibacterial property of ZPMx/Si@GO. The GO can easily wrap the bacterial cells. As a result, the uniformly distributed ZPMx nanorods can successfully come into contact with the bacteria in such a way that the GO can act as a storage site for the Zn^{2+} ions released from the ZPMx. The membrane stress caused by the sharp edges of GO also helps in the death of the bacteria (Deng *et al*., 2014; Akhavan *et al*., 2010). Along with this membrane stress induced by direct physical contact, oxidative stress also plays an important role in the bacterial death. This oxidative stress may arise from reactive oxygen species (ROS) mediated or ROS-independent pathways (Liu *et al*., 2011). ZPMx/Si@GO showed an enhanced antibacterial activity against the Gram-negative bacteria compared with the Gram-positive bacteria because of the thin cell walls in these bacteria, which made the destruction of these thin cell walls more prominent. Hence, the antibacterial property was somewhat less in the case of the Gram-negative bacteria because of the thick cell wall.

4.4.4.1 Morphological Changes of Bacteria After Treating with ZPMx/Si@GO

Figure 4.20A, 4.20C, and 4.20E show typical TEM micrographs of the control or untreated *S. aureus*, *E. coli*, and *K. pneumonia*, respectively. Figure 4.20B, 4.20D, and 4.20F show the TEM images of the test bacteria treated with the ZPM6000/Si@GO nanocomposites. In these TEM images, it can be observed that the untreated *S. aureus*, *E. coli*, and *K. pneumonia* have rod shapes. The TEM images before and after treatment with ZPM6000/Si@GO show a significant change in morphology induced by the damage to the bacterial cells (marked by brown colored arrows). The damage to the bacterial cell walls and leakage of the cytoplasm are clearly observed in the TEM images. The same

observations were obtained in the SEM images of the control and ZPM6000/Si@GO treated bacteria (Figure 4.21A, 4.21C, 4.21E, 4.21B, 4.21D, and 4.21F). The direct physical contact of the bacteria with the GO sheets induced irreversible damage in the bacteria, which can be observed in the SEM and TEM analyzes.

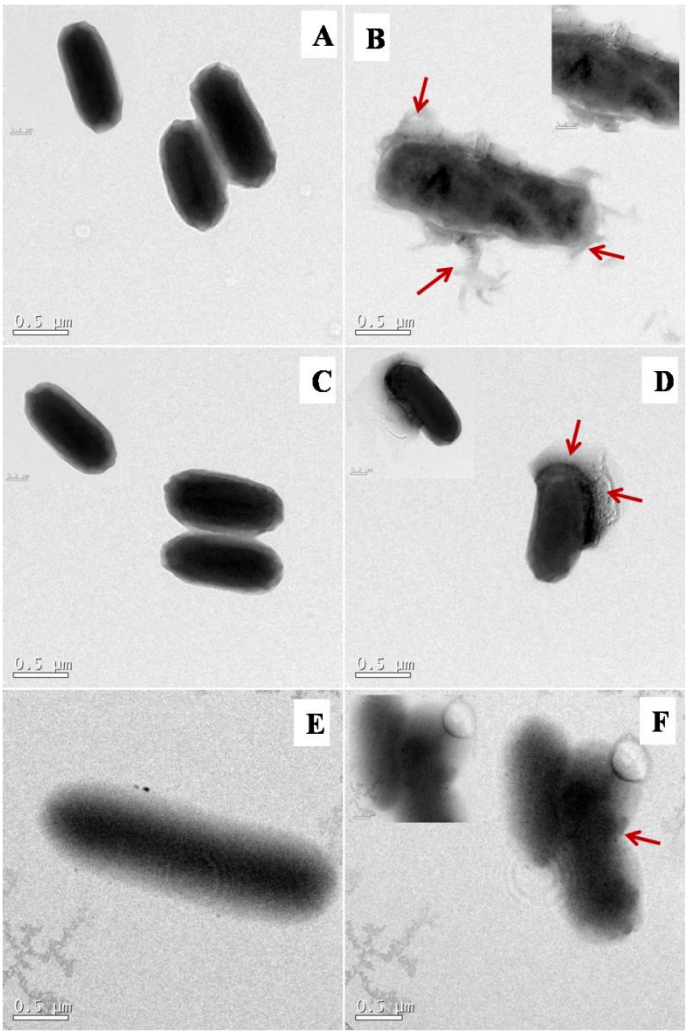

Figure 4.20 Typical TEM images of untreated and treated bacterial cells with ZPM6000/Si@GO: (A) TEM image of untreated *S. aureus* cells (B) TEM image of treated *S. aureus* cells (C) TEM image of untreated *K. pneumonia* cells (D) TEM image of treated *K. pneumonia* cells (E) TEM image of untreated *E-coli* cells (F) TEM image of treated *E. coli* cells.

For better understanding the antibacterial effect of the ZPMx/Si@GO nanocomposites quantitatively, the growth curves of the control and treated bacteria were also studied. The OD_{600nm} values at different incubation times (0, 1, 2, 4, 8, 12, 24, and

48h) were measured and are presented in Figure 4.22. The results are consistent with those of the qualitative analysis. From the OD curves of the controls (*S. aureus*, *E. coli,* and *K. pneumonia*) and ZPMx, GO, and ZPMx/Si@GO treated bacteria, it is clear that the optical

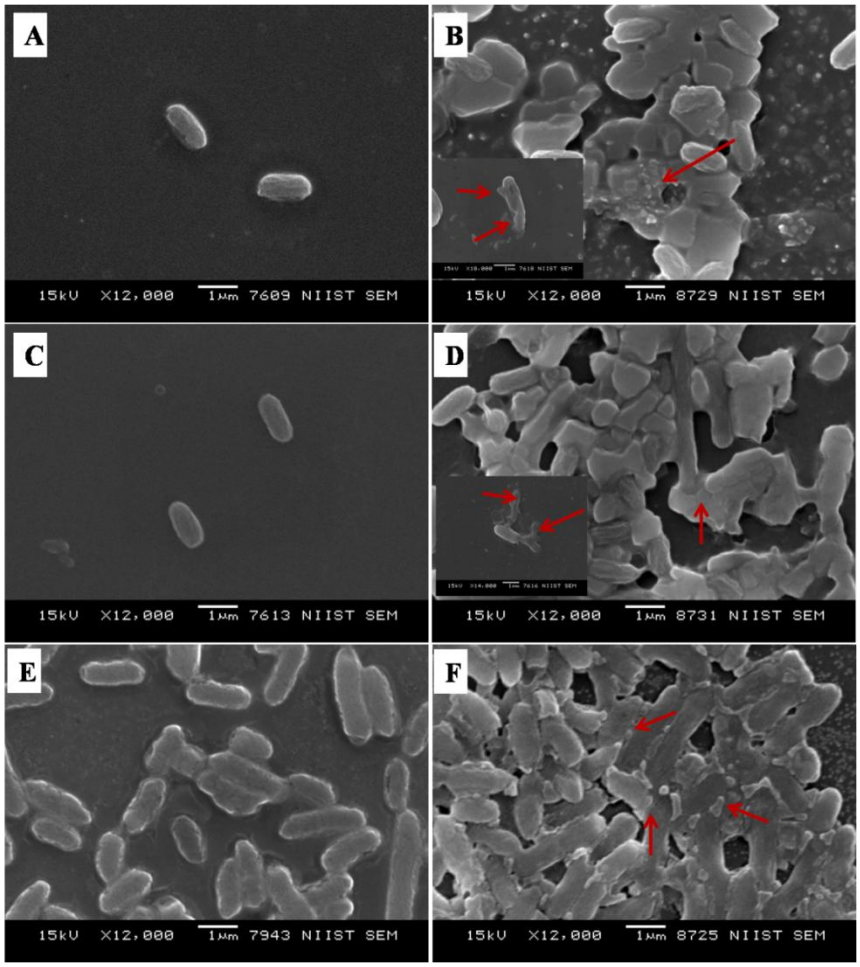

Figure 4.21 Typical SEM images of untreated and treated bacterial cells with ZPM6000/Si@GO: (A) SEM image of untreated *S. aureus* cells (C) SEM image of treated *S. aureus* cells (E) SEM image of untreated *K. pneumonia* cells (B) SEM image of treated *K. pneumonia* cells (D) SEM image of untreated *E-coli* cells (F) SEM image of treated *E. coli* cells.

density significantly decreases in the order of control > GO > ZPM0 > ZPM6000 > ZPM6000/Si@GO. This data again demonstrate that the ZPMx/Si@GO had a much stronger antibacterial ability compared to pure ZPMx. Overall, the synthesized ZPMx/Si@GO composites could be effectively used to eradicate bacteria. A schematic illustration of the mechanism for the irreversible damage to the bacterial cells is shown in Figure 4.23, which explains the synergistic effect of the GO and ZPMx.

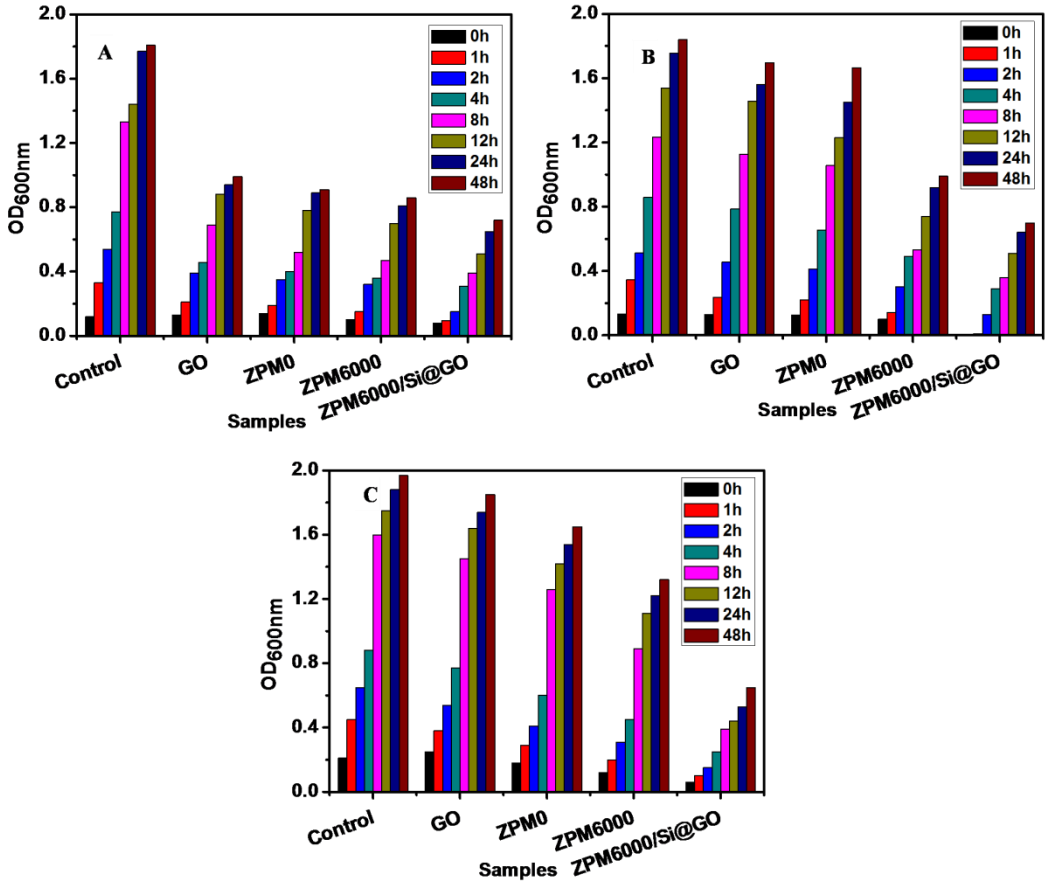

Figure 4.22 Growth curves of (A) *S. aureus* (B) *E. coli* (C) *K. pneumonia*: (a) control (b) GO (c) ZPM0 (d) ZPM6000, and (e) ZPM6000/Si@GO.

The reduction of GO as a result of bacterial contact has been reported in many studies. For example, the interaction of GO and *E. coli* under an anaerobic condition leads to the reduction of GO, but the degree of reduction is lower than that for GO by the hydrazine/photocatalytic route (Akhavan *et al*., 2012). Because an anaerobic condition favors the reduction of GO by *E. coli*, here all of the experiments were conducted under aerobic conditions. Hence, the reduction of GO did not occur in the study. In the present investigation, we conducted all of the experiments under a dark condition, and the materials were found to be stable under this condition.

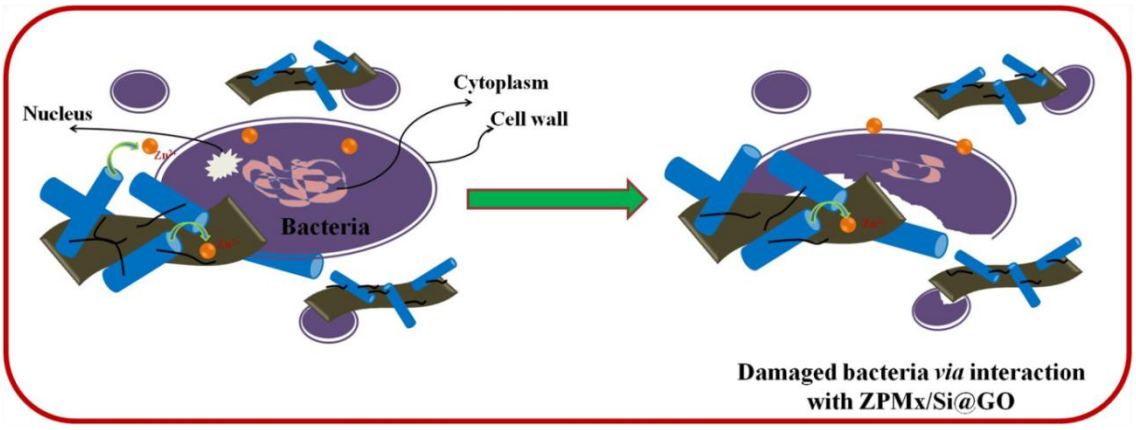

Figure 4.23 Schematic illustration showing the bacterial destruction of ZPM6000/Si@GO towards Gram-positive bacteria.

4.4.4.2 Application of ZPMx/Si@GO for Real Pond Water Treatment

The water disinfection property of ZPM6000/Si@GO was tested using real pond water (Figure 4.24A shows a photograph of real pond water) to demonstrate its efficiency in real water treatment. The percentage of bacterial inhibition was studied using various stirring times (2, 8, 12, 24, and 48 h) and is presented in Figure 4.24B. From the graph, it is clear that the percentage of bacterial inhibition increases over time. As the stirring time increases from 2 to 48 h, we can observe a gradual increase in the percentage of bacterial inhibition from 16 to 26.5%. A bacterial growth inhibition of ~10.5% was observed as a result of its contact with the nanocomposite. This was a direct measure of the reduction in the bacterial growth, but it was not drastic. This was because the pond water contained diversified impurities such as bacteria, viruses, fungi, algae, and chemical and solid wastes. Thus, no extensive reduction in bacterial growth was observed in the pond water. Figures 4.24C and 4.24D show photographs of the numbers of microorganisms in the treated and untreated samples, respectively. The untreated sample was observed to have a heavy microbial load (Figure 4.24C). However, in the treated sample, the ZPM6000/Si@GO nanocomposite used for the water treatment efficiently inhibited the

microbial population as can be validated through this enumeration technique, where there is no site of microbial colonies on the LB and NB agar plates.

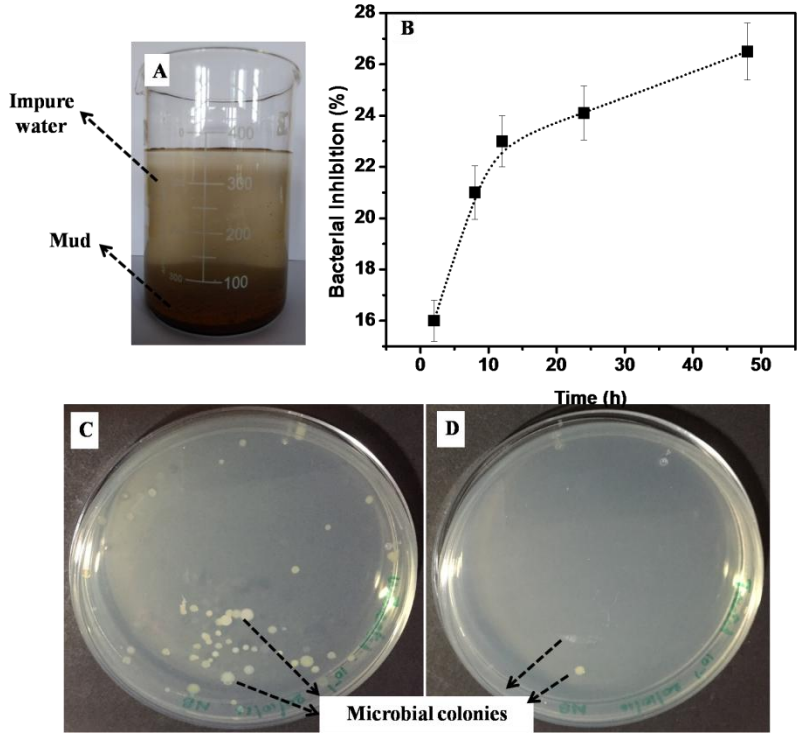

Figure 4.24 (A) Photograph of pond water. (B) % of bacterial inhibition against time in hour. (C and D) Photographs of enumeration of microorganisms in untreated and treated water samples.

4.5 Conclusions

ZPMx nanorods with various aspect ratios ranging from 2.47 to 7.98 were prepared *via* a PEG-assisted microwave method. APTMS was used for the surface modification, and the modified ZPMx nanorods (with aspect ratios ranging from 2.45 to 5.94) were effectively post-grafted on the surface of thin GO sheets. The obtained ZPMx/Si@GO nanocomposite was systematically characterized using a series of techniques such as XRD, SEM, TEM, optical microscopy, and FTIR. APTMS modification resulted in the uniform deposition of ZPMx nanorods on the GO sheets. The ZPMx/Si@GO nanocomposite was further used for the disinfection of water. *S. aureus*, *E. coli*, and *K. pneumonia* were taken as model

pathogens to study the antibacterial properties of the GO, ZPMx, and ZPMx/Si@GO. Among the ZPMx nanorods synthesized with and without PEG, the PEG 6000 mediated ZPMx nanorods with a higher aspect ratio showed higher antibacterial activity as a result of the effective diffusion of Zn^{2+} ions from the polar face to the bacterial medium. The overall studies showed that the ZPMx/Si@GO nanocomposite had a better antibacterial property than the pure ZPMx and GO, which was the result of the synergistic effect of the GO and ZPMx. In the experiments, it was found that the diameters of the inhibition rings of ZPM6000-Si@GO were ~3.7, 3.1, and 2.4 cm for *S. aureus*, *E. coli,* and *K. pneumonia*, respectively. Optical density measurements also supported these results. SEM and TEM analyzes assisted in visualizing the morphological changes in the bacteria before and after treatment with the ZPM6000/Si@GO nanocomposite. The use of this nanocomposite in real pond water treatment also showed a time-dependent bacterial growth inhibition.

CHAPTER 5

Development of ZnO@rGO Nanocomposites for the Enzyme Free Electrochemical Detection of Urea and Glucose

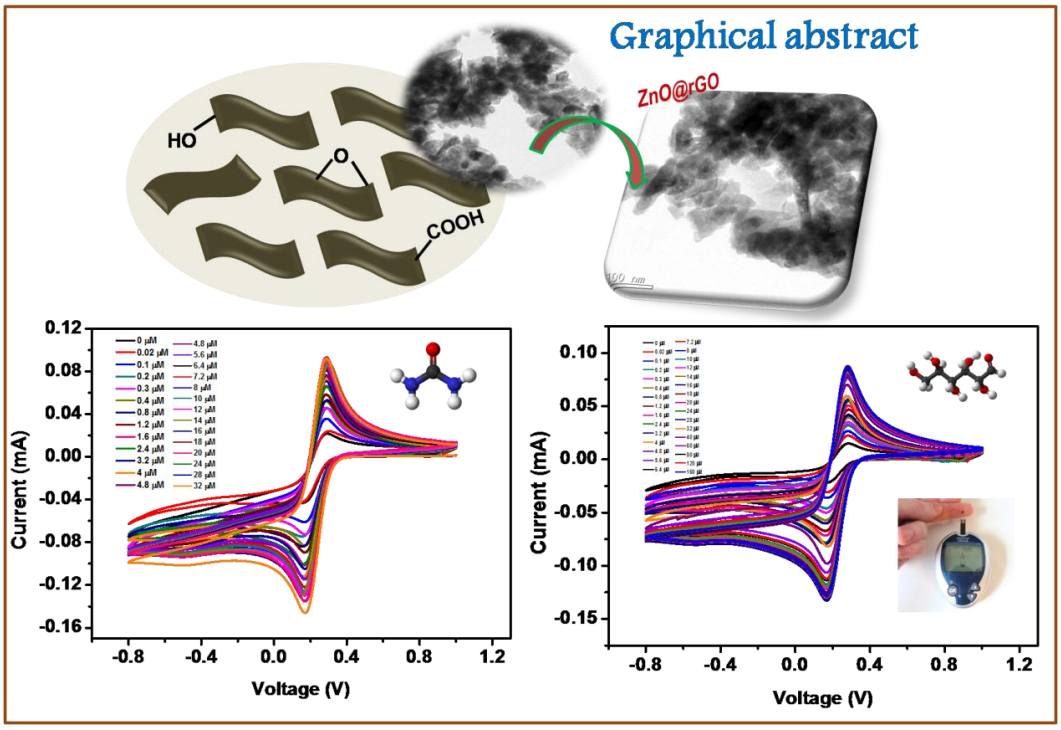

5.1 Abstract

Metal oxide-rGO based non enzymatic urea and glucose sensor was developed. The electrochemical performance of the nanocomposite for the detection of urea and glucose were investigated by cyclic voltammetry. Here in, we report a green synthetic strategy for the preparation of ZnO@rGO nanocomposites. A bioinspired synthesis of ZnO nanoarchitectures has been done using monosaccharide, disaccharide, and polysaccharide as biotemplates. A series of biotemplates such as dextrose, sucrose, soluble starch, and carboxy methyl cellulose, were used for the synthesis of ZnO nanoarchitectures. The as-prepared morphologically tuned ZnO nanoarchitectures thus obtained were uniformly distributed on the surface of rGO sheets, which results in the ZnO@rGO nanocomposites. For the first time zinc (Zn) dust, a waste byproduct from an industry (Binani Zinc Limited, Kerala, India) was employed for the chemical reduction of GO. The obtained ZnO@rGO nanocomposites were characterized with XRD, UV-vis, SEM, TEM, BET, and FTIR techniques. Finally, the as-prepared ZnO@rGO nanocomposites were employed for the electrochemical detection of urea and glucose.

5.2 Introduction

Urea is a most widely used fertilizer and its production and consumption in India are about 23 and 31 million tonnes. Due to its higher water solubility, a considerable amount of the applied urea may get dissolved in surface and ground water. In biological aspect, urea is the final product of protein degradation and nitrogen metabolism. The normal concentration of urea in the blood serum is 2.5-7.5 mM (Bianchi *et al*., 2014) and an increased or decreased urea level in blood and urine poses several diseases such as renal failure, urinary tract obstruction, dehydration, shock burns, gastrointestinal bleeding, hepatic failure, nephritic syndrome, and cachexia (Soldatkin *et al*., 2014). So the

monitoring of the urea level has got great significance in the environmental and clinical samples, drinking water and food.

Glucose is the primary source of energy in the human body (Dar *et al*., 2011). The normal range of blood glucose in human body is about 3.9-6.2 (empty stomach) or 3.9-7.8 (2h after food) mM (Chen *et al*., 2013). Diabetics mellitus, a metabolic disorder occurs when our body is unable to control the amount of glucose due to the malfunctioning of insulin or decreased insulin secretion (Shanbhag *et al*., 2016). It subsequently leads to various health issues such as cardiovascular, nervous, ocular, cerebral and peripheral vascular diseases, kidney failure, tissue damage, blindness *etc*. (Dar *et al*., 2011; Kumar *et al*., 2015). The adverse effect of diabetics can be avoided by the quantitative monitoring of blood glucose concentration (Dar *et al*., 2011). A quantum of research studies has been conducted for developing efficient and reliable method for urea and glucose sensing. Electrochemical detection has been considered as the most promising method for the detection of urea and glucose (Jiang *et al*., 2017; Yin *et al*., 2013). Details of the metal oxide based electrochemical sensors and the importance of ZnO nanoparticles in electrochemical sensing are provided in the Chapter 1.

Graphene based nanomaterials are widely used in electrocatalytic sensing applications. Among these, rGO is a preferred sensor platform due to the following reasons. rGO is electrical conductive as compared to the non-conductive GO. Large number of edges and defects facilitate electron transfer. Conductivity and surface functional groups could be turned for detection of specific chemical species. In 2010, X. Gao *et al*., investigated reaction mechanisms for deoxygenation of GO with hydrazine or heat treatment. They observed that in both reduction types, the oxygen functionalities attached to the interior of an aromatic domain in GO are removed more easily, by kinetically as well as thermodynamically, than those attached at the edges of an aromatic

domain (Gao *et al*., 2010). In 2011, S. Park *et al*., compared hydrazine reduction of graphite oxide which are not completely exfoliated and GO which are completely exfoliated. They found that while hydrazine reduction of GO platelets produced agglomerates of exfoliates platelets, the reduction of GO particles produced particles which were not exfoliated (Park *et al*., 2011). In 2011, P. Cui *et al*., report a new reducing system *i.e*. hydriodic acid with trifluroacetic acid, which can chemically convert GO into rGO at subzero temperature (below 0 ^{o}C) with a mass production (Cui *et al*., 2011). In 2012, V. H. Pham *et al*., reported a simple and effective method to reduce the aqueous suspension of GO using nascent hydrogen generated in-situ by the reaction between Al foil and HCl, Al foil and NaOH, and Zn powder and NaOH (Pham *et al*., 2012). In 2012, O. Akhavan *et al*., reported a single step green method for the reduction and functionalization of GO by glucose was developed (Akhavan *et al*., 2012). In 2012, R. S. Dey *et al*., demonstrated a facile route for the synthesis of rGO sheets by chemical reduction of GO using Zn/acid solution at room temperature (Dey *et al*., 2012). In 2013, C. K. Chua *et al*., presented a review article in which 50 types of reducing agents were discussed based on the two major categories (1) those which function according to the well supported mechanisms and (2) those which supported based on the proposed mechanisms (Chua *et al*., 2014). To best of our knowledge no attempts were done to conduct the reduction of GO using waste materials.

In the present work, ZnO nanoparticles with varied morphology were prepared *via* biotemplate assisted microwave method. Recently, the use of biomaterials as templates has become important in the green synthesis of morphology controllable nanomaterials. Because they are cheap, economical, environmentally begin, and renewable. Here monosaccharide, disaccharide and polysaccharide were used as biotemplates. At the same time, rGO was prepared by the chemical reduction of GO using nascent hydrogen. Zn dust,

a waste material obtained from an industry was used for the generation of nascent hydrogen and it act as a strong reducing agent in this reaction. ZnO has been attached on rGO *via* microwave assisted ex-situ technique which gives ZnO@rGO nanocomposite. Structural and morphological studies were carried out, which shows the formation of homogeneous distribution of ZnO on rGO. The as-prepared ZnO@rGO has been used for the non enzymatic sensing of urea and glucose. ZSs@1rGO shows higher sensing ability due to small particle morphology and reduced crystallite size.

5.3 Materials and Methods

5.3.1 Materials

Graphite (99.9%), Nafion solution (5 wt % in lower aliphatic alcohols and water, contains 15-20% water) and Potassium ferri cyanide (99.9%) were procured from Sigma Aldrich, Germany. Sodium nitrate ($NaNO_3$, 99.5%), potassium permanganate ($KMnO_4$, 99%) Hydrogen peroxide (H_2O_2, 99%), Dextrose anhydrous (D-glucose anhydrous, $C_6H_{12}O_6$, 99%), Sucrose (Saccharose, $C_{12}H_{22}O_{11}$, 99%), and Carboxy methyl cellulose sodium salt were obtained from S. D. Fine Chemicals limited, India. Zinc nitrate hexahydrate ($Zn(NO_3)_2.6H_2O$, 99%), conc. Sulphuric acid (H_2SO_4 , 99%) and Soluble starch ($(C_6H_{10}O_5)_n$, 99%) were supplied by Merck, India. Lithium hydroxide (LiOH, 99%) was purchased from SRL, India. Zn dust obtained from Binani Zinc Limited was used for the reduction of GO. All the reagents were used as received without any further purification.

5.3.2 Preparation of GO

GO has been prepared *via* Hummers method (Krishna *et al*., 2012) and the detailed procedure is given in Chapter 3 and 4.

5.3.3 Preparation of rGO *via* Nascent Hydrogen Chemical Reduction

In a typical procedure 20 mg of GO was dispersed in a 200 mL double distilled water using a probe sonicator. It was further treated with conc. HCl (1M) followed by the slow addition of Zn dust (2 g). The whole mixture was stirred overnight using a magnetic stirrer. The gradual change in the colour from orange brown to black indicates the reduction of GO to rGO. The obtained rGO was then collected by centrifugation further it was washed three times with 0.1 M HCl, followed by washing with double distilled water. After removing all impurities, the rGO nano sheets were freeze dried. Schematic illustration for the nascent hydrogen chemical reduction is given in Figure 5.1.

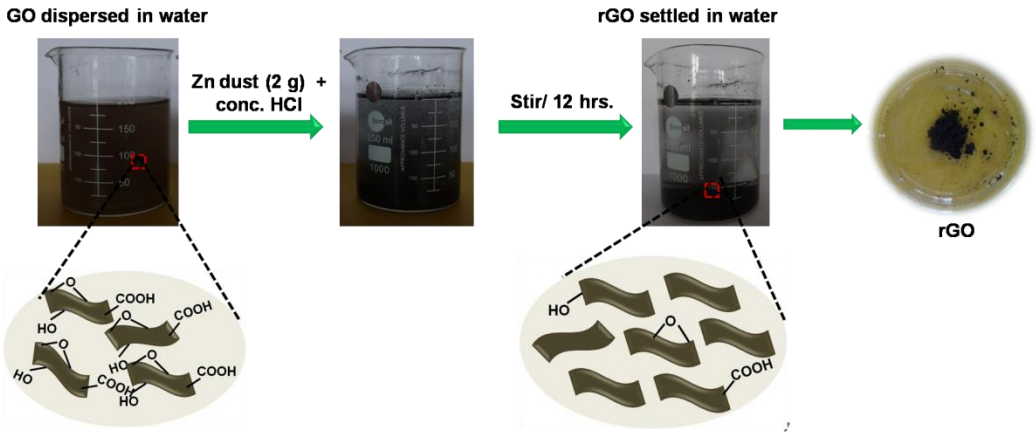

Figure 5.1 Scheme illustrating the Zn mediated nascent hydrogen chemical reduction of GO in presence of conc. HCl.

5.3.4 Synthesis of ZnO Nanoparticles *via* Biotemplate Method

ZnO nanoparticles were prepared *via* biotemplate assisted microwave technique (Scheme 5.2). In a typical procedure, 0.3 M $Zn(NO_3)_2.9H_2O$ was dissolved in 500 mL double distilled water and an appropriate amount of carbohydrate/cellulose was dispersed eventually by keeping the wt ratio of ZnO and carbohydrate/cellulose as 1:1. Dextrose, sucrose, soluble starch, and carboxy methyl cellulose were used as structure directing agents. Since carboxy methyl cellulose is sparingly soluble in water, ~1-1.5h was taken to

dissolve it in water at room temperature (slight yellowish colored transparent solution was obtained). The pH of the reaction mixture was adjusted with 10 wt % LiOH solution. The obtained solution was kept in the microwave synthesis work station (Sineo MAS II) at 80 ^{o}C for 30 min (P=300 W). The obtained powder was washed repeatedly with double distilled water to remove the impurities. The final product was dried in the oven at 50 ^{o}C. The obtained ZnO samples were denoted as ZD, ZS, ZSs, and ZC, respectively.

5.3.5 Preparation of ZnO@1rGO Nanocomposites

In a typical synthesis of the nanocomposites 0.0025 g of rGO (1 wt %) was uniformly dispersed in 30 mL of DMF with the aid of ultrasonication for 1h to obtain a uniform suspension of rGO. Then 0.2475 g of ZnO (ZD, ZSs, ZS, and ZC) was added. It was followed by magnetic stirring for 1 h to attain uniform dispersion. The product obtained was collected by centrifugation and washed repeatedly with ethanol to remove the impurities and dried at 85 ^{o}C. The illustration is provided in the Figure 5.2.

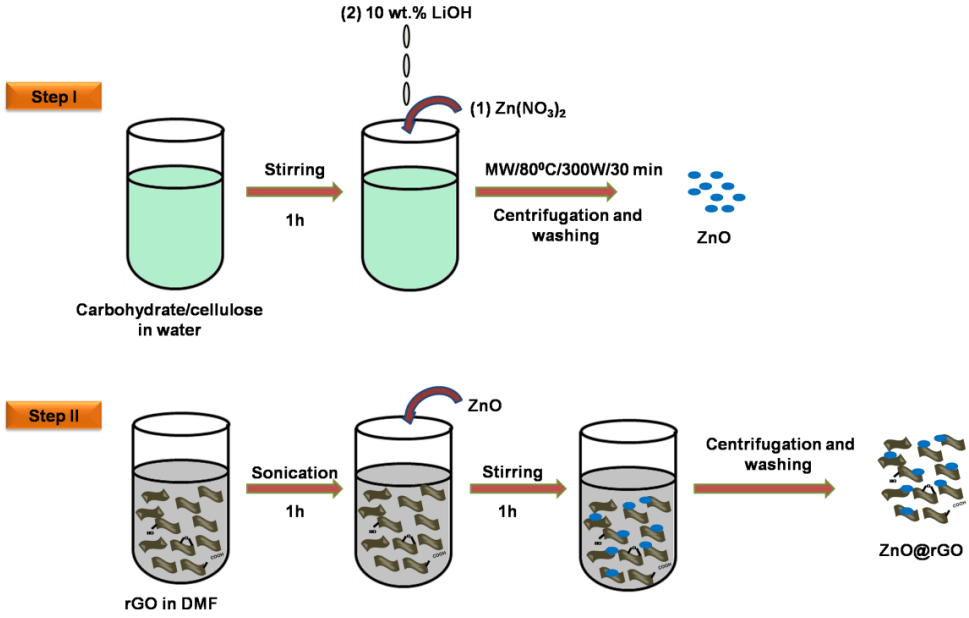

Figure 5.2 Schematic illustration showing the synthetic procedure of ZnO and ZnO@1rGO.

5.3.6 Electrochemical Studies

The electrochemical behaviour of ZnO@1rGO nanocomposites and its constituents (rGO and ZnO) has been performed. The electrochemical experiments such as cyclic voltammetry (CV) and electrochemical impedance spectroscopy (EIS) analysis were conducted in a conventional three electrode cell at room temperature using a cyclic voltametric instrument (VMP3-Biologic). The modified glassy carbon electrode (GCE) was used as the working electrode (with a GC disc diameter of 3 mm), a platinum (Pt) wire as the counter electrode, and Ag/AgCl (in saturated KCl) as the reference electrode in 0.1 M potassium ferricyanide solution.

The modified GCE has been prepared by the following procedure. GCE electrode was cleaned by polishing with 0.3 μm alumina powder. The electrode was further processed by sonication for 5 min each in acetone and double distilled water and dried under atmosphere. 1 mg mL^{-1} of ZnO or ZnO@1rGO was sonicated in nafion for 10 min to get a uniform dispersion. The cleaned GCE was drop casted with 2 μL of ZnO or ZnO@1rGO dispersed in nafion. This thin film of the materials deposited on the surface of the electrodes was left overnight at room temperature for drying the deposited material and the same was used as working electrode (sensor) for urea or glucose determination in combination with platinum wire as counter electrode. In the electrochemical cell, calomel was the Ag/AgCl reference electrode, and potassium ferricyanide was used as electrolyte. The electrodes were polished and cleaned before every deposition step. The EIS was performed in 0.1 M potassium ferricyanide solution at a potential of 0.32 V in a frequency range of $10-10^6$ Hz at signal amplitude of 10 mV.

5.4 Results and Discussion

5.4.1 Characterization of Zn Dust

Zn dust obtained as a waste by-product from an industry, was used for the generation of nascent hydrogen for the chemical reduction of GO. The XRD pattern of the Zn dust was given in the Figure 5.3. The characteristic diffraction peaks at the 2θ positions of 36.5 ^{o}, 39.2 ^{o}, 43.4 ^{o}, 54.36 ^{o}, and 70.54 ^{o} are corresponding to the (002), (100), (101), (103), and (110) planes of pure Zn metal, respectively (JCPDS file no. 00-004-0831) (Balanad *et al*., 2016).

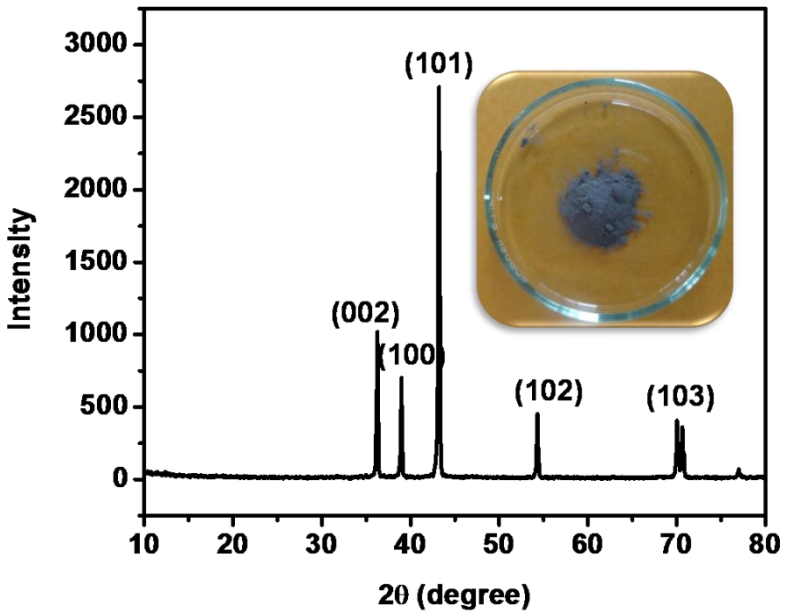

Figure 5.3 XRD pattern of Zn dust. Inset is the photographic image of Zn dust.

5.4.2 Characterization of GO

The detailed characterization studies of freeze dried GO prepared *via* Hummers method was presented in Chapter 4.

5.4.3 Characterization of rGO Prepared *via* Zn Mediated Nascent Hydrogen Reduction

Typical low and high magnification SEM images of rGO are presented in the Figure 5.4A and B. The fluffy and thin layered nature of rGO nanosheets was confirmed from the SEM images. This was again confirmed with TEM image of rGO as shown in the Figure 5.5.

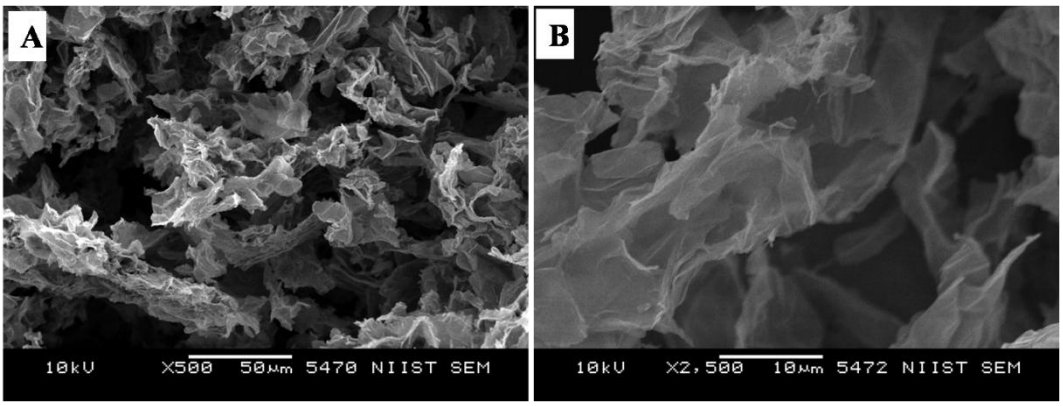

Figure 5.4 (A and B) Typical low and high magnification SEM images of rGO prepared *via* Zn dust mediated nascent hydrogen reduction of GO.

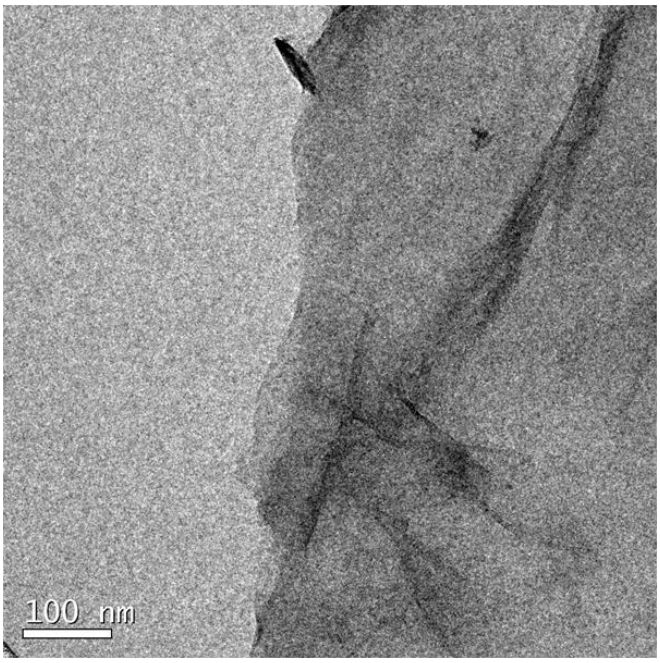

Figure 5.5 TEM image of rGO prepared *via* chemical reduction with Zn dust.

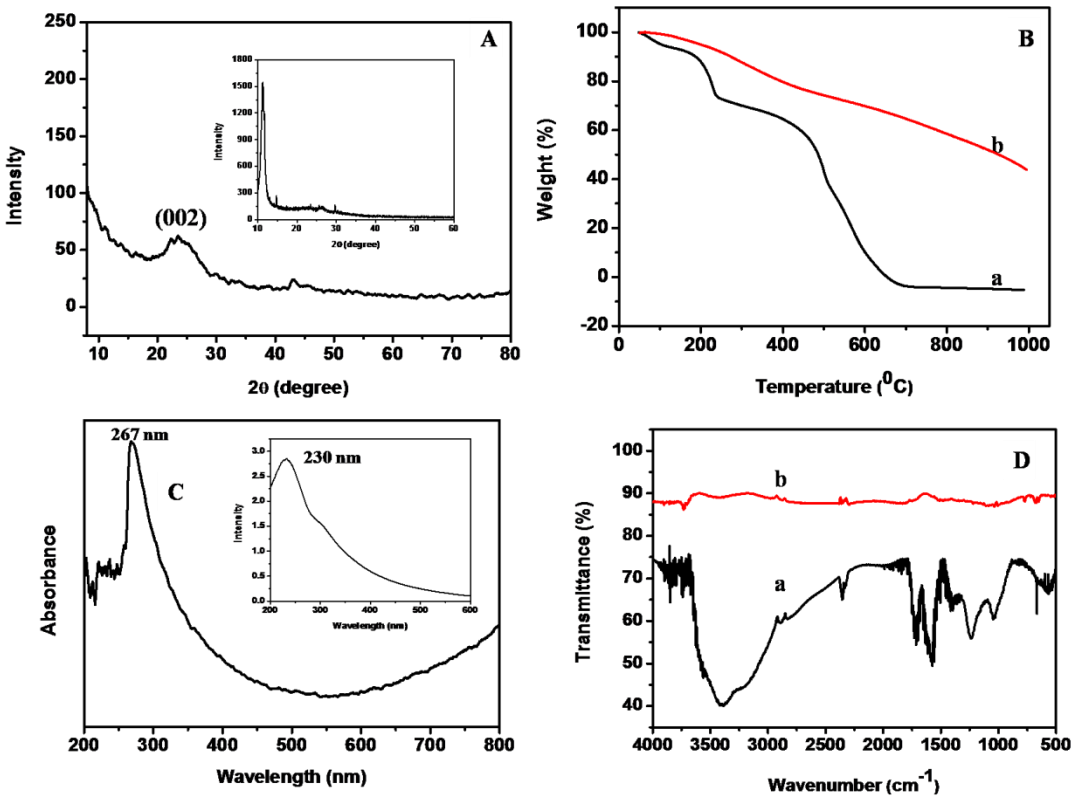

Figure 5.6 (A) XRD pattern of rGO prepared using Zn dust (B) TG analysis of (a) GO and (b) rGO (C) UV-vis spectra of rGO dispersed in DMF (D) FTIR spectra of (a) GO and (b) rGO. Inset of (A) is the XRD pattern of GO and inset of (C) is the UV-vis spectra of GO.

The XRD analysis of rGO sheets prepared using nascent hydrogen reduction with Zn dust is given in the Figure 5.6A. The XRD pattern of GO is given in the inset of Figure 5.6A. The main intensity peak of GO is at 10.8 ^{o} corresponding to the (001) reflection plane. After reduction with Zn dust this peak is completely disappeared and a new broad diffraction peak centred at ~ 24.5 ^{o} was appeared indicating the complete conversion of GO to rGO. This peak corresponds to the (002) plane of rGO nanosheets (Shah *et al.*, 2012). The appearance of a low intensity peak exhibited by rGO nanosheets at ~ 44 ^{o} corresponds to the (100) reflection plane of rGO (Lv *et al.*, 2012).

The thermal characteristics of GO and rGO were studied with TG analysis and is given in Figure 5.6B. As already mentioned in the Chapter 3 and 4, GO is thermally unstable due to the presence of oxygen containing surface functional groups and shows a

three step degradation pattern. But rGO shows relatively good thermal stability due to the absence of functional groups in the rGO surface. A wt loss of 24% is observed till 420 ^{o}C is due to the presence of relatively low amount of surface adsorbed water molecules and surface functional groups than GO. ~31% of wt loss observed in between 420-1000 ^{o}C corresponds to the decomposition of graphitic carbon substrate present in the rGO nanosheets.

The optical property of the rGO nanosheets was studied using UV–vis absorption spectroscopy by dispersing rGO in DMF (Figure 5.6C). From the figure we can see that the maximum absorption peak of rGO is at 267 nm. The band corresponding to the π-π^* transition of aromatic C-C at 230 nm is red shifted to 267 nm after the complete reduction of GO to rGO, reflecting the restoration of electronic conjugation and structural ordering within the carbon framework (Dey *et al*., 2012). Hence, the UV-vis absorption spectra gives clear evidence for the complete reduction of GO to rGO.

The FTIR spectra obtained for GO and rGO are given in the Figure 5.6D. In the FTIR spectra of GO we could see a broad absorption band in between 3000-3400 cm^{-1}, which corresponds to the –OH stretching. This peak is completely vanished in the FTIR spectra of rGO. Similarly, a remarkable decrease in the band intensity was observed in the bands corresponding to the stretching of oxygen containing functionalities such as C=O carbonyl (1720 cm^{-1}), epoxy C-O (1231 cm^{-1}), -OH deformation vibrations (1389 cm^{-1}), alkoxy C-O (1043 cm^{-1}) after the nascent hydrogen reduction of GO (Dey *et al*., 2012).

The probable mechanism for the nascent hydrogen chemical reduction of GO with Zn dust is presented here. Epoxy, carbonyl, and hydroxyl groups are the main oxygen containing functional groups present on the GO surface. In-situ generation of nascent hydrogen is occurred when Zn dust reacts with conc. HCl, which is highly reactive and

acts as a reducing agent for the chemical reduction of GO. Chemical reduction of GO involving the removal of these functional groups and it leads to the restoration of π conjugation in the carbon framework (Pham *et al*., 2012). Both deoxygenation of epoxides through ring opening reaction and decarboxylation of carboxylic acid gives olefins due to the interaction of Zn in acid medium (Dey *et al*., 2012). Carbonyl groups are reduced to the corresponding alcohols, which further gives olefins. The conversion of GO to rGO is indicated by the colour change of the reactant mixture from dark brown to blackish colour and the aggregation of the resultant particles due to the removal of oxygen functionalities (Chua *et al*., 2014). The homogeneous dispersion of GO in water facilitates the intimate contact between Zn dust and acid.

$$\text{Zn dust} + 2 \text{ conc. HCl} \longrightarrow ZnCl_2 + 2[H] \qquad 5.1$$

5.4.4 Characterization of ZnO Nanoparticles Prepared *via* Biotemplate Assisted Method

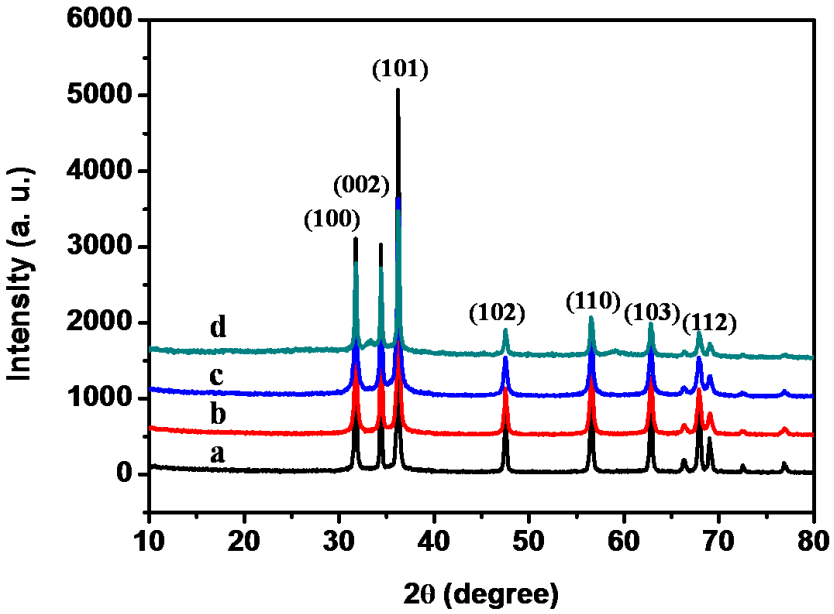

Figure 5.7 (A) XRD patterns of (a) ZD (b) ZS (c) ZSs, and (d) ZC.

Figure 5.7 shows the XRD patterns of pure ZnO particles synthesized with carbohydrates/cellulose. The XRD pattern indicates that all samples are highly crystalline. All of the diffraction peaks of the as prepared ZnO nanoparticles match well with those of the standard XRD file of ZnO (JCPDS standard card no. 79-0205) and can be indexed as the wurtize phase of ZnO. The diffraction peaks at 31.7 ^{o}, 34.57 ^{o}, 36.09 ^{o}, 47.53 ^{o}, 56.67 ^{o}, 62.78 ^{o}, and 67.86 ^{o} are corresponding to (100), (002) (101), (110), (103), and (112) lattice planes of wurtzite ZnO. No other impurity peaks arising due to carbohydrate/cellulose as well as no remarkable shift in all diffraction peaks were detected in the XRD patterns of as prepared samples, which confirms the phase purity of the products. The lattice parameters of the as prepared samples calculated and were given in the Table 5.1. The calculated values of lattice parameters a=b=0.32379-0.32406 nm and c=0.52865-0.5291 nm are consistent with the reported values of ZnO (Pradhan *et al*., 2008). The crystallite size was evaluated using Scherrer formula is presented in Table 5.1. From the Scherrer formula, the crystallite size was estimated to be ~44, 28, 27, and 34 nm, respectively.

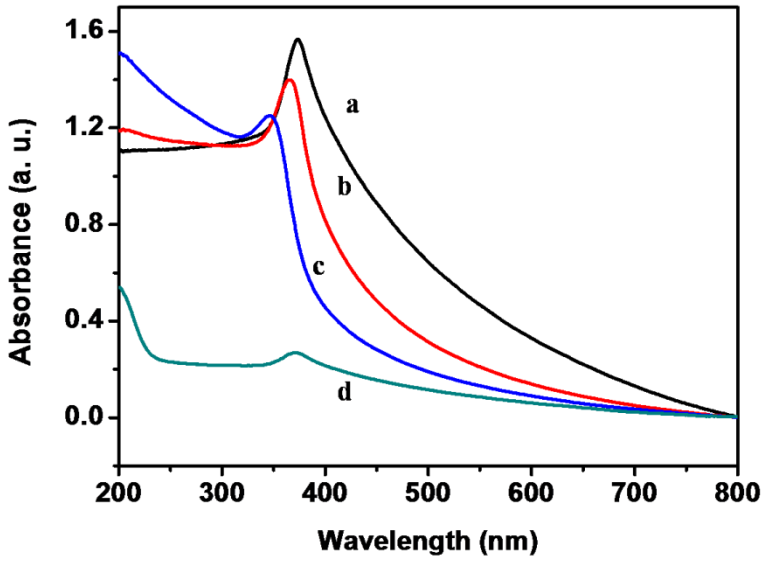

Figure 5.8 UV-vis absorption spectra of (a) ZD (b) ZS (c) ZSs, and (d) ZC.

The optical property of ZnO nanoparticles synthesized with different carbohydrates/cellulose is studied using UV-vis absorption spectroscopy and is given in the Figure 5.8. The maximum absorption peak of ZD is at 372.95 nm. A blue shift in the UV-vis absorption spectra was observed from ZD to ZSs (372.95-344.99 nm). This is mainly due to the crystallite size reduction from 43.99 to 26.62 nm. From ZSs to ZC a red shift was observed from 344.9 to 370.4 nm and is mainly attributed to the increase in the crystallite size from 26.62 to 33.75 nm.

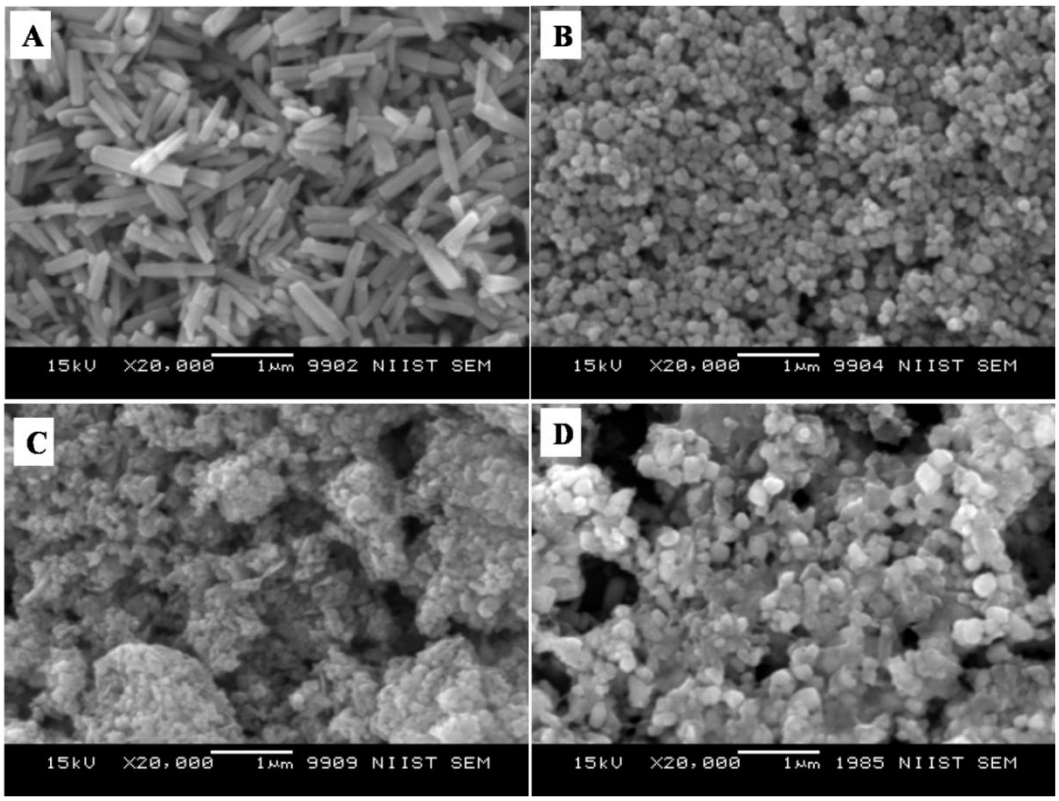

Figure 5.9 SEM images of (A) ZD (B) ZS (C) ZSs, and (D) ZC.

Figure 5.9 displays SEM images of ZnO nanoparticles prepared with different carbohydrates/cellulose. ZnO nanoparticles (ZD) synthesized with dextrose as structure directing agent found to be in rod shape with ~ 800 nm length and ~ 140 nm width (Figure 5.9A). From Figure 5.9B, it can be seen that sucrose leads to the formation of ZnO nanoparticles with diameter ~ 91.5 nm. Synthesized ZnO nanoparticles (ZSs) using soluble

starch as structure directing agent were found to be spherical in shape with lower particle size. But some agglomeration was also observed in this case. Carboxy methyl cellulose leads to the formation of ZnO nanoparticles (ZC) with agglomerates of spherical particles of relatively larger size compared to ZS and ZSs nanoparticles. Similar observations are obtained in the TEM imaging also. The synthesized ZD nanoparticles having rod shape with ~ 800.8 nm length and ~ 140.5 nm diameter. The spherical shape of the ZS nanoparticles are more clearly seen in the TEM image (Figure 5.10B) with a diameter of ~ 109.72 nm. Soluble starch leads to the formation of ZnO nanoparticles (ZSs) with relatively small size of ~ 50 nm. As seen in the SEM image, Figure 5.10C also shows uniform sized agglomerated particles of ZSs nanoparticles. Relatively square shaped particles are observed in the TEM image of ZC with particle size of 188.19 nm (Figure 5.10D)

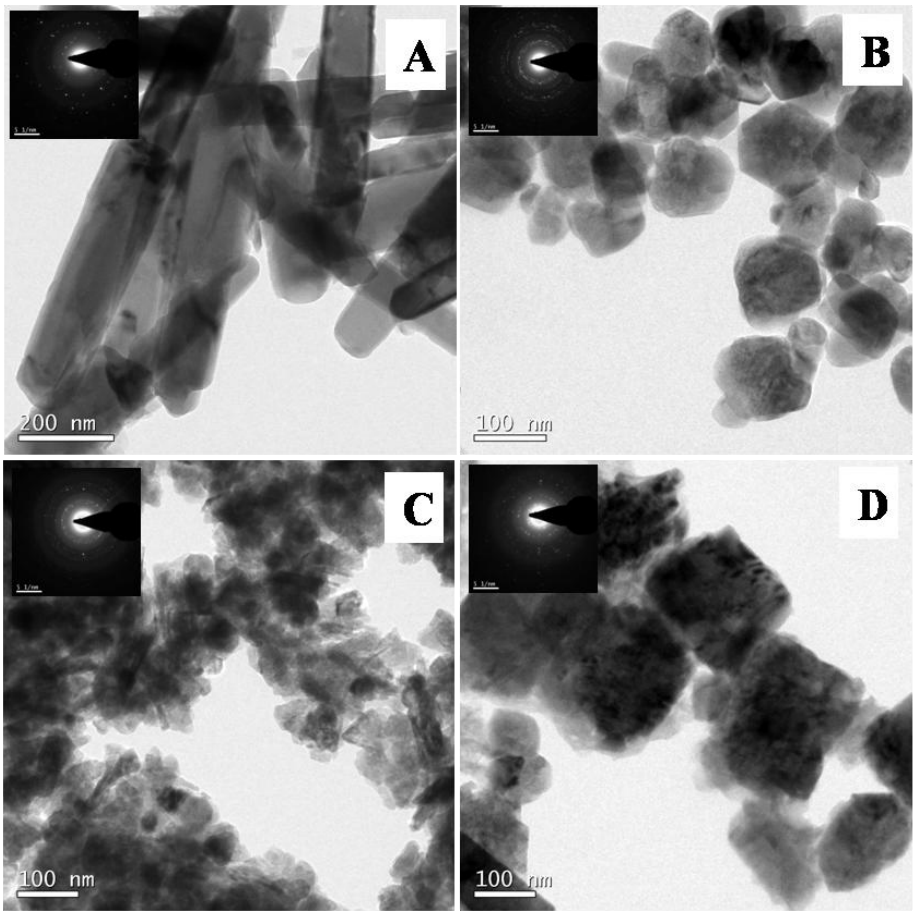

Figure 5.10 TEM images of (A) ZD (B) ZS (C) ZSs, and (D) ZC.

Table 5.1 Crystallite size (D_{XRD}), lattice parameters (a and c), absorption maxima (λ_{max}), morphology of ZnO samples prepared using different carbohydrate/cellulose

Samples	D_{XRD} (nm)	Lattice parameter (nm)			λ_{max}	Morphology	D_{TEM}
		a	c	c/a			
ZD	44	0.32406	0.5291	1.6327	372.95	Rods	L=800.8, W=140.5
ZS	28	0.32385	0.52875	1.6327	367.84	spheres	109.72
ZSs	27	0.32379	0.52865	1.6326	344.9	aggregates	50
ZC	34	0.32386	0.52877	1.6327	370.4	Square	188.19

5.4.5 Characterizations of ZnO@1rGO Nanocomposites

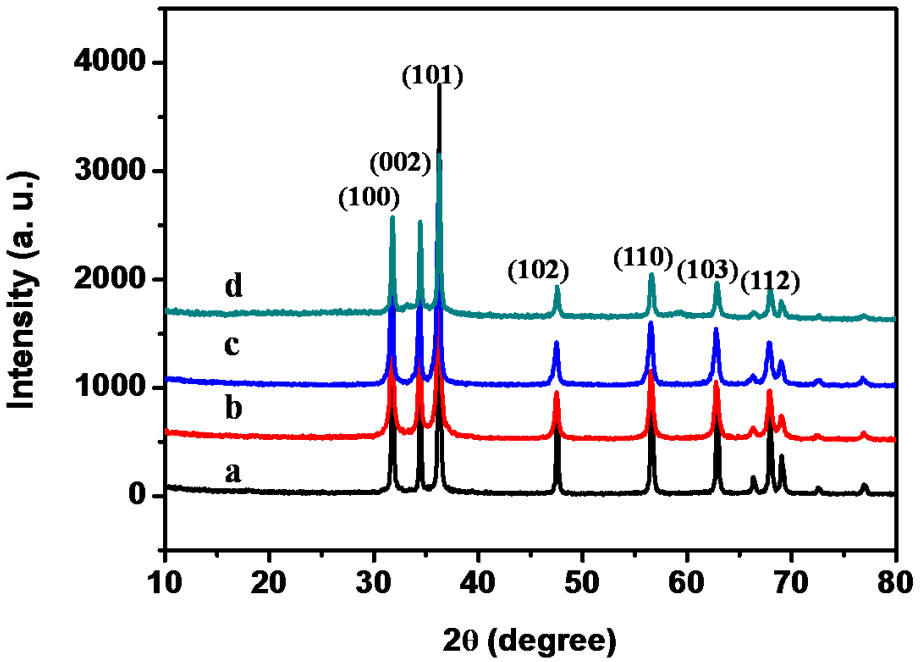

Figure 5.11 XRD patterns of (a) ZD@1rGO (b) ZS@1rGO (c) ZSs@1rGO, and (d) ZC@1rGO.

The XRD analysis of ZnO@1rGO prepared with different carbohydrate/cellulose are presented in the Figure 5.11. All samples show the diffraction patterns of wurtzite ZnO

even in the presence of rGO. The XRD results of all samples shows diffraction peaks at 31.77 ^{o}, 34.31 ^{o}, 36.09 ^{o}, 47.53 ^{o}, 56.67 ^{o}, 62.78 ^{o}, and 67.6 ^{o} corresponding to the lattice planes of (100), (101), (102), (110), (103), and (112). No remarkable shift in the diffraction peaks were observed in the presence of rGO in the nanocomposite. Since the amount of rGO in the nanocomposite is very small, no peaks of rGO were observed in the XRD patterns of nanocomposites. The lattice parameter calculated was listed in the Table 5.2. The lattice parameter values a=0.3232-0.3236 nm and c=0.52765-0.52834 nm are consistent with the reported lattice parameter values of ZnO. The crystallite size evaluated using Scherrer equation is given in the Table 5.2. From this it is clear that lattice parameter and crystallite size of ZnO nanoparticles does not remarkably affected by the presence of rGO in the nanocomposite.

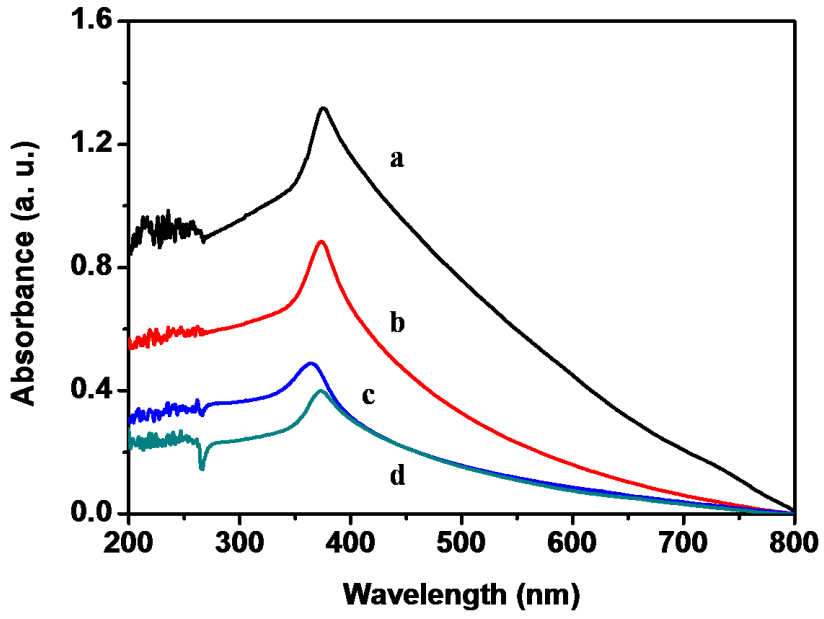

Figure 5.12 UV-vis absorption spectra of (a) ZD@1rGO (b) ZS@1rGO (c) ZSs@1rGO, and (d) ZC@1rGO.

The optical properties of the as prepared ZnO@1rGO nanocomposites were given in the Figure 5.12. We could see a red shift in the absorption spectra of all nanocomposites compared to the spectra of ZnO nanoparticles. The red shift in the λ_{max} values is attributed

to the incorporation of rGO in the nanocomposites and the λ_{max} values were presented in the Table 5.2.

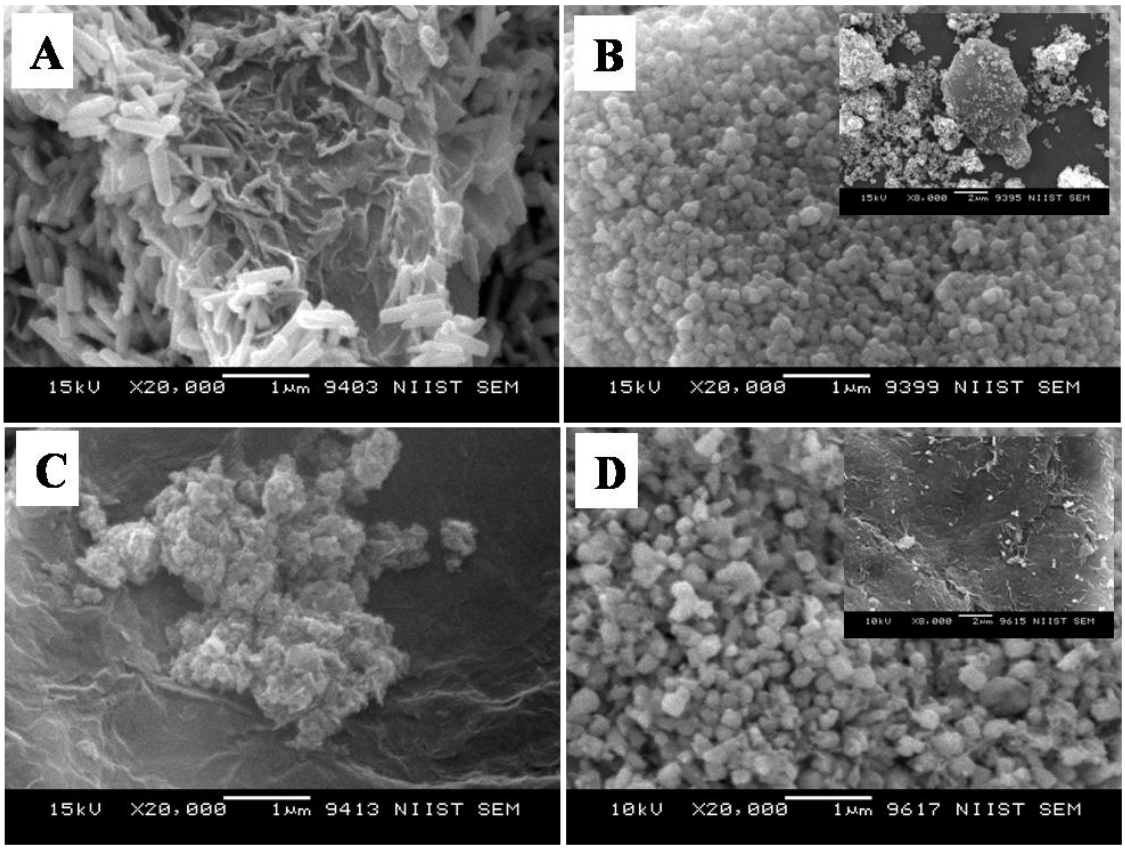

Figure 5.13 SEM images of (A) ZD@1rGO (B) ZS@1rGO (C) ZSs@1rGO, and (D) ZC@1rGO.

Figure 5.13 shows the SEM images of ZnO@1rGO nanocomposites synthesized with different carbohydrate/cellulose. Insets of 5.13B and 5.13D show the SEM images at high resolution. The presence of both rGO nanosheets and ZnO are clearly seen in the SEM images of all samples. It is clear that ZnO particles are deposited on the surface of rGO sheets. The same observations were again found in the TEM images of ZnO@1rGO (Figure 5.14). The SEM and TEM images also say that the morphology of pure ZnO is not altered after the preparation of composite with rGO.

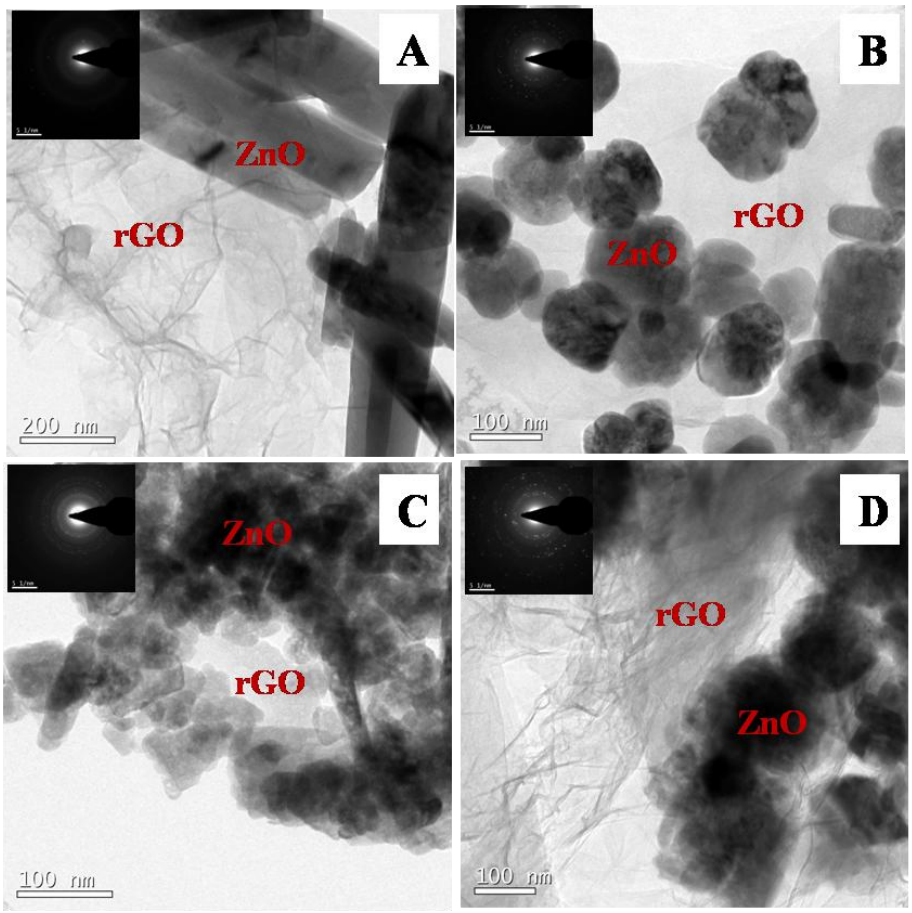

Figure 5.14 TEM images of (A) ZD@1rGO (B) ZS@1rGO (C) ZSs@1rGO, and (D) ZC@1rGO.

Table 5.2 Crystallite size (D_{XRD}), lattice parameters (a and c), absorption maxima (λ_{max}), morphology of ZnO@1rGO samples

Samples	**D_{XRD} (nm)**	**Lattice parameter (nm)**			**λ_{max}**	**Morphology**	**D_{TEM}**
		a	c	c/a			
ZD@1rGO	38	0.3236	0.52834	1.6326	375.77	Rods	L=780, W=140
ZS@1rGO	25	0.3236	0.52829	1.6325	373.71	spheres	102.5
ZSs@1rGO	24	0.3232	0.52765	1.6325	362.75	aggregates	50
ZC@1rGO	30	0.3236	0.52833	1.6326	373.71	Square	187.8

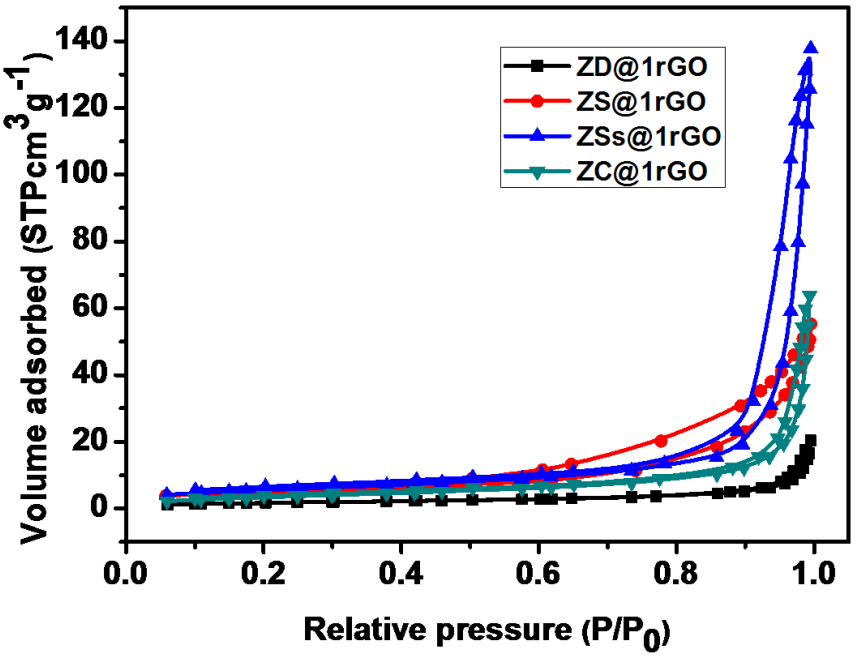

Figure 5.15 N_2 adsorption-desorption isotherms of ZnO@1rGO.

The N_2 adsorption-desorption isotherms of ZnO@1rGO nanocomposites are given in the Figure 5.15. All samples show type IV isotherms. The BET surface areas of ZD@1rGO, ZS@1rGO, ZSs@1rGO, ZC@1rGO are 6, 18, 20, and 13 m^2g^{-1}. Based on the BET surface area analysis, it is clear that higher surface area is obtained for ZSs@1rGO nanocomposite. This was in agreement with the XRD and TEM/SEM results. It is due to the low crystallite size or low particle size shown by the ZSs@1rGO nanocomposite.

The elemental analysis (EDS) spectra of rGO, and ZSs@1rGO are presented in the Figure 5.16. The EDS of rGO (Figure 5.16A) shows the peaks of carbon and oxygen. But the intensity of oxygen is less compared to carbon in rGO. The presence of Zn in the nanocomposite is confirmed by EDS spectrum of ZSs@1rGO. Additional peaks of C and O are also seen in the composite. The elemental mapping of ZSs@1rGO is shown in the Figure 5.17. The presents of elements such as C, O and Zn are well mapped in the images.

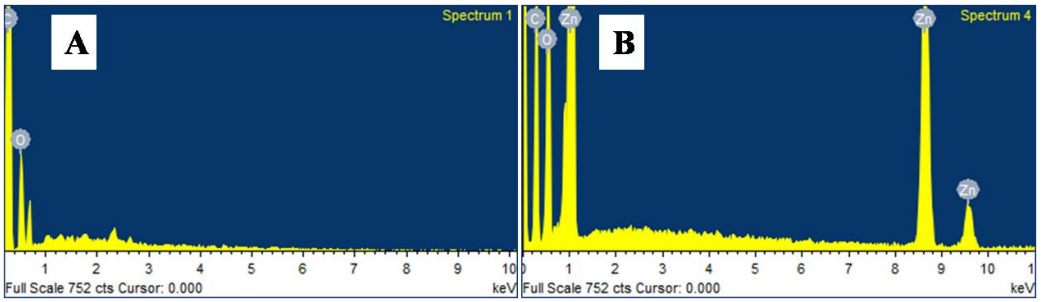

Figure 5.16 EDS spectra of (A) rGO and (B) ZSs@1rGO.

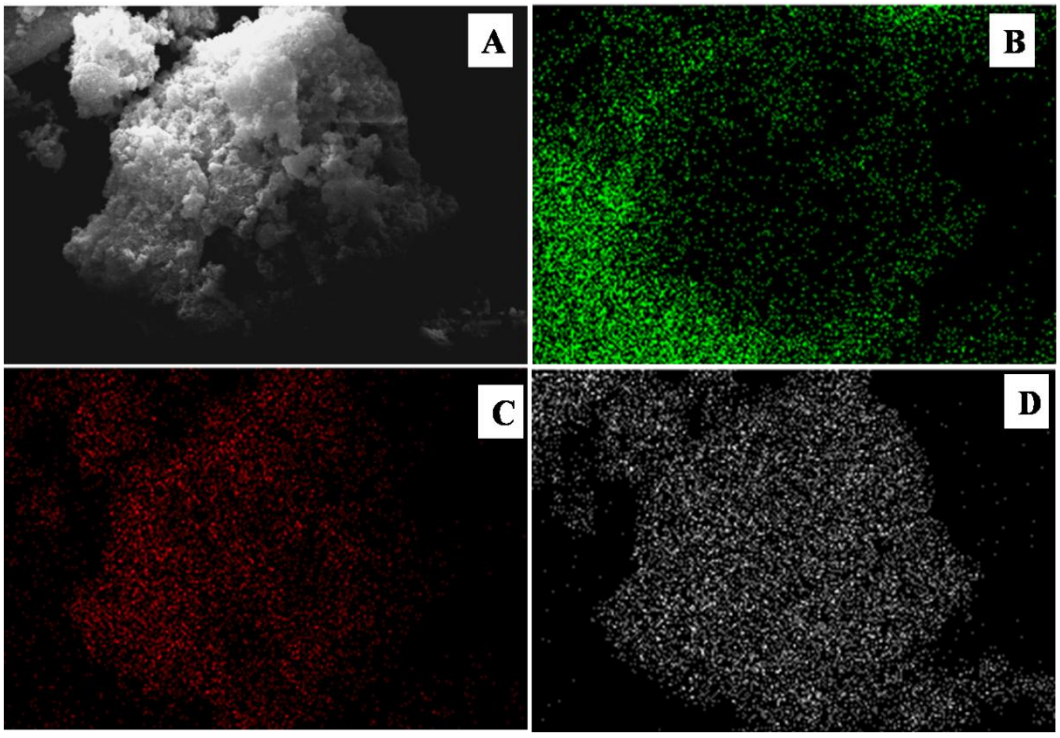

Figure 5.17 Elemental mapping of ZSs@1rGO (A) SEM image of ZSs@1rGO (B) Elemental mapping image for Carbon (C) Elemental mapping image for Oxygen (D) Elemental mapping image for Zinc.

5.4.6 Electrochemical Studies

5.4.6.1 Electrochemical Detection of Urea

The electrochemical behaviour of the ZD modified GCE towards urea detection was studied with cyclic voltammetry (CV). The cyclic voltammograms at a scan rate of 50 mV s^{-1} and potential ranges of -0.8 to 0.8 V at different urea concentrations from 0 to14 μM is given in the Figure 5.18. The improvement in the oxidation/reduction peak current after

the addition of urea into the electrolyte is very evident from the figure. After the addition of 14 μM urea, the oxidation current peak increases from 0.1 mV to 0.15 mV. The cyclic voltammograms of different nanocomposites (ZD@1rGO, ZS@1rGO, ZSs@1rGO, and ZC@1rGO) modified GCEs are given in the Figure 5.19A-D. In all these cases oxidation/reduction peak currents increase with the addition of urea in to the electrolyte. In the case of ZSs@1rGO modified GCE, the oxidation current increases from 0.1 mV to 0.36 mV (Figure 5.19C). The enhancement in the oxidation current was more than double with ZSs@1rGO nanocomposite modified GCE compared to ZD modified GCE. A comparative study of the CV measurements has been carried out using different nanocomposites modified GC electrodes (ZD@1rGO, ZS@1rGO, ZSs@1%rGO, and ZC@1rGO) after the addition of 14 μM urea in to the electrolyte solution and is given in the Figure 5.20. The best performance was exhibited by ZSs@1rGO. The higher electrochemical activity of ZSs@1rGO is due to the lower crystallite size or particle size as well as higher BET surface area of ZSs@1rGO compared to other nanocomposites.

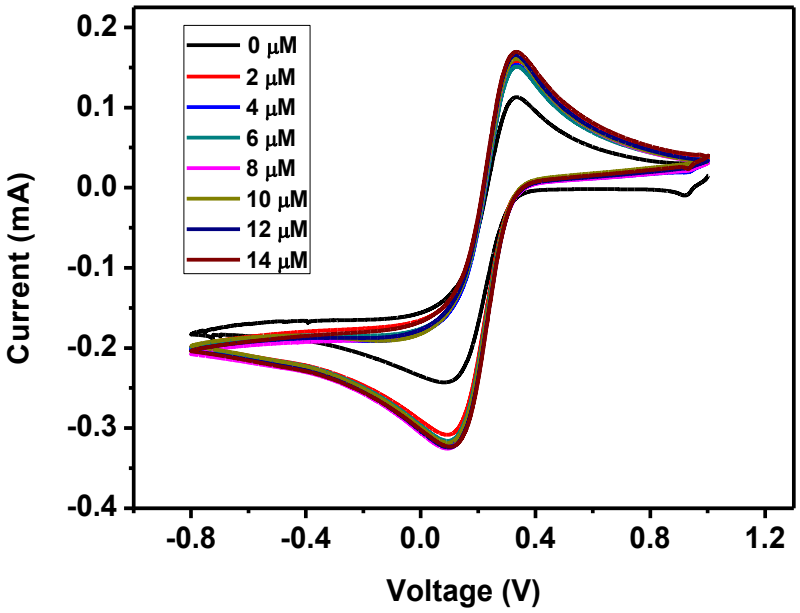

Figure 5.18 CV curves of ZD GCE with various additions of urea from 0 to14 μM.

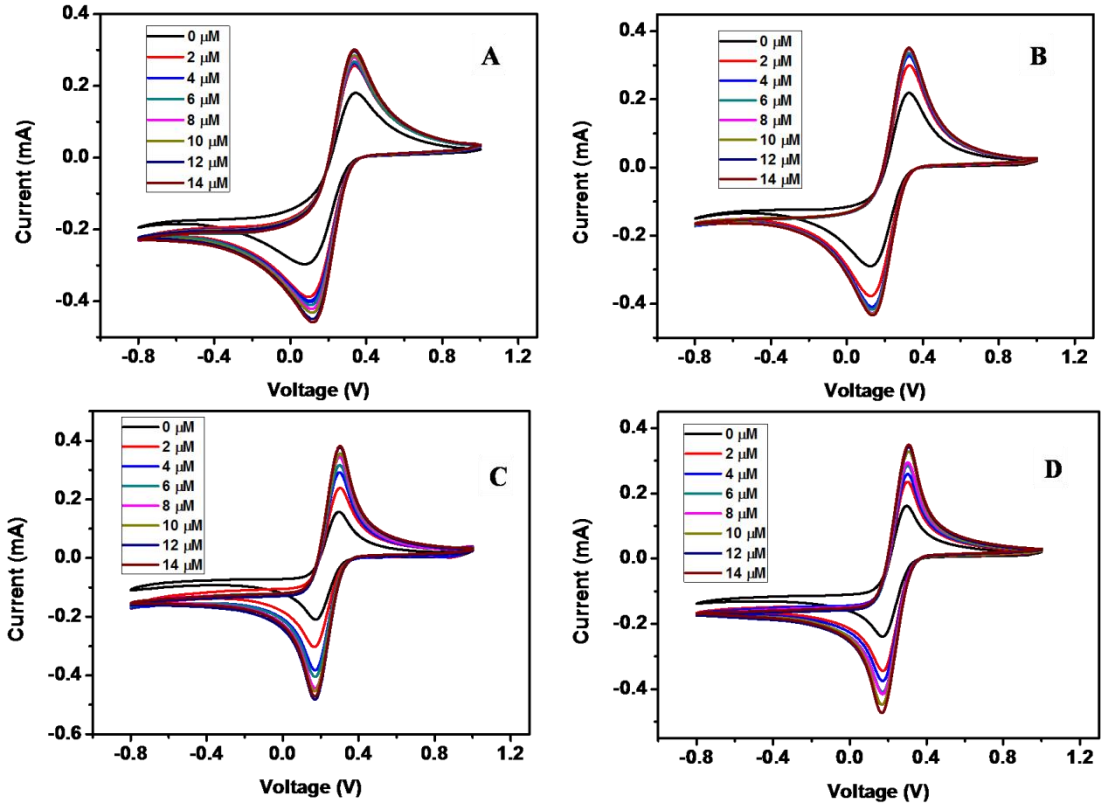

Figure 5.19 CV curves of (A) ZD@1rGO (B) Zs@1rGO (C) ZSs@1rGO, and (D) ZC@1rGO modified GCEs with various concentrations of urea addition from 0 to14 µM.

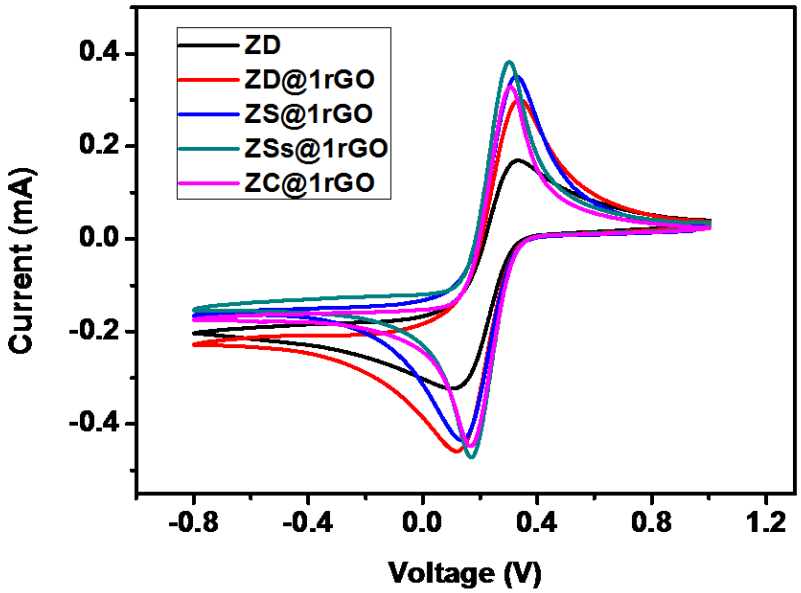

Figure 5.20 CV measurements of ZnO (ZD) and ZnO@1rGO nanocomposites (ZD@1rGO, ZS@1rGO, ZSs@1rGO, and ZC@1rGO) modified GCEs after the addition of 14 µM urea.

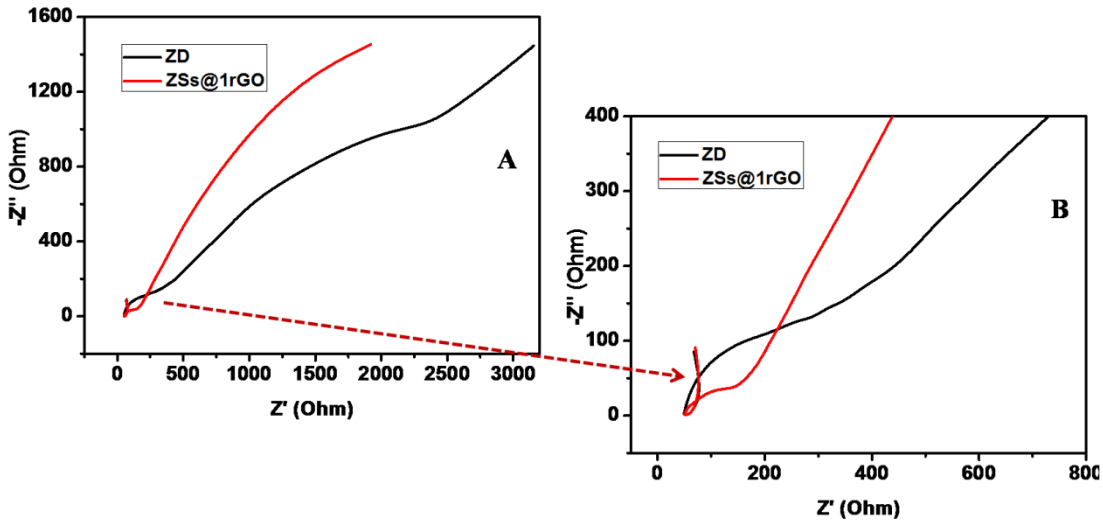

Figure 5.21 (A and B) Nyquist diagram of electrochemical impedance spectra of ZD and ZSs@1rGO modified GCEs in 0.1M $K_3[Fe(CN)_6]$ electrolyte solution.

The Nyquist diagram of the electrochemical impedance spectra (EIS) of ZD and ZSs@1rGO modified GCEs in 0.1M $K_3[Fe(CN)_6]$ electrolyte solution are given in the Figure 5.21. EIS is a commonly used characterization technique to study the impedance changes of the electrode surface mainly due to the electron transfer between electrolyte and electrode surface. Nyquist plot contains a semicircular part and a linear part. The semi-circular or real portion corresponds to the electron transfer limited process and linear or imaginary part corresponds to the diffusion process. The diameter of the semi-circular portion is equivalent to the electron transfer resistance (R_{ct}), which reflects the conductivity and the electron transfer process. Large semicircle with high R_{ct} indicates that the system has higher resistance to the flow of electrons. The ZnO modified GCE showed a higher R_{ct} with a larger semicircle diameter (R_{ct}=169 Ω) indicating that ZnO nanoparticles were successfully immobilized on the GCE surface, which hindered the electron transfer of the electrochemical probe. This hindrance was decreased (Rct=74 Ω) after the incorporation rGO in nanocomposites. The small semicircular diameter of the ZSs@1rGO modified GCE implies it has low resistance towards the electron transfer

process. These results showed the efficiency of ZSs@1rGO modified GCE compared to ZnO modified GCE (Shereema *et al*., 2015; Jiang *et al*., 2017).

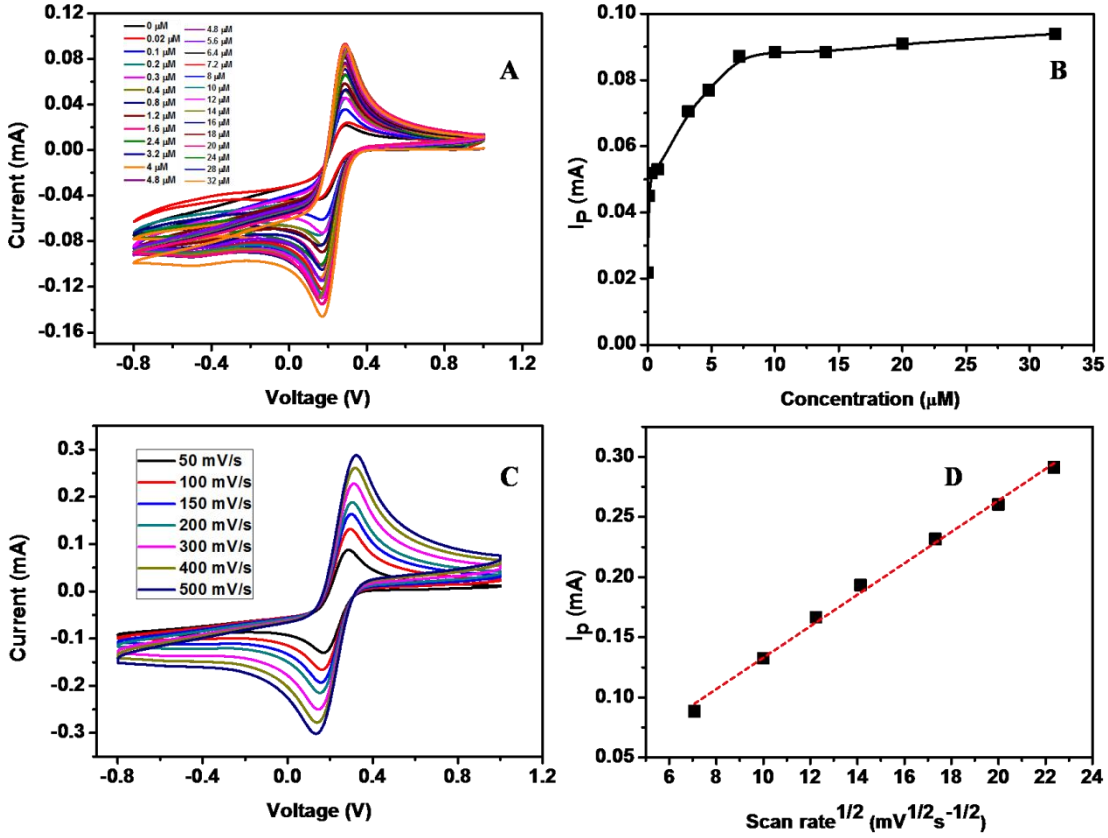

Figure 5.22 (A) Calibration curve of ZSs@1rGO modified electrode towards 4 mM urea (B) Plot of I_P versus concentration (C) Scan rate study using ZSs@1rGO modified electrode with different scan rates (D) Plot of I_p versus square root of scan rate.

The calibration curve has been plotted by the addition of 0.02 μM to 32 μM urea to the electrolyte solution (Figure 5.22A). From the plot of I_P versus concentration of urea given in the Figure 5.22B, the linear range was calculated and is between $0.02x10^{-3}$ to $7.2x10^{-3}$ mM**.** The effect of scan rate for 50, 100, 150, 200, 300, 400, and 500 mVs^{-1} towards the electrochemical oxidation of urea using cyclic voltammetry as determining mode is given in the Figure 5.22C. The oxidation/reduction peak current increases with increasing scan rate. It is evident that the oxidation peak current has a linear dependence upon the square root of scan rate (Figure 5.22D) compared to I_P versus scan rate. It means

that the electrochemical oxidation process is purely diffusion controlled on the surface of ZSs@1rGO modified GCE surface. The lowest detection limit calculated was 0.012 μM and the sensitivity was found to be 682.8 μA mM^{-1} cm^{-2}.

5.4.6.2. Electrochemical Detection of Glucose

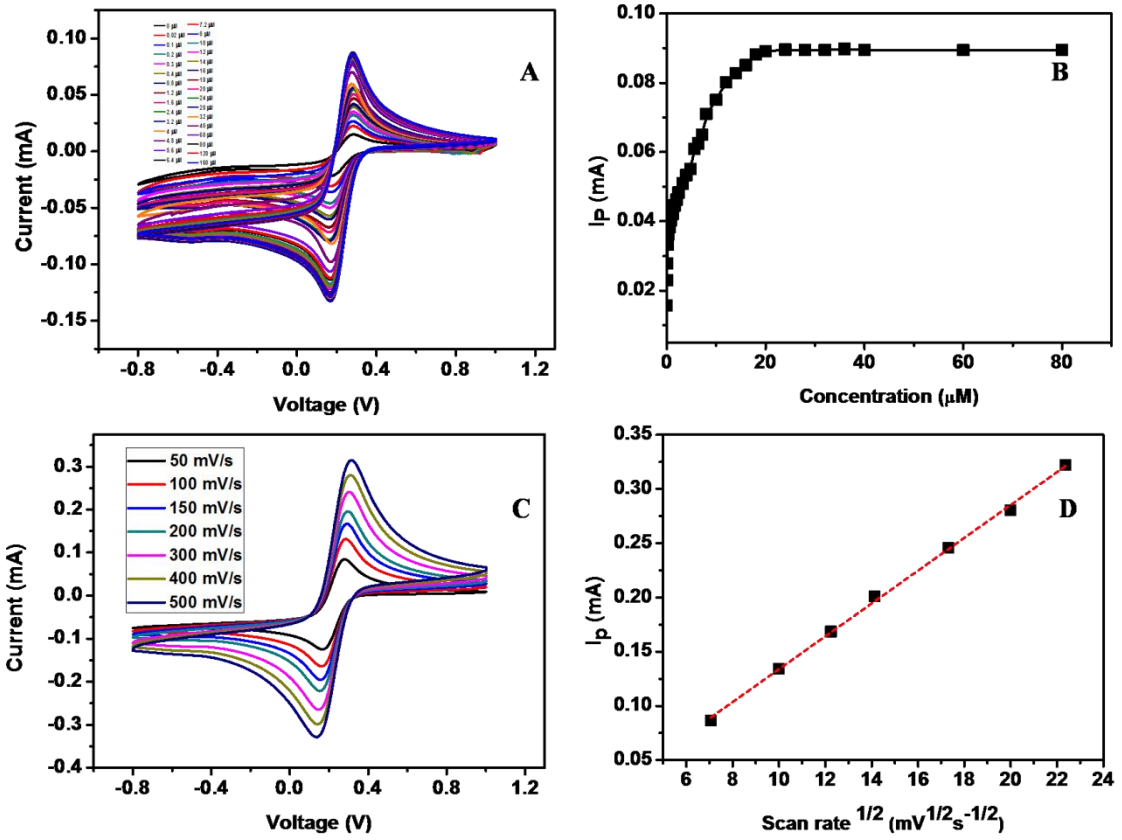

Figure 5.23 (A) Calibration curve of ZSs@1rGO modified electrode towards 4mM glucose (B) Plot of I_P versus concentration (C) Scan rate study using ZSs@1rGO modified electrode with different scan rates (D) Plot of I_P versus square root of scan rate.

The calibration curve has been plotted by the addition of 0.02 μM to 160 μM urea (Figure 5.23A). The I_P was plotted against concentration (Figure 5.23B), and the linear range was calculated ($0.02x10^{-3}$ to $18x10^{-3}$ mM). The effect of scan rate on the electrochemical behavior of ZSs@1rGO modified electrode towards the oxidation of glucose has been conducted using cyclic voltammetry and is given in the Figure 5.23C. From the graph it is clear that the oxidation/reduction peak current increases with increase

in the scan rate from 50-500 mV s^{-1}. A linearity of oxidation peak current (I_p) with square root of scan rates was observed within the scan rate of 50-500 mV s^{-1} (Figure 5.23D). This indicates that the electrochemical oxidation process is purely diffusion controlled. The lowest detection limit calculated was 0.008 μM and the sensitivity was found to be 481 μA mM^{-1} cm^{-2}.

ZnO nanostructures act an efficient electron mediator for the fabrication of efficient non enzymatic sensor. The proposed sensing mechanism for the fabricated urea sensor is described as

$$CO(NH_2)_2 + 8OH^- \longrightarrow 6\,H_2O + CO_3^{2-} + N_2 + e^- \quad 5.2$$

The proposed sensing mechanism for the fabricated glucose sensor is described as

$$O_2\ g\ (\text{air/liquid interface}) \longleftrightarrow O_2 ads\ (ZnO@rGO) \quad 5.3$$

$$O_2 ads\ (ZnO) + 2e^-\ (ZnO@rGO) \longleftrightarrow 2O^-\ ads\ (O^-/O_2^-) \quad 5.4$$

$$\text{Glucose} + O^- \longrightarrow \text{glucono-}\delta\text{-lactone} + 2e^- \quad 5.5$$

$$\text{glucono-}\delta\text{-lacone} \longrightarrow \text{gluconic acid} \quad 5.6$$

Table 5.3 Sensing characteristics of the developed urea and glucose sensors using ZSs@1rGO

Analyte	**Linear range (mM)**	**Lowest detection limit (μM)**	**Sensitivity (μA mM^{-1} cm^{-2})**
Urea	$0.02x10^{-3}$-$7.2x10^{-3}$	0.012	682.8
Glucose	$0.02x10^{-3}$-$18x10^{-3}$	0.008	481

5.5 Conclusions

In the present work, the as-prepared GO was reduced with nascent hydrogen reduction mechanism using metallic zinc obtained as a waste by-product from an industry India. The rGO formed then analysed with XRD, UV-vis, SEM, and TEM. The peak shift from 10.8 to 24.5 ^{o} in the XRD pattern and the red shift in the UV-vis absorption spectra from 230 to 267 nm confirms the complete reduction of GO to rGO. In addition to this, ZnO nano-architectures with various morphologies were prepared using carbohydrate/cellulose as a bio-template. The as-prepared ZnO nanoparticles have been used to decorate rGO sheets, which results in the ZnO@rGO nanocomposite. The SEM/TEM analysis of the as obtained nanocomposite shows the uniform distribution of ZnO nanoparticles on the surface of rGO sheets. Due to the synergistic effect of ZnO and rGO, the prepared ZnO@rGO nanocomposite was found to be an excellent probe for the non enzymatic electrochemical sensing of urea and glucose. The electrochemical studies indicate that the electrode is sensitive to urea in the concentration range of $0.02x10^{-3}$-$7.2x10^{-3}$ mM with a detection limit of 0.012 μM. Similarly the developed electrode is sensitive to glucose in the concentration range of $0.02x10^{-3}$-$18x10^{-3}$ mM with a detection limit of 0.008 μM. The developed sensor exhibited ultra high sensitivity of 682.8 μA mM^{-1} cm^{-2} towards urea and 481 μA mM^{-1} cm^{-2} towards glucose.

CHAPTER 6

Fabrication of Flexible ZnO/Si/GO@Gelatin Nanocomposite Films for Functional Applications

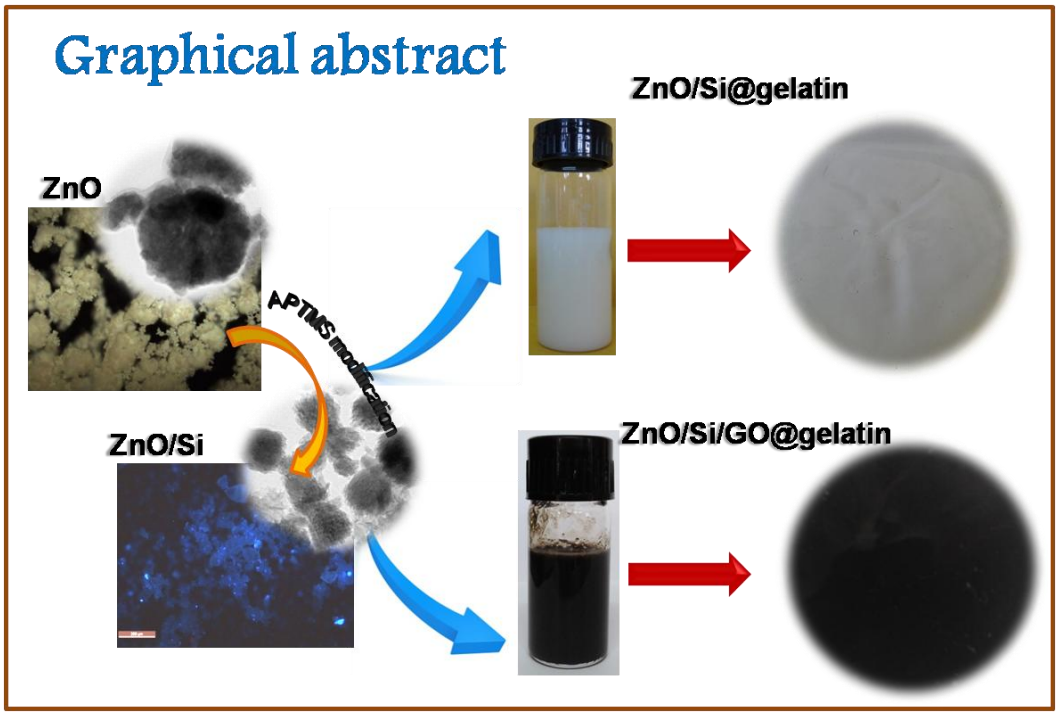

6.1 Abstract

The present study describes the fabrication of ZnO/Si@gelatin and ZnO/Si/GO@gelatin nanocomposite films for functional applications. Here, a facile microwave assisted green synthetic strategy was followed for the in-situ preparation of organosilane modified ZnO nanoarchitectures (ZnO/Si) under aqueous medium. Through this method, mesoporous high surface area ZnO/Si nanoarchitectures with an average crystallite size of 3 nm were successfully prepared in aqueous medium at 80 ^{o}C. An in-situ functionalization with 3-aminopropyl trimethoxy silane (APTMS) resulted in the formation of polysiloxane network and controlled the exaggerated growth of ZnO with a highly stable dispersion in aqueous medium. By APTMS modification we could observe an enhancement in the surface area also *i.e.* from 18 to 80 $m^2 g^{-1}$. A series of flexible and free standing gelatin based bionanocomposite films were fabricated *via* solution casting technique with the addition of ZnO/Si. The incorporation of GO along with ZnO/Si in the gelatin matrix results in the formation of ZnO/Si/GO@gelatin film. APTMS modification found to results in the homogeneous distribution of ZnO in the gelatin matrix which was observed in the SEM images. The water contact angle measurements showed hydrophobic nature of the fabricated bionanocomposite films. The experimental results suggest, ZnO/Si and ZnO/Si/GO has the novel potential as filler in gelatin films for application as functional biomaterials.

6.2 Introduction

Gelatin is a renewable (Spanneberg *et al*., 2012) biopolymeric fibrous protein (Shi *et al*., 2012) derived from the partial hydrolysis of collagen (Kang *et al*., 2010; Cao *et al*., 2007; Griffiths *et al*., 1996) extracted from animal tissues, bones, skin, organs and intestines

(Wisotzki *et al*., 2014). Gelatin is found to be a good candidate for the replacement of the petroleum derived organic polymers (Farris *et al*., 2011). It found wide range of applications in drug delivery, tissue engineering, gene transfection, wound dressing, corneal endothelial cell therapy, food, cosmetics, separation membranes, and photographic industries (Likos *et al*., 2000; Wisotzki *et al*., 2014). The diversified applications of gelatin are govern by its biocompatibility, biodegradability, and commercial availability at low cost (Liu *et al*., 2011). The physical, chemical, and colloidal properties of gelatin able this material to form films. Different functional groups presented in gelatin helps the modification of this biopolymer with nanoparticles. The main drawbacks of gelatin such as hydrophilicity and weak mechanical stability limit its applications (Frydrych *et al*., 2011). The incorporation of nanofillers or crosslinking agents will helps to improve the beneficial properties, but the addition of crosslinking agents can make side effects (Wan *et al*., 2011).

Biopolymeric nanocomposites represent an emerging class of materials obtained from the combination of natural polymers and inorganic nanomaterials (Khadro *et al*., 2014). Since ZnO is a green material with wide range of properties, the incorporation of ZnO can enhance the properties and can tackle its limitations to some extent. An effective surface modification can reduce the aggregation among ZnO nanoparticles and can easily crosslink with the functional groups of gelatin. Surface modification can reduce the energy of the surface, which regulate the growth of particle and consequently controls the crystallite size, morphology, stability and attachment of the functional groups (Tian *et al*., 2012). From the reports it was clear that, organosilanes are interesting candidate than any other modifying agents such as phosphonic acids or carboxylic acids for the surface modification of ZnO nanoparticles. The acidic protons produced from such modifying agents can etch the surface of ZnO

nanoparticles during the modification process, which can be avoided with silane modification (Montagnaro *et al*., 2009). The main advantage of the organosilane is that, the polysiloxane network formed during the hydrolysis and condensation process can act as an effective coverage to protect the ZnO nanocrystals and again enables the anchoring of different functional groups (Karaqozoqlu *et al*., 2007).

To best of our knowledge, most of the in-situ modifications of ZnO nanoparticles were carried out *via* non-aqueous method. Here in, we report a microwave assisted aqueous synthesis of ZnO/Si nanoarchitectures *via* in-situ surface modification strategy. In this work, we have systematically studied the physico-chemical properties of ZnO/Si nanoarchitectures obtained *via* in-situ APTMS modification and its effect on the crystallite size, morphology, zeta potential and surface area. Even though, bionanocomposites based on metal oxides received much attention in the recent years, there are limited literatures on ZnO according to the open literature. In the present work, the fabrication of a freestanding, flexible and hydrophobic ZnO/Si decorated gelatin film has been carried out without using glutaraldehyde cross-linking agent. Similarly, the addition of GO along with ZnO/Si results in the improvement in the viscosity. The surface topological studies showed that, ZnO/Si as well as ZnO/Si/GO was homogeneously embedded in the gelatin matrix. The material can be used in pharmaceutical, food packaging, and as functional biomaterial.

6.3 Experimental

6.3.1 Materials

The precursor used for the preparation of ZnO was **Z**inc nitrate hexahydrate ($Zn(NO_3)_2.6H_2O$, 99%) and was purchased from Merk chemicals, India. 3-Aminopropyl trimethoxy silane

(APTMS, 97%) was procured from Sigma Aldrich, Germany. Lithium hydroxide (LiOH, 99%) was obtained from Sisco Research Laboratory, India. Bacto gelatin purified (>95%) was procured from S. D. Fine Chemicals Limited, India. All the chemicals were used without further purification. Aqueous solutions were prepared with double distilled water.

6.3.2 Microwave Assisted Synthesis of Nano ZnO

Initially, a 0.07 M $Zn(NO_3)_2.6H_2O$ solution was prepared. The pH was adjusted to ~ 8.5 by drop wise addition of 10 wt % LiOH. The reactant mixture was magnetically stirred at ice cold condition for 30 min and subsequently ultrasonicated for 10 min in order to obtain agglomerate free homogeneous zinc hydroxide precipitate. It was then transferred into a 100 mL R. B. flask. The reflux reaction for the nucleation and growth of nanocrystalline ZnO was carried out using a microprocessor based variable power microwave synthesis work station [Sineo, MAS II] operating at a frequency of 2.45 GHz and a microwave power range of 0 - 1000 W. The instrument is equipped with a non-contacting infrared temperature detector which can control the temperature from room temperature to 300 ^oC, with an accuracy of ±1 ^oC. The R. B. flask was kept inside the cavity and the reflux temperature was set at 80 ^oC. Microwave energy was generated at a power of 300 W and was used to raise the temperature to 80 ^oC via dielectric heating. Once the temperature was reached, the reflux reaction was maintained for 30 min and then the experiment was stopped. After cooling, the end product was separated by centrifugation, washed with distilled water for multiple times and subsequently dried at 80 ^oC.

6.3.3 In-situ Synthesis of APTMS Modified ZnO/Si Nanoarchitectures

In order to prepare size controlled ZnO/Si nanoarchitectures, in-situ addition of APTMS was employed at the initial stage itself along with 0.07 M $Zn(NO_3)_2$ $.6H_2O$ precursor solution maintained at ice cold temperature. After stirring for 30 min, the pH was adjusted to ~ 8.5 with the addition of LiOH. APTMS/ZnO molar ratios were maintained as 0.15, 0.2, 0.3, and 0.4. The reactant mixture was transferred into microwave synthesis work station and then refluxed at identical conditions mentioned above. The obtained APTMS modified ZnO/Si nanoarchitectures (represented as ZnO/Si 0.15, ZnO/Si 0.2, ZnO/Si 0.3 and ZnO/Si 0.4) were centrifuged and washed with distilled water and then dried at 80 ^oC. The schematic illustration for the preparation of ZnO and ZnO/Si nanoarchitectures are shown in Figure 6.1.

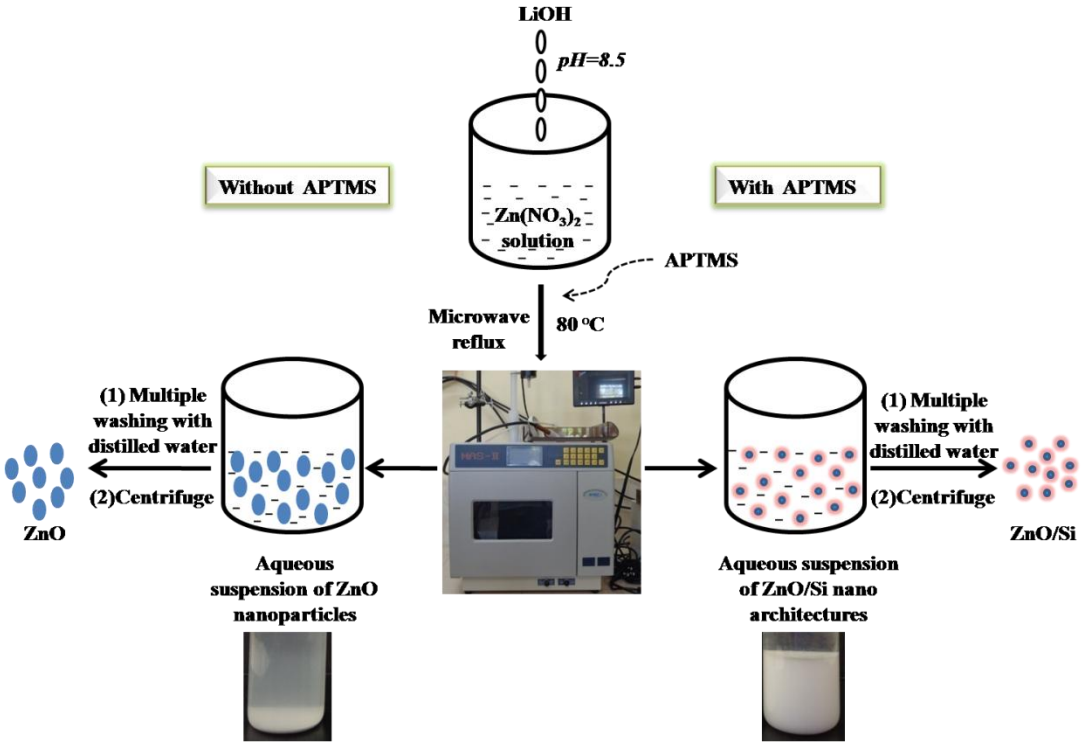

Figure 6.1 Schematic illustration for the preparation of ZnO and APTMS modified ZnO/Si nanoarchitectures.

6.3.4 Synthesis of GO

GO nanosheets were synthesized *via* the modified Hummer's method using the detailed procedure provided in the chapter 3 and 4.

6.3.5 Fabrication of ZnO/Si and ZnO/Si/GO Decorated Gelatin Bionanocomposite Films *via* a One-pot Route

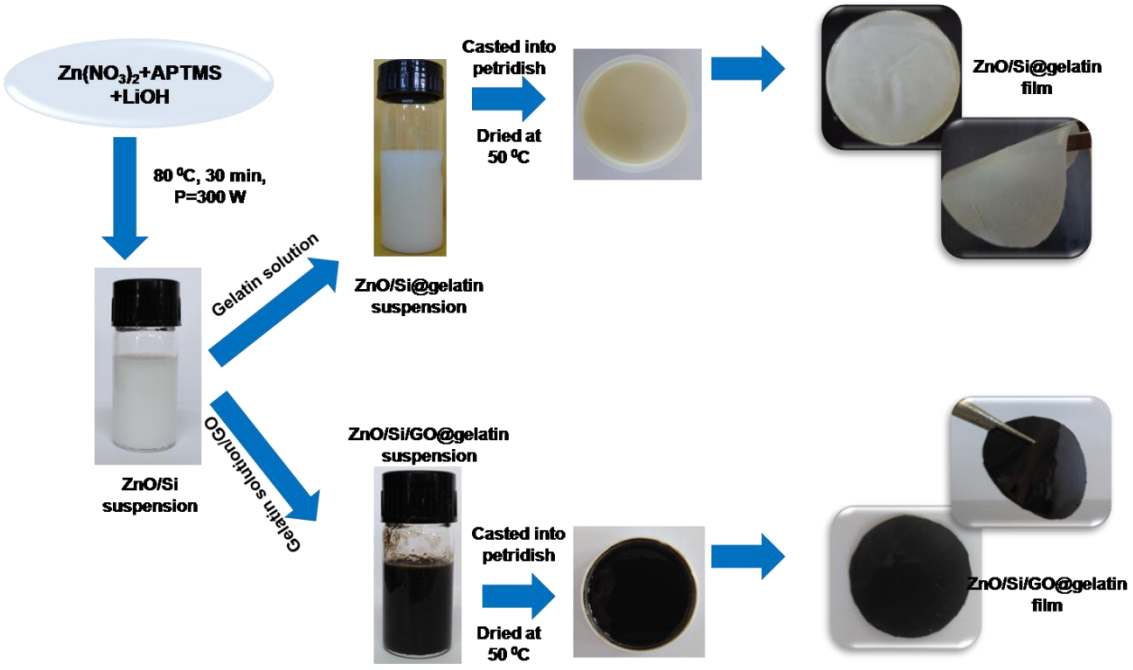

Figure 6.2 Illustration of the synthetic route to fabricate ZnO/Si and ZnO/Si/GO decorated gelatin bionanocomposite films.

In-situ synthesis of ZnO/Si (ZnO/Si 0.3) has been carried out *via* microwave assisted method. The obtained white colored colloidal suspension containing ZnO/Si then homogeneously dispersed in 4 wt % gelatin solution under magnetic stirring. The obtained yellow colored homogeneous suspension of ZnO/Si dispersed gelatin bionanocomposite then transferred to a polystyrene petridish and dried in an oven at 50 ^{o}C. After drying, the film peeled off from the petridish and characterization studies have been carried out. Same procedure has been

followed for the fabrication of 0.1, 0.2, and 0.4, wt. % ZnO/Si decorated gelatin bionanocomposite films. The addition of 0.2 wt % GO in the mixture resulted in the formation of ZnO/Si/GO decorated bionanocomposite films. The schematic illustration for the preparation of ZnO/Si and ZnO/Si/GO decorated gelatin bionanocomposite films was given in the Figure 6.2.

6.4 Results and Discussion

6.4.1 Aqueous Synthesis of APTMS Modified Mesoporous ZnO *via* Microwave Assisted Route

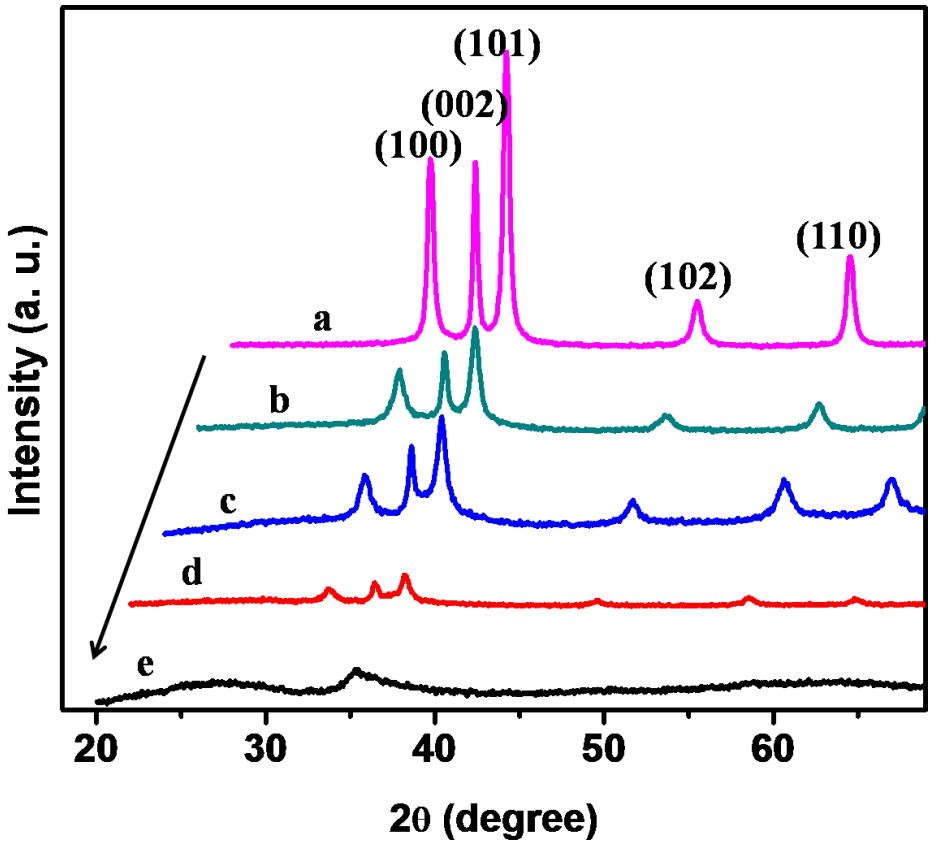

Figure 6.3 XRD patterns of ZnO/Si nanoarchitectures (a) ZnO without APTMS treatment (b) APTMS/ZnO molar ratio 0.15 (c) 0.2 (d) 0.3 and (e) 0.4.

XRD patterns presented in Figure 6.3 explain the effect of APTMS on the crystalline nature of ZnO. The growth of fully crystalline, hexagonal wurtzite ZnO was observed within 30 min under microwave reflux conditions at a reaction temperature of 80 ^{o}C. The diffraction pattern in Figure 6.1a corresponds to ZnO without APTMS modification. All the diffraction peaks can be well indexed to the (100), (002), (101), (102) and (110) crystalline planes at the diffraction angles (2θ) 31.6, 34.4, 36.1, 47.5 and 56.5 ^{o} respectively. It is in good agreement with the standard hexagonal crystalline ZnO given in the JCPDS No. 79-0205. The in-situ addition of APTMS strongly affected the crystallinity of ZnO as observed from the intensity decrease of ZnO/Si nanoarchitectures in Figure 6.3 (b, c, d and e) along the crystalline planes (100), (002) and (101). The decreasing trend was in the order of increasing APTMS/ZnO molar ratio. At maximum APTMS/ZnO molar ratio (ZnO/Si 0.4), the (100) and (002) crystalline planes have completely disappeared indicating the strong interaction of APTMS presumably forming a thick cover on the surface of the grown ZnO crystal. The effective coverage of APTMS on ZnO is clearly seen from the average crystallite size values determined using Debye-Scherrer equation. ZnO has the crystallite size of 17.34 nm which decreased to ~ 3 nm on reaching the APTMS/ZnO molar ratio of 0.4. From the earlier reports, APTMS was found to be an effective capping agent for obtaining quantum size ZnO nanocrystals of the range 4-6 nm (Shi *et al*., 2011). In this work, the in-situ silanization gives capping effect by forming a polysiloxane network which hinders the accelerated growth of ZnO crystals which finally resulting in ZnO/Si nanoarchitectures. Microwave refluxing and in-situ silanization helps in yielding small size and shape controlled ZnO/Si nanoarchitectures in bulk within a short span of time. The presence of APTMS also gives an additional advantage of stable dispersion of ZnO/Si nanoarchitectures in aqueous medium. From the XRD data, the lattice constants

a=0.32 nm and c=0.52 nm were also computed for the ZnO and for ZnO/Si nanoarchitectures, the values marginally changed to a=0.33 nm and c=0.54 nm. These lattice constants confirm with the theoretical values of hexagonal wurtzite ZnO (Preetam *et al*., 2008).

The SEM images of ZnO prepared without APTMS and ZnO/Si nanoarchitectures prepared in the presence of APTMS were given in the Figure 6.4. It displays that pure ZnO prepared without APMTS was made up of aggregates of small spherical particles of ZnO with a particle size of ~200-300 nm. This morphological behaviour is almost same for APTMS modified ZnO with APTMS/ZnO ratio 0.15. But for ZnO/Si 0.2 onwards we could see a little change in the morphology and the siliceous coverage is more and more found in ZnO/Si 0.3 and 0.4. This will result in the encapsulation of nano sized ZnO particles in the siloxane coverage and leads to the formation of large aggregated particles. So these morphological changes confirm silane modification on ZnO particles.

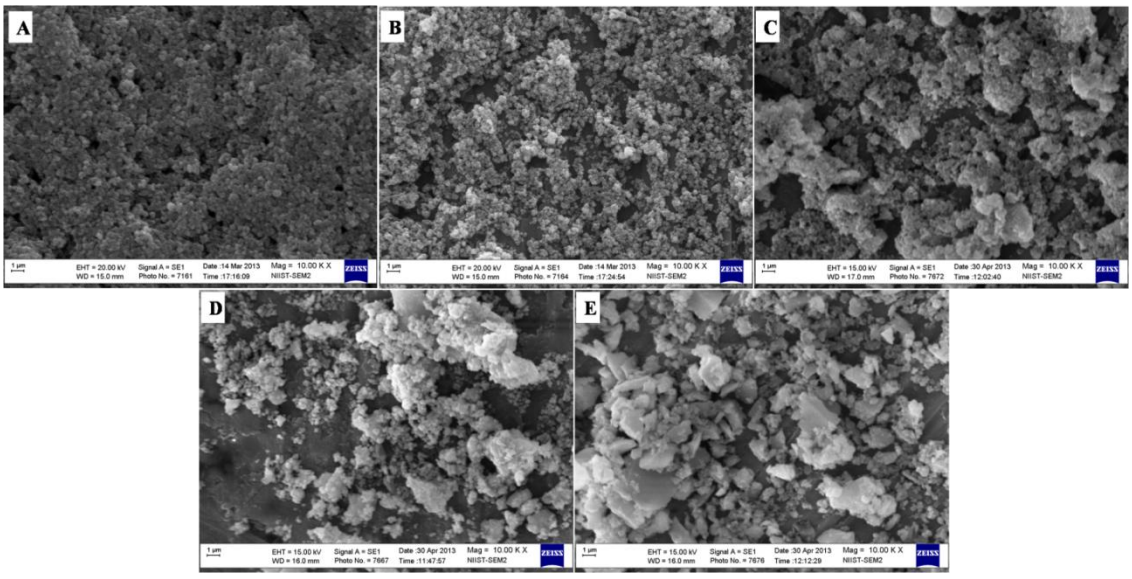

Figure 6.4 SEM images of (a) ZnO without APTMS treatment (b) ZnO/Si nanoarchitectures with APTMS/ZnO molar ratios 0.15 (c) 0.2 (d) 0.3, and (e) 0.4.

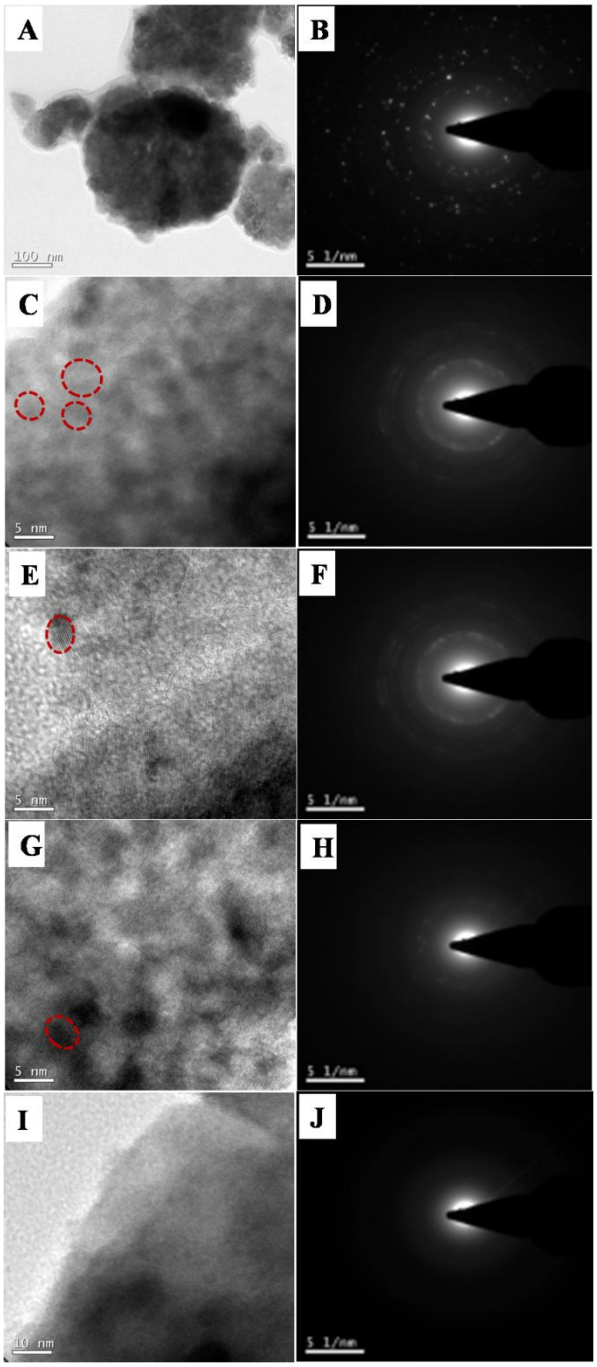

Figure 6.5 TEM images of (A) ZnO and ZnO/Si nanoarchitectures with APTMS/ZnO molar ratios (C) 0.15 (E) 0.2 (G) 0.3, and (I) 0.4, (B, D, F, H, J) corresponding SAED patterns.

TEM images along with the respective SAED patterns of ZnO prepared without APTMS and ZnO prepared in presence of APTMS having APTMS/ZnO molar ratios 0.15, 0.2, 0.3 and 0.4 were presented in the Figure 6.5. The TEM image and corresponding SAED

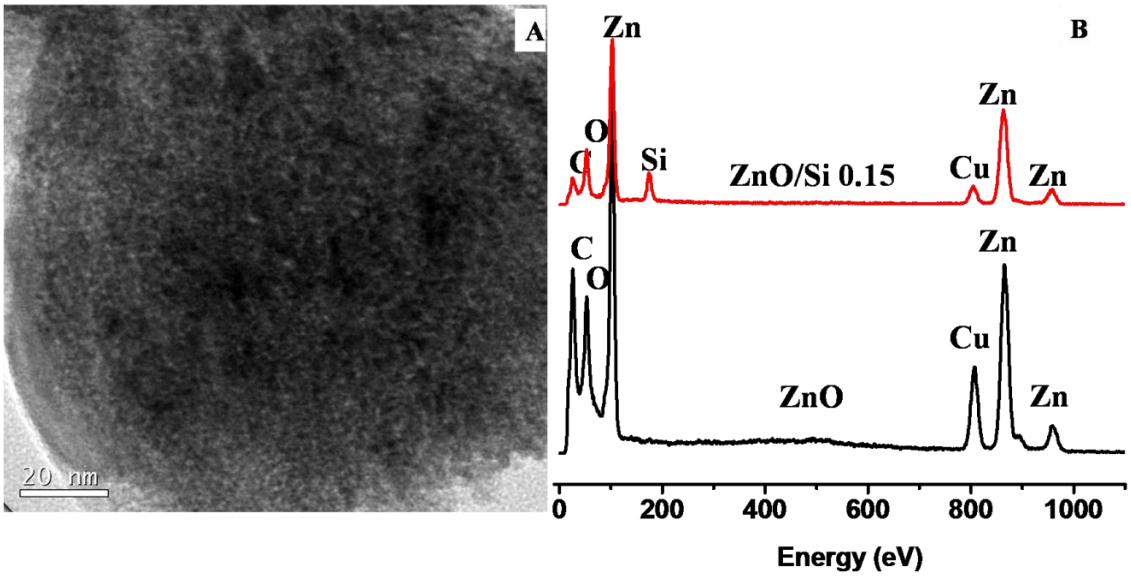

Figure 6.6 (A) HRTEM image of ZnO/Si 0.15, (B) EDS analysis of ZnO and ZnO/Si 0.15.

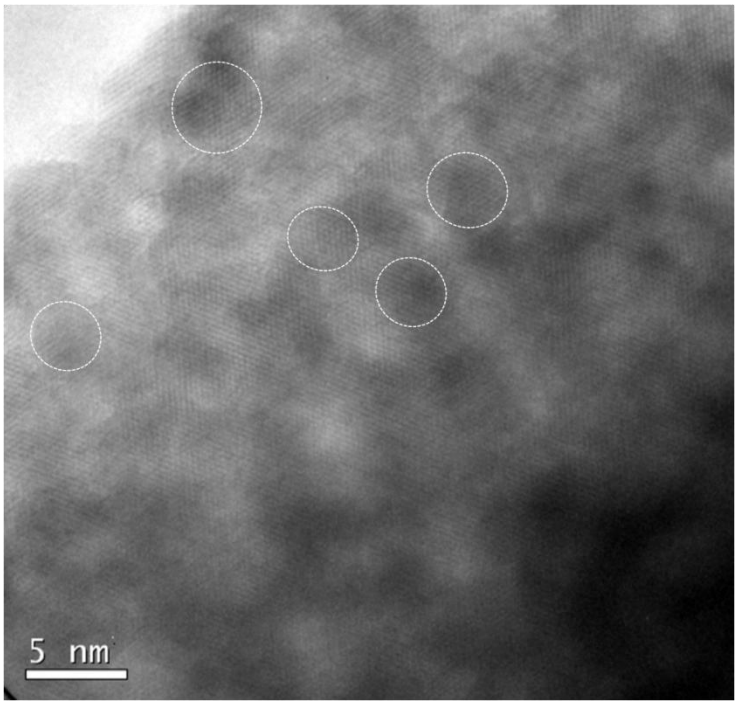

Figure 6.7 HRTEM image of ZnO/Si 0.15.

pattern of ZnO (Figure 6.5A and 6.5B) confirm that the sample is highly crystalline but appears as agglomerate of size ~ 200 nm. It again matches with information obtained from the

SEM images. The TEM images of ZnO/Si nanoarchitectures with APTMS/ZnO molar ratios 0.15, 0.2, 0.3 and 0.4 in Figure 6.5C, 6.5E, 6.5G, and 6.5I shows the growth of ZnO crystallites dispersed in a porous matrix confirming the formation of polysiloxane network. These results matches with the results obtained from the SEM images.

The HRTEM image of ZnO/Si is given in the Figure 6.6A. The EDS spectra of pure ZnO and that of ZnO/Si 0.15 are shown in the Figure 6.6B. The EDS in Figure 6.6B of ZnO sample contains the stochiometric amount of Zn and O. However, ZnO/Si 0.15 shows the presence of Si along with the major phases of Zn and O. The reduced crystallite size of ZnO having ~ 5 nm is clearly seen in the HRTEM shown in the Figure 6.7.

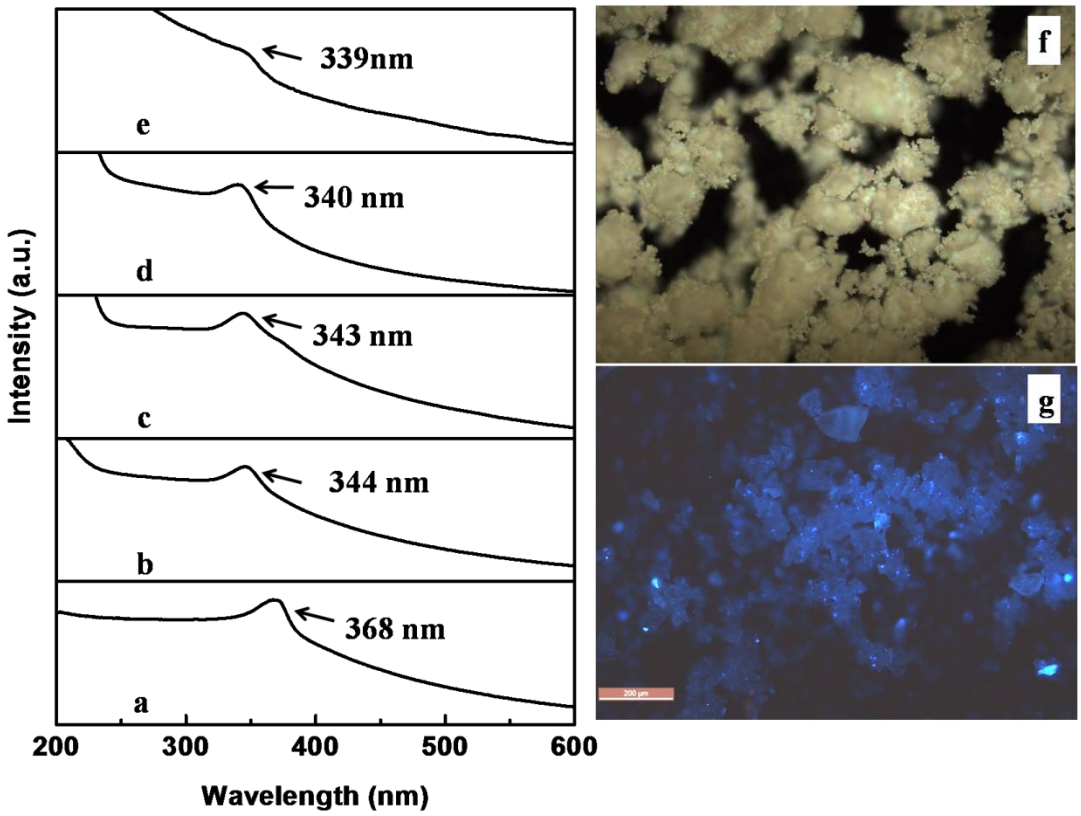

Figure 6.8 (a)-(e) UV-Vis absorption spectra of ZnO and ZnO/Si nanoarchitectures with APTMS/ZnO molar ratios 0.15, 0.2, 0.3, and 0.4. The fluorescent images of (f) ZnO and (g) ZnO/Si 0.4.

UV-Vis absorption spectra of ZnO and ZnO/Si nanoarchitectures with different APTMS/ZnO molar ratios (0.15, 0.2, 0.3 and 0.4) are shown in Figure 6.8 (a, b, c, d and e). In microwave refluxed ZnO, the maximum excitonic absorption peak was observed at 368 nm. In case of ZnO/Si nanoarchitectures, a strong blue shift was observed. Similar to ZnO, ZnO/Si nanoarchitectures have also showed good UV absorption property. The blue shift in UV analysis again confirms the capping effect of APTMS as seen in the XRD and TEM. The band gap energy of ZnO is found to increase from 2.91 to 3.34 eV with respect to APTMS concentration. This blue shift in ZnO/Si nanoarchitectures after APTMS modification is also confirmed from the fluorescent images (Figure 6.8f and 6.8g).

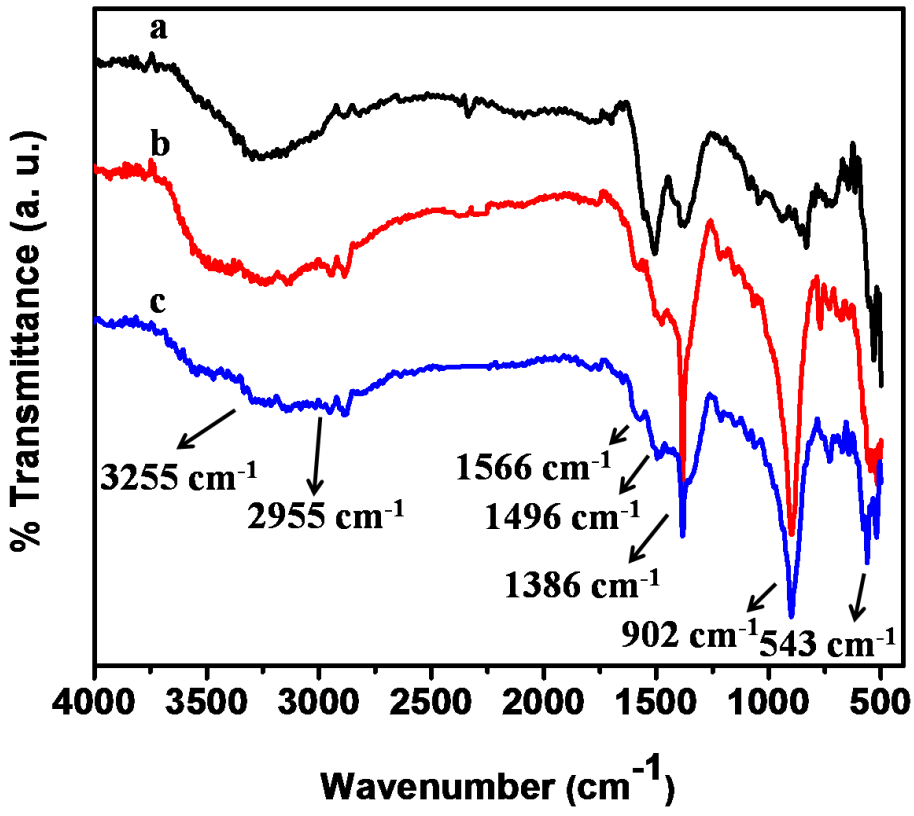

Figure 6.9 FTIR Spectra of ZnO with and without APTMS modification (a) ZnO (b) ZnO/Si 0.3, and (c) ZnO/Si 0.4.

The FTIR spectra for ZnO and ZnO/Si 0.3 and 0.4 are shown in the Figure 6.9. The band located at 543 cm^{-1} is assigned to the stretching vibration of Zn-O bond. The stretching vibration of surface hydroxyl groups (-OH) as well as the moisture adsorbed on the surface of ZnO were confirmed by the broad absorption band at 3255 cm^{-1} (Prabhakar *et al*., 2013). In ZnO/Si, the asymmetric stretching vibrations of the C - H bond were observed at 2955 cm^{-1} (Guo *et al*., 2009). The absorption band at 1386 and 1496 cm^{-1} correspond to the characteristic peaks of $–CH_2$ present in APTMS. The peak appeared at 1566 cm^{-1} is due to the symmetric bending modes of ammonium species [$-NH_3^+$]. Furthermore, the peak corresponding to Zn-O-Si bond was observed around 902 cm^{-1} indicating the condensation reaction between ZnO and silanol groups (Xu *et al*., 2010).

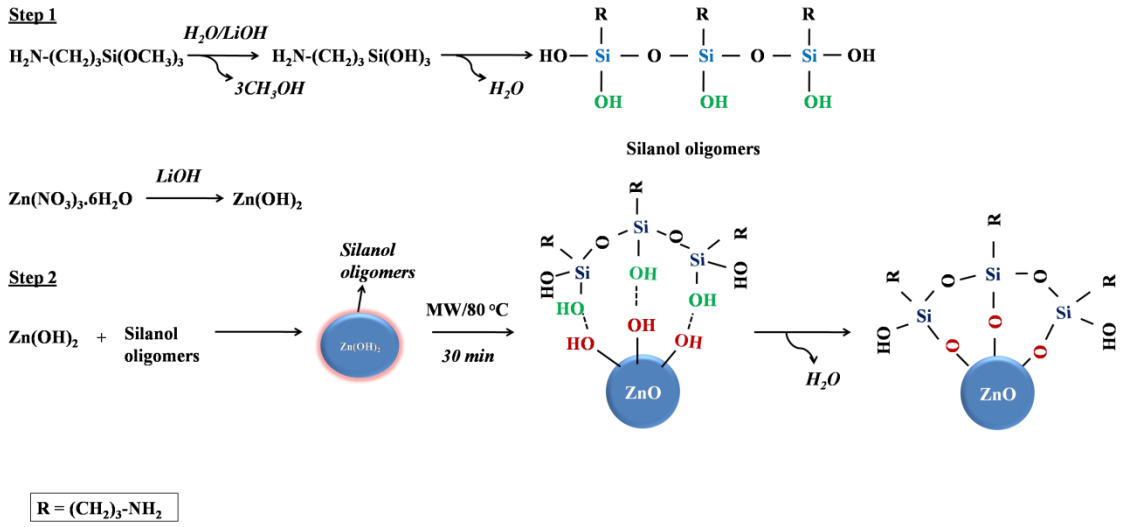

Figure 6.10 Schematic illustration for the chemical modification of APTMS on the surface of ZnO.

The possible mechanism for the in-situ formation of ZnO/Si nanoarchitectures is illustrated in Figure 6.10. APTMS is chemically basic in nature and in aqueous medium the alkoxy groups undergo hydrolysis to produce silanol groups. Upon partial condensation, silanol oligomers are formed and simultaneous co-hydrolysis of zinc precursor form hydroxyl

zinc oxide ($Zn(OH)_2$). Then silanol oligomers readily interact with $Zn(OH)_2$ nuclei and change the bulk dielectric nature of silanized $Zn(OH)_2$ intermediates. This changes the bulk polarization and growth of ZnO. However, when the $Zn(OH)_2$ transforms to ZnO during microwave heating, the surface hydroxyl groups in ZnO get hydrogen bonded with the polymeric siloxane *via* Zn-O-Si bonds. This restricts the growth of ZnO crystals ultimately resulting in crystalline ZnO/Si nanoarchitectures. The formation of polysiloxane network on the surface of ZnO/Si by the presence of excessive APTMS can be understood from the FTIR spectra.

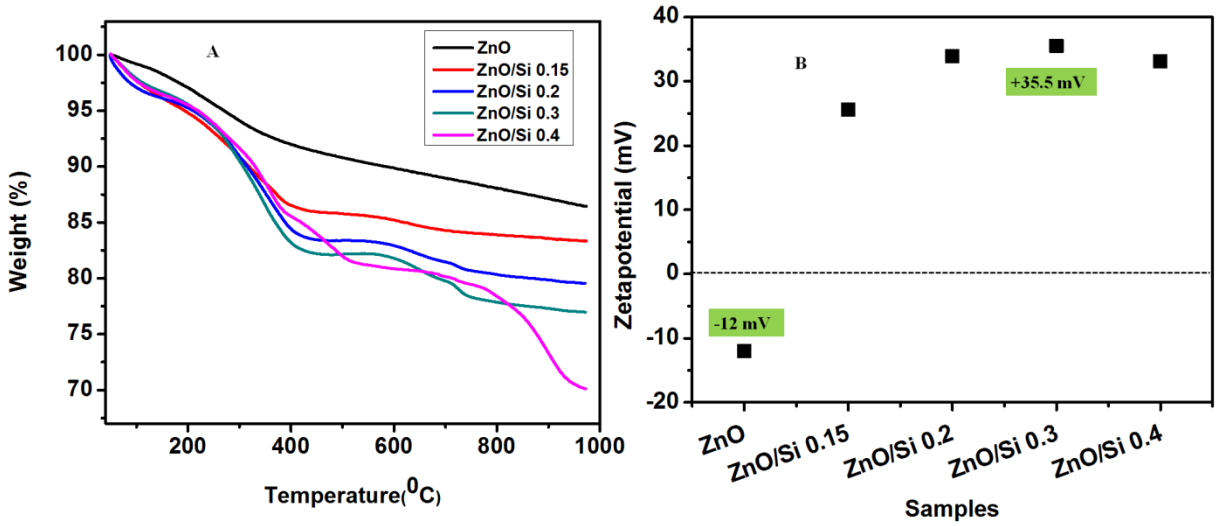

Figure 6.11 (A) TG analysis of ZnO and APTMS modified ZnO/Si nanoarchitectures (B) Variation in the zeta potential of ZnO with APTMS modification.

The wt % of APTMS present in ZnO/Si is further confirmed by the thermal analysis. The % wt loss in the temperature range of 150 to 400 ^{o}C is a direct representation of the APTMS modification since APTMS thermally decomposes at 230 ^{o}C yielding SiO_2 as residue. A comparison of weight loss between ZnO and ZnO/Si nanoarchitectures in this temperature range can give the efficiency of APTMS modification. Accordingly, the weight loss curves in Figure 6.11A shows the APTMS modification efficiency of ~ 2 % for the

ZnO/Si 0.15. It was found to increase with increase in the APTMS concentration in the reaction medium. For samples prepared with high molar ratios of APTMS, a modification efficiency of 8 % was observed. The increased APTMS modification strongly influences the surface charge characteristics of ZnO. Figure 6.11B shows the variation in the zeta potential of ZnO with ZnO/APTMS molar ratios. The zeta potential measurements were carried out at pH = 7. From the zeta potential measurements, it is clear that ZnO has surface charge value of -12 mV. After modification, it is increased to +35 mV; producing positively charged ZnO/Si. The increased positive charge is generated by the protonation of NH_2 groups present in the ZnO/Si, as observed in FTIR (Mallakpour *et al*., 2012).

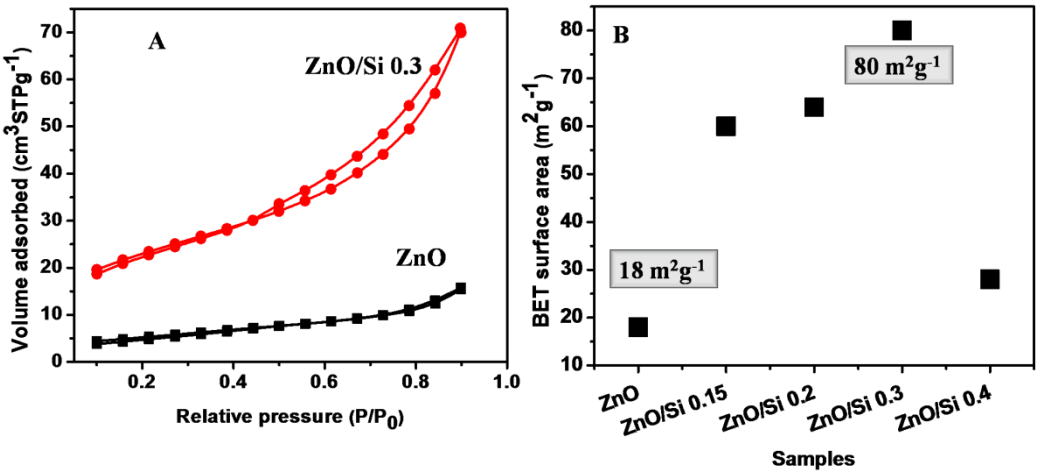

Figure 6.12 BET surface area of ZnO and ZnO/Si nanoarchitectures with APTMS/ZnO ratios 0.15, 0.2, 0.3, and 0.4.

The BET surface area values determined for ZnO and ZnO/Si nanoarchitectures using N_2 adsorption/desorption measurements are given in Figure 6.12. It was found that the surface area increases up to 4 times with increase in concentration of APTMS in ZnO/Si. A high surface area of 80 $m^2 g^{-1}$ was observed for ZnO/Si 0.3. At higher concentration of APTMS, the pores generated by the porous siloxane network on the surface get blocked due to the

formation of 2 to 3 bi-layers. It reduces the bulk surface area of the ZnO/Si 0.4 (Mallakpour *et al*., 2012).

6.4.2 Fabrication of Flexible ZnO/Si and ZnO/Si/GO Decorated Gelatin Bionanocomposite Films

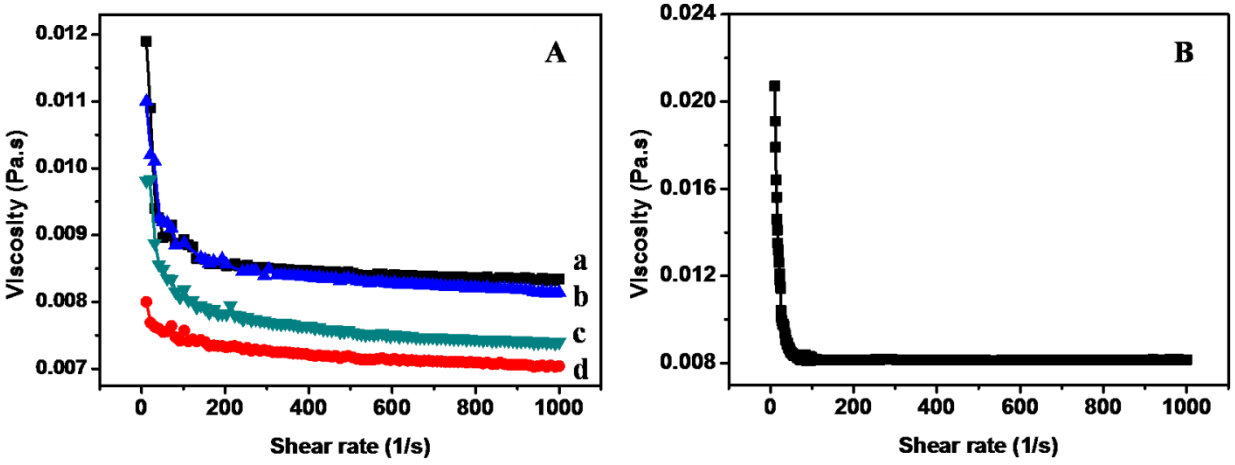

Figure 6.13 (A) Viscosity measurements of (a) pure gelatin sol and (b)-(d) ZnO/Si@gelatin sol containing (b) 0.1 wt %, (c) 0.2 wt %, and (d) 0.4 wt % ZnO/Si nanoarchitetures (B) Viscosity measurements of ZnO/Si/GO@gelatin sol.

Figure 6.13A shows the rheological studies of gelatin sol with respect to the loading of different amounts of ZnO/Si (0.1 to 0.4 wt %). All the samples show non-Newtonian behavior, particularly shear thinning behavior. The viscosity found to decrease with increase in the concentration of ZnO/Si in the gelatin matrix. Pure gelatin sol shows higher viscosity and the addition of ZnO/Si reduces the viscosity, because ZnO/Si breaks the interaction between the gelatin molecules in the matrix. The shear thinning behavior can be attributed to the collapse of the gel structure by further application of shear rate. The rheological behaviour of ZnO/Si/GO bionanocomposite sol is given in the Figure 6.13B. As shown in the figure, the

viscosity improved in the presence of GO. The addition of GO imparts a colloidal nature to the system which attributes to the higher viscosity in the ZnO/Si/GO bionanocomposite sol.

The XRD patterns of ZnO/Si decorated gelatin bionanocomposite films with different wt % of ZnO/Si (0.1, 0.2, and 0.4 wt %) in the gelatin matrix were given in the Figure 6.14A. The amorphous nature of the film is clearly seen in the XRD pattern and is due to the presence of gelatin matrix. Since the loading of ZnO/Si is very low, it is difficult to get X-ray diffraction peaks of ZnO in the first two samples. But the composition with 0.4 wt % and 0.6 wt % ZnO/Si loading shows the characteristic peaks of ZnO and all the detectable peaks can be indexed to the ZnO wurtzite structure (JCPDS No. 79-0205). The crystalline size of the ZnO particles in the gelatin matrix was found to be ~10 nm. Figure 6.14B shows the XRD pattern of ZnO/Si/GO decorated gelatin film. The presence of both GO and ZnO is clear from the XRD pattern. Compared to ZnO/Si@gelatin films, the XRD peaks of ZnO is not that much clearly visible in ZnO/Si/GO@gelatin film. This is because of the reason that most of the ZnO nanoparticles got covered with GO nanosheets in ZnO/Si/GO@gelatin nanocomposite.

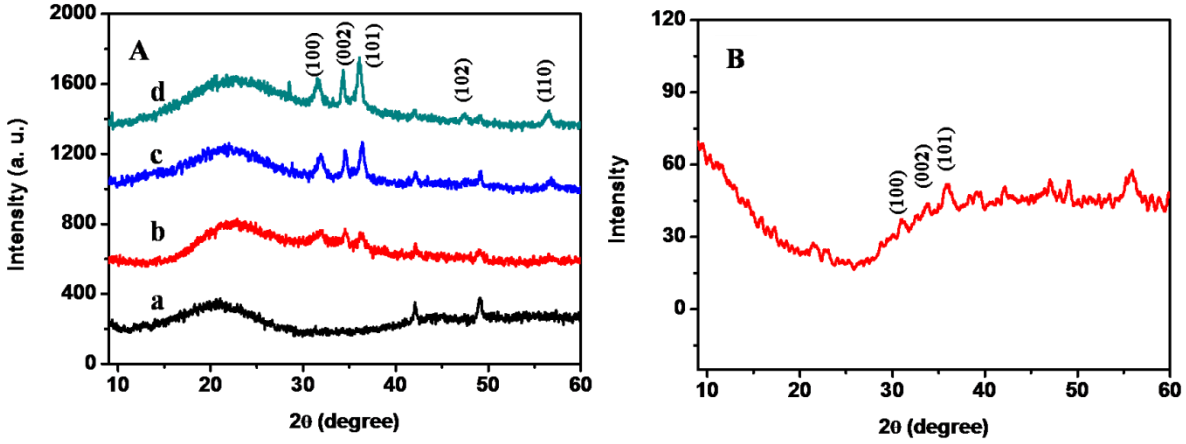

Figure 6.14 (A) XRD patterns ZnO/Si decorated bionanocomposite films containing (a) 0 (b) 0.1 wt. %, (c) 0.2 wt. %, and (d) 0.4 wt. % ZnO/Si nanoarchitectures (B) XRD pattern of ZnO/Si/GO@gelatin film.

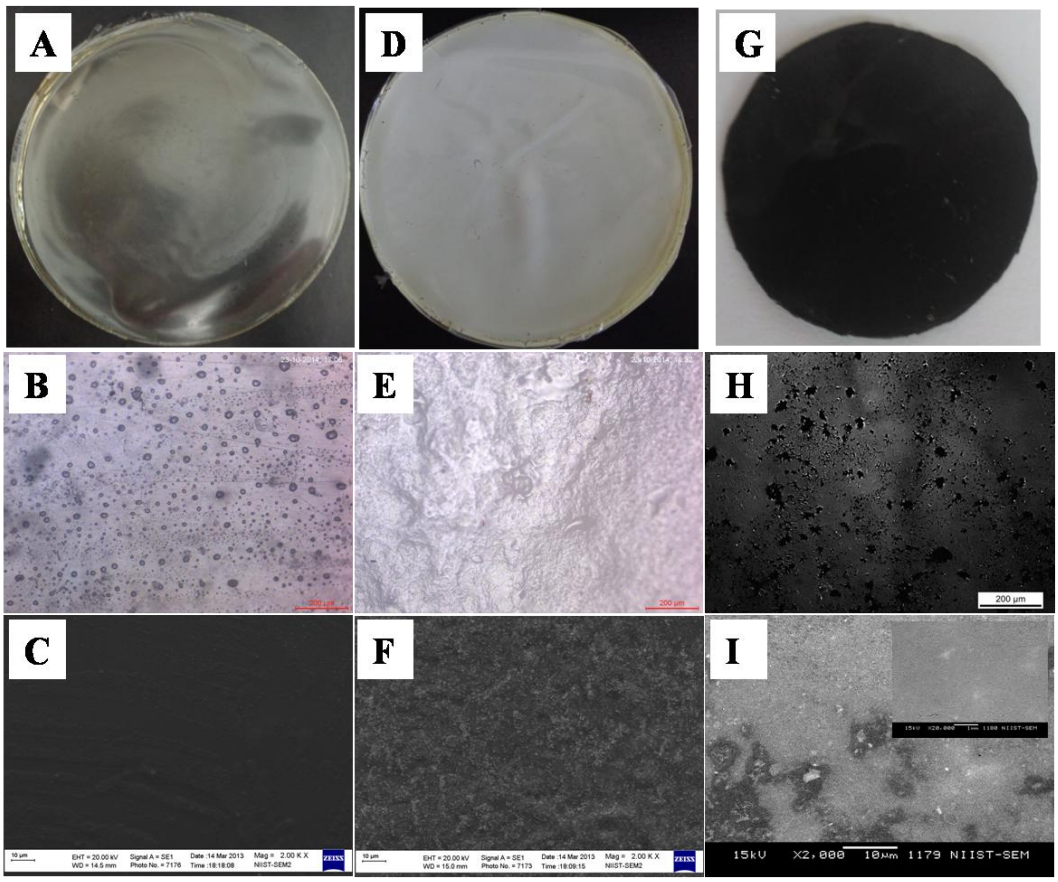

Figure 6.15 (A, B, and C) Photograph, optical image and SEM image of gelatin film (D, E, and F) photograph, optical image and SEM image of ZnO/Si@gelatin bionanocomposite film (G, H, and I) photograph, optical image and SEM image of ZnO/Si/GO decorated gelatin bionanocomposite film.

Figure 6.15A, D, and G presents the photographic images of gelatine film, ZnO/Si decorated gelatin film, and ZnO/Si/GO decorated gelatin film. The colour change in the gelatin film by the addition of ZnO/Si and ZnO/Si/GO are clearly seen from the photographs. Figure 6.15B, E, and H shows the optical microscopic images of pure gelatin film, ZnO/Si decorated gelatin film, and ZnO/Si/GO decorated gelatin film. Pure gelatin film contains small pores and water droplets are adsorbed on the surface, which shows the hydrophilic nature of gelatin. But a smooth surface was observed for ZnO/Si and ZnO/Si/GO decorated gelatin films due to the uniform distribution of ZnO/Si and ZnO/Si/GO. The mophological analysis of

gelatin film, ZnO/Si@gelatin bionanocomposite film and ZnO/Si/GO decorated gelatin bionanocomposite film were presented in the Figure 6.15C, F, and I. The modification of ZnO with APTMS results in the homogeneous distribution of ZnO nanoparticles in the gelatin matrix (Figure 6.15F). The uniform distribution of GO along with ZnO nanoparticles is clearly seen in the SEM imgage of ZnO/Si/GO@gelatin film.

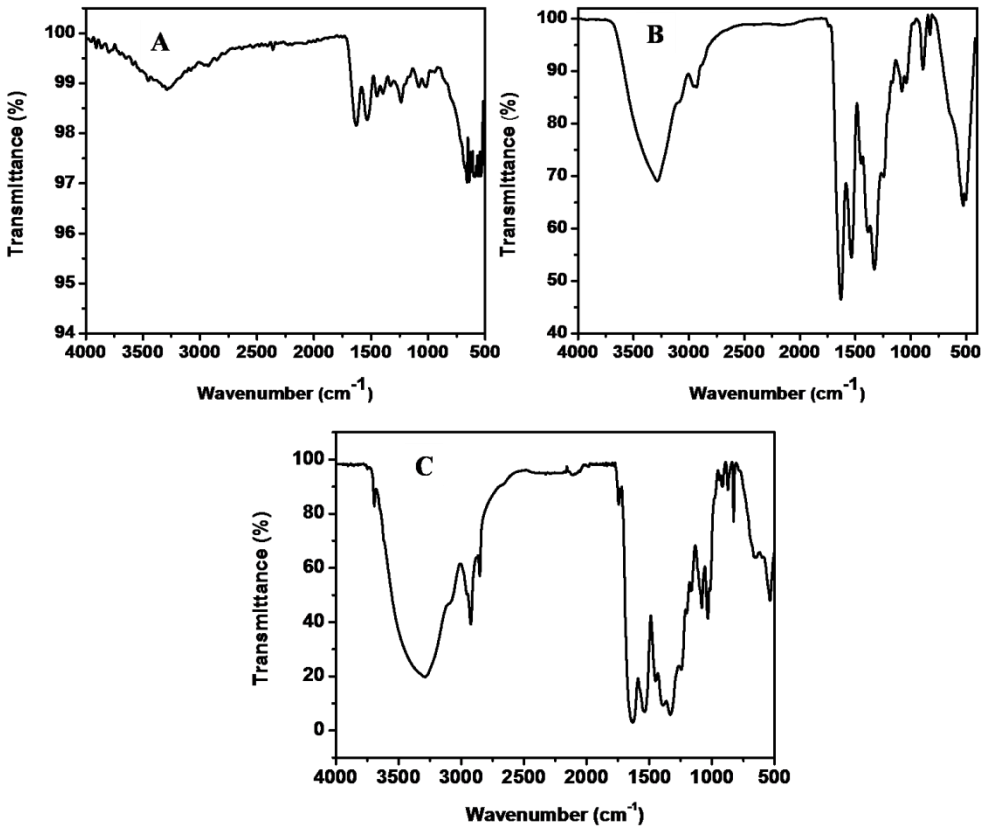

Figure 6.16 ATR spectra of (A) gelatin film, (B) ZnO/Si decorated gelatin film, and (C) ZnO/Si/GO decorated gelatin film.

The ATR spectroscopy was used to study the chemical interactions between the organic and inorganic structural units in ZnO/Si and ZnO/Si/GO decorated bionanocomposite films Figure 6.16A, B and C shows ATR spectra of pure gelatin, ZnO/Si@gelatin, and ZnO/Si/GO@gelatin films, respectively. Pure gelatin contains O-H, O=C-NH, C=O (amide),

C-OH, NH_2 functional groups, which are clearly seen in the ATR spetra with IR bands at 3281, 1632, 1532, 1230, 1087 cm^{-1}, respectively. Peaks corresponding to N-H group is merged with that of O-H groups at 3281 cm^{-1}. The ATR spectra of ZnO/Si and ZnO/Si/GO decorated gelatin film shows additional bands at 1323, 1030, 827, and 532 cm^{-1} and are assigned to the Zn-O-Si, Si-O-Si, Si-C, and Zn-O bonds, respectively. The alkyl C-H stretching band located at 2924 cm^{-1} in ZnO/Si@gelatin and ZnO/Si/GO@gelatin films are not remarkably seen in the ATR spectrum of gelatin. This may due to the merging of this band with the band located at 3281 cm^{-1}.

The surface hydrophobicity of the as prepared samples were evaluated using water contact angle measurement and the photographs are presented in the Figure 6.17. The contact angle values of the prepared samples are given in Table 6.1. The hydrophilic nature of the gelatin film is confirmed with a lower contact angle value of 84.8 ^{o}. The incorporation of ZnO/Si in the gelatin matrix had a significant influence on the hydrophobicity and the contact angle was found to increased to 122.4 ^{o}. The water contact angle measurement of ZnO/Si/GO@gelatin nanocomposite film showed compartively lower hydrophobicity (112.5 ^{o}) than ZnO/Si@gelatin nanocomposite film. This feature was due to the presence of hydrophilic functional groups on the GO nanosheets. These results demonstrate that the incorporation of ZnO/Si and ZnO/Si/GO had a great potential to overcome the limitation of hygroscopic property of gelatin.

The enhanced antibacterial property of the ZnO/Si/GO nanocomposite is already studied in the Chapter 4. The uniform incorporation of these nanoparticles accompanied by the enhanced water contact angle in ZnO/Si/GO@gelatin films leads to its application in food packaging, pharmaceutical, and even as a biomaterial.

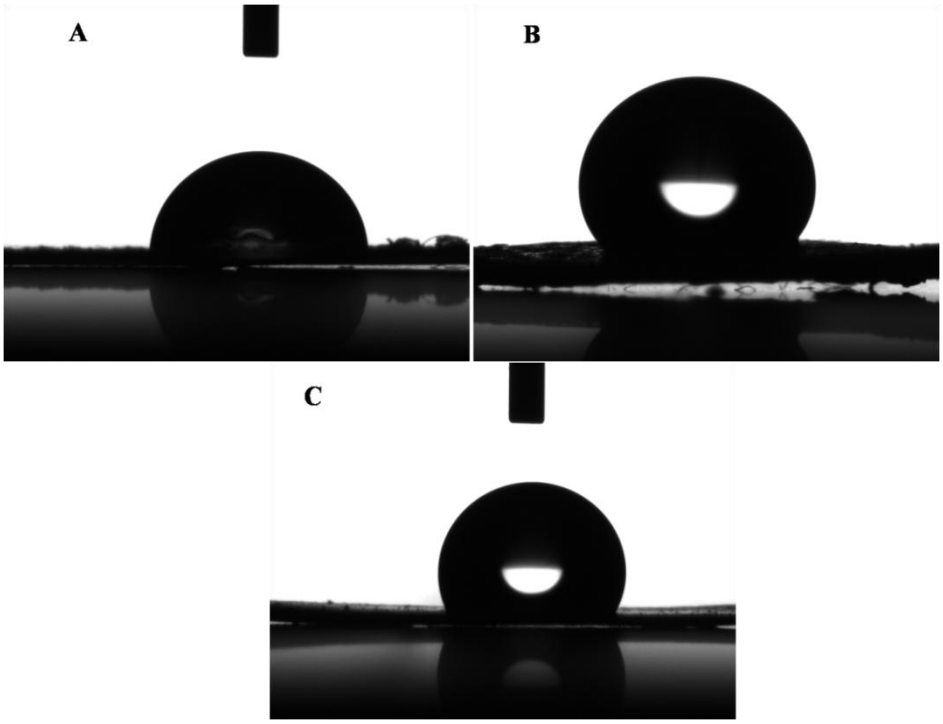

Figure 6.17 Photographs of the water contact angle measurements of (A) gelatin film (B) ZnO/Si decorated gelatin film, and (C) ZnO/Si/GO decorated gelatine film.

Table 6.1 Water contact angle values of the as-prepared films

Samples	**Contact angles (^{o})**
Gelatin film	84.8
ZnO/Si@gelatin film	122.4
ZnO/Si/GO@gelatin film	112.5

6.5 Conclusions

In this study, a simple microwave assisted aqueous synthesis of bulk ZnO/Si nanoarchitectures (ZnO/Si) has been successfully demonstrated *via* an in-situ APTMS modification strategy. The formation of ZnO/Si *via* APTMS modification was confirmed with a series of characterization techniques such as XRD, TEM, UV-Vis absorption spectra, FTIR, and TGA.

The mechanism for the novel in-situ APTMS modification resulted in the formation of polysiloxane coverage on the ZnO surface, which arrested the growth process of ZnO nuclei. The zeta potential of ZnO was found to be -12 mV at pH = 7. This was shifted to the positive region upon APTMS treatment due to protonated NH_2 groups. A high surface area mesoporous ZnO/Si having a BET surface area of 80 $m^2 g^{-1}$ has been obtained by APTMS modification which is 4 times higher than ZnO. Gelatin matrix can be loaded with silane modified ZnO particles as well as GO to fabricate flexible and hydrophobic ZnO/Si@gelatin and ZnO/Si/GO@gelatin bionanocomposite films. Structural and morphological properties of the films were studied. Contact angle apparently increased from 84.8 to 122.4 ^{o} in the presence of ZnO, which indicates that the hydrophobicity increased with the addition of inorganic filler in the gelatin matrix. The water contact angle slightly reduced in the case of ZnO/Si/GO@gelatin nanocomposite, but still the value is higher than that of bare gelatin film.

CHAPTER 7

Summary and Scope for Future Work

7.1 Summary

It is a fact that processing industries are highly keen to employ most economical catalytic materials for simplifying the effluent treatment process. In this regard ZnO is a candidate. However the limitations such as poor adsorption, low surface area, resistance against acid/alkali attack *etc*., should be definitely rectified. If ZnO is suitably engineered for the simultaneous adsorption and catalytic degradation, then this can be a most potential nano-catalyst. With this simple idea, in this thesis investigation is made on the processing of ZnO nanomaterials by adopting *'composite strategy'* where the matrix ZnO is reinforced with recently emerged graphene based carbon nanostructures. Interestingly, this material architecture offered versatile 'multifunctional' properties ranging from tailored meso/nano porous microstructures, moderate surface area, better adsorption as well as catalytic qualities along with antibacterial nature.

A notable outcome of this thesis work can be claimed as follows; it is experimentally demonstrated that microwave synthesis is a facile technique to obtain range of ZnO nanostructures at mild reaction conditions. When this nano ZnO is modified with graphene based nanomaterials like GO and rGO, the whole process produced efficient ZnO nanocomposites. Such nanocomposites exhibit 'sorptive-catalytic' nature for treating the hazardous organic dyes *via* simultaneous adsorption and catalytic degradation. This kind

catalytic ZnO nanomaterial also found useful water disinfection property. An attempt is also made to explore this nanocomposite for sensing organic molecules successfully. All these aspects are covered in individual working chapters and the most significant results can be summarized as follows;

Introductory chapter presents the background literature for selecting the research problem. It is emphasized that ZnO nanostructures as well as graphene based nanomaterials are candidates for catalytic applications. Subsequent chapter briefly mention the instrumentation techniques. The first working chapter deals with the oxidation and exfoliation of graphite to successfully obtain thin layer of GO nanosheets with surface area 77 $m^2 g^{-1}$. It is further used for the processing of three varieties of ZnO-graphene based nanocomposites such as ZnO@rGO, ZnO/Si@rGO, and ZnO-rGO, which are further exploited as 'adsorptive- catalysts'. A simultaneous adsorption and catalytic degradation was conducted on different organic cationic dyes. The study revealed that the microwave irradiation transforms the GO nanosheets to rGO nanosheets that act as excellent nano-support layers for the nucleation and growth of ZnO nanostructures. When the rGO favors in promoting the adsorption of cationic dyes, the rGO supported ZnO nanostructures show good photo degradation of the dye molecules. The phase pure nano ZnO shows no adsorption and only 30% photo degradation of MB dye. This is significantly enhanced in ZnO/rGO nanocomposites. The ZnO@rGO nanocomposite shows 69% photocatalytic activity and 42% of adsorption property. Also ZnO/Si@rGO nanocomposite exhibits surface area 78 $m^2 g^{-1}$that led to increase the adsorption from 42% to ~59%.

The microwave irradiation technique was further extended to develop ZnO nano rods with different aspect ratios (2.47 to 7.98) using PEG with different molecular weights. These nanorods were post grafted on the surface of GO sheets using APTMS as crosslinking agent. The dependence of the antibacterial behaviour on the aspect ratio of the

ZnO nanorods and GO has been investigated and presented as a separate chapter. The ZnO nanorod grafted GO sheets were examined for the antibacterial properties using both Gram-positive and Gram-negative bacteria. The results showed that ZnO/GO nanocomposite has excellent antibacterial property. However, the samples prepared with nanorods having higher aspect ratio showed comparatively more antibacterial activity which was subsequently exploited for water disinfection. The real pond water was treated with ZnO/GO nanocomposite and the results showed that highly contaminated pond water is disinfected successfully.

The nascent hydrogen reduction of GO to rGO has been carried out using waste Zn dust in chapter 5. The efficiency of Zn dust to convert GO to rGO is visibly seen from the XRD and UV analyses. A peak shift is noticed from 2θ =10.8 to 24^{o} in the XRD pattern and the red shift in the UV-vis absorption spectra from 230 to 269 nm confirmed the reduction of GO to rGO. This rGO is further used for making the ZnO@rGO nanocomposites. For this nanocomposite, ZnO morphology was tailored using carbohydrate/cellulose biotemplates. Subsequently, the effect of morphology of ZnO was studied for the non enzymatic electrochemical detection of urea and glucose. The electrochemical studies show that ZnO@rGO nanocomposite can sense glucose in the concentration range of $0.02x10^{-3}$-$18x10^{-3}$ mM with a detection limit of 0.008 μM. Similarly the ZnO@rGO nanocomposite modified electrode is sensitive to urea in the concentration range of $0.02x10^{-3}$-$7.2x10^{-3}$mM with a detection limit of 0.012 μM. The prepared ZnO@rGO nanocomposite glucose or urea sensor exhibit ultra-high sensitivity of 683 μA mM^{-1} cm^{-2} towards urea and 481μA mM^{-1} cm^{-2}towards glucose.

Mesoporous ZnO nanoarchitectures with surface area ~ 78 m^2 g^{-1} were successfully prepared using in-situ silane treatment. This silane modified high surface area ZnO is further explored as functional nanofillers along with GO nanosheets for obtaining

ZnO/Si/GO@gelatin bionanocomposite films. The water contact angle for this gelatin bionanocomposite film is measured and reported. The pure gelatin film has the contact angle of 84.8 ^{o}. The same is increased to 120 ^{o} for ZnO/Si/gelatin film. The addition of 0.2 wt % of GO with ZnO/Si/gelatin found to increase the value from 84.8 ^{o} to 112 ^{o}. The hydrophobic property indicates that ZnO/Si/gelatin film is more water stable. The experimental results suggest that ZnO/Si/GO is the novel nanofiller for gelatine bionanocomposite film that can be used for bio-friendly coatings on food-packs, wound dressing and adsorbent pads for surgical uses *etc*.

7.2 Future Perspectives

- The biocompatibility of ZnO@GO/rGO nanocomposites may be considered for further study to develop antifouling membranes
- The detection, adsorption, and photodegradation of pesticides can be taken up with this futuristic ZnO/rGO and ZnO/GO nanocomposites for the benefits of the agricultural fields
- Microwave irradiation can be explored for the direct exfoliation of graphite in presence of non-polar layered inorganic substrates. *e.g*. Mica.
- Bulk processing of GO to rGO *via* microwave irradiation is also one of the interesting field for further study
- GO and rGO are promising carbon nanostructures but they lack in the surface area when compared to graphene nanostructures. Since it limits the applications, this also should be considered seriously for further research.
- GO-ZnO nanocomposite modified gelatin is a potential non-toxic biofilm. This can be further tested for food packaging coatings.

Research Highlights

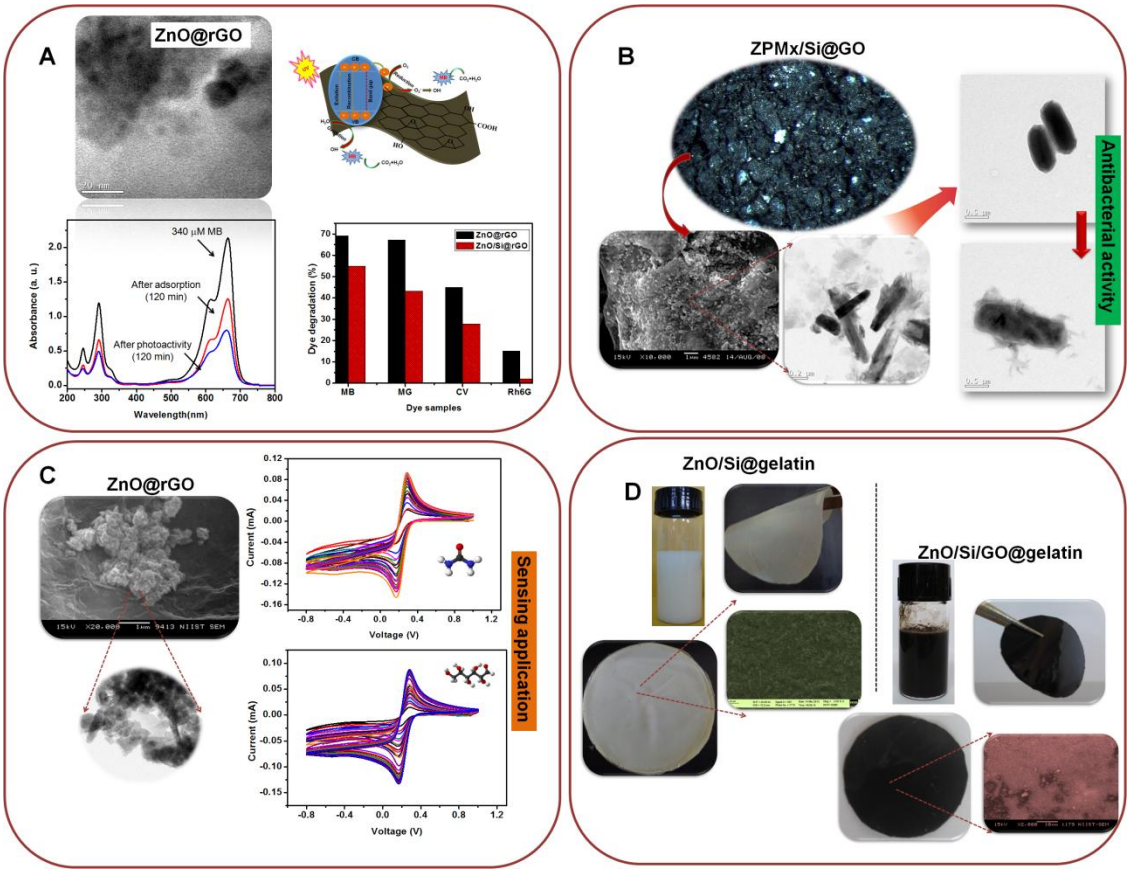

Notes: (A) Demonstration of enhanced photocatalytic performance of ZnO@rGO nanocomposite reported in Chapter 3 (B) Demonstration of enhanced antibacterial activity of ZPM6000/Si@GO nanocomposite reported in Chapter 4 (C) Demonstration of non enzymatic electrochemical sensing of ZnO@rGO nanocomposite reported in Chapter 5 (D) Fabrication of ZnO/Si@gelatin and ZnO/Si/GO@gelatin nanocomposites reported in Chapter 6.

REFERENCES

Adams L. K., Lyon D. Y., Alvarez P. J. J. "Comparative eco-toxicity of nanoscale TiO_2, SiO_2, and ZnO water suspensions" *Water Research*, **2006**, 40, 3527-3532.

Aghabeygi S., Shamami M. K., "ZnO/ZrO_2 Nano-composite: Sonosynthesis, Characterization and its Application for Wastewater Treatment" *Ultrasonics Sonochemistry*, **2017**, 41, 458-465.

Agnihotri S., Bajaj G., Mukherji S., Mukherji S., "Arginine-assisted immobilization of silver nanoparticles on ZnO nanorods: an enhanced and reusable antibacterial substrate without human cell cytotoxicity" *Nanoscale*, **2015**, 7, 7415-7429.

Ahmed F., Arshi N., Anwar M. S., Danish R., Koo B. H., "Morphological evolution of ZnO nanostructures and their aspect ratio-induced enhancement in photocatalytic properties" *RSC Advances*, **2014**, 4, 29249-29263.

Akhavan O., Ghaderi E., "Escherichia coli bacteria reduce graphene oxide to bactericidal graphene in a self-limiting manner" *Carbon*, **2012**, 50, 1853-1860.

Akhavan O., Ghaderi E., "Toxicity of graphene and graphene oxide nanowalls against bacteria" *ACS Nano*, **2010**, 4, 5731-5736.

Akhavan O., Ghaderi E., Aghayee S., Fereydoonia Y., Talebia A., "The use of a glucose-reduced graphene oxide suspension for photothermal cancer therapy" *Journal of Materials Chemistry*, **2012**, 22, 13773-13781.

Ali A., Ansari A. A., Kaushik A., Solanki P. R., Barik A., Pandey M. K., Malhotra B. D., "Nanostructured zinc oxide film for urea sensor" *Materials Letters*, **2009**, 63, 2473-2475.

Ambrozic G., Orel1 Z. C., Zigon M., "Microwave-assisted non-aqueous synthesis of ZnO nanoparticles" *Materials and technology,* **2011**, 45, 173-177.

An X., Yu J. C., "Graphene-based photocatalytic composites" *RSC Advances*, **2011**, 1, 1426-1434.

Ao W. Q., Li J. Q., Yang H. M., Zeng X. R., Ma X. C., "Mechanochemical synthesis of zinc oxide nanocrystalline" *Powder technology,* **2006**, 168, 148-151.

Arain M., Nafady A., Sirajuddin, Ibupoto Z. H., Sherazi S. T. H., Shaikh T., Khan H., Alsalme A., Niaz A., Willander M., "Simpler and highly sensitive enzyme free sensing of urea via NiO nanostructures modified electrode" *RSC Advances*, **2016**, 6, 39001-39006.

Baiju K. V., Shukla S., Sandhya K. S., James J., Warrier K. G. K., "Photocatalytic Activity of Sol−Gel-Derived Nanocrystalline Titania" *Journal of Physical Chemistry C,* **2007**, 111, 7612-7622.

Balanand S., Babitha K. B., Jeen Maria M., Peer Mohamed A. A., Ananthakumar S., "Aqueous Mechanical Oxidation of Zn Dust: An Inventive Technique for Bulk Production of ZnO Nanorods" *ACS Sustainable Chemistry and Engineering*, **2018**, 6, 143-154.

Bao D., Haoshuang G., Anxiang K., "Sol gel derived c-axis oriented ZnO thin films" *Thin solid films,* **1998**, 132, 37-39.

Bao S. J., Li C. M., Zang J. F., Cui X. Q., Qiao Y., Guo J., "New Nanostructured TiO_2 for Direct Electrochemistry and Glucose Sensor Applications" *Advanced Functional Materials*, 2008, 18, 591-599.

Baranov A. N., Kurakevych O. O., Tafeenko V. A., Sokolov P. S., Panin G. N., Solozhenko V. L., "High-pressure synthesis and luminescent properties of cubic

ZnO/MgO Nanocomposites" *Journal of Applied Physics*, **2010**, 107, 073519-073524.

Bhatnagar A., Jain A. K., "A comparative adsorption study with different industrial wastes as adsorbents for the removal of cationic dyes from water" *Journal of Colloid and Interface Science*, **2005**, 281, 49-55.

Bianchi R. C., Silva E. R. D., Dall'Antonia L. H., Ferreira F. F., Alves W. A., "A Nonenzymatic Biosensor Based on Gold Electrodes Modified with Peptide Self-Assemblies for Detecting Ammonia and Urea Oxidation" *Langmuir*, **2014**, 30, 11464-11473.

Bressy C., Ngo V. G., Ziarelli F., Margaillan A., "New Insights into the Adsorption of 3-(Trimethoxysilyl)-propylmethacrylate on Hydroxylated ZnO Nanopowders" *Langmuir*, **2012**, 28, 3290-3297.

Bykkam S., Narsingam S., Ahmadipour M., Dayakar T., Rao K. V., Chakra C. S., Kalakotla S., "Few layered graphene Sheet decorated by ZnO Nanoparticles for anti-bacterial application" *Superlattice Microstructure*, **2015**, 83, 776-784.

Cai R., Rao W., Zhang Z., Longa F., Yina Y., "An imprinted electrochemical sensor for bisphenol A determination based on electrodeposition of a graphene and Ag nanoparticle modified carbon electrode" *Analytical Methods*, **2014**, 6, 1590-1597.

Cao N., Fua Y., Hea J., "Mechanical properties of gelatin films cross-linked, respectively, by ferulic acid and tannin acid" *Food Hydrocolloids*, **2007**, 21, 575-584.

Chaudhury C. R., Roychowdhury A., Das A., Das D., "Magneto-optical properties of α-Fe_2O_3@ZnO nanocomposites prepared by the high energy ballmilling Technique" *Journal of Physics and Chemistry of Solids*, **2016**, 92, 38-44.

Chen A., Chatterjee S., "Nanomaterials based electrochemical sensors for biomedical applications" *Chemical Society Review*, **2013**, 42, 5425-5438.

Chen C., Xie Q., Yang D., Xiao H., Fu Y., Tan Y., Yao S., "Recent advances in electrochemical glucose biosensors:a review" *RSC Advances*, **2013**, 3, 4473-4491.

Chen J., Zhao M., Li Y., Fan S., Ding L., Liang J., Chen S., "Synthesis of reduced graphene oxide intercalated ZnO quantum dots nanoballs for selective biosensing detection" *Applied surface science*, **2016**, 376, 133-137.

Chen Z., Zhang N., Xu Y. J., "Synthesis of graphene–ZnO nanorod nanocomposites with improved photoactivity and anti-photocorrosion" *Crystal Engineering Communications*, **2013**, 15, 3022-3030.

Chowdhuri A. R., Tripathy S., Chandra S., Sahu S. K., "A ZnO decorated chitosan-graphene oxide nanocomposite shows significantly enhanced antimicrobial activity with ROS generation" *RSC Advances*, **2015**, 5, 49420-49428.

Chu, D., Masuda Y., Ohji T., Kato K., "Formation and Photocatalytic Application of ZnO Nanotubes Using Aqueous Solution" *Langmuir*, 2010, 26, 2811-2815.

Chua C. K., Pumera M., "Chemical reduction of graphene oxide: a synthetic chemistry viewpoint" *Chemical Society Reviews*, **2014**, 43, 291-312.

Chun Z. Y., Yitai Q., "Solution-phase synthesis of nanomaterials at low Temperature" *Science in China Series G: Physics, Mechanics and Astronomy*, **2009**, 52, 13-20.

Costenaro D., Carniato F., Gatti G., Bisio C., Marchese L., "On the Physico-Chemical Properties of ZnO Nanosheets Modified with Luminescent CdTe Nanocrystals" *Journal of Physical Chemistry C*, **2011**, 115, 25257-25265.

Cui P., Lee J., Hwang E., Lee H., "One-pot reduction of graphene oxide at subzero temperatures" *Chemical Communications*, **2011**, 47, 12370-12372.

Curridal M. L., Comparelli R., Cozzli P. D., Mascolo G., Agostiano A., "Colloidal oxide nanoparticles for the photocatalytic degradation of organic dye" *Material Science and Engineering C*, **2003**, 23, 285-289.

Daniel M.C., Astruc D., "Gold Nanoparticles: Assembly, Supramolecular Chemistry, Quantum-Size-Related Properties, and Applications toward Biology, Catalysis, and Nanotechnology" *Chemical Reviews*, **2004**, 104, 293-346.

Danon A., Stair P. C., Weitz E., "FTIR Study of CO_2 Adsorption on Amine-Grafted SBA-15: Elucidation of Adsorbed Species" *Journal of Physical Chemistry C*, **2011**, 115, 11540-11549.

Dar G. N., Umar A., Zaidi S. A., Baskoutas S., Kim S. H., Abaker M., Al-Hajry A., Al-Sayari S. A., "Fabrication of Highly Sensitive Non-Enzymatic Glucose Biosensor Based on ZnO Nanorods" *Science of Advanced Materials*, **2011**, 3, 901-906.

Das S., Srivastava V. C., "Synthesis and characterization of ZnO/CuO nanocomposite by electrochemical method" *Materials Science in Semiconductor Processing*, **2017**, 57, 173-177.

Davis M., Hikal W. M., Mecia C. G., Hope Weeks L. J., "Aerogel nanocomposites of ZnO-SnO_2 as efficient photocatalysts for the degradation of rhodamine B" *Catalysis Science Technology*, **2012**, 2, 922-924.

Deng C. H., Gong J. L., Zeng G. M., Niu C. G., Niu Q. Y., Zhang W., Liu H.Y., "Inactivation performance and mechanism of *Escherichia coli* in aqueous system exposed to iron oxide loaded graphene nanocomposites" *Journal of Hazardous Materials*, **2014**, 276, 66-76.

Dey R. S., Hajra S., Sahu R. K., Raj C. R., M. K. Panigrahic, "A rapid room temperature chemical route for the synthesis of graphene: metal-mediated reduction of graphene oxide" *Chemical Communications*, **2012**, 48, 1787-1789.

Dhar R., Pedrow P. D., Liddell K. C., Ming Q., Moeller T. M., "Plasma-enhanced metal-organic chemical vapour deposition(PEMOCVD) of catalytic coatings for fuel cell reformaers" *IEEE Transactions Plasma Science*, **2005**, 33, 138-146.

Dhara K., Stanley J., Ramachandran T., Nair B. G., Satheesh Babu T. G., "Cupric Oxide Modified Screen Printed Electrode for the Nonenzymatic Glucose Sensing" *Journal of Nanoscience and Nanotechnology*, **2016**, 16, 8772-8778.

Dia Z. H., Liu K., Tang Y. W., Yang X. D., Bao J. C., Shen J., "A novel tetragonal pyramid-shaped porous ZnO nanostructure and its application in the biosensing of horseradish peroxidise" *Journal of Materials Chemistry*, **2008**, 18, 1919-1926.

Dreyer D. R., Park S., Bielawski C. W., Ruoff R. S., "The chemistry of graphene oxide" *Chemical Society Review*, **2010**, 39, 228-240.

Farris S., Schaich K. M., Liu L., Cooke P. H., Piergiovanni L., Yam K. L., "Gelatin-pectin composite films from polyion-complex hydrogels" *Food Hydrocolloids*, **2011,** 25, 61-70.

Feldmann C., "Polyol-Mediated Synthesis of Nanoscale Functional Materials" *Advanced Functional Materials*, **2003**, 13, 101-107.

Frydrych M., Wan C., Stengler R., O'Kellya K. U., Chen B., "Structure and mechanical properties of gelatin/sepiolite nanocomposite foams" *Journal of Materials Chemistry*, **2011**, 21, 9103-9111.

Gao N., Chen Y., Jiang J., "Ag@Fe_2O_3-GO Nanocomposites Prepared by a Phase Transfer Method with Long-Term Antibacterial Property" *ACS Applied Materials and Interfaces*, **2013**, 5, 11307-11314.

Gao P., Ng K., Sun D. D., "Sulfonated graphene oxide–ZnO–Ag photocatalyst for fast photodegradation and disinfection under visible light" *Journal of Hazardous Materials*, **2013**, 262, 826-835.

Gao X., Jang J., Nagase S., "Hydrazine and Thermal Reduction of Graphene Oxide: Reaction Mechanisms, Product Structures, and Reaction Design" *Journal of Physical Chemistry C*, **2010**, 114, 832-842.

Gao Y. F., Nagai M., "Morphology Evolution of ZnO Thin Films from Aqueous Solutions and Their Application to Solar Cells" *Langmuir*, **2006**, 22, 3936-3940.

Gawande S., Thakare S. R., "One pot sonochemical synthesis of CdS-reduced graphene oxide compositeand its application for photocatalytic degradation of methylene blue" *Indian journal of Chemistry*, **2013**, 52A, 614-618.

Geethakarthi A., Phanikumar B. R., "Industrial sludge based adsorbents/ industrial byproducts in the removal of reactive dyes – A review" *International Journal of Water Resources and Environmental Engineering*, **2011**, 3, 1-9.

Ghosh S., Goudar V. S., Padmalekha K. G., Bhat S. V., Indic S. S., Vasan H. N., "ZnO/Ag nanohybrid: synthesis, characterization, synergistic antibacterial activity and its mechanism" *RSC Advances*, **2012**, 2, 930-940.

Ghule K., Ghule A. V., Chen B. J., Ling Y. C. "Preparation and Characterization of ZnO Nanoparticles Coated Paper and its Antibacterial Activity Study" *Green Chemistry*, **2006**, 8, 1034-1041.

Govindhan M., Adhikari B. R., Chen A., "Nanomaterials-based electrochemical detection of chemical contaminants" *RSC Advances*, **2014**, 4, 63741-63760.

Griffiths P. C., Stilbs P., Howe A. M., Whitesides T. H., "Interaction between Gelatin and Anionic Surfactants" *Langmuir*, **1996**, 12, 5302-5306.

Gu H., Yang Y., Tian J., Shi G., "Photochemical Synthesis of Noble Metal (Ag, Pd, Au, Pt) on Graphene/ZnO Multihybrid Nanoarchitectures as Electrocatalysis for H_2O_2Reduction" *ACS Applied Materials and Interfaces*, **2013**, 5, **6762-**6768.

Gu L., Wang J., Cheng H., Zhao Y., Liu L., Han X., "One-Step Preparation of Graphene-Supported Anatase TiO_2 with Exposed {001} Facets and Mechanism of Enhanced Photocatalytic Properties" *ACS Applied Materials and Interfaces*, **2013**, 5, 3085-3093.

Guo S., Dong S., "Graphene nanosheet: synthesis, molecular engineering, thin film, hybrids, and energy and analytical applications" *Chemical Society Review*, **2011**, 40, 2644-2672.

Guo Y., Wang H., He C., Qiu L., Cao X., "Uniform Carbon-Coated ZnO Nanorods: Microwave-Assisted Preparation, Cytotoxicity, and Photocatalytic Activity" *Langmuir*, **2009**, 8, 4678-4684.

Haga K., Kamidaira M., Kashiwaba Y., Sekiguchi T., Watanabe H., "ZnO thin films prepared by remote plasma enhanced CVD method" *Journal of crystal growth*, **2000**, 214, 77-80.

Hahn Y. B., Ahmad R., Tripathy N., "Chemical and biological sensors based on metal oxide nanostructures" *Chemical Communications*, **2012**, 48, 10369-10385.

Han C., Chen Z., Zhang N., Colmenares J. C., X Y. J., "Hierarchically CdS decorated 1D ZnO nanorods-2D graphene hybrids: low temperature synthesis and enhanced photocatalytic performance" *Advanced Functional Materials*, **2014**, 25, 221-229.

Han C., Yang M. Q., Wengab B., Xu Y. J., "Improving the photocatalytic activity and anti-photocorrosion of semiconductor ZnO by coupling with versatile carbon" *Physical Chemistry Chemical Physics*, **2014**, 16, 16891-16903.

Han C., Zhang N., Xu Y. J., "Structural diversity of graphene materials and their multifarious roles in heterogeneous photocatalysis" *Nano today*, **2016**, 11, 351-372.

Hareesh P., Babitha K. B., Shukla S., "Processing fly ash stabilized hydrogen titanate nano-sheets for industrial dye-removal application" *Journal of Hazardous Materials,* **2012**, 229, 177-182.

Hong R. Y., Li J. H., Chen L. L., Liu D. Q., Li H. Z., Zheng Y., Ding J., "Synthesis, surface modification and photocatalytic property of ZnO nanoparticles" *Powder Technology,* **2009**, 189, 426-432.

Huang Y., Wang T., Zhao X., Wang X., Zhou L., Yang Y., Liao F., Ju Y., "Poly(lactic acid)/graphene oxide–ZnO nanocomposite films with good mechanical, dynamic mechanical, anti-UV and antibacterial properties" *Journal of Chemical Technology and Biotechnology*, **2015**, 90, 1677-1684.

Hwang S. H., Song J., Jung Y., Kweon O. Y., Song H., Jang J., "Electrospun ZnO/TiO_2 composite nanofibers as a bactericidal agent" *Chemical Communications*, **2011**, 47, 9164-9166.

Ibupoto Z. H., Nafady A., Soomro R. A., Sirajuddin, Sherazi S T. H., Abro M. I., Willander M., "Glycine-assisted synthesis of NiO hollow cage-like nanostructures for sensitive non-enzymatic glucose sensing" *RSC Advances*, **2015**, 5, 18773-18781.

Jaimy K. B., Baiju K. V., Ghosh S. K., Warrier K. G. K., "A novel approach for enhanced visible light activity in doped nanosize titanium dioxide through the excitons trapping" *Journal of Solid State Chemistry*, **2012**, 186, 149-157.

Jankovský O., Lojka M., Nováček M., Luxa J., Sedmidubský D., Pumera M., Kosinac J., Sofer Z., "Reducing emission of carcinogenic by-products in the production of thermally reduced graphene oxide" *Green Chemistry*, **2016**, 18, 6618-6629.

Jayanthi K., Chawla S., Joshi A.G., Khan Z.H., Kotnala R. K, "Fabrication of luminescent, magnetic hollow core nanospheres and nanotubes of Cr doped ZnO by inclusive coprecipitation method" *Journal of Physical Chemistry C,* **2010**, 114, 18429-18434.

Jeong, W. J., Kim S. K., Park G. C., "Preparation and Characteristic of ZnO Thin Film with High and Low Resistivity for an Application of Solar Cell" *Thin Solid Films*, **2006**, 506, 180-183.

Jia L., Wang D. H., Huang Y. X., Xu A.W., Yu H. Q., "Highly Durable N-Doped Graphene/CdS Nanocomposites with Enhanced Photocatalytic Hydrogen Evolution from Water under Visible Light Irradiation" *Journal of Physical Chemistry C*, **2011**, 115, 11466-11473.

Jiang J., Zhang P., Liua Y., Luo H., "A novel non-enzymatic glucose sensor based on Cu nanoparticles modified graphene edge nanoelectrode" *Analytical Methods*, **2017**, 9, 2205-2210.

Jun Y., Choi J., Cheon J., "Shape control of semiconductor and metal oxide nanocrystals through nonhydrolytic colloidal routes" *Angewandte Chemie Inernationalt Edition*, **2006**, 45, 3414-3439.

Jung S., Yong K., "Fabrication of CuO–ZnO nanowires on a stainless steel mesh for highly efficient photocatalytic applications" *Chemical Communications*, **2011**, 47, 2643-2645.

Junior E. A. A., Nobre F. X., Sousa G. D. S., Cavalcante L. S.,. Santos M. R. D. M. C, Souza F. L., Matos J. M. E. D., "Synthesis, growth mechanism, optical properties and catalytic activity of ZnO microcrystals obtained via hydrothermal processing" *RSC Advances*, **2017**, 7, 24263-24281.

Kajbafvala A., Shayegh M. R., Mazloumi M., Zanganeh S., Lak A., Mohajerani M. S., Sadrnezhaad S.K., "Nanostructure sword-like ZnO wires: Rapid synthesis and characterization through a microwave-assisted route" *Journal of Alloys and Compounds*, **2009**, 469, 293-297.

Kamat, V. P., Huehn, R., Nicolaescu R., A "Sense and Shoot" Approach for Photocatalytic Degradation of Organic Contaminants in Water" *Journal of Physical Chemistry B*, **2002**, 106, 788-794.

Kang S. Z., Wub T., Li X., Mub J., "A facile gelatin-assisted preparation and photocatalytic activity of zinc oxide nanosheets" *Colloids and Surfaces A: Physicochemical and Engineering Aspects*, **2010**, 369 268-271.

Kannan P. K., Late D. J., Morgan H., Rout C. S., "Recent Developments in 2D Layered Inorganic Nanomaterials for Sensing" *Nanoscale*, **2015**, 32, 13293-13312.

Karaqozoqlu B., Tasdemir M., Demirbas E., Kobya M., "The adsorption of basic dye from aqueous solution onto sepiolite, flyash and apricot shell activated carbon: kinetic and equilibrium studies" *Journal of Hazardous Materials*, **2007**, 147, 297-306.

Karunakaran C., SakthiRaadha S., Gomathisankar P., Vinayagamoorthy P., "The enhanced photocatalytic and bactericidal activities of carbon microsphere-assisted solvothermally synthesized cocoon-shaped Sn^{4+}-doped ZnO nanoparticles" *Dalton Transaction*, **2013**, 42, 13855-13865.

Kaur J., Bhukal S., Gupta K., Tripathy M., Bansal S., Singhal S., "Nanocomposite of CeO_2 and ZnO: An active material for the treatment of contaminated water" *Materials Chemistry and Physics*, **2016**, 177, 512-520.

Kenmoe S., Biedermann P. U., "Water aggregation and dissociation on the ZnO $(10\bar{1}0)$ surface" *Physical Chemistry Chemical Physics*, **2017**, 19, 1466-1486.

Khadro B., Baroudi I., Goncalves A. M., Berini B., Pegot B., Nouar F., Le T. N. H., Ribot F., Gervais C., Carn F., Cadot E., Mousty C., J´egata C. S., Steunou N., "Interfacing a heteropolytungstate complex and gelatin through a coacervation process: design of

bionanocomposite films as novel electrocatalysts" *Journal of Materials Chemistry A*, **2014**, 2, 9208-9220.

Khan M., Tahir M. N., Adil S. F., Khan H. U., Siddiqui M. R. H, Al-warthan A. A., Tremel W., "Graphene based metal and metal oxide nanocomposites: synthesis, properties and their applications" *Journal of Material Chemistry A*, **2015**, 3, 18753-18808.

Kim H. Y., Kim J. H., Kim Y. J., Chae K. H., Whang C. N., Song J. H., Im S., "Photoresponse of Si detector based on n-ZnO/p-Si and n-ZnO/n-Si structures" *Optical Materials*, **2001**, 17, 141-144.

Kim J. H., Choi W. C., Kim H. Y., Kang Y., Park Y. K., "Preparation of monodispersed mixed metal oxide micro hollow spheres by homogeneous precipitation in a micro precipitator" *Powder Technology*, **2005**, 153,166-175.

Kim K., Park S. Y., Lim K. H., Shin C., Myoungc J. M., Kim Y. S., "Low temperature and solution-processed Na-doped zinc oxide transparent thin film transistors with reliable electrical performance using methanol developing and surface engineering" *Journal Material Chemistry*, **2012**, 22, 23120-23128.

Kim, J. H., Yong K. J., "Mechanism Study of ZnO Nanorod-Bundle Sensors for H_2S Gas Sensing" *Journal of Physical Chemistry C*, **2011**, 115, 7218-7224.

Kochuveedu S. T., Jang Y. H., Kim D. H., "A study on the mechanism for the interaction of light with noble metal-metal oxide semiconductor nanostructures for various photophysical applications" *Chemical Society Reviews*, **2013**, 42**,** 8467-8493.

Komarneni S., Bruno M., mariani E., "Synthesis of ZnO with and without microwaves" *Mateials Research Bullentin*, **2000**, 35, 1843-1847.

Krishna M. B. M., Venkatramaiah N., Venkatesan R., Rao D. N., "Synthesis and structural, spectroscopic and nonlinear optical measurements of graphene oxide and its composites with metal and metal free porphyrins" *Journal of Material Chemistry*, **2012**, 22, 3059-3068.

Kulkarni S. B., Patil U. M., Salunkhe R. R., Joshi S. S., Lokhande C. D., "Temperature impact on morphological evolution of ZnO and its consequent effect on physico-chemical properties" *Journal of Alloys and Compounds*, **2011**, 509, 3486-3492.

Kumar S. G., Koteswara Rao K. S. R, "Zinc oxide based photocatalysis: tailoring surface-bulk structure and related interfacial charge carrier dynamics for better environmental applications" *RSC Advances*, **2015**, 5, 3306-3351.

Kumar T. R., Babu K. J., Yoo D. J., Kim A. R., Kumar G. G., "Binder free and free-standing electrospun membrane architecture for sensitive and selective non-enzymatic glucose sensors" *RSC Advances*, **2015**, 5, 41457-41467.

Le H. Q., Chua S. J., Koh Y.W., Loh K.P., Fitzgerald E. A., "Systematic studies of the epitaxial growth of single-crystal ZnO nanorods on GaN using hydrothermal synthesis" *Journal of crystal growth*, **2006**, 293, 36-42.

Li J., Fan H. Q., Jia X. D., **"**Multilayered ZnO Nanosheets with 3D Porous Architectures: Synthesis and Gas Sensing Application" *Journal of Physical Chemistry C***, 2010**, 114, 14684-14691.

Li X., Sun P., Yang T., Zhao J., Wang Z., Wang W., Liu Y., Lu G., Du Y., "Template-free microwave-assisted synthesis of ZnO hollow microspheres and their application in gas sensing" *Crystal Engineering Communication*, **2013**, 15, 2949-2955.

Li Y. B., Bando Y., Sato T., Kurashima K., "ZnO nanobelts grown on Si substare" *Applied Physical Letter*, **2002**, 81 , 144-146.

Li Y., Xu J., Sun C., "Chemical Sensors and Biosensors for the Detection of Melamine" *RSC Advances*, **2015**, 5**,** 1125-1147.

Liang Y., Guoa N., Lia L., Lia R., Jia G., Gana S., "Facile synthesis of Ag/ZnO micro-flower and improved the ultraviolet and visible light photocatalytic activity" *New Journal of Chemistry*, **2016**, 40, 1587-1594.

Liao R., Tang Z., Lin T., Guo B., "Scalable and Versatile Graphene Functionalized with the Mannich Condensate" *ACS Applied Materials and Interfaces*, **2013**, 5, 2174−2181.

Likos C. N., Vaynberg K. A., Lo¨wen H., Wagner N. J., "Colloidal Stabilization by Adsorbed Gelatin" *Langmuir*, **2000**, 16, 4100-4108.

Lin K. L., "Phase Identification Using Series of Selected Area Diffraction Patterns and Energy Dispersive Spectrometry with in TEM" *Microscopy Research*, **2014**, 2, 57-66.

Liu B., Zeng, H. C., "Hydrothermal Synthesis of ZnO Nanorods in the Diameter Regime of 50 nm" *Journal of American Chemical Society*, **2003**, 125, 4430-4431.

Liu C., Masuda Y., Wu Y., Takai O., "A simple route for growing thin films of uniform ZnO nanorod arrays on functionalized Si surfaces" *Thin solid films*, **2006**, 503, 110-114.

Liu H. T., Zeng X. F., "Highly transparent and multifunctional polymer nanohybrid film with super high ZnO content synthesized by a bulk polymerization method" *Industrial Engineering Chemical Research*, **2012**, 51, 6753-6759.

Liu H., Hu C., Zhai H., Yang J., Liu X., Jia H., "Fabrication of In_2O_3/ZnO@Ag nanowire ternary composites with enhanced visible light photocatalytic activity" *RSC Advances*, **2017**, 7, 37220-37229 .

Liu J., Liu F., Gao K., Wu J. S., Xue D., "Recent developments in the chemical synthesis of inorganic porous capsules" *Journal of Materials Chemistry*, **2009**, 19, 6073-6084.

Liu J., Rojas-Andrade M. D, Chata G., Peng Y., Roseman G., Lu J. E., Millhauser G. L., Saltikov C., Chen S., "Photo-enhanced antibacterial activity of ZnO/graphene quantum dot nanocomposites" *Nanoscale*, **2018**,10**,** 158-166 .

Liu K., Zhang J. J., Cheng F. F., Zheng T. T., Wang C., Zhu J. J., "Green and facile synthesis of highly biocompatible graphene nanosheets and its application for cellular imaging and drug delivery" *Journal of Materials Chemistry*, **2011**, 21, 12034-12040.

Liu L. L., An M. Z., Yang P. X., Zhang J. Q., "Few-layer graphene prepared via microwave digestion reduction and its electrochemical performances in lithium ion batteries" *International Journal of Electrochemical Science*, **2015**, 10, 1582-1594.

Liu S., Chen Z., Zhang N., Tang Z. R., Xu Y. J., "An Efficient Self-Assembly of CdS Nanowires–Reduced Graphene Oxide Nanocomposites for Selective Reduction of Nitro Organics under Visible Light Irradiation" *Journal of Physical Chemistry C,* **2013**, 16, 8251-8261.

Liu S., Zeng T. H., Hofmann M., Burcombe E., Wei J., Jiang R., Kong J., Chen Y., "Antibacterial Activity of Graphite, Graphite Oxide, Graphene Oxide, and Reduced Graphene Oxide: Membrane and Oxidative Stress" *ACS nano*, **2011**, 5, 6971-6980.

Liu T. J., Wang Q., Jiang P., "Morphology-dependent photo-catalysis of bare zinc oxide nanocrystals" *RSC Advances*, **2013**, 3, 12662-12670.

Liu T. Q., Sakurai O., Mizutani N., Kato M., "Preparation of spherical fine ZnO particles by the spray pyrolysis method using ultrasonic atomization techniques" *Journal of Material Science*, **1986**, 21, 3698-3702.

Liu X., Pan L., Lv T., Lu T., Zhu G., Sun Z., Sun C., "Microwave-assisted synthesis of ZnO–graphene composite for photocatalytic reduction of Cr(VI)" *Catalysis Science and Technology*, **2011**, 1, 1189-1193.

Long M., Qin Y., Chen C., Guo X., Tan B., Cai W., "Origin of Visible Light Photoactivity of Reduced Graphene Oxide/TiO_2 by in Situ Hydrothermal Growth of Undergrown TiO_2 with Graphene Oxide" *Journal of Physical Chemistry C*, **2013**, 117, 16734-16741.

Look D. C. "Recent Advances in ZnO Materials and Devices" *Materials Science and Engineering B* , **2001**, 80, 383-387.

Lv T., Pan L., Liu X., Sun Z., "Enhanced photocatalytic degradation of methylene blue by ZnO–reduced graphene oxide–carbon nanotube composites synthesized via microwave-assisted reaction" *Catalysis Science Technology*, **2012**, 2, 2297-2301.

Mallakpour S., Iderli M., "Preparation of new polymer nanocomposites based on chiral poly(amide-imide)/surface-modified ZnO nanoparticles containing 4,40-methylene bis(3-chloro- 2,6-diethylaniline) linkages via ultrasonication-assisted process" *Polymer Bulletin*, **2013**, 70, 2137-2149.

Mallakpour S., Madani M., "Use of silane coupling agent for surface modification of zinc oxide as inorganic filler and preparation of poly(amide-imide)/zinc oxide nanocomposite containing phenylalanine moieties" *Bulletin Materials Science*, **2012**, 35, 333-339.

Montagnaro F., Santoro L., "Reuse of combustion ashes as dyes and heavy metal adsorbents: effects of sieving and demineralization on waste properties and adsorption capacity" *Chemical Engineering Journal*, **2009**, 150, 174-180.

Moritz, M., Geszke-Moritz M., "The Newest Achievements in Synthesis, Immobilization and Practical Applications of Antibacterial Nanoparticles" *Chemical Engineering Journal*, **2013**, 228, 596-613.

Nair M. G., Nirmala M., Rekha K., Anukaliani A., "Structural, Optical, Photo Catalytic and Antibacterial Activity of ZnO and Co doped ZnO Nanoparticles" *Materials Letters*, **2011**, 65, 1797-1800.

Nourmohammadi A., Rahighi R., Akhavan O., "A. Moshfegh, Graphene oxide sheets involved in vertically aligned zinc oxide nanowires for visible light photoinactivation of bacteria" *Journal of Alloys and Compounds*, **2014**, 612,380-385.

Omar F. S., Ming H. N., Hafiz S. M., Ngee L.H., "Microwave synthesis of zinc oxide/reduced graphene oxide hybrid for adsorption–photocatalysis application" *International journal of photoenergy*, **2014**, 2014, 176835-176843.

Ozgur U., Alivov Y. I., Liu C., Teke A., Reshchikov M. A., Dogan S., Avrutin V. Cho S. J., Morkoc H. "A Comprehensive Review of ZnO Materials and Devices" *Journal of Applied Physics*, **2005**, 98, 041301-041404.

Pan Z. W., Dai Z. R., Wang Z. L., "Nanobelts of semiconducting oxides" *Science*, **2001**, 291, 1947-1949.

Pang B., Yan J., Yao L., Liu H., Guan J., Wang H., Liu H., "Preparation and characterization of antibacterial paper coated with sodium lignosulfonate stabilized ZnO nanoparticles" *RSC Advances*, **2016**, 6, 9753- 9759.

Panigrahy B., Aslam M., Misrab D. S., Bahadur D., "Polymer-mediated shape-selective synthesis of ZnO nanostructures using a single-step aqueous approach" *Crystal Engineering Communications*, **2009**, 11, 1920-1925.

Park J. H., Choi H. J., Choi Y. J, Sohn S. H., Park J. G., "Ultrawide ZnO nanosheets" *Journal of Materials Chemistry*, **2004**, 14, 35-36.

Park S., An J., Potts J. R., Velamakanni A., Murali S., Ruoff R. S., "Hydrazine-reduction of graphite- and graphene oxide" *Carbon*, **2011**, 49, 3019-3023.

Pham V. H., Pham H. D., Dang T. T., Hur S. H., Kim E. J., Kong B. S., Kima S., Chung J. S., "Chemical reduction of an aqueous suspension of graphene oxide by nascent Hydrogen" *Journal of Materials Chemistry*, **2012**, 22, 10530-10536.

Prabhakar R., Woon K. K., Yeon T. Y., "Solvothermal synthesis of ZnO nanostructures and their morphology dependent gas sensing properties" *ACS Applied Materials and Interfaces*, **2013**, 5, 3026-3032.

Pradhan D., Leung K. T., "Controlled Growth of Two-Dimensional and One-Dimensional ZnO Nanostructures on Indium Tin Oxide Coated Glass by Direct Electrodeposition" *Langmuir*, **2008**, 24, 9707-9716.

Preetam S., Ashvani K., Ajay K., Kaur D., Pandey A.,. Goyal R. N, "In situ high temperature XRD studies of ZnO nanopowder prepared via cost effective ultrasonic mist chemical vapor deposition" *Bulletin Materials Science*, **2008**, 31, 573-577.

Pueyo C. L., "Shape anisotropy influencing functional properties: trigonal prismatic ZnO nanoparticles as an example" *Advanced Functional Materials*, **2011**, 21, 295-304.

Qayyum S., Khan A. U., "Nanoparticles vs. biofilms: a battle against another paradigm of antibiotic resistance" *Medical Chemistry Communications*, **2016**, 7, 1479-1498

Qi L., Shahzad M. B., Qi Y., "A reproducible low temperature chemical solution deposition of non-polar [11 $\bar{2}$ 0] and [10 $\bar{1}$ 0] ZnO films for optoelectronic applications" *Crystal Engineering Communication*, **2016**, 18, 6573-6578.

Rafiq M. Y., Iqbal F., Aslam F., Bilal M., Munir N., Sultana I., Ashraf F., Manzoor F., Hassan N., Razaq A., "Fabrication and characterization of ZnO/MnO_2 and ZnO/TiO_2

flexible nanocomposites for energy storage applications" *Journal of Alloys and Compounds*, **2017**, 729, 1072-1078.

Raghupathi K. R., Koodali R. T., Manna A. C., "Size-Dependent Bacterial Growth Inhibition and Mechanism of Antibacterial Activity of Zinc Oxide Nanoparticles" *Langmuir*, **2011**, 27, 4020-4028.

Raqo I., Chandrajahqari C. R., Bracciale M. P., Bellis G. D., Guidi M. C., Sali D., Broggi A., Palleschi C., Sarto M. S., Uccelletti D., "Zinc oxide microrods and nanorods: different antibacterial activity ad their mode of action against Gram-positive bacteria" *RSC Advances*, **2014**, 4, 56031-56040.

Rashid J., Barakat M. A., Salah N., Habib S. S., "Ag/ZnO nanoparticles thin films as visible light photocatalyst" *RSC Advances*, **2014**, 4, 56892-56899.

Ren L., Chen D., Hu Z., Gao Z., Luo Z., Chen Z., Jiang Y., Zhao B., Lawrence Wu C. M., Shek C. H., "Facile fabrication and application of SnO2-ZnO nanocomposites: Insight into chain-like frameworks, heterojunctions and quantum dots" *RSC Advances*, **2016**, 6, 82096-82102

Rodrıiguez A., Ovejero G., Mestanza M., Garcia J., "Removal of Dyes from Wastewaters by Adsorption on Sepiolite and Pansil" *Industrial Engineering Chemistry Research.* **2010**, *49*, 3207-3216.

Sawai J., "Quantitative Evaluation of Antibacterial Activities of Metallic Oxide Powders (ZnO, MgO and CaO) by Conductimetric Assay" *Journal of Microbiological Methods*, **2003**, 54, 177-182.

Shah M. S. A. S., Park A. R., Zhang K., Park J. H., Yoo P. J., "Green Synthesis of Biphasic TiO_2−Reduced Graphene Oxide Nanocomposites with Highly Enhanced Photocatalytic Activity" *ACS Applied Materials and Interfaces*, **2012**, 4, 3893-3901.

Shanbhag V. K. L., Prasad K. S., "Graphene based sensors in the detection of glucose in saliva - A promising emerging modality to diagnose diabetes mellitus" *Analytical Methods*, **2016**, 8, 6255-6259.

Sharma P., Das M. R., "Removal of a Cationic Dye from Aqueous Solution Using Graphene Oxide Nanosheets: Investigation of Adsorption Parameters" *Journal of Chemical Engineering Data*, **2013**, 58, 151-158.

Shereema R. M., Nambiar S. R., Shankar S. S., Rao T. P., "CeO_2-MWCNT nanocomposite based electrochemical sensor for acetaldehyde*" Analytical methods,* **2015**, 7, 4912-4918.

Shi H. Q., Li W. N., Sun L.W., Liu Y., Xiao H. M., Fu S.Y., "Synthesis of silane surface modified ZnO quantum dots with ultrastable, strong and tunable luminescence" *Chemical Communications*, **2011**, 47, 11921-11923.

Shi F., Xue C., "Morphology and growth mechanism of novel zinc oxide nanostructures synthesized by a carbon thermal evaporation process" *Crystal Engineering Communication*, **2012**, 14, 5407-5411.

Shi L., Yu Q., Mao Y., Huang H., Huang H., Ye Z., Peng X., "High catalytic performance of gold nanoparticle–gelatin mesoporous composite thin films" Journal *of Materials Chemistry*, **2012**, 22, 21117-21124.

Shukla S., Chaudhary S., Umar A., Chaudhary G. R., Mehta S. K., "Tungsten oxide (WO_3) nanoparticles as scaffold for the fabrication of hydrazine chemical sensor" *Sensors and Actuators B: Chemical*, **2014**, 196, 231-237.

Singh S., Barick K. C., Bahadur D., "Shape-controlled hierarchical ZnO architectures: photocatalytic and antibacterial activities" *Crystal Engineering Communications*, **2013**, 15, 4631-4639.

Sinha A. K., Basu M., Pradhan M., Sarkar S., Pal T., "Fabrication of large-scale hierarchical ZnO hoillow spheroids for hydrophobicity and photocatalysis" *Chemistry-A European Journal*, **2010**, 16, 7865-7874.

Sirelkhatim A., Mahmud S., Seeni A., Mohamad Kaus N. H., Ann L. C., Bakhori S. K. M., Hasan H., Mohamad D., "Review on zinc oxide nanoparticles: antibacterial activity and toxicity mechanism" *Nano Micro Letters*, **2015**, 7, 219-242.

Soldatkin O.O., Kucherenko I.S., Marchenko S.V.,Ozansoy K. B., Akata B., Soldatkin A. P., Dzyadevych S.V., "Application of enzyme/zeolite sensor for urea analysis in serum" *Material Science and Engineering C Materials for Biological Applications*, **2014**, 42,155-160.

Song J., Wang X., Chang C. T., "Preparation and characterization of graphene oxide" *Journal of Nanomaterials*, **2014**, 2014, 276143-276149.

Soomro R. A., Hallam K. R., Ibupoto Z. H., Tahira A., Jawaid S., Sherazi, Sirajuddin S. T. H., Willander M., "A highly selective and sensitive electrochemical determination of melamine based on succinic acid funtionalized copper oxide nanostructures" *RSC Advances*, **2016**, 5, 105090 -105097.

Soomro R. A., Nafady A., Ibupoto Z. H., Sirajuddin., Sherazi S. T. H, Willander M., Abro M. I., "Development of sensitive non-enzymatic glucose sensor using complex nanostructures of cobalt oxide" *Materials Science in Semiconductor Processing"*, **2015**, 34, 373-381.

Spanneberg R., Schymanski D., Stechmann H., Figurab L., Glomb M. A., "Glyoxal modification of gelatin leads to change in properties of solutions and resulting films" Soft *Matter*, **2012**, 8, 2222-2229.

Stengl V., Popelkov D., Vlacil P., "TiO_2–Graphene Nanocomposite as High Performace Photocatalysts" *Journal of Physical Chemistry C*, **2011**, 115, 25209-25218.

Sun L. W., Shi H. Q., Li W. N., Xiao H. M., Fu S. Y., Cao X. Z., Li Z. X., "Lanthanum doped ZnO quantum dots with greatly enhanced fluorescent quantum yield" *Journal of Materials Chemistry*, **2012**, 22, 8221-8227.

Sun X., Maeda K., Le Faucheur M., Teramura K., Domen K. "Preparation of $(Ga_{(1-x)}Zn_x)(N_{(1-x)}O_x)$ Solid-solution from $ZnGa_2O_4$ and ZnO as a Photo-catalyst for Overall Water Splitting under Visible Light" *Applied Catalysis A*, **2007**, 327, 114-121.

Suyana P., Nishanth Kumar S., Dileep Kumar B. S., Nair B. N., Pillai S. C., Mohamed A. P., Warrier K. G. K., Hareesh U. S., "Antifungal properties of nanosized ZnS particles synthesized by sonochemical precipitation" *RSC Advances*, **2014**, 4, 8439-8445.

Szunerits S., Boukherroub R., "Antibacterial activity of graphene-based materials" *Journal of Materials Chemistry B*, **2016**, 4**,** 6892-6912.

Tajizadegana H., Jafari M., Rashidzadehb M., Teluri A. S., "A high activity adsorbent of $ZnO–Al_2O_3$ nanocomposite particles: Synthesis, characterization and dye removal efficiency", *Applied Surface Science*, **2013**, 276, 317- 322.

Thevenot D. R., Toth K., Durst R., Wilson G. S., "Electrochemical biosensors: recommended definitions and classification" *Pure Applied Chemistry*, **1999**, 71, 2333-2348.

Thool G. S., Singh A. K., Singh R. S., Gupta A., Susan M. A.B. H., "Facile synthesis of flat crystal ZnO thin films by solution growth method: a micro-structural investigation" *Journal of Saudi Chemical Society*, **2014**, 18, 712-721.

Tian L., Likun P., Xinjuan L., Sun Z., "Enhanced photocatalytic degradation of methylene blue by ZnO–reduced graphene oxide–carbon nanotube composites synthesized via microwave-assisted reaction" *Catalysis Science Technology*, **2012**, 2, 2297-2301.

Tran D. N., Balkus K. J., "Perspective of Recent Progress in Immobilization of Enzymes" *ACS Catalysis*, **2011**, 1, 956-968.

Tu W., Zhou Y., Zou Z., "Versatile Graphene-Promoting Photocatalytic Performance of Semiconductors: Basic Principles, Synthesis, Solar Energy Conversion, and Environmental Applications" *Advanced Functional Materials*, **2013**, 23, 4996-5008.

Upadhyay R. K., Soinb N., Roy S. S., "Role of graphene/metal oxide composites as photocatalysts, adsorbents and disinfectants in water treatment: a review" *RSC Advances*, **2014**, 4, 3823-3851.

Valentini L., Bon S. B., Monticelli O., Kenny J. M., "Deposition of amino-functionalized polyhedral oligomeric silsesquioxanes on graphene oxide sheets immobilized onto an amino-silane modified silicon surface" *Journal of Materials Chemistry*, **2012**, 22, 6213-6217.

Vijayalakshmi K., Sivaraj D., "Enhanced antibacterial activity of Cr doped ZnO nanorods synthesized using microwave processing" *RSC Advances*, **2015**, 5, 68461-68469.

Wan C., Frydrych M., Chen B., "Strong and bioactive gelatine-graphene oxide nanocomposites" *Soft Matter*, **2011**, 7, 6159-6166.

Wan, Q., Li Q. H., Chen Y. J., Wang T. H., He X. L., Li J. P., Lin, C. L. "Fabrication and Ethanol Sensing Characteristics of ZnO Nanowire Gas Sensors" *Applied Physics Letters*, **2004**, 84, 3654-3656.

Wang H., Li G., Jia L., Wang G., Tang C., "Controllable Preferential-Etching Synthesis and Photocatalytic Activity of Porous ZnO Nanotubes" *Journal of Physical Chemistry C*, **2008**, 112, 11738-117343.

Wang J. X., Wu C. M. L., Cheung W. S., Luo L. B., He Z. B., Yuan G. D., Zhang W. J., Lee C. S., Lee S. T., "Synthesis of Hierarchical Porous ZnO Disklike

Nanostructures for Improved Photovoltaic Properties of Dye-Sensitized Solar Cells" *Journal of Physical Chemistry C*, **2010**, 114, 13157-131561.

Wang J., Gao L., "Wet chemical synthesis of ultralong and straight single-crystalline ZnO nanowires and their excellent UV emission properties" *Journal of Materials Chemistry*, **2003**, 13, 2551-2554.

Wang J., Tsuzuki T., Tang B., Hou X., Sun L., Wang X., "Reduced Graphene Oxide/ZnO Composite: Reusable Adsorbent for Pollutant Management" *ACS Applied Materials and Interfaces*, **2012**, 4, 3084-3090.

Wang P., Zhao J., Xuan R., Wang Y., Zou C., Zhang Z., Wand Y., Xu Y., "Flexible and monolithic zinc oxide bionanocomposite foams by a bacterial cellulose mediated approach for antibacterial applications" *Dalton Transactions*, **2014**, 43, 6762-6768.

Wang W. S., Wang D. H., Qu W. G., Lu L. Q., Xu A. W., "Large Ultrathin Anatase TiO_2 Nanosheets with Exposed {001} Facets on Graphene for Enhanced Visible Light Photocatalytic Activity" *Journal of Physical Chemistry C*, **2012**, 116, 19893-19901.

Wang Y. W., Cao A., Jiang Y., Zhang X., Liu J. H., Liu Y., H. Wang, "Superior antibacterial activity of zinc oxide/graphene oxide composites originating from high zinc concentration localized around bacteria" *ACS Applied Materials and Interfaces*, **2014**, 6, 2791-2798.

Wang Y., Liu J., Liu L., Sun D. D., "Enhancing Stability and Photocatalytic Activity of ZnO Nanoparticles by Surface Modification of Graphene Oxide" *Journal of Nanoscience and Nanotechnology*, **2012**, 12, 1-7.

Wisotzki E. I., Hennes M., Schuldt C., Engert F., Knolle W., Decker U., K¨as J. A., Zink M., Mayr S. G., "Tailoring the material properties of gelatine hydrogels by high energy electron irradiation" *Journal of Materials Chemistry B,* **2014**, 2, 4297-4309.

Wolf A., Schuth F., "A systematic study of the synthesis conditions for the preparation of highly active gold catalysts" *Applied Catalysis A: General*, **2002**, 226, 1-13.

Wu R., Xie C. S., "Formation of tetrapod ZnO nanowhiskers and its optical properties" *Materials Research Bulletin,* **2004**, 39, 637-645.

Wu X. F., Zhang J., Zhuang Y. F., Fu S. D., Yu X. Y., "Synergetic reduction of graphene oxide by sodium hydroxide and microwave Irritation" *Micro Nano Letters*, **2014**, 9, 804-806.

Xiong Z., Lei Z., Xu Z., Chen X., Gong B., Zhao Y., Zhao H., Zhang J., Zheng C., "Flame spray pyrolysis synthesized ZnO/CeO_2 nanocomposites for enhanced CO_2 photocatalytic reduction under UV–Vis light irradiation" *Journal of CO_2 Utilization*, **2017**, 18, 53-61.

Xu B., Yue S., Sui Z., Zhang X., Hou S., Caoa G., Yanga Y., "What is the choice for supercapacitors: graphene or graphene oxide?" *Energy Environmental Science*, **2011**, 4, 2826-2830.

Xu J., Wang L., Zhu Y., "Decontamination of Bisphenol A from Aqueous Solution by Graphene Adsorption" *Langmuir,* **2012**, 28, 8418-8425.

Xu L., Hu Y. L., Pelligra C., Chen C. H., Jin L., Huang H., Sithambaram S., Aindow M., Joesten R., Suib S. L.**,** "ZnO with Different Morphologies Synthesized by Solvothermal Methods for Enhanced Photocatalytic Activity" *Chemistry of Materials***, 2009**, 21, 2875-2885.

Xu S., Shen Y., Ding Y., Wang Z. L., "Growth and transfer of monolithic horizontal ZnO nanowire superstructures onto flexible substrates" *Advanced Functional Materials*, **2010**, 20, 1493-1497.

Yadav B. C., Srivastava R., Dwivedi C. D., "Synthesis and characterization of ZnO-TiO_2 nanocomposite and its application as a humidity sensor" *Philosophical Magazine*, **2008**, 88, 1113-1124.

Yan C., Xue D., "Morphosynthesis of Hierarchical Hydrozincite with Tunable Surface Architectures and Hollow Zinc Oxide" *Journal of Physical Chemistry B*, **2006**, 110, 11076-11080.

Yan H., He R., Pham J., Yang P., "Morphologies of one dimentional of ZnO nano and microcrystals" *Advanced Materials*, **2003,** 15, 402-405.

Yan H., Johnson J., Law M., He R., kuutsen K., McKinney J. R., Pham j., Saykally R., Yang P., "ZnO nanoribbon microcavity lasers" *Advanced Materials*, **2003**, 15, 1907-1911.

Yang L., Wang G. Tang C. Wang H. Zhang L., "Synthesis and photoluminescence of corn-like ZnO nanostructures under solvothermal-assisted heat treatment" *Chemical Physics Letters*, **2005**, 409, 337-341.

Yang X., Chen C., Li J., Zhao G., Ren X., Wang X., "Graphene oxide-iron oxide and reduced graphene oxide-iron oxide hybrid materials for the removal of organic and inorganic pollutants" *RSC Advances*, **2012**, 2, 8821-8826.

Yin P. T., Kim T. H., Choi J. W., Lee K. B., "Prospects for graphene–nanoparticle-based hybrid sensors" *Physical Chemistry Chemistry Physics*, **2013**,15, 12785-12799.

Yoshitake M., Masao Y., Won S. S., Kunihito K., "Photoluminescence from ZnO nanoparticles embedded in an amorphous matrix" *Crystal Growth and Design*, **2008**, 8, 1503-1508.

Zeng X., Wang G., Liu Y., Zhang X., "Graphene-based antimicrobial nanomaterials: rational design and applications for water disinfection and microbial control" *Environmental Scence: Nano*, **2017**, 4, 2248-2266.

Zhang N., Yang M. Q., Liu S., Sun Y., X Y. J., "Waltzing with the versatile platform of graphene to synthesize composite photocatalysis" *Chemical Review*, **2015**, 18, 10307-10377.

Zhang N., Zhang Y., Pan X., Yang M. Q., Xu Y. J., "Constructing Ternary CdS–Graphene–TiO_2 Hybrids on the Flatland of Graphene Oxide with Enhanced Visible-Light Photoactivity for Selective Transformation" *Journal of Physical Chemistry C*, **2012**, 116, 18023-18031.

Zhang N., Zhang Y., Xu Y. J., "Recent progress on graphene-based photocatalysts: current status and future perspectives" *Nanoscale*, **2012**, 4, 5792-5813.

Zhang Q., Tian C., Wu A., Tan T., Sun L., Wang L., Fu H., "A facile one-pot route for the controllable growth of small sized and well-dispersed ZnO particles on GO-derived graphene" *Journal of Material Chemistry*, **2012**, 22, 11778-11784.

Zhang Y., Xu J. Q., Xiang Q., Li H., Pan Q. Y., Xu P. C., "Brush-Like Hierarchical ZnO Nanostructures: Synthesis, Photoluminescence and Gas Sensor Properties" *Journal of Physical Chemistry C*, **2009**, 113, 3430-3435**.**

Zhao Y., Fan L., Hong B., Ren J., Zhanga M., Queb Q., Jib J., "Nonenzymatic detection of glucose using three-dimensional PtNinanoclusters electrodeposited on the multiwalled carbon nanotubes" *Sensors and Actuators B*, **2016**, 231, 800-810.

Zhao Y., Song X., Song Q., Yin Z., "A facile route to the synthesis copper oxide/reduced graphene oxide nanocomposites and electrochemical detection of catechol organic pollutant" *Crystal Engineering Communications,* **2012**, 14, 6710-6719.

Zheng M. J., Zhang L. D., Li G. H., Shen W. Z., "Fabrication and optical properties of large-scale uniform zinc oxide nanowire arrays by one-step electrochemical deposition technique" *Chemical Physical Letters*, **2002**, 363, 123-128.

Zhong Z., Xu Z., Sheng T., Yao J., Xing W., Wang Y., "Unusual air filters with ultrahigh efficiency and functionality enabled by ZnO nanorods" *ACS Applied Materials and Interfaces,* **2015**, 7, 21538-21544.

Zhou J., Zhou M., Chen Z., Zhang Z., Chen C., Li R., Gao X., Xie E., "SiC nanotubes arrays fabricated by sputtering using electronspun PVP nanofiber as templates" *Surface Coating Technology*, **2009**, 203, 3219-3223.

Zhu H., Li L., Zhou W., Shaode Z., Chen X., "Advances in non-enzymatic glucose sensors based on metal oxides" *Journal Materials Chemistry B,* **2016**, 4, 7333-7349.

Zhu Y. P., Li M., Liu Y. L., Ren T. Z., Yuan Z. Y., "Carbon-Doped ZnO Hybridized Homogeneously with Graphitic Carbon Nitride Nanocomposites for Photocatalysis" *Journal of Physical Chemistry C*, **2014**, 118, 10963-10971.

Zhu Y., Murali S., Cai W., Li X., Suk J. W., Potts J. R., Ruoff R. S., "Graphene and Graphene Oxide: Synthesis, Properties, and Applications" *Advanced Materials,* **2010**, 22, 3906-3924.

List of international Publications

Publications from the thesis

(1) **K. B. Babitha**, V. Linsha, S. Anas, A. Peer Mohamed, M. Kiran, and S. Ananthakumar, Microwave assisted aqueous synthesis of organosilane treated mesoporous Si@ZnO nanoarchitectures as dual-functional, photocatalysts, *Journal of Environmental Chemical Engineering*, 3 (2015) 1337-1345.

(2) **K. B. Babitha**, Jani Matilda, A. Peer Mohamed, and S. Ananthakumar, Catalytically engineered reduced graphene oxide/ZnO hybrid nanocomposites for the adsorption, photoactivity and selective oil pick-up from aqueous media, *RSC Advances*, 5 (2015) 50223-50233.

(3) **K. B. Babitha**, S. Nishanth Kumar, Vijayan Pooja, B. S. Dileep Kumar, A. Peer Mohamed, and S. Ananthakumar, Design and synthesis of ZPMx-Si@GO hybrid nanocomposite with various aspect ratios for water disinfection, *Chemical Engineering Journal*, 324 (2017) 154-167.

(4) **K. B. Babitha**, R. B. Rakhi, P. S. Soorya, A. Peer Mohamed and S. Ananthakumar, Synthesis of ZnO@rGO nanocomposites for the enzyme free electrochemical detection of urea and glucose (To be communicated).

(5) **K. B. Babitha**, Priya, B. Krishanakumar, A. Peer Mohamed, S. Ananthakumar, Fabrication of flexible and hydrophobic ZnO decorated gelatin bio-hybrid films for pharmaceutical and food packaging applications (Under preparation).

Publications other than thesis

(6) N. Harsha, K. R. Ranya, **K. B. Babitha**, S. Shukla, S. Biju, M. L. P. Reddy, K. G. K. Warrier, Hydrothermal processing of hydrogen titanate/anatase-titania nanotubes and their application as strong dye-adsorbents, *Journal of Nanoscience and Nanotechnology*, 11 (2011) 1175-1187.

(7) **K. B. Babitha**, K. G. K. Warrier, S. Shukla, Decolorization of aquoeus solution containing organic synthetic dye *via* dark catalysis process using hydrothermally synthesized semiconductor oxides nanotubes, *Advanced Science, Engineering and Medicine*, 6 (2014) 173-183.

(8) P. Hareesh, **K. B. Babitha**, S. Shukla, Processing flyash stabilised hydrogen titanate nano sheets for industrial dye removal application, *Journal of Hazardous Materials*, 229-230 (2012) 177-182.

(9) **Babitha K. Babu**, Jeena Vadakke Purayil, Hareesh Padinhattatyil, Satyajit Shukla, Krishna Gopakumar Warrier, Silica-Based NTPC-Fly Ash for Dye-Removal Application and Effect of Its Modification, *International Journal of Applied Ceramic Technology*, 10 (2013) 186–201.

(10) S. Anas, S. Rahul, **K. B. Babitha**, R. V. Managlaraja, S. Ananthakumar, Microwave accelerated synthesis of zinc oxide nanoplates and their enhanced photocatalytic activity under UV and solar illuminations, *Applied Surface Science*, 355 (2015) 98-103.

(11) N. Harsha, **K. B. Babitha**, S. Shukla, K. G. K. Warrier, Comparing effects of silver and iron deposition on dye adsorption in dark using anatase-titania nanotubes-catalyst, *Nanoscience and Nanotechnology Letters*, 3 (2011) 809-814.

(12) K. Aboo Shuhailath, Vazhayal Linsha, Sasidharan Nishanth Kumar, **K. B. Babitha**, A. Peer Mohamed, S. Ananthakumar, Photoactive antimicrobial CeO_2 decorated AlOOH/PEI hybrid nanocomposte: a multifunctional catalyst-sorbent for lignin and organic dye, *RSC Advances*, 6 (2016) 54357-54370.

(13) Santhosh Balanand, **K. B. Babitha**, Mathews Jeen Maria, A. Peer Mohamed, S. Ananthakumar, Aqueous Mechanical Oxidation of Zn Dust: An inventive Technique for Bulk Production of ZnO Nano rods and Catalyst free H_2 gas synthesis, *ACS Sustainable Chemistry & Engineering*, 6 (2018) 143-154.

List of conference attended

(1) **K. B. Babitha**, J. Jani Metilda, A. Peer Mohamed and S. Ananthakumar, In-situ Growth of ZnO nanocrystals on Graphene Oxide Exfoliates and Its Deposition on Cotton Textiles to Design Self-Regenerative Oil Adsorbent, Heam 2014, Kerala university, November 17-18, 2014 (Oral Presentation).

(2) **K. B. Babitha**, M. Jani, A. Peer Mohamed and S. Ananthakumar, A one pot microwave mediated in-situ growth of ZnO nanocrystals on the graphene oxide sheets for the environmental application, Nano Mission's National Level meet, [NANO-INDIA-2015], SASTRA University, Thanjavur, Tamil Nadu, January 29-30, 2015 (Poster Presentation).

(3) **Babitha K. B**., Linsha V., Suchithra P.S., Peer Mohamed and Ananthakumar S., Al_2O_3 & CuO doped mesoporous ZnO-SiO_2 aerogel catalysts for energy sector, 75^{th} Annual Session of ICS, Agra, December 20-22, 2011(Poster Presentation).

(4) **Babitha K. B**., Suchithra P. S., Linsha V., Soumya S. and Ananthakumar S., Design of Al_2O_3 and CuO doped mesoporous ZnO-SiO_2 composite via sol-gel assisted microwave method, CTRIC 2012, Cochin University of Science and Technology (CUSAT), January 20-21, 2012(Poster Presentation).

(5) **Babitha K. B.,** Chitra P., Soumya S., Peer Mohammed, Ananthakumar S, Fabrication of multifunctional high surface area organosilane grafted ZnO particles via a novel microwave assisted aqueous deposition technique , Emerging Trends in Chemical Sciences. National Seminar on Emerging Trends in Chemical Sciences (ETCS-2013), Department of Chemistry, University of Kerala, Kariavattom, May 29-31, 2013 (Poster Presentation) **(BEST POSTER AWARD)**.

(6) **Babitha K. B.,** Linsha V., Suchithra P. S., Peer Mohamed and Ananthakumar S., Gel Mediated Grown ZnO Aerogel-A potential light harvesting and Energy Conversion Porous Ceramics, International Conference on Emergence of new era in Glass and Ceramic, (NEGC), Ahmedabad, Gujarat, India, January 17-20, 2013 (Poster Presentation).

(7) **Babitha K. B**., Linsha V., Peer Mohammed., Ananthakumar S., Green synthesis of organosilane grafted ZnO nanohybrids - a promising ZnO based material, for the enhanced adsorption and degradation of organic anionic dye, National seminar: Materials; Process and Applications of Novel Technologies [NMAT], Department of Physics, HHMSPB NSS College, Thiruvananthapuram, 7-8 November 2013(Oral Presentation).

(8) **Babitha K. B**., R. B. Rakhi, P. S. Soorya, M. L. Lekshmi, A. Peer Mohamed and S. Ananthakumar, Development of ZnO@rGO nanocomposites for the enzyme free electrochemical detection of urea and glucose, National Seminar on Advanced Materials (NSAM-2017), Department of Chemistry, University of Kerala, Kariavattom, October 4^{th}, 2017(Oral Presentation).